

**First Measurement of the
Branching Ratio Fraction
 $BR(W \rightarrow \tau\nu \rightarrow \mu\nu\nu)/BR(W \rightarrow \mu\nu)$
in $\sqrt{s} = 7$ TeV Proton-Proton Collisions
with the ATLAS Detector and
Realization of a Production Facility for Large Scale
Micromegas Drift Boards**

Dissertation
zur Erlangung des Grades
"Doktor
der Naturwissenschaften"
am Fachbereich Physik, Mathematik und Informatik
der Johannes Gutenberg-Universität
in Mainz

Andreas Christian Düdder

geb. in Bad Kreuznach

Mainz, den 14.03.2019



JOHANNES GUTENBERG
UNIVERSITÄT MAINZ

Ich versichere, dass ich die Arbeit selbstständig verfasst und keine anderen als die angegebenen Quellen und Hilfsmittel benutzt sowie Zitate kenntlich gemacht habe.

Andreas Döhle

Mainz, den 14.03.2019

Mündliche Prüfung: 26.11.2019

1. Berichterstatter: [REDACTED]

2. Berichterstatter: [REDACTED]

Zusammenfassung

Die Forschungseinrichtung CERN in Genf ist das weltgrößte Teilchenphysiklabor und beheimatet mit dem Large Hadron Collider (LHC) den höchstenergetischen Teilchenbeschleuniger. Mit der Entdeckung des Higgs Bosons 2012 durch die LHC Experimente ATLAS und CMS wurde ein Meilenstein im Verständnis des Standard Modells der Teilchenphysik erreicht.

Die Suche nach neuen Teilchen und im Allgemeinen, nach neuer Physik, ist eine der Hauptgründe für Hochenergieteilchenphysikexperimente. Unbekannte Teilchen können zum einen durch ihre direkte Erzeugung in Teilchenkollisionen nachgewiesen werden, zum anderen kann auf sie aber auch durch Abweichungen von Präzisionsmessungen von der Standard Modell Vorhersage geschlossen werden. Treten neue Teilchen oder Wechselwirkung als Beitrag in bekannten Prozessen auf, kann beispielsweise das Verzweigungsverhältnis von Teilchenzerfällen verändert werden.

In dieser Arbeit wird eine erste Messung des W Boson Zerfallsverhältnisses $BR(W \rightarrow \tau\nu \rightarrow \mu\nu\nu)/BR(W \rightarrow \mu\nu)$ am LHC vorgestellt. Dieser Prozess ist relevant, da frühere Messungen Hinweis auf eine Verletzung der Leptonuniversalität in der dritten Generation gegeben haben. Die Messung wurde als ein Templatefit kinematischer Variablen der Monte Carlo simulierten Detektorsignale an die gemessenen Daten implementiert. Im Rahmen dieser Analyse wurde die wohlverstandenen Daten und Simulationen der W Boson Massenmessung bei einer Schwerpunktenenergie von $\sqrt{s} = 7$ TeV verwendet. Innerhalb der kinematischen Schnitte dieser Analyse wurde das Verzweigungsverhältnis $BR(W \rightarrow \tau\nu \rightarrow \mu\nu\nu) = 0.228_{-0.023}^{+0.024(0.010)}$ bei einer Messgenauigkeit von 13% gemessen, wobei eine untersuchte Erweiterung des kinematischen Bereichs eine 4% Ungenauigkeit und damit einen Einfluss auf den Weltmittelwert erwarten lässt.

Da der LHC dauerhaft weiterentwickelt wird und die Umsetzung des Hochraten LHC beschlossen wurde, müssen auch die Teilchendetektoren an die höheren Interaktionsraten angepasst werden um zukünftige Präzisionsmessungen zu gewährleisten. Im Rahmen des ATLAS New Small Wheel Upgrades für verbesserte Hochratentriggerbedingungen wurde im Rahmen dieser Arbeit eine Produktionsstätte für hochplanare großflächige Detektorkomponenten aufgebaut.

Neben den Produktionsprozessen und der Infrastruktur wurde die Qualitätssicherung und -kontrolle entwickelt, die anlaufende Produktion geleitet und die laufende Pro-

duktion begleitet. Die Ergebnisse der Qualitätskontrolle zeigen, dass die Produktion nicht nur mit Abstand als erste in der Kollaboration abgeschlossen werden konnte, sondern auch 90 % der Produkte die ATLAS Anforderungen erfüllten. Die übrigen Komponenten konnten nach einer geringfügigen Aufarbeitung ebenfalls zum Einbau im New Small Wheel freigegeben werden. In dieser Arbeit wird der komplette Ablauf von der Werkzeugentwicklung über die Produktionsabläufe bis zur Qualitätssicherung dargelegt.

Abstract

The CERN research complex at Geneva is the worldwide largest high energy particle lab hosting with the Large Hadron Collider (LHC) the most powerful accelerator. A major step in our understanding of the Standard Model, as the base of particle physics, was achieved by the LHC experiments ATLAS and CMS with the discovery of the Higgs boson in 2012.

The search for new particles and in general new physics is the driving motivation for high energy particle physics experiments. New particles can be either detected at the so called high energy frontier, by their direct production in particle collisions, or via hints in precision measurement. As new particles or couplings occur as contributions to known Standard Model processes, for example the branching ratio of a decay may be altered.

This thesis presents the first branching ratio fraction measurement of the W boson decay $BR(W \rightarrow \tau\nu \rightarrow \mu\nu\nu)/BR(W \rightarrow \mu\nu)$ at the LHC. This process is of interest, as hints for a violation of the lepton universality were found in decays to the third generation. The measurement was implemented as a template fit of the Monte Carlo simulated detector signals for the relevant processes to the measured data and the expected sensitivity has been estimated. This analysis was based on the well understood data and simulation used for the measurement of the W mass at $\sqrt{s} = 7$ TeV. Within the kinematic range of that measurement, the branching ratio $BR(W \rightarrow \tau\nu \rightarrow \mu\nu\nu) = 0.228^{+0.024(0.010)}_{-0.023(0.010)}$ with a sensitivity of 13 % was found, with a perspective to a 4 % sensitivity for relaxed kinematic cuts, which becomes compatible for the inclusion in the world average.

As the LHC is under constant development and improvement and the perspective for the high luminosity LHC with larger interaction rates was set, the detectors need to improved to keep up with the event reconstruction at higher occupancies to allow for future precision measurements. In the perspective of the ATLAS New Small Wheel upgrade for a improved event triggering during the data taking at high multiplicities, a production facility for high planarity large scale gas detector components was set up in the scope of this thesis.

Besides the mechanical infrastructure for the component production, the quality control methods have been developed and characterized, the starting production was lead and the whole series production was accompanied. The quality control

results show, that not only the production could be finished by far as the first production site in the collaboration, but also 90 % of the components fulfill the quality requirement of the ATLAS collaboration and the remaining parts could be accepted for the assembly after a small reworking. In this work the full chain of the detector construction, from the tooling development over the production principle to the quality control methods, documentation and results is presented.

Contents

1	Introduction	1
2	A Glance on High Energy Particle Physics	3
2.1	The Standard Model	3
2.1.1	Quantum Electrodynamics: $U(1)$ Local Gauge Invariance . . .	3
2.1.2	Quantum Chromodynamics: $SU(3)$ Local Gauge Invariance . .	4
2.1.3	The Electroweak Unification	5
2.1.4	The Higgs Mechanism	7
2.1.5	W -Boson Creation in Proton-Proton Collisions	8
2.2	Accelerators and Detectors	10
2.2.1	The LHC at CERN	10
2.2.2	The ATLAS Detector at CERN	11
3	Measurement of $BR(W \rightarrow \tau\nu \rightarrow \mu\nu\nu)/BR(W \rightarrow \mu\nu)$	21
3.1	Motivation and Measurement Procedure	21
3.2	Data and Monte Carlo Samples	23
3.2.1	Data Sample and Event Topology	24
3.2.2	Event Selection	25
3.2.3	Monte Carlo Simulation	28
3.3	Signal and Background Processes	29
3.3.1	Monte Carlo simulated Prozesses	29
3.3.2	Multijet Background	30
3.4	Physics Modeling Corrections and Related Uncertainties	33
3.4.1	Electroweak Corrections	33
3.4.2	Rapidity and Angular Coefficient Corrections	34
3.4.3	Boson Transverse Momentum Corrections	34
3.4.4	Reweighting	34
3.4.5	Uncertainty Propagation	35
3.5	Reconstruction Corrections and Related Uncertainties	35
3.5.1	Recoil Calibration	35
3.6	Detector Corrections and Uncertainty Estimation	40
3.6.1	Muon Scale Factors	40
3.6.2	Muon Transverse Momentum Calibration	41
3.7	Fitting Procedure	45

3.7.1	Overview of the Fitting Framework	45
3.7.2	Asimov and Toy Datasets	48
3.7.3	Input Smoothing	49
3.7.4	Systematic shape Variations	49
3.7.5	Preparation of the Shape Systematics	50
3.7.6	Approaches to Parametrize the Branching Ratio Fraction . . .	53
3.8	Asimov and Toy Data Results	54
3.8.1	Fitting Settings	54
3.8.2	Fitting Results	55
3.8.3	Fit Stability	59
3.8.4	Fit Closure	59
3.8.5	Conclusion	62
3.9	Measurement Result	62
3.10	Extrapolation of the Fitting Range	64
3.11	Summary and Outlook	67
4	Micromegas Drift Panels for the ATLAS NSW Upgrade	71
4.1	Micromegas Detectors	71
4.1.1	Multiple Scattering	71
4.1.2	Ionization	72
4.1.3	Electron Transport in Gases	74
4.1.4	Gas Amplification	75
4.1.5	Layout of Micromegas Detectors	75
4.1.6	Performance of Micromegas detectors	76
4.2	The ATLAS New Small Wheel Upgrade	80
4.2.1	Micromegas Quadruplet Layout	82
4.2.2	Drift Panels Mechanical Design	84
4.2.3	Drift Panel Specifications	87
4.3	Material Irradiation Studies	88
4.4	Production Infrastructure	91
4.4.1	Lab Infrastructure	91
4.4.2	Vacuum Table Construction	94
4.4.3	Alignment System	98
4.5	Drift Panel Production	100
4.5.1	First Production Step	101
4.5.2	Second Production Step	105
4.5.3	Panel Finalization	107
4.5.4	Delamination Repair Procedure	108
4.6	Quality Control Methods	110
4.6.1	Database and Interface	110
4.6.2	Raw Material Quality Control	111
4.6.3	Drift Panel Quality Control	113

4.6.4	Planarity Measurements	114
4.6.5	Gas Tightness Measurement	124
4.7	Project Perspective	130
4.7.1	Degassing Studies	130
4.7.2	Sparking impacts	133
4.8	Summary and Outlook	135
5	Conclusion	139
A	Appendix	141
A.1	Branching Ratio Fraction Determination	141
A.1.1	Smoothing Results	141
A.1.2	Fit Stability	142
A.1.3	Fitting Results	146
A.2	NSW Drift Panel Construction	150
A.2.1	Alignment Frame Drawings	150
A.2.2	SM2 Drift Panel Construction Manual	166
A.2.3	SM2 Drift Panel Construction Database Manual	185
A.2.4	SM2 Drift Panel Gluing Check List	195
A.2.5	SM2 Drift Panel Gluing Quality Control Sheet	197
A.2.6	SM2 Drift Panel Quality Control Result Overview	198
A.2.7	Material Degassing	201
B	Acknowledgements	213

The Standard Model of particle physics stands in a long queue of descriptions of the fundamental laws of physics. While the concept of a structure formed by elementary, undeviable particles was already developed by Greek philosophers, the Standard Model is based on an elaborated mathematical structure and is able to formulate precise predictions. These predictions allow to test the model and make it a theory in the sense of philosophy of science. A brief introduction to the Standard Model and the detector facilities used to probe this theory will be given in Chapter 2.

One of the Standard Model prediction is lepton universality. It predicts that the coupling of the fundamental forces to leptons is equal for representatives of all three generations. Recent measurements have shown a tension in the coupling to the third lepton generation in the decay of hadrons into tau leptons.

This work aims for a first precision measurement of the W boson decay branching ratio fraction $BR(W \rightarrow \tau\nu \rightarrow \mu\nu\nu)/BR(W \rightarrow \mu\nu)$ at the Large Hadron Collider (LHC). The elaborate simulation frameworks for high energy particle physics not only allows for the precise theoretical calculation of the physical process, but also includes an accurate modeling of the particle reconstruction in the detector. Such single processes, which cannot be resolved in the detector reconstruction can be simulated independently. A slight shape difference of observable spectra between the single processes makes the measured inclusive distribution sensitive to a change in the ratio of the subprocesses. The branching ratio fraction therefore can be measured by a template fit of the simulated single processes to the measured data of the full W boson decay.

In Chapter 3 the measurement strategy and a perspective to the expected sensitivity is presented. First a detailed motivation and description of the detector calibration and physics modeling in the simulation is given. The fitting framework comprising different parametrizations of the branching ratio fraction is validated with Asimov and toy data. A possible, future sensitivity increase by the extension of the studied kinematic range is highlighted and a first results are discussed with the outlook to planned activities on this study.

While the current precision measurements can only be performed after a yearslong calibration procedure and modeling improvement of the simulated data also the preparation of the current and future data taking and guarantee of a high data quality is essential to allow for future precision measurements. The LHC will operate at higher energies and luminosities in the next years, on one hand producing a massive amount of data with a large potential for new discoveries, on the other hand

delivering higher and higher interaction rates, which make the event reconstruction more and more challenging. To counteract this effect, the particle detectors are under constant development.

One of the major current upgrade programs of the ATLAS detector is the New Small Wheel (NSW) upgrade with a planned installation during the LHC shutdown in 2019 and 2020. The exchange of the first chambers of the muon system in the direction of the beam pipe becomes necessary, as the currently used detector technology is not capable to deal with the expected high interaction rates and not only the event reconstruction, but already the event recording on the base of a valid trigger decision would be endangered.

The New Small Wheel upgrade and the related work is presented in Chapter 4. First the detector technology and the upgrade program is described. The developed production facility, tooling and procedure for high planarity detector components is explained in detail. The Mainz production site was responsible to build the cathode surfaces enclosing the detector gas volume. These parts require a high surface planarity ($\text{RMS} < 37 \mu\text{m}$) for a stable detector operation. The production results are shown together with a specification of the quality control methods. In the outlook of the project status, possible reasons for observed high voltage instabilities are investigated.

A Glance on High Energy Particle Physics

2.1 The Standard Model

The Standard Model of particle physics is a gauge quantum field theory with the underlying symmetry $SU(3) \times SU(2) \times U(1)$. While a global gauge invariance leads, according to the Noether theorem, to a conservation law, as the time invariance of a system results in the conservation of energy, the structure of the Standard Model interactions is derived as a consequence of the field's local gauge invariance. This concept is easiest to understand in the derivation of the electromagnetic interaction as a consequence of an underlying $U(1)$ gauge symmetry.

2.1.1 Quantum Electrodynamics: $U(1)$ Local Gauge Invariance

The Lagrangian of a vector field is given by

$$\mathcal{L} = i\bar{\Psi}\gamma^\mu\delta_\mu\Psi - m\bar{\Psi}\Psi, \quad (2.1)$$

with the four dimensional spinors Ψ , the Dirac matrices γ^μ and the particle mass m . With the Euler-Lagrange equations applied to this Lagrangian, the resulting Dirac equation already predicts antimatter and requires the quantization of the field Ψ . Such it forms a quantum field theory of non interacting particles.

The interaction is introduced by requiring a local gauge invariance following the $U(1)$ symmetry

$$\Psi(x) \rightarrow e^{i\alpha(x)}\Psi(x), \quad (2.2)$$

with the position-dependent parameter $\alpha(x)$ making the gauge transformation local. While the last term of the Lagrangian is invariant under the transformation, the derivative transforms as

$$\delta_\mu \rightarrow e^{i\alpha(x)}\delta_\mu\Psi + i\delta_\mu\alpha(x)e^{i\alpha(x)}\Psi. \quad (2.3)$$

To satisfy the local gauge invariance, a vector field A_μ which transforms as

$$A_\mu \rightarrow A_\mu + \frac{1}{e}\delta_\mu\alpha(x) \quad (2.4)$$

is introduced and the partial derivative in 2.1 is replaced by the covariant derivative

$$D = \delta_\mu - ieA_\mu. \quad (2.5)$$

The gauge invariant Lagrangian is now given as

$$\mathcal{L} = i\bar{\Psi}\gamma^\mu D_\mu\Psi - m\bar{\Psi}\Psi. \quad (2.6)$$

Expanding the Lagrangian again to a simple partial derivative and introducing the field strength tensor

$$F_{\mu\nu} = \delta_\mu A_\nu - \delta_\nu A_\mu, \quad (2.7)$$

to cover the kinetic energy of the field A_μ , one obtains

$$\mathcal{L} = \bar{\Psi}(i\gamma^\mu\delta_\mu - m)\Psi + e\bar{\Psi}\gamma^\mu A_\mu\Psi - \frac{1}{4}F_{\mu\nu}F^{\mu\nu}. \quad (2.8)$$

The first term identifies as the interaction free Lagrangian. The second part includes the interaction of the gauge field A_μ with the spinor Ψ . This describes the interaction of photons, as gauge bosons, with fermion and the coupling strength e is identified as the electric charge. The third term describes the energy stored in the gauge field. This examples shows how the introduction of a new field A_μ can restore the local gauge invariance while introducing an interaction to the theory. It also becomes obvious, that a massive gauge boson, adding a term $\propto mA_\mu A^\mu$, is forbidden by the local gauge invariance.

2.1.2 Quantum Chromodynamics: $SU(3)$ Local Gauge Invariance

Similar to the example of quantum electro dynamics, the structure of the strong interaction can be retrieved from the underlying $SU(3)$ symmetry. The strong interaction couples to the color charge. Similar to additive color mixing, the colors "red", "green" and "blue" are defined together with corresponding anti-colors for anti-particles. The gauge transformation is given by

$$q(x) \rightarrow e^{i\alpha_a(x)T_a(x)}q(x). \quad (2.9)$$

Here, in contrast to the previous case, given in equation 2.2, the spinor is named $q(x)$ to indicate that only the quark fields are considered. The index $a \in [1, 8]$ on the scaling parameter $\alpha_a(x)$ illustrates, that the parameter depends on the linear independent, traceless 3×3 matrices T_a , which stand for the interaction with one of the eight possible color combinations for gluons, the mediators of the strong force. The number of colors is a direct consequence of the underlying $SU(3)$ symmetry. As $SU(3)$ is a non-Abelian group, the generators T_a do not commute

$$[T_a, T_b] = if_{abc}T_c, \quad (2.10)$$

given the structure constant of the gauge group f_{abc} . This gives rise to an additional term in the transformation of the gauge fields, representing the gluons, compared to equation 2.4

$$G_\mu^a \rightarrow G_\mu^a - \frac{1}{g} \delta_\mu \alpha_a(x) - f_{abc} \alpha_b G_\mu^c. \quad (2.11)$$

With the covariant derivative

$$D_\mu = \delta_\mu + ig T_a G_\mu^a \quad (2.12)$$

the Lagrangian becomes

$$\mathcal{L} = \bar{q}(i\gamma^\mu \delta_\mu - m)q - g(\bar{q}\gamma_\mu T_a q)G_\mu^a - \frac{1}{4}G_{\mu\nu}^a G_{\mu\nu}^a. \quad (2.13)$$

To keep the kinetic energy invariant under the gauge field transformation 2.11, the tensor $G_{\mu\nu}^a$ has a more complex structure than in the case of the $U(1)$ gauge invariance

$$G_{\mu\nu}^a = \delta_\mu G_\nu^a - \delta_\nu G_\mu^a - gf_{abc} G_\mu^b G_\nu^c. \quad (2.14)$$

This results in contributions of the shape " $\propto G^3$ " and " $\propto G^4$ " which describe, by a three or four gluon vertex, the gluon self interaction as part of the kinetic energy. The self interaction of the mediator particle has a major impact on the properties of the interaction and results in the so called confinement of quarks. As the distance between quarks rises the energy stored in the gluon self interaction also rises and new quark-antiquark pairs are created resulting in the formation of color neutral bound quark states. Therefore they either carry all three different colors or a combination of one kind of color and the corresponding anti-color. Free quarks can only be assumed at high energies, the regime of asymptotic freedom. Only in this case, quantum chromodynamics can be treated as a perturbation theory.

2.1.3 The Electroweak Unification

The symmetry of the electroweak interaction is based on a $SU(2) \times U(1)$ symmetry. Observations have shown, that the weak interaction only couples to left handed fermions. The left and right handed component of a spinor Ψ is defined as

$$\Psi_L = \frac{1}{2}(1 - \gamma_5)\Psi \quad (2.15)$$

$$\Psi_R = \frac{1}{2}(1 + \gamma_5)\Psi, \quad (2.16)$$

where $\gamma_5 = i\gamma_0\gamma_1\gamma_2\gamma_3$ is the product of the Dirac matrices.

The weak interaction couples to the weak isospin T assigned to the left handed fermions and is generated by T_t , $t \in [1, 3]$, the generators of $SU(2)_L$. The three corresponding gauge boson are described by the gauge field W_t^μ .

The $U(1)_Y$ couples to the hypercharge Y and is included by a gauge field B^μ . The electromagnetic charge Q is defined by

$$Q = T^3 + \frac{Y}{2}. \quad (2.17)$$

The gauge transformations are defined independently for the left and right handed part of the spinor

$$\Psi_L \rightarrow e^{i\theta_i(x)T + i\beta(x)Y} \Psi_L \quad (2.18)$$

$$\Psi_R \rightarrow e^{i\beta(x)Y} \Psi_R. \quad (2.19)$$

This transformation results in the Lagrangian

$$\begin{aligned} \mathcal{L} = & \bar{\Psi}_L \gamma^\mu \left(i\delta_\mu + \frac{1}{2}g\vec{\tau} \cdot \vec{W}_\mu - \frac{1}{2}g'B_\mu \right) \Psi_L + \bar{\Psi}_R \gamma^\mu (i\delta_\mu - g'B_\mu) \Psi_R \\ & - \frac{1}{4}W_{\mu\nu}^i W^{i\mu\nu} - \frac{1}{4}B_{\mu\nu} B^{\mu\nu}, \end{aligned} \quad (2.20)$$

with

$$W_{\mu\nu}^i = \delta_\mu W_\nu^i - \delta_\nu W_\mu^i + g\epsilon_{ijk} W_\mu^j W_\nu^k \quad (2.21)$$

$$B_{\mu\nu} = \delta_\mu B_\nu - \delta_\nu B_\mu. \quad (2.22)$$

The physical boson fields W_μ^\pm , Z_μ and A_μ are retrieved as a linear combination of the gauge fields W^i and B

$$W_\mu^\pm = \frac{1}{\sqrt{2}} (W_\mu^1 \mp W_\mu^2) \quad (2.23)$$

$$Z_\mu = \frac{gW_\mu^3 - g'B_\mu}{\sqrt{g^2 + g'^2}} \quad (2.24)$$

$$A_\mu = \frac{g'W_\mu^3 + gB_\mu}{\sqrt{g^2 + g'^2}}. \quad (2.25)$$

The coupling constants g and g' are related to the electrical charge by the Weinberg angle θ_W

$$e = g \sin \theta_W = g' \cos \theta_W. \quad (2.26)$$

Equation 2.21 shows similar self interaction terms, as observed for the gluon field of quantum chromodynamics. This poses the question, why no confinement is observed for the weak interaction. The reason is the mass of the weak gauge bosons, which effectively shortens the range of the interaction. Neither fermion nor gauge boson masses can be included in the electroweak Lagrangian, as the combination of the left handed doublet Ψ_L and the right handed singlet Ψ_R would break the gauge invariance. The mass of the particles is therefore created by spontaneous symmetry breaking of a Higgs field.

2.1.4 The Higgs Mechanism

To recover the masses in the electroweak Lagrangian, a $SU(2)$ doublet Φ with weak hypercharge $Y = 1$ is introduced. The Lagrangian is given by

$$\mathcal{L} = (D_\mu \Phi)^\dagger (D^\mu \Phi) - V(\Phi^\dagger \Phi), \quad (2.27)$$

with the electroweak covariant derivative D_μ and the potential

$$V(\Phi^\dagger \Phi) = -\mu^2 \Phi^\dagger \Phi + \lambda (\Phi^\dagger \Phi)^2. \quad (2.28)$$

This choice of the potential is the most general one, as higher order terms would violate the renormalizability of the theory. For $\mu^2 > 0$ and $\lambda > 0$, the potential has a minimum at

$$\Phi^\dagger \Phi = -\frac{\mu^2}{2\lambda}, \quad (2.29)$$

which forms a circle in the complex plane. To break this $SU(2)$ symmetry, a particular choice for the vacuum expectation value can be made. Choosing

$$\Phi_0 = \frac{1}{\sqrt{2}} \begin{pmatrix} 0 \\ \nu \end{pmatrix} \quad (2.30)$$

the field can be expressed as expansion

$$\Phi = e^{i\vec{\tau} \cdot \vec{\xi}/2\nu} \begin{pmatrix} 0 \\ \nu + H/\sqrt{2} \end{pmatrix}. \quad (2.31)$$

The Goldstone boson field $\vec{\xi}$ can be gauged and the theory only introduces the massive Higgs field H as a new particle. Substituting equation 2.31 into the Lagrangian the boson mass terms can be read off as

$$M_W = \frac{1}{2} g \nu \quad (2.32)$$

$$M_Z = \frac{1}{2} \frac{\nu}{\cos \theta_W} \quad (2.33)$$

$$M_H = \sqrt{2\mu^2}. \quad (2.34)$$

In a similar way the mass terms for the fermions can be retrieved as

$$m_f = \frac{G_f}{\sqrt{2}} \nu. \quad (2.35)$$

As each mass term comes with a fermion specific coupling constant G_f the absolute fermion mass is not predicted and stays a free parameter of the Standard Model.

An overview of all Standard Model particles and their interactions, together with the values of measurements of the particle masses can be found in Figure 2.1. The

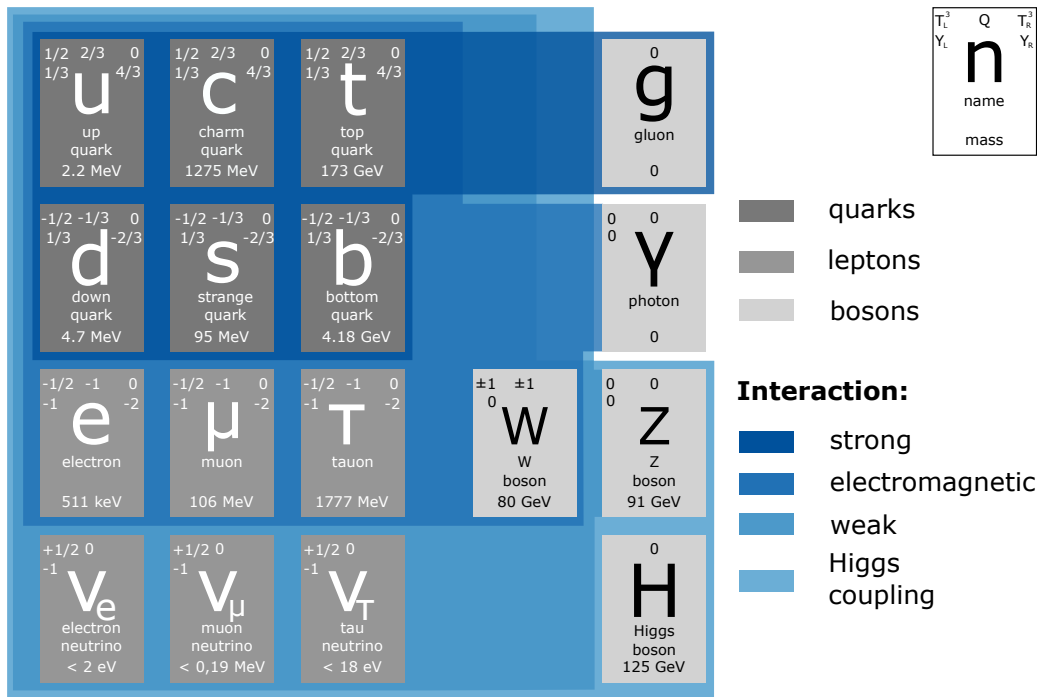


Figure 2.1. Schematic overview of the particle and interaction structure of the Standard Model. The colored surfaces highlight the coupling of a particle to a certain interaction. If the particle lays on the surface it takes part in the interaction. If it is only in contact with the surface, it is the mediator of the force without self interaction. The particle masses are taken from [3]

particles are structured in three families, where only the first family is stable and form the observable matter. A detailed description of the Standard Model and the derived interactions can be found in [1, 2].

2.1.5 W-Boson Creation in Proton-Proton Collisions

In high energy proton-proton collisions, as they are studied in this thesis, the interaction of protons is a complex process of interactions between the proton's components. The hard scatter process is the approximation of the proton-proton interaction as an interaction of single partons. The collision kinematics are defined by the proton's composition of the valence quarks, two up and one down quark and the quark gluon sea. The sea is formed by the interaction of the valence quarks via gluons, which can create quark-anti-quark loops. Therefore the composition changes dynamically and only statistical predictions can be made. The proton momentum is split upon all partons. The momentum fraction which is carried by a single parton is given by the Bjorken scale variable x .

The parton structure in the proton is described by the parton distribution functions (PDF). The PDFs give the probability density for a single parton, quark or gluon, with a certain x to be part of the proton. The proton composition cannot be calculated theoretically as it covers the non-perturbative regime of QCD and the knowledge on the parton distribution functions $f(x, \mu_F)$ comes from deep inelastic scattering

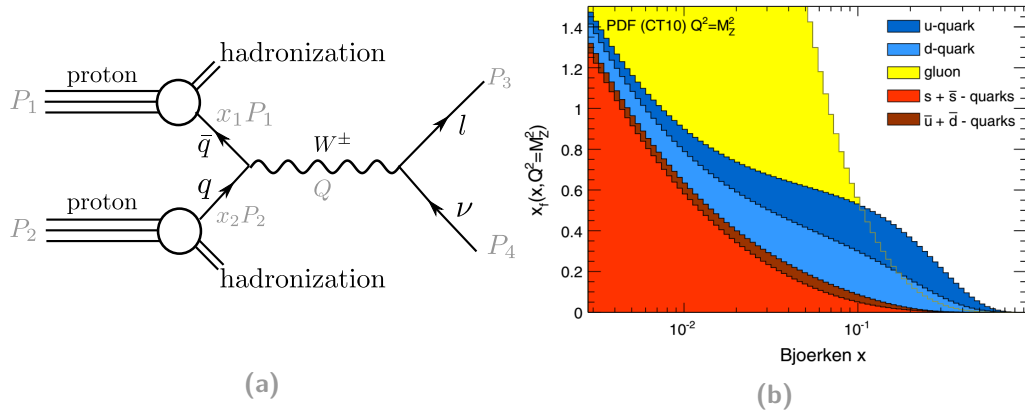


Figure 2.2. Leading order W boson production in proton-proton collisions (a) The kinematic variables are displayed in gray. The parton distribution function of the relevant partons (b) is shown for a momentum transfer $Q^2 = m_Z^2$ [4].

experiments. The factorization scale μ_F splits the long range interaction, covered by the PDF from the hard scattering process and absorbs resummation divergences. Commonly, the scale is set to the invariant mass of the final state lepton-anti-lepton pair. An example for the parton distribution function for a momentum transfer at the scale of the Z boson mass is given in 2.2b.

A schematic picture of the W boson creation in proton-proton collisions is shown in Figure 2.2a. The diagram describes the process $pp \rightarrow W + X \rightarrow l\nu + X$. The overall process can be factorized in two component, the hard scattering process of two quark with the creation and immediate decay of the W boson and the soft scattering and hadronization of the proton remnants. Mathematically, this process can be described by the cross-section

$$\sigma_{pp \rightarrow W+X \rightarrow l\nu+X} = \sum_q \int dx_1 dx_2 f_1(x_1, \mu_F) f_2(x_2, \mu_F) \times \sigma_{q\bar{q} \rightarrow W+X \rightarrow l\nu+X}. \quad (2.36)$$

Thereby, the cross section $\sigma_{q\bar{q} \rightarrow W+X \rightarrow l\nu+X}$ describes the hard scattering cross section for two quarks. Currently, the cross section can be calculated by perturbation theory up to next-to-next-to-leading order. A detailed description on the modeling of the W boson generation and decay is given in Section 3.4.

The W boson decays with a probability of $\approx 11\%$ into each of the three charged leptons and a corresponding neutrino and with $\approx 67\%$ probability into hadrons. As hadrons are difficult to identify in the multijet interaction background, the reconstruction of the W boson is usually done in the leptonic channel. Lepton-universality predicts, as one of the fundamental assumption of the Standard Model, the same branching ratio for all leptons. Small differences attributed to the different available kinematic phase space due to the different lepton masses can be neglected, as the lepton mass is small compared to the W boson mass.

2.2 Accelerators and Detectors

The methods of particle physics have dramatically evolved in the last hundred years. Starting with the electron discovery in 1897 by J. J. Thomson through the observation of cathode rays in a gas [5] and the positron discovery from pair production of cosmic rays in 1933 by C. Anderson [6] particle detectors which record pictures of optical trace have been used for a long time.

The emission of cathode rays, leading to the electron detection, can be considered as one of the first accelerators to generate elementary particles. While the particle energy was limited at accelerators, most discoveries have been made in the cosmic radiation. Accelerator based discoveries have the major impact on particle physics since the discovery of the J/Ψ in 1974 [7, 8], which completed, as charmonium state, the second quark family.

The development in the accelerator technology was accompanied by the development of particle detectors with digital readout and the computer processing of data. The W and Z Boson were discovered in 1983 by the CERN experiments UA1 and UA2 at the Super Proton Synchrotron (SPS) [9, 10]. The latest discovery was the Higgs boson by the ATLAS and CMS experiment at the LHC accelerator on 2012 [11, 12]. The Standard Model was completed by this discovery. Ongoing and future experiments search for new particles beyond the Standard Model and aim for the precision measurement of the Standard Model parameters.

In the following, a description of the CERN accelerator complex is given in Section 2.2.1 and the ATLAS experiment is described in Section 2.2.2

2.2.1 The LHC at CERN

The largest European nuclear and particle physics research center is CERN (Conseil Européen pour la Recherche Nucléaire), located near Geneva at the Swiss-French border. With the Large Hadron Collider (LHC), with a center of mass energy of $\sqrt{s} = 13$ TeV, the accelerator with the highest center of mass energy is located at CERN. Two contra-rotating proton beams with 1.2×10^{11} protons in each of the 2808 bunches, accelerated up to a beam energy of 6.5 TeV, rotate in the 27 km storage ring in the standard operation mode.

The CERN accelerator chain, not only feeding the LHC, but also serving other particle physics experiments, is shown in Figure 2.3. The protons are generated as ionized hydrogen atoms and pre-accelerated by the linear accelerator LINAC2, the proton synchrotron BOOSTER, the Proton Synchrotron (PS) and the Super Proton Synchrotron (SPS) before they are injected into the LHC for the final acceleration. The LHC provides four interaction points where the beams collide and the created particles are measured by the four experiments ALICE, ATLAS, CMS and LHCb. While the ATLAS and CMS experiment are general purpose detectors which are

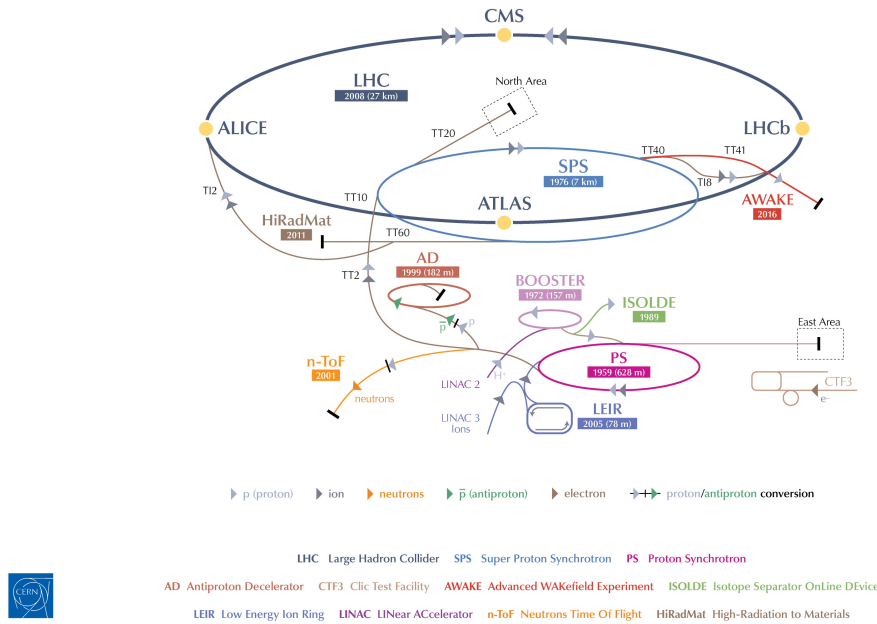


Figure 2.3. Schematical drawing of the CERN accelerator complex [13].

mainly used for Standard Model precision measurements and the search for physics beyond the Standard Model, the LHCb experiment is specialized for the detection of particles created in the beam direction, such as B mesons. The ALICE experiment is optimized to study heavy ion collisions. High matter density states, as short after the Bing Bang, are create in these collisions.

The data used in this thesis was recorded with the ATLAS experiment in 2011 at the center of mass energy of 7 TeV and a luminosity of $3.5 \times 10^{33} \text{ cm}^{-2} \text{ s}^{-1}$. This was the first year of data taking for the LHC experiments. The accelerator was ramped up to 8 TeV in 2012 and after a revision restarted in 2015 with the current center of mass energy. After a further revision in 2019 and 2020 a restart is planned for 2021 with the final design energy of 14 TeV. After 2015 the High Luminosity LHC aims to operate with a luminosity of $10 \times 10^{35} \text{ cm}^{-2} \text{ s}^{-1}$, exceeding the design luminosity by a factor of 10.

2.2.2 The ATLAS Detector at CERN

The ATLAS detector [14] is a multi purpose high energy particle detector at the LHC. The 25 m high and 44 m long detector covers a wide physics range. The most popular goal of the LHC detectors was the discovery of the Higgs boson in 2012 and still is the search for physics beyond the Standard Model. New physics can be either found by the discovery of a new particle, or by a deviation from Standard Model predictions. Therefore, also precision measurements of the Standard Model parameters, like the mass of the W boson [15] or the here presented branching ratio fraction measurement are of high interest.

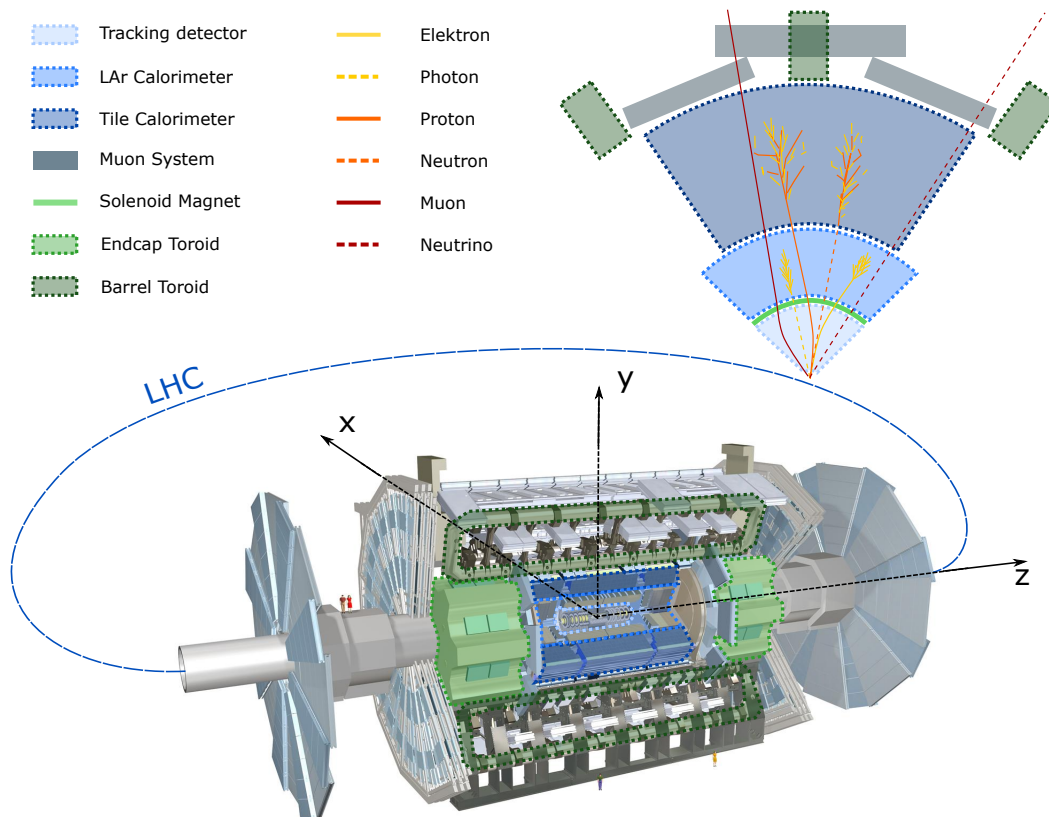


Figure 2.4. Schematic view of the ATLAS detector and the detection principle of long lived particles. Adapted from [16, 17].

The design of the ATLAS detector follows the common onion shell principle of particle detectors. Figure 2.4 shows an overview of the detector structure and the particle detection. The detector is built symmetrically around the beam interaction point and divided in the barrel, a cylindrical structure around the beam pipe, and the forward (end-cap) region closing the barrel along the beam pipe with all detector sub-systems. Silicon based detectors (Section 2.2.2.2) and a transition radiation tracker (TRT) are part of the tracking system, which is the most inner part of the detector. Most particles, except for muons and neutrinos are absorbed in the calorimeter system (Section 2.2.2.3), which forms the next detector level to measure the particle energy. The calorimeter is divided in two parts. The electromagnetic calorimeter absorbs electrons and photons, while the hadron showers extend to the hadronic calorimeter which is build of a higher material density. The energy of particles is reconstructed from their penetration depth in the calorimeter system. As the only measurable particles emerging the calorimeter are muons, a dedicated tracking system (Section 2.2.2.4) built from gaseous detectors follows the calorimeter system. The inner and muon tracking system are hosted in a magnet structure (Section 2.2.2.1) to measure the particle momentum from the bending radius in the magnetic field. The collected data is stored in a buffer at the chambers and only written to disk, if the trigger system (Section 2.2.2.5), which analyses part of the measured data online, identifies a potentially interesting event.

The detector coordinate system is defined as a right-handed system, where the x axis points to the center of the LHC. The y axis points toward the earth's surface and the z axis tangential along the beam pipe. The $x - y$ plane forms the transversal plane. For physics analysis it is common to work in the angular frame of cylindrical coordinates, defining the azimuthal angle in the transverse plane ϕ around the beam axis and the polar angle θ to the beam pipe. Instead of the the polar angle, the pseudo-rapidity

$$\eta = -\ln\left(\tan\left(\frac{\theta}{2}\right)\right)$$

is widely used in collider experiments. For massless particles, this quantity is equal to the for boost in Z invariant rapidity

$$Y = \frac{1}{2} \ln \frac{E + p_Z}{E - p_Z},$$

with the total particle energy E and the momentum along the beam pipe p_Z . In this reference frame, a distance is defined as

$$\Delta R = \sqrt{\Delta\eta^2 + \Delta\phi^2}.$$

The following section describes the ATLAS detector, as it was during the data taking period, studied in this thesis. Several upgrade programs have been included since

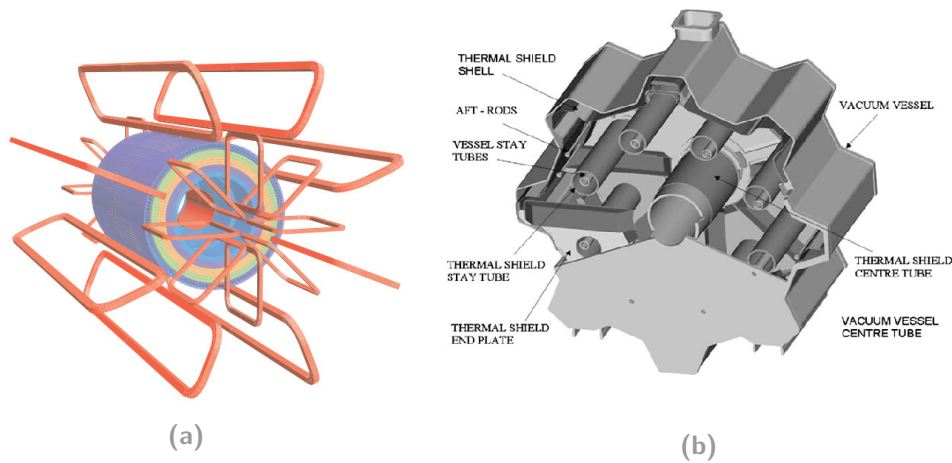


Figure 2.5. The magnet system of the ATLAS detector. Figure (a) shows an overview of the winding of the toroid magnet subsystems [14]. The flux return of the central solenoid, is realized by the steel structure of the hadronic calorimeter indicated by the colored cylinders. The end-cap toroid is enclosed in a cryostat and the windings are not visible in the detector (b) [19].

then and the detector is still under constant improvement, as it is described for the New Small Wheel project in chapter 4.

2.2.2 The ATLAS Magnet System

The ATLAS magnet system [18] consists of four superconducting magnet systems [14] of aluminum stabilized Cu-NbTi, the central solenoid magnet, the two end-cap toroids and the barrel toroid, with the eight individual coils forming the characteristic picture of the ATLAS detector. An overview of the components of the magnet system is given in Figure 2.5.

The central solenoid is inserted around the inner tracker and provides a $0.9 - 2$ T magnetic field with at a nominal current of 7.73 kA. The solenoid is hosted in a common cryostat with the liquid argon calorimeter and kept at a constant temperature of 4.5 K. The flux of the solenoid is returned over the steel structure of the hadronic calorimeter and an outside return yolk.

The two end-cap toroids are individually housed in a cryostat and consist of eight coils each. A $0.2 - 3.5$ T magnetic field is induced by a 20.5 kA current.

The barrel air coil toroid is built by eight coils, each enclosed in an individual race-track shaped cryostat. 20.5 kA current induce a magnetic field of $0.2 - 2.5$ T.

The stored energy in the magnet system is 1.6 GJ, which requires a careful design to absorb the induced stress on mechanical components. As the momentum measurement relies on the magnetic field in the detector, a precise mapping of the magnetic field is performed and monitored online.

2.2.2 The Inner Detector

The inner detector of the ATLAS detector [20] has a length of 6.2 m and a diameter of 2.1 m and serves two main purposes. The measurement of tracks and the identifi-

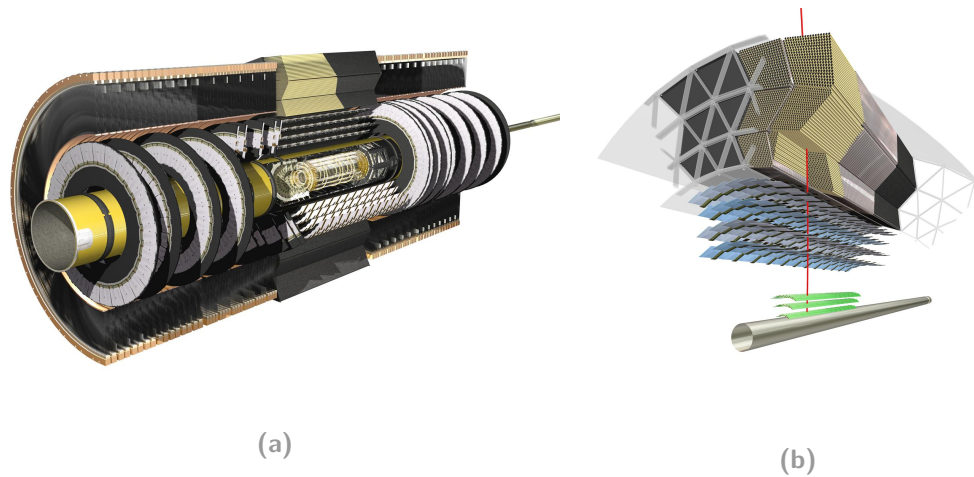


Figure 2.6. Computer generated images of the ATLAS inner detector. (a) shows the complete tracking system and (b) a cross section at the central position. The pixel layers are highlighted in green, the silicon tracker is marked in blue and the transition radiation tracker is indicated by its straw structure [21].

cation of vertices, the points where particles are created. For the latter purpose, a high resolution and high granularity detection is necessary close to the beam pipe. To achieve the design goals, the tracker is divided in three subsystems. Close to the beam pipe three layers of silicon pixel detectors are installed, followed by four silicon microstrip layers (SCT). The silicon detectors are kept at an operation temperature of -5°C to -10°C to keep a low noise level. The outer layer of the inner detector is formed by a transition radiation tracker. A schematical view of the inner detector layout is given in Figure 2.6.

The Pixel Detector

The pixel detector is built to withstand high radiation doses. Therefore it is designed to operate even after the type inversion of the oxygenated n-type bulk. This is achieved by n⁺ implanting on the readout pixel side of the detector and a p-n junction on the opposite side. For the non-irradiated detector, the depletion zone grows from the n-type bulk and a full pixel insulation is only achieved after the full growth of the depletion zone. After irradiation and the conversion of the n-type into a p-type bulk, the depletion zone grows from the pixel side and thus provides full isolation even for a partial growth of the depletion zone.

The pixel detector is built of 1744 $250\ \mu\text{m}$ thick sensors with an external dimension of $19 \times 63\ \text{mm}^2$. The nominal pixel size is $50 \times 400\ \mu\text{m}^2$ with 46080 readout channels per module. The intrinsic measurement accuracy of the pixel detector is $10\ \mu\text{m}$ in the $R - \phi$ plane and $115\ \mu\text{m}$ in z .

The Silicon Microstrip Detector

The sensors of the SCT are built as classical single sided p-in-n technology with AC-coupled readout strips. The higher distance to the beam pipe and therefore lower radiation dose compared to the pixel sensors allows for this more cost efficient approach. The 15912 sensors have a thickness of $285\mu\text{m}$ and a strip pitch of $80\mu\text{m}$. The pitch of the forward disk sensors is slightly varied around this value in order to keep a constant azimuthal pitch. Each sensor houses 768 12 cm long readout strips. The intrinsic sensor resolution is $17\mu\text{m}$ in the $R - \phi$ plane and $580\mu\text{m}$ in z direction for the barrel sensors and R for the disks in forward direction.

The Transition Radiation Tracker

The TRT consist of 4 mm diameter drift tubes. The tubes are oriented parallel to the beam pipe in the barrel and in radial direction in the end-cap region. A $31\mu\text{m}$ diameter tungsten wire is stretched in the middle of the multilayer polyimide tube. The electron collection time of 48 ns in the $Xe : CO_2 : O_2$ ($70 : 27 : 3$) gas mixture leads to a position resolution of $\approx 130\mu\text{m}$.

Besides the track reconstruction with a challenging pattern recognition of the ≈ 30 hits per track in the TRT, the detector is also used for the electron-pion differentiation. A polyethylene content in the tubes enhances the production of transition radiation photons, which are efficiently detected in the Xe gas. As the generation of transition radiation photons depends on the particle mass an electron identification is possible from the signal characteristics.

2.2.2 The Calorimeter

Calorimeters are detectors which measure the energy of a particle by its absorption. The typical approach in high energy particle physics is a sampling calorimeter. Detection layers alternate with high density absorption layers. The depth of the impact of a particle into the sandwich structure is a measure for it's energy and the width and structure of the shower created during the absorption gives a hint on the particle type.

As electrons and photons range shorter than hadrons in matter, the calorimeter is typically divided in a higher granular electromagnetic and a hadronic calorimeter. Electrons lose energy by bremsstrahlung and the created photons undergo pair-production. Thus the energy is subsequently divided until the total absorption of all particles and therefore all energy. The thickness of an electromagnetic calorimeter is usually given in radiation length X_0 , the mean length, where an electron loses a fraction $1/e$ of its energy and $7/9$ of the mean free path for pair production.

The shower production in a hadronic calorimeter is not purely dominated by electrons and photons. During the interaction with matter further hadrons are created, which decay or interact with the material. Therefore a hadronic shower is wider compared to an electromagnetic shower and a hadronic calorimeter can be built with a more coarse segmentation. The thickness of a hadronic calorimeter is given

in units of the interaction length λ , the mean free path of a hadron in the detector.

For the measurement principle it is highly important to detect the full energy of all particles, except for muons which are measured in the muon system after the calorimeter and neutrinos which cannot be measured at all. The energy of the un-detected neutrinos has to be estimated from the missing transverse energy, as the initial beam particles only carry longitudinal momentum and therefore the energy sum in the transverse plane has to vanish. Un- or partially detected particles would bias the neutrino energy estimation.

Therefore the ATLAS calorimeter is built with a geometrical coverage of 99.5 % and a total thickness of 22 radiation length in the barrel and 24 X_0 in the end-cap region. A total of 11 λ is achieved for the interaction length of the hadronic calorimeter, making a possible punch-through negligible.

The layout of the ATLAS calorimeter system [22, 23] is shown in Figure 2.7. The barrel electromagnetic and forward electromagnetic and hadronic calorimeter use liquid argon as detection medium. Liquid argon provides a high signal linearity and radiation hardness, which makes it well suitable for the ATLAS detector. The argon is ionized and the charge signal is collected on an accordion shaped electrode. The accordion geometry is chosen to achieve a full ϕ coverage and avoid dead regions due to passive material. The electromagnetic calorimeter, using lead as absorber material, covers a range of $0 < |\eta| < 1.475$ and $1.375 < |\eta| < 3.2$ in the barrel and end-cap region respectively. The hadronic end-cap calorimeter covers a range of $1.5 < |\eta| < 3.2$ and uses copper as absorber material. For a hermetic closure, the liquid argon forward calorimeter is installed around the beam pipe in the region $3.1 < |\eta| < 4.9$ which uses copper and tungsten as absorber.

The barrel hadronic calorimeter is realized as a sampling calorimeter of alternating plastic scintillator plates (tiles) and steel absorber plates. The barrel tile calorimeter extends in the range $0 < |\eta| < 1.7$.

2.2.2 The Muon System

The muon system of the ATLAS detector [25] is built of different gaseous detector technologies, optimized for their usage. The chambers are designed to provide precision tracking up to $|\eta| < 2.7$ while being able to trigger on muons within $|\eta| < 2.4$. The aim of the particle reconstruction is a momentum resolution of $\delta(p_T)/p_T < 10\%$ for particles with $p_T = 1$ TeV. To achieve the goal, the chamber alignment must be known with a precision of $30\ \mu\text{m}$. This is achieved by an optical alignment system and a track based alignment reconstruction.

Monitored Drift Tubes (MDT) are used for the precision tracking in the whole range and Cathode Strip Chamber (CSC) for $2.0 < |\eta| < 2.7$ in the most inner forward muon system, the Small Wheel. In the barrel ($|\eta| < 1.05$) Resistive Plate Chamber (RPC) are used for the trigger purpose and the measurement of the coordinate not influence by the magnetic field deflection, while Thin Gap Chambers (TGC) are used

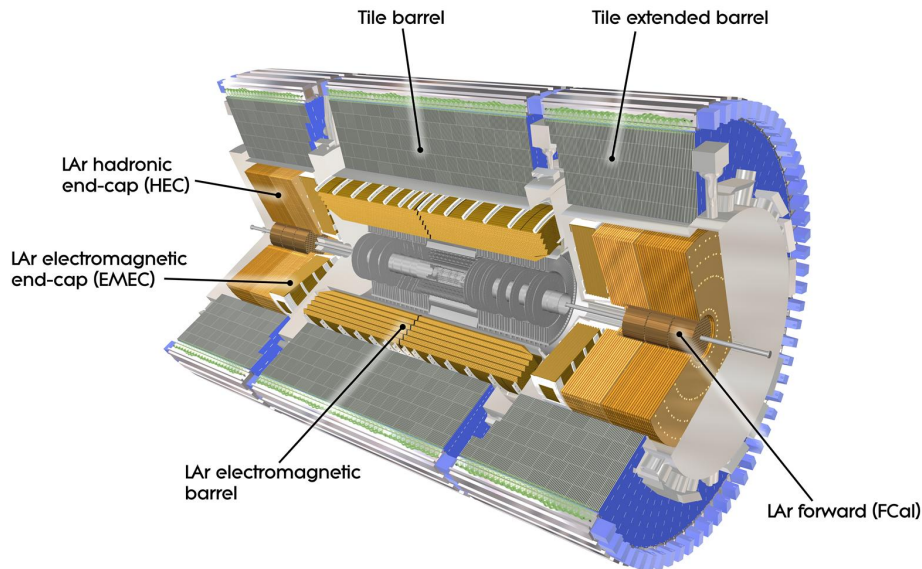


Figure 2.7. Schematical image of the ATLAS calorimeter system [24].

in the forward region. These chambers provide a worse spatial resolution, which is sufficient to match particles to trigger objects, but offer an excellent time resolution.

All detector types work with the same principle. A counting gas is ionized by the traversing muons. The primary electrons are guided by an electric field to a readout structure. Close to the readout structure, a high electric field is generated (for example the radial symmetric field of the thin wire), where the electrons gain enough energy between collision with the gas molecules for further ionization. The charge is amplified by the resulting avalanche process to a measurable signal. During this process, the electrons and the, in opposite direction, drifting ions induce not only a signal to the readout structure, but also to the cathode which can be measured as well.

The Monitored Drift Tubes

The MDTs are 3 cm diameter drift tubes with a central $50\ \mu\text{m}$ tungsten-rhenium wire. The tubes are filled with an $Ar : CO_2$ (93 : 7) gas mixture at 3 bar overpressure. With several layers of tubes staged per chamber and three layers of chambers in each direction, 20 independent measurements of the precision coordinate, the bending coordinate in the magnetic field, is achieved. The precision coordinate can be reconstructed with $35\ \mu\text{m}$ resolution.

The Cathode Strip Chambers

The CSCs are multi-wire proportional chambers. A layer of $30\ \mu\text{m}$ wires, which create the high electric field for the avalanche formation is tensioned in the middle

of a planar chamber. The wires are oriented in the radial direction and the two cathode surfaces enclosing the gas volume around the wires are segmented in strips with ≈ 5 mm pitch in the precision coordinate. A stack of four gas volumes per chamber leads to four independent measurements of both coordinates with a spatial resolution of $40\ \mu\text{m}$ in the precision coordinate and 5 mm in the second coordinate.

The Resistive Plate Chambers

The RPCs are plane chambers consisting of two conducting surfaces coated with a high resistive material. The electric field between the plates is chosen such, that avalanches are created along the particle track and thus no wires are necessary. The signal induced to the resistive surface is capacitively coupled to electrically insulated readout strips underneath. The resistive layer is necessary to cut a possible streamer formation. For high charge deposits, a conducting plasma channel can be created in the high electric field between the cathode and the anode. The resistive surface collects the charge and an opposing field is formed which ends the avalanche process.

The 2 mm thin gas volume and the choice of the gas mixture $C_1H_2F_4 : Iso - C_4H_{10} : SF_6$ (94.7 : 5 : 0.3) ensure short drift times and provides 1.5 ns time resolution, while offering 10 mm spatial resolution in both coordinates.

The Thin Gap Chambers

TGC are multi-wire proportional chambers, where the distance between wires is larger than the distance to the cathode surfaces. This allows for a good time resolution of 4 ns. The cathode is formed by a graphite coated insulator whose backside (facing away from the gas volume) is copper coated. The copper surface is segmented into strips for the reconstruction of the precision coordinate. The second coordinate is reconstructed from groups of wires.

2.2.2 The Trigger System

At the end of 2018, in average 2.4×10^9 interactions per second have been produced. The recording of all events in the ATLAS detector would lead to a data rate and amount which is neither possible to be processed nor to be stored. Therefore, the ATLAS detector uses a trigger system [14] with three consecutive stages: the Level 1 and 2 (L1, L2) trigger and the event filter. At L1, the information from the muon trigger chambers and calorimeter data with coarse granularity is used. The trigger algorithms select high momentum particles and events with large missing transverse energy. For the further processing, Regions of Interest (RoI) along the particle path are defined for each object passing the selection.

The information is passed to a central trigger processor, which combines the selection to trigger menus. Single menus can be pre-scaled, to ideally use the available bandwidth and not only record high cross section processes. The L1 trigger decision is made within $2.5\ \mu\text{s}$ and reduces the rate to about 75 kHz

The information on the RoIs is passed to the L2 stage. The L2 trigger accesses the full granularity information in the RoIs, which is approximately 2% of the total event data. The data rate is reduced to 3.5 kHz with an average time of 40 ms needed for the decision taking.

The event filter selection uses offline data analysis procedures and reduces the data rate to 200 Hz with a decision taking time of ≈ 4 s. During the trigger decision, all data is kept in a buffer at the detectors and only read and permanently stored in case of the positive trigger decision. The raw data is processed in a world wide computing grid and data samples, where the raw detector data is transformed into physical objects as particles and their tracks for the further analysis.

The trigger path as described here was implemented for the data taking in 2011. The dataset of this period is used in this thesis. Since then the beam energy and luminosity, and therefore the average number of interactions, was constantly raised. Therefore the trigger was adapted to fulfill a larger rate reduction. Topological information is already included in the L1 trigger stage to include the geometrical correlation between objects.

Measurement of $BR(W \rightarrow \tau\nu \rightarrow \mu\nu\nu)/BR(W \rightarrow \mu\nu)$

The following chapter describes the measurement of the branching ratio fraction of the tauonic and muonic W boson decay $(W \rightarrow \tau\nu \rightarrow \mu\nu\nu)/(W \rightarrow \mu\nu)$. The measurement is performed with data from proton-proton-collisions at a center of mass energy $\sqrt{s} = 7$ TeV taken by the ATLAS detector in 2011 with a total integrated luminosity of 4.6 fb^{-1} .

A motivation of the measurement and a description of the analysis strategy is given in Section 3.1. A detailed overview on the data and simulated Monte Carlo samples is presented in Section 3.2 and the signal and background processes are introduced in Section 3.3. Corrections applied to the simulated events during the physics modeling, the event reconstruction and the detector response emulation in order to enhance the data and Monte Carlo agreements are described in Section 3.4, Section 3.5 and Section 3.6, respectively. The fitting procedure including the utilized framework, the data preparation and the treatment of systematic uncertainties of the measurement is presented in Section 3.7. An first estimation of the expected sensitivity and a consistency test of the framework are given in Section 3.8 and the obtained result is discussed in Section 3.9. A perspectives to a possible sensitivity increase are presented in Section 3.10 and the chapter concludes with an outlook in Section 3.11.

3.1 Motivation and Measurement Procedure

The decay of the W boson into leptons shows a tension with the Standard Model. As shown in Figure 3.1, while lepton universality and therefore the same branching ratio is predicted for all lepton generations, the measurements at the LEP accelerator show a discrepancy of more than two standard deviations from the combined lepton measurement for the tau decay channel, while the electron and the muon decay channel are in agreement with the combined measurement [26].

A similar tension in the third lepton generation was found in b quark decay. As shown in Figure 3.1 a discrepancy of 2.3 standard deviations to the theory value is found in the combination of the measurements [27]. An discrepancy of 3.4 standard deviations was found for the decay of the B meson into an excited D^* meson. Similar hint to a slightly larger cross section for the tauonic decay of the W boson have been found in [28].

These results give a hint for possible new physics beyond the Standard Model in couplings of third generation leptons. The evidence is more pronounced, as they are found in the decay of the W , as a gauge boson, and in the decay of b quarks

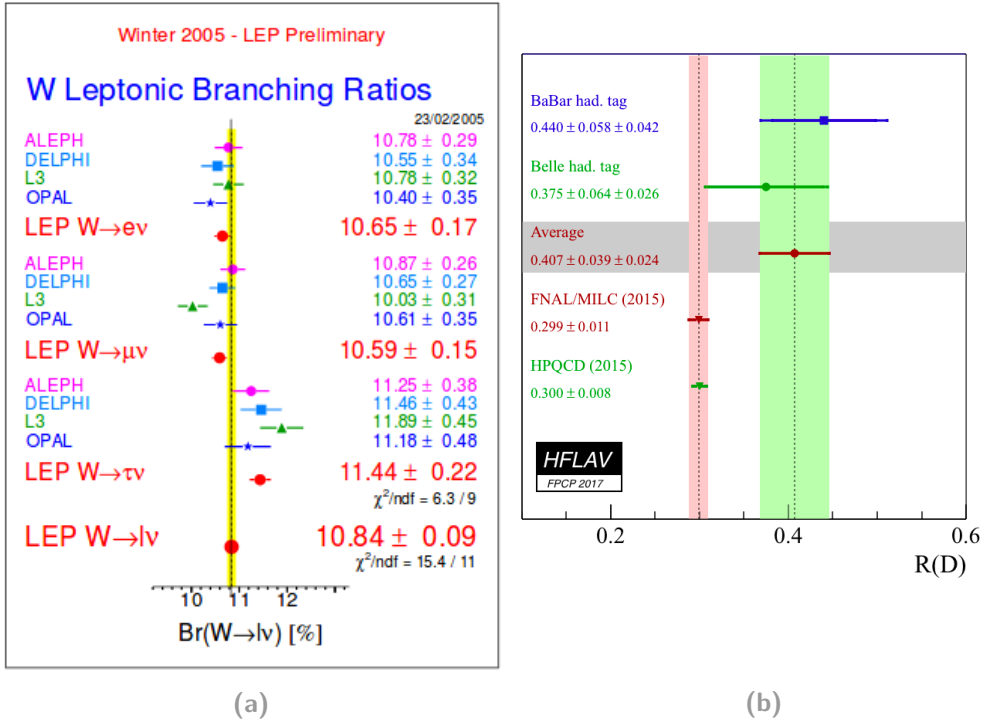


Figure 3.1. Leptonic decay channels of the W boson (a) [26] and the b quark (b) [27]. Both decays show a deviation of more than two standard deviations from the combined value or theory value respectively. $R(D)$ is defined the branching ratio of a B meson decaying into D mesons and taus over the branching ratio into D mesons and electrons or muons.

independently. Moreover the results are obtained with different experiments at electron and proton accelerators, which makes a systematic effect unlikely. To decide, whether new physics is hidden in these decay channels, or statistical fluctuations lead to the observed discrepancies, more precise measurements are necessary. In the following a first measurement of the branching ratio fraction

$$\frac{BR(W \rightarrow \tau\nu_\tau \rightarrow \mu\nu_\tau\nu_\mu)}{BR(W \rightarrow \mu\nu_\mu)}$$

at the LHC is presented.

A direct identification of the short lived tau lepton with the ATLAS detector is experimentally challenging and afflicted by a large error. The measurement strategy therefore is to identify the process $W \rightarrow \mu\nu$, which is possible with high precision, as proven by the measurement of the W mass [15]. The process $W \rightarrow \tau\nu$ appears as a background to $W \rightarrow \mu\nu$ for taus decaying into muons. As the branching ratio $\tau \rightarrow \mu\nu$ is known with a precision of 0.04% [29], no significant uncertainty is thereby induced to the measurement.

The chosen approach is based on the template fit of simulated Monte Carlo data for the decay channels to the measured data which naturally includes both channels. The principle is shown in Figure 3.2a. The points represent the measured distribution of a particle decay's kinematic variable. The decay can happen in two decay channels,

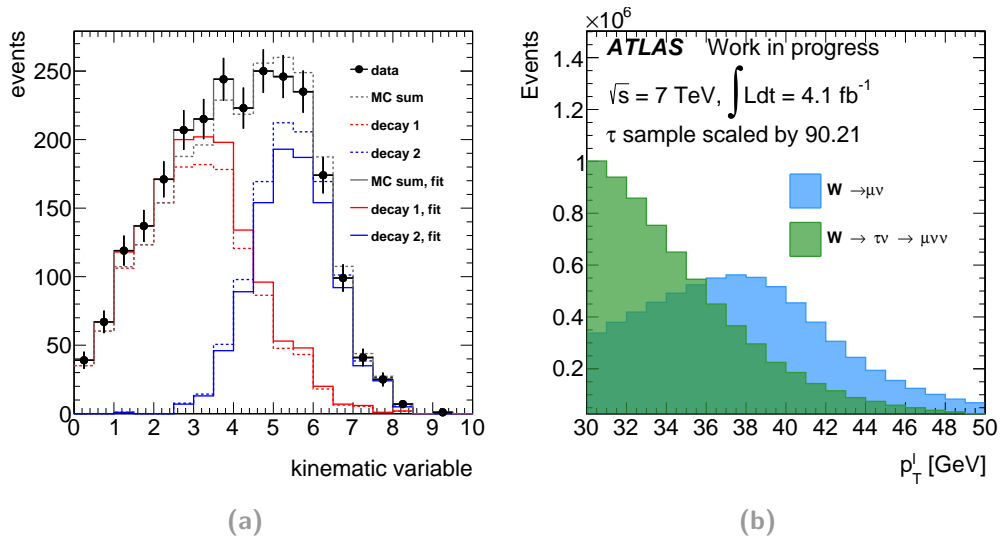


Figure 3.2. Principle of a template fit (a). The kinematic distributions of the different channels are scaled such that their sum fits the data best. The Monte Carlo samples for the distribution of the leading lepton transverse momentum for the $W \rightarrow \mu\nu$ and the $W \rightarrow \tau\nu \rightarrow \mu\nu\nu$ are shown in (a). The clear shape separation between the two processes allows for a shape fit.

indicated by the red and blue lines. If the distribution shape for the single decay channels is well separated, their physical scale can be obtained by a fit of the sum distribution of the two simulated channels to the measured data. The situation before the fit is indicated by the dashed lines in Figure 3.2, where the sum clearly does not match the data. The, by the fit rescaled, distribution in a solid line in contrast matches the data well. This approach needs very well modeled simulated samples of all contributing processes where, besides the underlying physics, all detector effects have to be fully implemented. The correct estimate of all systematic variations for a proper error estimation in the fit is mandatory.

Figure 3.2b shows the distribution of the leading lepton transverse momentum. The clear shape difference between the studied decay channels makes the template fit approach applicable. The, compared to the $W \rightarrow \mu\nu$ small $W \rightarrow \tau\nu$ sample makes the determination of the difference in the branching ration fraction a technical challenging task.

3.2 Data and Monte Carlo Samples

In the following, the used dataset and the event selection from the measurement of the W mass is described in section 3.2.1. The selection is optimized for a the muonic decay of the W -boson. The therefore necessary event selection is describes in section 3.2.2. Since the presented analysis focuses on the decay channel $W \rightarrow \mu\nu_\mu$ in Section 3.2.1 the reconstruction of the data measured with the ATLAS detector is described based on this process. Section 3.2.3 describes the produced Monte Carlo samples.

3.2.1 Data Sample and Event Topology

The data sample, collected in 2011 with the ATLAS detector at a center of mass energy of $\sqrt{s} = 7 \text{ TeV}$ is used in this analysis. The data sample from this data taking period offers several benefits. After tremendous work for precision measurements with this dataset, the best detector calibration compared to other datasets was achieved. Moreover, it is the dataset with the lowest pile-up and therefore offers the best resolution of the missing transverse energy and transverse mass. The sample for the decay of the W boson into a muon and a neutrino is based on an integrated luminosity of $\int \mathcal{L} = 4.1 \text{ fb}^{-1}$ with an relative uncertainty of 1.8% [30] and contains 7.86×10^6 W boson event candidates.

The goal of this work is to provide a feasibility study and a sensitivity estimation for the branching ratio fraction of the W decay to tau leptons and muons with data from the ATLAS detector. To guarantee well estimated systematic uncertainties and a well studied data and Monte Carlo agreement, the samples from the analysis for the measurement of the W mass with data from proton-proton collision at $\sqrt{s} = 7 \text{ TeV}$ were used [15].

The signature of a W boson decay is shown in Figure 3.3. In the hard scattering, two quark from the proton content, collide and create the W boson. The W almost immediately decays into a lepton pair. The neutrino of the lepton pair cannot be detected and escapes the detector. The remnants of the protons hadronize. They form together with gluons, irradiated from the colliding quarks, the hadronic recoil. The main component of the hadronic recoil is given by the irradiated gluons.

3.2.1 Observable Definition

The lepton momentum and the hadronic recoil are measured in the plane transverse to the beampipe. Thus the measured quantity is free from an unknown momentum transfer in beam direction and therefore the vector sum of all particle momenta should vanish. The hadronic recoil is reconstructed from the energy measured in the calorimeter. For each cluster of energy deposits in the calorimeter a transverse energy vector $E_{T,i}$ is constructed. This vector has the magnitude of the energy deposit in the calorimeter E divided by $\cosh \eta$, with the pseudorapidity η . Each cluster is reconstructed by overlaying a topological pattern of typical events on a seed with a signal higher than four times the expected noise [31]. The vector is formed by the reconstructed energy as magnitude and the geometrical position of the cluster defining the orientation. In the cluster energy measurement, a sole energy loss by electromagnetic interaction is assumed at first. As a next step, corrections for the response to hadrons, losses caused by dead material and for energy not covered by the clustering process, are applied.

To avoid bias from the energy deposited by the charged lepton from the W decay, clusters which are in a distance of $\Delta R < 0.2$ of the lepton track are discarded for

the reconstruction of the hadronic recoil. The size of the cone ensures, that neither contributions from the lepton itself, nor from photons emitted as final state radiation or bremsstrahlung have an influence on the measurement. With this approach, not only contributions from the charged lepton but also the contributions from the multijet background are discarded in the excluded region. This is compensated by summing all energy deposits in a same size cone $\Delta R = 0.2$ at the same η with random sign, but a different ϕ and adding the contribution to u_T at the position of the charged lepton.

The transverse hadronic recoil u_T is split into a component parallel u_{\parallel} and perpendicular u_{\perp} to the transverse momentum of the lepton p_T^l as indicated in Figure 3.3. The W boson is boosted in the transverse plane by the initial state radiation leading to a transverse momentum of the W boson $\vec{p}_T^W = -\vec{u}_T$.

Since the neutrino from the W decay is not reconstructed in the detector, its transverse momentum is estimated from the imbalance of the momenta in the transverse plane p_T^{miss} :

$$\vec{p}_T^{miss} = -(\vec{p}_T^l + \vec{u}_T).$$

The transverse mass of the W boson can be reconstructed from transverse momenta of the lepton and the neutrino and the azimuthal opening angle $\Delta\phi$ between the lepton momentum and the missing transverse momentum:

$$m_T = \sqrt{2p_T^l p_T^{miss}(1 - \cos \Delta\phi)}.$$

3.2.1 Muon Reconstruction

As described in section the ATLAS detector has a dedicated system for measuring muons, since they are, except for the not at all interacting neutrinos, the only particles escaping the calorimeter. For muons, two independent measurement are available. One from the inner detector and one from the muon system. This information is used to form combined muon candidates by the statistical combination of both measurements [32]. This redundancy allows for a precise efficiency estimation. In this analysis, the reconstruction of the muon's kinematic properties is only done with the measurements in the inner detector, to simplify the calibration procedure. The efficiency loss as a consequence thereof is with 10-15 % small in the studied range of transverse momenta [15]. The requirements for the muon, to ensure a high quality reconstruction and to reduce the background are shown in Table 3.1

3.2.2 Event Selection

The selection of candidates for the production of W bosons happens in two stages. During data taking, interesting events are identified by a trigger and stored for the further reconstruction and processing. After the reconstruction, additional cuts

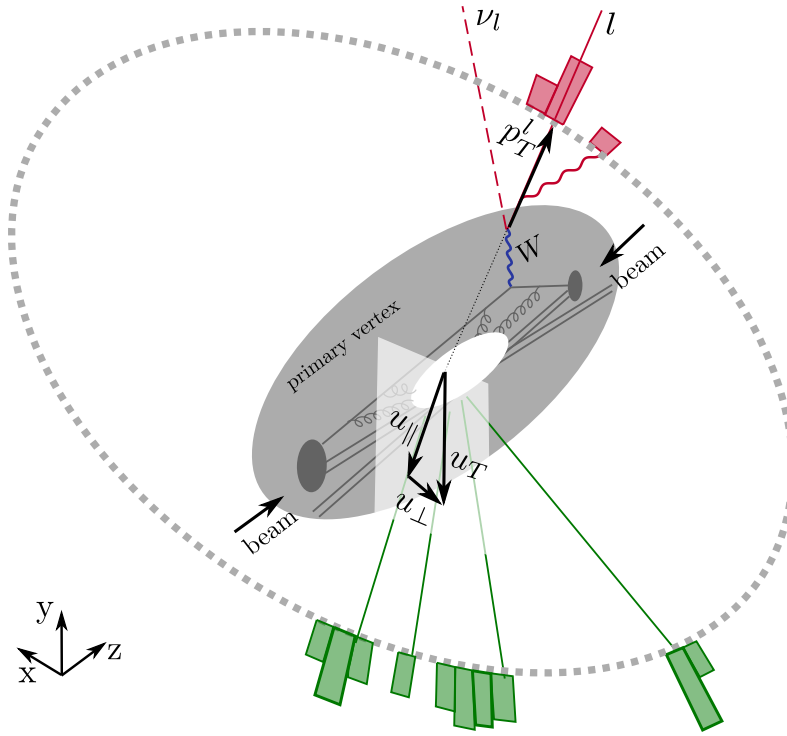


Figure 3.3. Schematic view of the W boson production and decay. Two quarks of the colliding protons form a W boson, which instantly decays into a lepton pair. The transverse momentum p_T^l of the lepton which is not the invisible neutrino is measured. The remnants of the proton and mainly gluons, irradiated from the colliding quarks, hadronize and form the hadronic recoil u . The measured transverse component u_T is divided in u_{\parallel} , the component parallel to p_T^l , and the perpendicular component u_{\perp} . The energy measured in the calorimeter for the determination of the hadronic recoil is indicated by the colored boxes on the dashed gray ellipse.

Table 3.1. Requirement on muon candidates for the W boson reconstruction

Requirement	Reason
> 1 hit in pixel detector	
> 5 hits in SCT detector	High quality of the reconstructed inner detector track
< 2 active pixel or SCT detector areas penetrated by the track, but not showing a hit	
> 9 TRT hits for $0.1 < \eta < 1.9$	
Closest distance to the beamline less than 10 mm from the collision vertex	Rejection of cosmic rays
$p_T > 20$ GeV	Trigger threshold
$ \eta < 2.4$	Detector acceptance
$p_T^{\mu, cone} < 0.1 p_T^{\mu}$ $p_T^{\mu, cone}$: sum of all tracks close to the muon track ($\Delta R < 0.2$)	Rejection of multijet background

Table 3.2. Requierements for the selection of W candidates in the trigger and after the event reconstruction.

Requierement	Reason
Trigger	
at least one muon candidate with $p_T^\mu > 18$ GeV	Detection threshold
Reconstruction	
Primary vertex with at least three associated tracks	Track from charged lepton plus > 2 tracks for hadronic recoil reconstruction
Reconstructed charged lepton with $p_T^l > 30$ GeV	Reduction of multijet background
Neutrino candidate symmetric to charged lepton: $p_T^{miss} > 30$ GeV	
$m_T > 60$ GeV	Reduce uncertainties from high p_T W bosons
$p_T^W < 30$ GeV	

taken from the optimization for the W mass measurement, are applied to reduce the background. The cuts at the trigger and reconstruction stage are shown in Table 3.2.

These selections will not result in a pure sample of only W bosons decaying into muons. Also other processes pass the selection criteria and are contained to some extent in the sample. First of all the decay of the W boson into a tau lepton which further decays into a muon is a relevant process, which is under study in this analysis. Other processes, which are not of interest in this study are the decay of the Z boson in two muons, where one muon is not reconstructed, the contribution from the $t\bar{t}$ production, semi-leptonic decaying diboson events and the inclusive multijet production in strong interaction processes. While the last background is estimated in a data driven approach, as described in Section 3.3.2 all the other background are estimated with Monte Carlo generators and calibrated to data.

Since the W boson is decaying into one invisible neutrino, it is not possible to calibrate the detector response and the hadronic recoil with the data from the W boson decay. For that purpose the decay of the Z boson into two charged particles, which both are seen by the detector, is used. The Z boson decay leads to similar signatures in the detector as the W boson decay. Both bosons have a similar mass and decay. In a first approximation, a W boson decay is equal to a Z boson decay, where one of the leptons is not reconstructed.

A dataset enriched with Z boson decays is retrieved by using the same lepton and

Table 3.3. Monte Carlo generators used for the simulation of single processes contributing to the measured data.

Process	Monte Carlo Generator
Hard-scattering for W and Z boson production and decay in the leptonic channel	POWHEG (v1/r1556) [33–35] using CT10 PDF set [36]
Parton shower, hadronization and underlying event	PYTHIA 8 (v8.170) [37, 38] using CTEQ6L1 PDF set [39]
QED final-state radiation (FSR)	PHOTOS (v2.154) [40]
Tau lepton decay	PYTHIA 8
Top quark pair production and single top processes	MC@NLO MC generator [41–43] interfaced to HERWIG (v6.520) [44] and JIMMY (v4.31) [45]
Diboson production(WW , wZ , ZZ)	HERWIG using CT10PDF set
Multijet events to validate data driven estimation	PYTHIA 8

isolation requirements as for the W selection, but cutting on the specific properties of the Z decay. Two same flavor but opposite charge leptons with a transverse momentum $p_T^l > 25$ GeV each are required. Besides the invariant mass of the dilepton system has to be in a range symmetric around the Z mass $80 < m_{ll} < 100$ GeV.

3.2.3 Monte Carlo Simulation

To simulate the samples necessary for the template fit to the data, several Monte Carlo generators have been used for the individual processes. The simulation chain distinguishes different levels of the particle reconstruction. The truth level contains the particles as they are created by the Standard Model simulation. The particle content after detector simulation is called reconstruction level.

An overview of the used generators can be found in Table 3.3. The Monte Carlo generators, need the parton density function (PDF) for the composition of the proton as input. These density functions need experimental constraints in the theoretical calculation. The used set is also indicated in Table 3.3. For the simulation the mass of the W and Z boson are set to $m_W = 80.399$ GeV and $m_Z = 91.1875$ GeV.

To compare the simulation results to data, the expected detector response to the generated particles has to be applied to the generator result. The detector is modeled in GEANT 4 to convert the particle interactions into measured signals.

The inaccuracies in the simulation are revealed in a comparison with data and discussed in Section 3.6

Table 3.4. Percent contribution of the electroweak and top-quark processes. [46]. The uncertainties on the backgrounds are discussed in the text.

Channel	$W \rightarrow \tau\nu$	$Z \rightarrow \mu\mu$	$Z \rightarrow \tau\tau$	diboson	top quark
$W^+ \rightarrow \mu^+\nu$	1.00	4.83	0.10	0.06	0.09
$W^- \rightarrow \mu^-\nu$	1.01	6.124	0.13	0.07	0.11

3.3 Signal and Background Processes

In the following, the estimations of the backgrounds to the signal selection for the W mass measurement with $W \rightarrow \mu\nu$, introduced in Section 3.2.1, are described. Besides the signal channel of the analysis $W \rightarrow \mu\nu$, one of the background components, namely $W \rightarrow \tau\nu$, is used in this study to measure the branching ratio fraction of these two processes.

The contribution of the backgrounds introduced in Tab 3.4 can be well modeled by Monte Carlo simulations, as shown in Table 3.3. The contribution of the soft QCD multijet background in contrast cannot be estimated by simulation. The data driven approach used to retrieve this background is described in Section 3.3.2.

3.3.1 Monte Carlo simulated Prozesses

3.3.1 Muon Signal

The main process recorded in data, due to the optimization for the W mass measurement, is the decay of the W boson into a muon-neutrino-pair $W \rightarrow \mu\nu$. The contribution of this process is more than 90%.

3.3.1 Tau Lepton Signal

The second W boson decay under study in this analysis is the decay into a tau lepton. Even though the contribution is only in the order of 1%, it provides discrimination power from the muonic decay in the fit, due to the enhancement of the tau samples at lower transverse momenta. This is a result of the larger tau mass compared to the muon mass and the creation of two neutrinos, leading to a reduced kinematic phase space for this process.

3.3.1 Z Boson Background

The largest background contribution comes from the decay of a Z boson, where one of the final state muons is not reconstructed. While the direct decay of the Z bosons into muons contributes the major component of this background, the decay into tauons, which further decay into muons, is also considered. The relative cross section uncertainty of 1.8% and 2.25% for the cross section ratio W^+/Z and W^-/Z , respectively, is used. [46,47].

3.3.1 Top Quark Background

Contributions from top pair production or the s - and t - channel production of single top quarks occur mainly due to the leptonic decay of an associated W boson. The contribution of this process is around 0.1%. The uncertainty is given by the cross section uncertainty of 3.9% for the top pair production and 12% for the single top production [46, 48]

3.3.1 Diboson Background

The production of two bosons (WW , WZ and ZZ), where only one of them is decaying leptonically, is a contribution to the measured data of less than 0.1%. These processes are well modeled in the MC generators and their uncertainty is estimated by the cross section uncertainty of 5% [46, 49].

3.3.2 Multijet Background

Multijet events are due to their large cross section a considerable background. The decays of b - and c -quarks, pions and kaons containing a real muon and neutrino can mimic the desired signal. The muon signal can also be faked by long-lived hadrons penetrating through the calorimeter. Since these processes are not reliably modeled in the Monte Carlo generators, a data driven estimation of the multijet background was used.

The estimation of the multijet background is a two-stage process. First the total number of multijet background events is evaluated. In the second step the shape of the distribution of these events is estimated.

3.3.2 Number of Background Events

To estimate the number of multijet background events, a pure multijet sample has to be constructed. The isolation of the detected muons $I_\mu = p_T^{\mu, cone} / p_T$ gives discrimination power for multijet background events over signal events. As the muons in the background emerge from jets, a high activity is expected around the muon track. To retrieve the pure multijet sample, a multijet enriched sample is constructed by loosening the isolation (*anti - iso*) from 0.1 to a maximum of 0.4. Regions in steps of 0.03 are defined in the whole range of the isolation. Simulated samples of the electroweak and top background are subtracted from the enriched sample to obtain the pure multijet sample.

The number of background events is measured by a fraction fit of the pure multijet sample and simulated electroweak and top samples to data. For the signal selection, the model uncertainties are too large for a proper estimation of the multijet contribution. Therefore two fitting regions FR1 and FR2 are defined by removing cuts from the event selection. In FR1 the cut on the missing transverse momentum and the transverse mass is removed, while in FR2 also the cut on the W boson transverse momentum is removed. An overview of the applied cuts is shown in Table 3.5.

The number of multijet events is estimated for the two fitting regions FR1 and

Table 3.5. Definition of the signal region (SR) and the different fitting regions (FR) [46].

region	p_T^{miss}	m_T^W	p_T^W
SR	$p_T^{miss} > 30 \text{ GeV}$	$m_T^W > 60 \text{ GeV}$	$p_T^W < 30 \text{ GeV}$
FR1	-	-	$p_T^W < 30 \text{ GeV}$
FR2	-	-	-

FR2 and three different kinematic variables (p_T^{miss} , m_T and p_T^l/m_T) to get a hand on the systematic error of the procedure. The results for each fitting region and each kinematic variable in dependence of the isolation are extrapolated to $I_\mu = 0$. The extrapolation encounters for different process contributions appearing with different isolation criteria and therefore different shapes of the multijet background distribution. By the extrapolation, the correct value for the signal cut of $I_\mu < 0.1$ is achieved.

In the following, the actual fraction fit is described for one kinematic variable $x \in \{p_T^{miss}, m_T, p_T^l/m_T\}$ and a fitting region $FR \in \{FR1, FR2\}$.

1. The x distribution for data and Monte Carlo is retrieved in the signal region and the fitting region FR with isolated muons. The number of events is counted in the samples, resulting in N_{data}^{FR-iso} , N_{mc}^{FR-iso} , N_{data}^{SR-iso} and N_{mc}^{SR-iso} .
2. The x distribution for data and Monte Carlo is calculated for the signal and the fitting region. For both regions, the Monte Carlo distribution is subtracted from data to retrieve a pure multijet sample, where the number of pure multijet events $N_{jet}^{FR-anti-iso}$ and $N_{jet}^{SR-anti-iso}$ is counted.
3. The fraction fit to the x distribution is performed assuming the following numerical model:

$$T \cdot N_{jet}^{FR-anti-iso} \times x_{jet}^{FR-anti-iso} + \alpha \cdot N_{mc}^{FR-iso} \times x_{mc}^{FR-iso} = N_{data}^{FR-iso} \times x_{data}^{FR-iso}.$$

The free parameter T and α are extracted in a binned likelihood fit. The parameter α is expected to be in order of $\alpha = 1$, since the Monte Carlo sample is normalized by the cross section and the integrated luminosity of the data. The parameter T is the transfer factor to scale the multijet sample from the anti-isolated region to the isolated region.

4. The number of multijet events in the signal region can be retrieved as:

$$N_{jet}^{SR-iso} = T \cdot N_{jet}^{SR-anti-iso}.$$

The results of the fitting and the extrapolation is shown in Figure 3.4. In the extrapolation is visible, that the expected number of multijet events depends on the

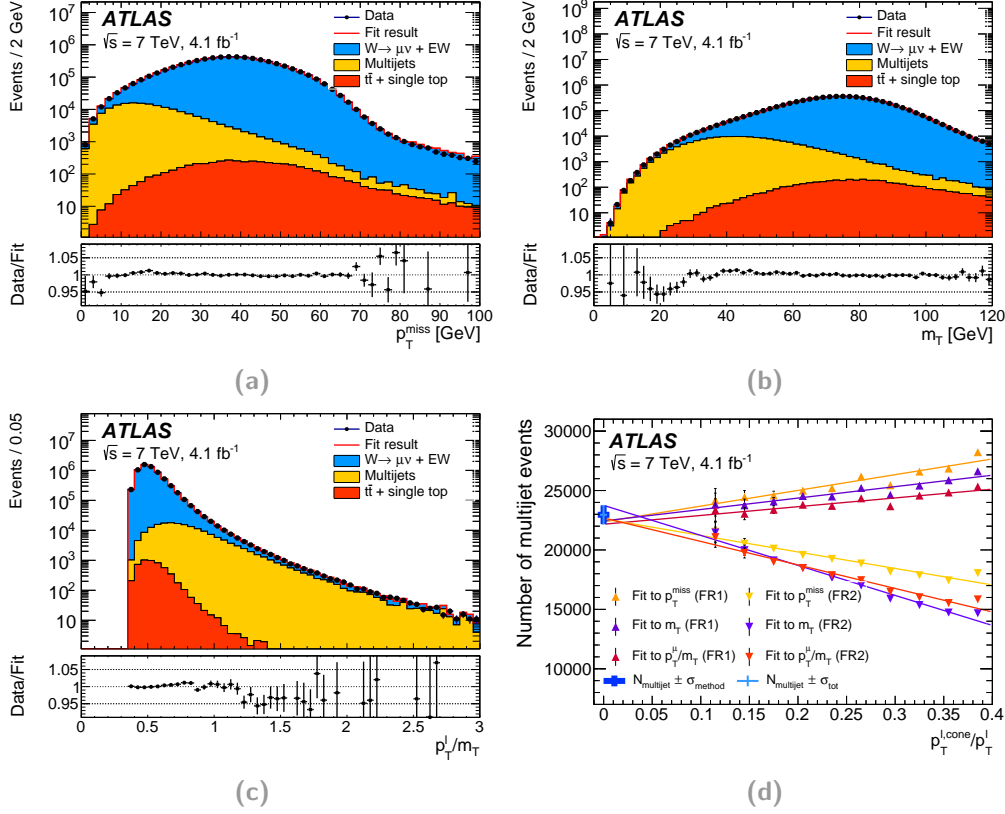


Figure 3.4. Result of the multijet background fitting for the missing transverse momentum p_T^{miss} (a), the W boson transverse mass m_T (b) and the ratio p_T^l/m_T (c) for the isolation requirement $0.2 < I_\mu < 0.4$. The results of the extrapolation to the isolation region of the analysis is shown in (d). The combined result is indicated by the cross at $I_\mu = 0$. The thick cross only includes the error from the extrapolation, while the thin cross also includes the uncertainty from the contamination of the control region with electroweak and top quark processes.

applied isolation cut, the region and the kinematic variable, where the background is extracted. The convergence of all extrapolations below $I_\mu < 0.1$, the cut applied during the event selection, shows the validity of the method. The value for the number of multijet events is evaluated at $I_\mu = 0$ and the error is estimated as half of the largest difference of all extrapolations.

3.3.2 Shape of the Multijet Background

To obtain the distribution of the multijet background, a similar approach as for the estimation of the number of background events is used. Two background enriched control regions (CR1: $0.1 < I_\mu < 0.25$ and CR2: $0.25 < I_\mu < 0.4$) are defined, with CR1 closer to the signal region. The pure multijet distributions for the kinematic variables under study in the signal region are obtained following the same procedure as in the yield estimation. The ratio of the distributions in the control region is parameterized by a linear function. This function is used to extrapolate from the distribution of CR1 to the signal region at $I_\mu = 0$.

3.4 Physics Modeling Corrections and Related Uncertainties

The simulated events are generated with Monte Carlo generators, as described in Section 3.2.3. A reweighting is applied to include available higher order QCD corrections and electroweak corrections. A matching to measured distributions is performed to enhance the agreement of the simulated kinematic distributions with data [15, 50].

The corrections are applied to the fully factorized cross section [51]:

$$\frac{d\sigma}{dp_1 dp_2} = \left[\frac{d\sigma(m)}{dm} \right] \left[\frac{d\sigma(y)}{dy} \right] \left[\frac{d\sigma(p_T, y)}{dp_T dy} \left(\frac{d\sigma(y)}{dy} \right)^{-1} \right] \cdot \left[(1 + \cos^2 \theta) + \sum_{i=0}^7 A_i(p_T, y) P_i(\cos \theta, \phi) \right], \quad (3.1)$$

with the lepton and anti-lepton four-momenta p_1 and p_2 , the invariant mass m , the rapidity of the dilepton system y , the transverse momentum p_T , the polar and azimuth angle of the lepton (negative lepton for W^- and Z and neutrino for W^+ events) in any rest frame of the dilepton system, the numerical coefficients A_i and the spherical harmonics P_i .

This parametrization splits the dependence of the fully differential cross section into three boson production dimensions (m , y and p_T) and two boson decay dimensions (θ and ϕ). The later two are expressed in the Collins-Soper frame [52].

The corrections to the factors and their estimation is described in the following, grouped by the origin of the corrections. The reweighting procedure to apply the corrections to the nominal POWHEG+PYTHIA 8 generator output is described in Section 3.4.4 and the treatment of related uncertainties is discussed in Section 3.4.5.

3.4.1 Electroweak Corrections

The main source of corrections to pure vector boson production events is the emission of final state radiation. This effect is already included in the simulation chain with PHOTOS, as described in Section 3.2.3. Corrections to final state radiation of the nominal PYTHIA 8 parton shower modeling were found to be negligible, by examining the deviation to predictions with NLO matrix elements instead of the leading order photon emission matrix [50].

Other electroweak corrections are treated as systematic uncertainties and propagated to the p_T^W distribution, such as interference between initial and final state radiation, pure electroweak higher order contributions from box and virtual loop diagrams and final state emission of lepton pairs.

3.4.2 Rapidity and Angular Coefficient Corrections

The electroweak boson cross sections are calculated at NNLO with POWHEG+PYTHIA8 using the CT10nnlo PDF set [53]. POWHEG+PYTHIA implement the factorized cross section shown in Equation 3.1. The parameters A_i are calculated as the ratio of the helicity cross section to the unpolarized cross section [54]. In general the parameters depend on properties of the boson production. Since the values of $A_5 - A_7$ are unequal to zero for $\mathcal{O}(\alpha_s^2)$ and very small in the considered p_T range of the W boson, they are neglected in this analysis.

3.4.3 Boson Transverse Momentum Corrections

Only fixed order perturbative QCD calculations do not allow for a realistic estimation of the W boson transverse momentum p_T^W simulated with PYTHIA8. As the majority of events has a low transverse momentum ($p_T^W < 30$ GeV), terms of the type $\log(M_W/p_T^W)$ have to be resummed and non-perturbative effects need to be included via parton showers or predictions from analytic resummations [55–59]. The nominal PYTHIA 8 parton shower generator includes reweighting to the leading order vector boson production with associated jets [60]. The values of the QCD parameters used by the generator are obtained from fits to Z boson p_T distributions at $\sqrt{s} = 7$ TeV [61]. The fitted parameters are the intrinsic p_T of the incoming particles, $\alpha_s(m_Z)$ for QCD initial state radiation and the initial state radiation infrared cut off. This adaption of the generator parameters is referred to as AZ tune.

3.4.4 Reweighting

The factorized model is applied to the POWHEG+PYTHIA 8 generated samples through an event-by-event reweighting, in the boson production dimensions and the boson decay dimensions. Such the simulated distributions can be transferred to the distributions of any other Monte Carlo generator.

As the first reweighting step, the inclusive rapidity distribution is transferred to NNLO QCD predictions from DYNNLO [62]. As the second step, the p_T^W shape is reweighted for the fixed rapidity to the shape of the PYTHIA 8 prediction with the AZ tune. The last reweighting step for the decay follows

$$w(\cos \theta, \phi, p_T, y) = \frac{1 + \cos^2 \theta + \sum_i A'_i(p_T, y) P_i(\cos \theta, \phi)}{1 + \cos^2 \theta + \sum_i A_i(p_T, y) P_i(\cos \theta, \phi)},$$

where A_i are the numerical coefficients used in POWHEG+PYTHIA 8 and A'_i are the coefficients obtained for the helicity cross sections at $\mathcal{O}(\alpha_s^2)$. In the angular coefficients, this reweighting step includes, besides the rapidity corrections, also the corrections from p_T^W and QCD modeling uncertainties, which are described in Section 3.4.5

3.4.5 Uncertainty Propagation

The uncertainties from the correction and reweighting procedure are propagated to the p_T^W distribution by the variation of the impacted parameters within their uncertainties and the comparison of the retrieved distribution with the nominal one. The source of the uncertainties is the imperfect knowledge of the QCD parameters. The parameters varied in the AZ tune are affected by the error of the experimental estimation. These errors are propagated to the p_T^W distribution by variation along the eigenvectors of the error matrix from the estimation.

Also QCD parameters which are not retrieved with the AZ tune contain uncertainties. The conservative variation of the charm and bottom quark mass by ± 0.5 GeV and ± 0.8 GeV respectively in PYTHIA 8 are propagated to p_T^W by the estimation of the distribution with the varied parameters.

The variation of the factorization scale gives an access to uncertainties due to higher order QCD corrections. The variation of the renormalization scale of the QCD initial state radiation has to be performed independent for the W and Z boson, due to different quark contributions and the generation of the charged in uncharged vector boson.

An additional source of QCD modeling uncertainties is the imperfect knowledge of the parton density functions. These uncertainties are treated separately and form the dominant source of uncertainty in the measurement of the branching ratio fraction. The variation of the PDF affects the differential vector boson production cross section as a function of p_T^W , A_i and y . The variation of the CT10nnlo PDF set is estimated with the Hessian method [63]. The Hessian matrix of the second derivatives at the global minimum of the PDF fit is calculated and the eigenvectors are extracted. For each of the 25 error eigenvectors a pair of PDF variations, corresponding to the 90% confidence level along the eigenvector was retrieved. The kinematic distributions are retrieved for each of the variations and the difference to the nominal distribution is scaled by a factor of $1/1.645$ to transfer the uncertainty to a one sigma (68%) confidence level.

3.5 Reconstruction Corrections and Related Uncertainties

3.5.1 Recoil Calibration

The reconstruction of the hadronic recoil is necessary to obtain the W boson transverse momentum, as the neutrino from the decay products cannot be reconstructed. The p_T^l distribution, which is used in the fitting for the branching ratio fraction can be biased by a mismatch of the recoil reconstruction in data and Monte Carlo due to the influence of the recoil cut in the event selection. A calibration of the Monte Carlo

events to match data is necessary. Four different calibration steps are performed using samples of the process $Z \rightarrow \mu\mu$ since the reconstruction of both decay products offers and independent measurement of the recoil for comparison [64]. The first correction step focuses on the average number of interactions $\langle\mu\rangle$. The simulated number of interactions is adapted to data. As the next step, the distribution of the sum of the difference of the scalar transverse energy and magnitude of the recoil $\Sigma E_T - u$ is matched to data. The effect of the non-uniformity of the calorimeter on the hadronic recoil reconstruction is corrected by studying the ϕ distribution of the recoil. The final recoil response and resolution corrections are retrieved from the comparison of measured and simulated Z events.

3.5.1 Pile-Up Activity

The average number of interactions per bunch crossings is defined as $\langle\mu\rangle = \mathcal{L}\sigma_{pp}/f_{BC}$, with the instantaneous luminosity \mathcal{L} the total inelastic cross section in proton-proton collisions σ_{pp} and the average rate of the bunch crossing f_{BC} . The cross section uncertainty and the exact conditions of the inelastic scattering lead to a mis-modeling of the event activity in data, which significantly changes the reconstructed transverse energy entering the hadronic recoil distribution in the Monte Carlo samples. Therefore, $\langle\mu\rangle$ is scaled by a factor α in the simulation to compensate for this effect. To estimate α , the data and Monte Carlo agreement is evaluated for distributions of $\Sigma E_T - u$ and u_{\perp}^Z with a different assumed α . The χ^2 function of the data and Monte Carlo agreement is minimized to obtain the best guess for $\alpha = 1.10 \pm 0.04$. The uncertainty on the scale factor covers the difference of the minimization in the two distributions. The impact of the systematic uncertainty originating in this correction is estimated by varying the scale factor to its uncertainties and repeating all following calibration steps. Statistical uncertainties of the calibration are estimated by performing the calibration procedure on toy samples, which are randomly varied within the errors.

3.5.1 $\Sigma E_T - u$ Corrections

A correction of the $\Sigma E_T - u$ distribution based on a Smirnov transform [65] is used to match the data distribution to Monte Carlo. By this transform the variable $\Sigma E_T - u$ with a distribution in data $h_{data}(\Sigma E_T - u)$ and Monte Carlo $h_{MC}(\Sigma E_T - u)$ is transformed in Monte Carlo into a variable $(\Sigma E_T - u)'$ with distribution

$$h'_{MC}((\Sigma E_T - u)') \equiv h_{data}(\Sigma E_T - u).$$

The variable is transformed using the cumulative distribution function

$$H(x) = \int_{-\infty}^x h(t)dt$$

by applying

$$(\Sigma E_T - u)' = H_{data}^{-1}(H_{MC}(\Sigma E_T - u)).$$

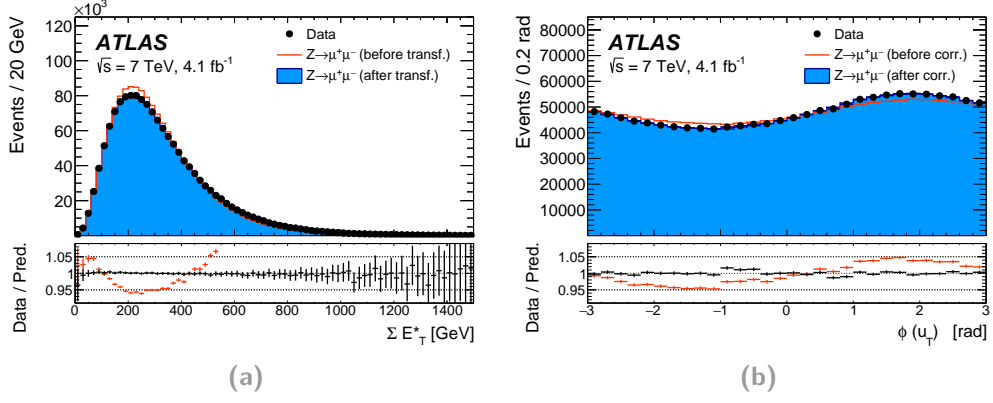


Figure 3.5. Effect of the hadronic recoil calibrations of $Z \rightarrow \mu\mu$ events. The influence of the Smirnov transform on the $\Sigma E_T - u$ distribution (a) and the change of the ϕ distribution with the corrected shift in u_X and u_Y (b) are illustrated. [15]

A p_T dependence of the correction is observed for Z events. Since the poorer p_T resolution in the W sample only allows for an inclusive measurement, the p_T dependence is propagated in data from the Z sample by

$$\tilde{h}_{data}^W(\Sigma E_T - u, p_T) \stackrel{!}{=} h_{data}^Z(\Sigma E_T - u, p_T) \times \frac{\frac{h_{data}^W(\Sigma E_T - u)}{h_{MC}^W(\Sigma E_T - u)}}{\frac{h_{data}^Z(\Sigma E_T - u)}{h_{MC}^Z(\Sigma E_T - u)}}$$

and used in the p_T dependent Smirnov transform for the W sample. The result of the correction can be seen in Figure 3.5a. The systematic uncertainty of the method from the dependence of $\Sigma E_T - u$ on p_T is estimated through a comparison with the p_T -inclusive corrections.

3.5.1 Correction of the ϕ Dependence

Neglecting detector effects, the vector of the hadronic recoil should not show any preference in the polar angle ϕ . Several experimental effects can influence the recoil reconstruction to show a dependence on ϕ . Calorimeter density non-uniformities lead to more or less reconstructed energy and a shift of the collision point from the geometrical detector center also biases the recoil estimation. This effect can be corrected by centering the distributions of the spatial x and y component of the recoil u_X and u_Y around zero. The corrections are evaluated in dependence of $\Sigma E_T - u$ and the following transformation is applied:

$$u'_X = u_X + (\langle u_X \rangle_{data} - \langle u_X \rangle_{MC}) \quad u'_Y = u_Y + (\langle u_Y \rangle_{data} - \langle u_Y \rangle_{MC}).$$

The distribution of ϕ with and without the correction is shown in Figure 3.5b. The systematic errors arising from the calculation of the correction parameters were found to be small compared to the other systematic uncertainties in the correction procedure and therefore have been neglected.

3.5.1 Final Recoil Corrections

As a last step, the difference in the distributions of the hadronic recoil u for data and Monte Carlo is addressed. As the Z boson transverse momentum can be reconstructed from the lepton pair with a precision of 1-2 GeV. It gives an excellent reference for the hadronic recoil, which is reconstructed with significantly worse precision. Given energy conservation, the sum of the lepton transverse momentum p_T^l and the to it parallel component of the Z boson hadronic recoil u_{\parallel}^Z should be centered around zero. The difference in the distributions for data and Monte Carlo is the energy-scale correction $b(p_T^V, (\Sigma E_T - u)')$. The hadronic recoil's resolution difference is derived as the ratio $r(p_T^V, (\Sigma E_T - u)')$ of the standard deviations of the u_{\perp}^Z distributions in data and Monte Carlo. The corrections are derived as a function of the vector bosons transverse momentum p_T^V with $V \in [W, Z]$ and the Smirnov corrected sum of the difference of the transverse energy and the hadronic recoil $(\Sigma E_T - u)'$. Since this dependence is independent of the decaying vector boson, the correction retrieved with the Z -sample can be applied to the W -events and only differences in the reconstruction have to be considered. The final corrections on Monte Carlo are:

$$\begin{aligned} u_{\parallel}^{V,corr} &= \left[u_{\parallel}^{V,MC} - \langle u_{\parallel}^{Z,data} \rangle (p_T^V, (\Sigma E_T - u)') \right] \cdot r(p_T^V, (\Sigma E_T - u)') + \\ &\quad \langle u_{\parallel}^{Z,data} \rangle (p_T^V, (\Sigma E_T - u)') + b(p_T^V, (\Sigma E_T - u)'), \\ u_{\perp}^{V,corr} &= u_{\perp}^{V,MC} \cdot r(p_T^V, (\Sigma E_T - u)') \end{aligned}$$

The calibration is evaluated for three bins of $\langle \mu \rangle$ since the u_T distribution and therefore the resolution correction depends on the amount of pile-up. The impact of all corrections on the recoil distributions for $Z \rightarrow \mu\mu$ events is shown in Figure 3.5. Since the corrections are retrieved with Z events and used on the W events, differences in the reconstruction of those have to be considered. Theoretical differences in the u_T distribution for the two processes like the boson kinematic properties, initial and final state photon radiation differences and different selection requirements are accurately modeled in the simulation and do not need to be taken into account. Differences in the detector response in contrast have to be examined for the estimation of the statistical error.

The matching is preformed on particle truth level. The neutrino of the W decay is treated as a charged lepton in the hadronic recoil calculation. Furthermore, events with photons from final state radiation are removed. With these requirements an agreement of 0.03% is achieved for the standard deviation of the u_T distribution for both processes. This deviation is equivalent to a 6% variation of the resolution correction factor r . The systematic uncertainty therefore is retrieved by varying r by 6% in the calculation of the corrected hadronic recoil distributions.

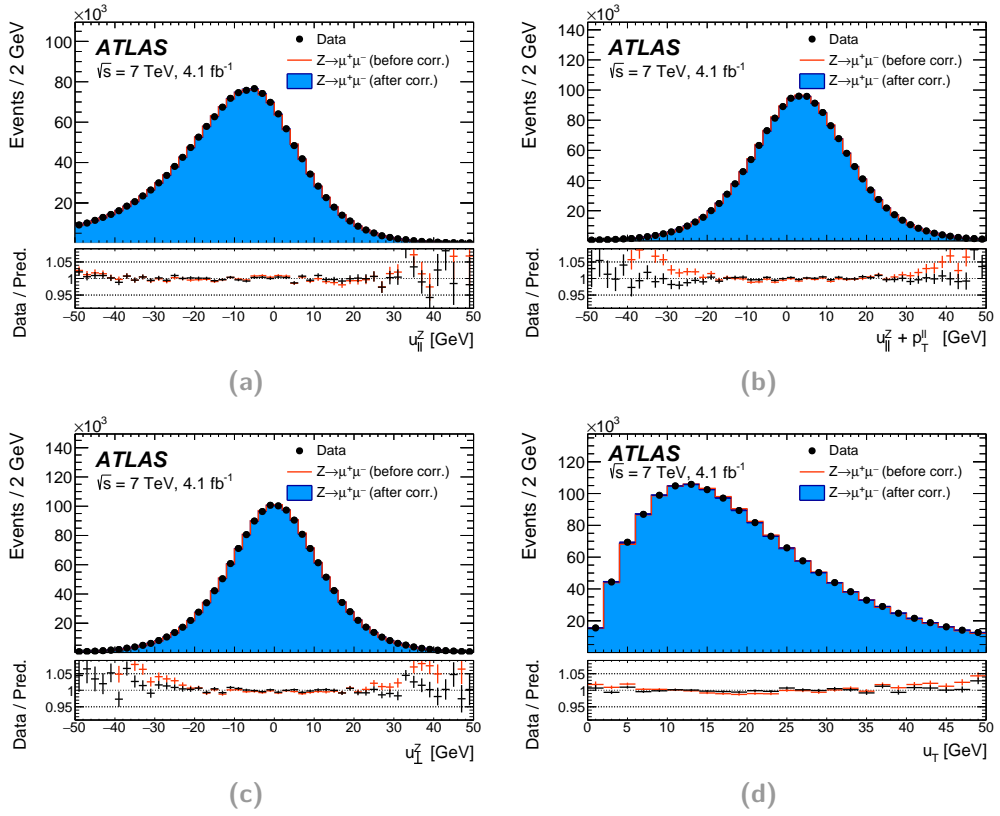


Figure 3.6. Data and Monte Carlo agreement after all described recoil correction are applied to the distribution of u_{\parallel}^Z (a), $u_{\parallel}^Z + p_T$ (b), u_{\perp}^Z (c) and u_T^Z (d). The shown error bars only represent the statistical errors. [15]

3.6 Detector Corrections and Uncertainty Estimation

For the simulation of the Monte Carlo samples, as described in Section 3.2.3, the detector geometry is precisely implemented including all known imperfections and defects. To cover for remaining differences between data and simulation, corrections have to be applied to the Monte Carlo samples in order to match data sufficiently for the desired template fit. In the following the retrieved scale factors to match the reconstruction efficiency are described in Section 3.6.1 and the corrections for the scale of the muon transverse momentum p_T^μ are described in Section 3.6.2.

3.6.1 Muon Scale Factors

The efficiencies of the muon reconstruction, the trigger and the isolation selection differ in Monte Carlo and data and hence have to be corrected by scale factors. For a precise measurement of the W mass, these scale factors have been evaluated in the dependence of the lepton charge, the spatial coordinates η and ϕ , the muon transverse momentum p_T and the thereto parallel component of the hadronic recoil w_{\parallel}^l .

The scale factors are calculated using a tag-and-probe method [32] on $Z \rightarrow \mu\mu$ data and MC events. A schematic illustration of the method is shown in Figure 3.7a. Events with two muon candidates whose kinematic properties allow to conclude their origin from the Z decay are selected. One of the muons, used as tag, is required to pass strict quality criteria while the probe muon only has to pass looser selection criteria. The exact criteria depend on the evaluated scale factor and are discussed in the following sections. The efficiency ϵ in data and Monte Carlo is defined as the number of measured probes, divided by the expected probe events, as estimated from tag. The scale factor is defined as the ratio of the efficiency in the background corrected data and Monte Carlo samples $SF = \epsilon_{data}/\epsilon_{MC}$.

There are several sources of uncertainties on the estimation of the scale factors as the muon momentum scale uncertainty (Section 3.6.2), the hadronic recoil correction (Section 3.5.1), the uncertainties coming from the weights applied to the Monte Carlo events (Section 3.4.4) and the uncertainties on the background (Section 3.3). For each of the contributions, the muon scale factors are evaluated without the $\pm 1\sigma$ deviations of the corrections applied. The systematic scale factor uncertainty is the difference between the nominal calculation and the calculation with the variation. The total uncertainty on the scale factor is estimated as a combination of these results. A detailed description on the scale factor estimation can be found in [66].

3.6.1 Trigger Scale Factor

The trigger scale factor corrects the incorrect identification of a reconstructed muon as a trigger object. The tag muon is required as an isolated ($p_T^{\mu, cone} < 0.1p_T^\mu$),

combined (matching tracks in inner detector and muon system) and triggered (matched with trigger object) muon, while the probe is only required to be combined and isolated and forming together with the tag muon an invariant mass close to the Z mass. The probe object is considered as reconstructed if a trigger object can be matched with it.

3.6.1 Reconstruction Scale Factor

The reconstruction scale factor estimation probes for the efficiency of the reconstruction of a track in the muon system matching to an inner detector track. Therefore the tag is required to be an isolated combined muon, while the probe is set as an isolated inner detector track which combines with the tag to an invariant mass close to the Z mass. The probe is matched, if a track in the muon system is found within $\Delta R < 0.05$ of the extrapolated inner detector track.

3.6.1 Isolation Scale Factor

The isolation of a track in Monte Carlo depends on the implementation of the hadronisation. Therefore the correct scale to data has to be evaluated in a data driven approach. The tag muon is required to be isolated and combined and the probe muon, matching together with the tag muon the Z mass, needs to be a combined muon without any requirements on the isolation. If the isolation criteria is fulfilled for the probe the event is considered to be efficiently reconstructed.

An overview of the obtained scale factors is given in Figure 3.7b. The reconstruction scale factor shows, in contrast to the trigger and isolation scale factor, a slight dependence on p_T as a decrease in the scale factor with increasing p_T . The uncertainties on the scale factor reconstruction are originating from the statistical uncertainty of the Z -sample, the uncertainty of the multijet background suppression and the uncertainty on the momentum scale.

3.6.2 Muon Transverse Momentum Calibration

A distorted reconstruction of the muon transverse momentum, as the only measurable final state of the studied W boson decay, leads to a biased measurement of the branching ratio fraction. Such, a correction of the bias in the reconstruction has to be performed. Two different classes of bias are possible [15]. The so called radial bias is caused by a detector displacement in the direction of the particle path and is corrected by a momentum scale. The resolution of the reconstructed muon is affected by the limited detector alignment and knowledge of the sub-detector resolution, the uniformity and absolute value of the magnetic field and the interaction with passive detector material. These effects are corrected on the Monte Carlo samples, while the charge dependent contribution from a curl deformation of the cylindrical or twist

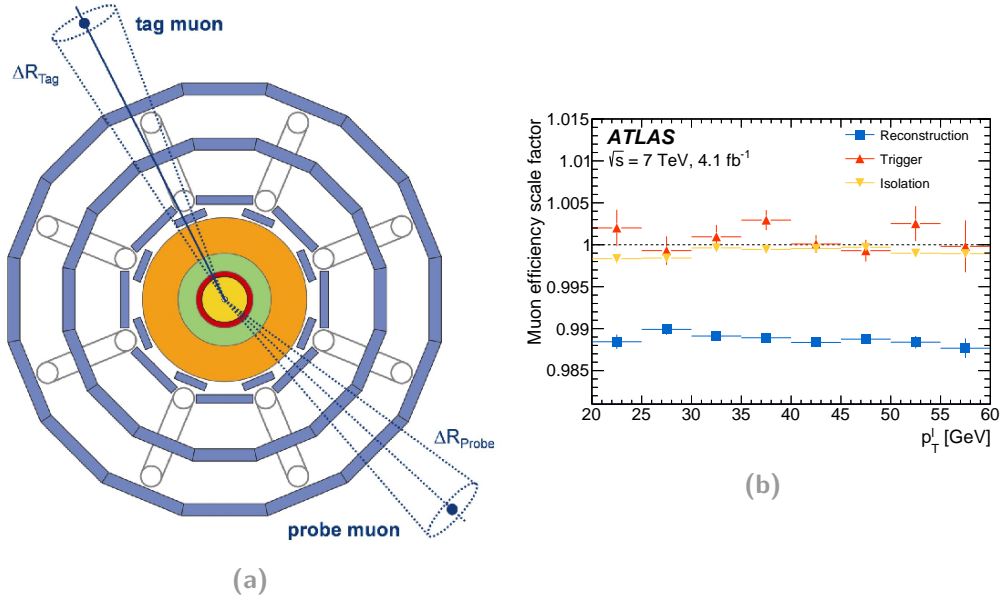


Figure 3.7. Schematic illustration of the tag-and-probe method (a) [67]. A fully reconstructed muon is selected as tag in a sample of $Z \rightarrow \mu\mu$. Muon candidates which form together with the tag muon an invariant mass close to the Z mass are selected as probes. By applying different requirements to the tag and probe muon different efficiencies can be estimated when comparing the number of reconstructed tags with the number of reconstructed probes. The method is used to estimate the trigger, reconstruction and isolation scale factors (b) [15].

deformation of the disk-like sub-detectors is applied to data. This bias contribution is referred to as sagitta bias. The corrected p_T distribution are retrieved as:

$$p_T^{\text{MC,corr}} = p_T^{\text{MC}} \times [1 + \alpha(\eta, \phi)] \times [1 + \beta_{\text{curv}}(\eta) \cdot G(0, 1) \cdot p_T^{\text{MC}}]$$

$$p_T^{\text{data,corr}} = \frac{p_T^{\text{data}}}{1 + q \cdot \delta(\eta, \phi) \cdot p_T^{\text{data}}}.$$

This correction is applied to the transverse momentum of each reconstructed muon. The parameter α , β and δ are the correction of the scale, resolution and sagitta bias, respectively. $G(0, 1)$ is a random number, evaluated from a standard normal distribution for each event to encounter for the statistical nature of the resolution bias.

3.6.2 Momentum Scale and Resolution

The standard method for the estimation of the scale α and the resolution β of the reconstruction transverse muon momentum is a template approach using a binned likelihood function [32, 68]. The parameters are evaluated for several bins of η and ϕ . Since, for the W boson decay, there is no access to the full kinematics because of the undetected escaping neutrino, the fully reconstructible decay of a Z boson into a muon pair is used for the estimation of the parameters. Furthermore the calibration profits from the precise knowledge of the Z mass and the results on the W mass

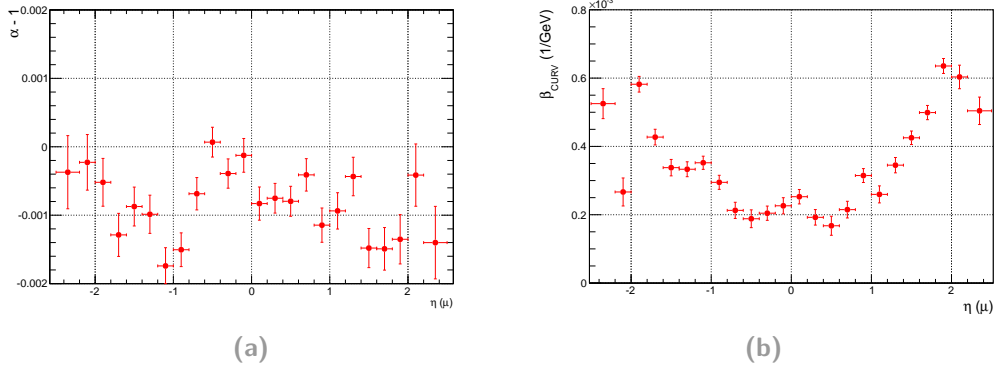


Figure 3.8. Result of the momentum scale (a) and resolution (b) estimation in bins of η . The displayed errors are statistical errors only [68].

cannot be biased by the calibration. The distribution of the dimuon invariant mass $m_{\mu\mu}$ is constructed requiring exactly two opposite charged muons with a transverse momentum $p_T^l > 22$ GeV each. This sample is considered to be free of background in the fitting range of two standard deviations around the mean of the mass distribution obtained in data.

An iterative χ^2 approach based on templates of distributions with different bias from α and β is used to estimate the best guess of the parameters. The procedure is repeated for a binning in the pseudorapidity of the two leptons (η_i, η_j). Monte Carlo templates are produced where the p_T correction is performed with values of α and β varying in small steps in the range of the expected corrections. First, for each value of one parameter (in the following called p_1) the χ^2 test of data and Monte Carlo is performed for the second parameter (p_2). The best guess for $p_{2,best}$ and the corresponding minimum of the χ^2 parabola χ_{best}^2 are calculated and their evolution in dependence of p_1 is considered. $\chi_{best}^2(p_1)$ forms again a parabola, where the best guess for $p_{1,ij}$ for the studied pseudorapidities (η_i, η_j) is retrieved at the minimum of the parabola. The error $\Delta p_{1,ij}$ is obtained as the value of p_1 for $\chi_{best}^2(p_1) = \min(\chi_{best}^2(p_1)) + 1$. A first order polynomial fit to the dependence of $p_{2,best}(p_1)$ evaluated at $p_{1,ij} \pm \Delta p_{1,ij}$ finally results in the best estimator for $p_{2,ij} \pm \Delta p_{2,ij}$. The results of the estimation are shown in Figure 3.8

Since the parameters are estimated for the decay of the Z boson, which has due to the smaller boson mass smaller values of p_T , an error in the extrapolation to the W boson decay kinematics is present. This error on the scale parameter is parametrized as

$$\Delta\alpha = a_0 + \frac{a_1}{\langle p_T^l(W) \rangle},$$

with the average muon p_T in W boson events and the free parameter a_0 and a_1 . The result of the determination of the parameters for different η ranges is shown in Figure 3.9a.

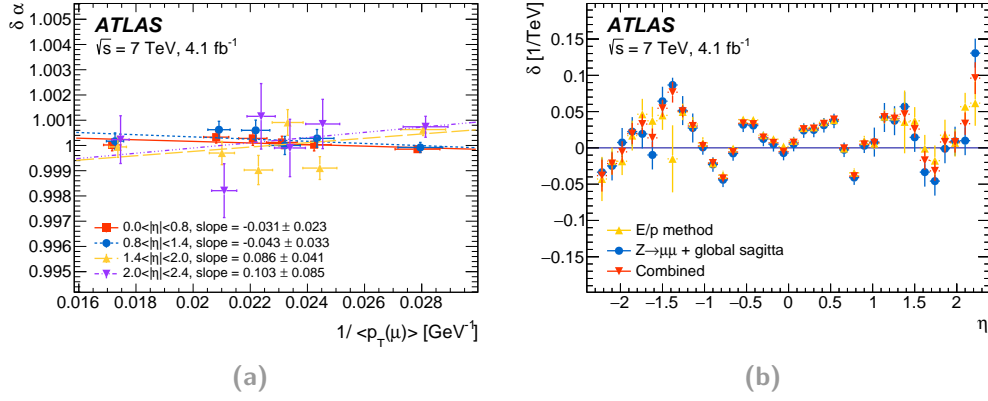


Figure 3.9. Dependence of the muon momentum scale correction error on $1/p_T$ measured with Z boson events (a). A linear fit is performed to extrapolate the errors to the W boson momentum range. The sagitta bias δ measured with different methods, as described in the text (b). [15]

3.6.2 Sagitta bias

Since the sagitta bias is a charge dependent correction on the muon transverse momentum, the decay $Z \rightarrow \mu^+\mu^-$ gives an excellent probe on it. The invariant mass distribution of the dimuon pair from the Z decay is evaluated for a binning of the pseudorapidity η of each of the decay muons. The correction of p_T in data is assumed to be of the following form [68]:

$$p_T^{corr} = \frac{p_T^{reco}}{(1 + \alpha)(1 + q \cdot \delta \cdot p_T^{reco})},$$

with a scale correction α , the sagitta correction δ and the charge q . For each of the pseudorapidity bins, the ratio $R = m_Z^{data}/m_Z^{MC}$ of the calculated position of the Z peak in the dimuon invariant mass spectrum in data and Monte Carlo is calculated together with its uncertainty. The scale and sagitta bias are simultaneously estimated by the minimization of the following distribution, where the indices on the scale and the sagitta bias stand for the different muon charges:

$$\chi^2 = \sum \left(\frac{R - \sqrt{(1 + \alpha_+)(1 + p_T \delta_+) \cdot (1 + \alpha_-)(1 + p_T \delta_-)}}{\sigma(R)} \right)^2.$$

This estimation results in the determination of the shape of the sagitta bias variation. The overall scale is obtained by the comparison of the $p_T(\mu^+)$ and the $p_T(\mu^-)$ distributions.

A second method is used to verify the sagitta bias calculation. For this purpose the determination of the particle momentum measured in the inner detector is compared to the energy measured in the calorimeter. Since the calorimeter is not optimized for the measurement of the muon energy, the decay of W bosons into electrons is considered. As the sagitta bias is a detector effect independent of the considered particle, the result can be transferred to the muon measurement. A sample of $W \rightarrow e\nu$

events with tight electron selection [69] is used, providing higher statistics than the $Z \rightarrow \mu\mu$ sample used in the first estimation. The charge independent energy measurement makes the mean of the ratio E/p sensitive to the charge. Therefore the sagitta bias can be defined as:

$$\delta = \langle E_T \rangle \frac{\langle E/p \rangle^+ - \langle E/p \rangle^-}{2}.$$

The sagitta bias is again evaluated in bins of the pseudorapidity. The results of both methods is shown in Figure 3.9b. A clear structure coming from detector distortions is visible over the full range of η .

3.7 Fitting Procedure

The following section describes the setup of the fitting framework and the implementation of the fit. As described in Section 3.1, the idea is to make use of the softer kinematic distributions of the tau lepton branch compared to the muon branch in the W decay and measure the branching ratio fraction of the two processes using a template fit of the two distributions to data. As kinematic distributions, the transverse momentum of the muon in the final state p_T^l and the transverse mass of the W boson m_T are chosen, as they show the best separation of the two processes. The distributions, together with the background processes, as described in Section 3.3, are shown in Figure 3.10. These distributions form the input of the fitting framework.

An overview of the framework and the implementation of the fitting is given in Section 3.7.1. The initial studies to verify the fitting setup and estimate the expected sensitivity are performed with toy and Asimov datasets as described in Section 3.7.2. As visible in Figure 3.10, especially for the m_T distributions, the low statistic background processes suffer from statistical bin to bin fluctuations. Since this behavior complicates the convergence of the fit a smoothing procedure described in Section 3.7.3 is applied to these distributions.

An overview on the systematic uncertainties from the physics modeling, the background estimation and the applied corrections is given in Section 3.7.4. The preparation of the input to the fitting to treat these uncertainties is presented in Section 3.7.5. Two different implementations to retrieve the branching ratio fraction directly as one fit parameter are discussed in Section 3.7.6.

3.7.1 Overview of the Fitting Framework

HistFactory [70], a framework integrated in the C++ particle physics data analysis package ROOT [71], is used to create and minimize the probability density function (pdf) for the template fit. The fit model is build from the input histograms for data, or respectively Asimov or toy data, and the simulated Monte Carlo processes. They

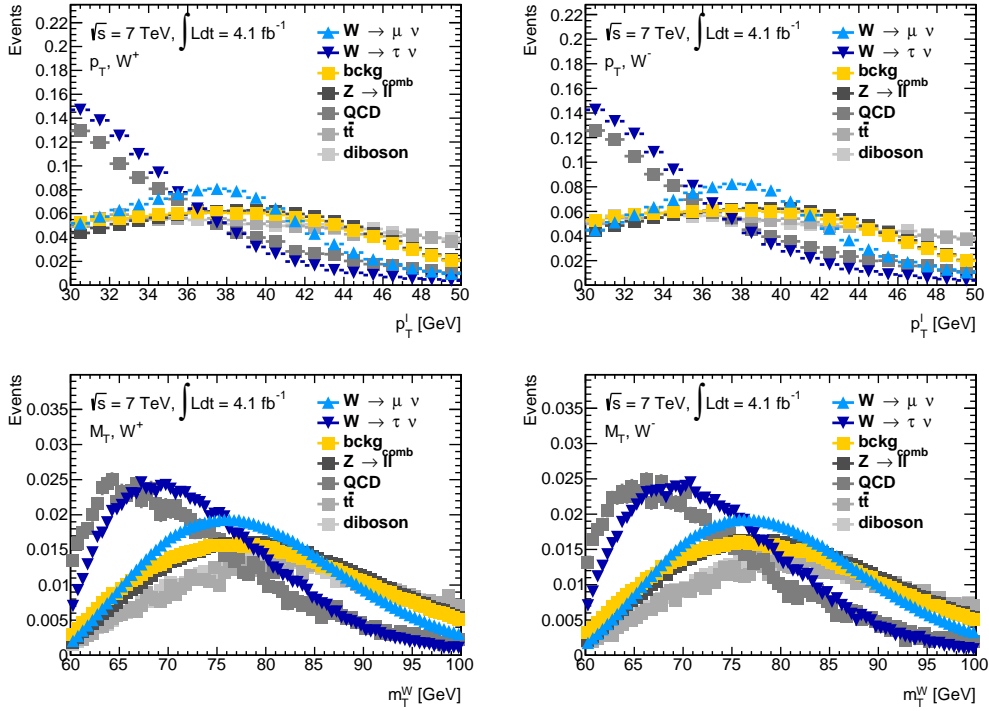


Figure 3.10. Normalized distributions of the signal and background processes for the transverse momentum (top row) and the transverse mass (bottom row) of the W^+ (left column) and W^- (right column) decay. The background processes are shown as single processes and as the sum of all.

are added as samples s implemented in the `HistFactory::Sample` class to the overall fitting workspace. For each kinematic variable (p_T or m_T), the decay of the positive and negative charged W boson is treated as one channel c (`HistFactory::Channel`) of the measurement (`HistFactory::Measurement`). Both kinematic variables cannot be considered together in one fit, as they do not have a disjoint event selection and the correlations between the kinematic variables are unknown. Two different classes of parameters p , normalizations and shape variations, are used to implement the variation of the branching ratio fraction and the systematic uncertainties. The full set of all parameters of these two classes is resumed in the vector α .

The normalization of each sample is denoted as a parameter ϕ_p implemented as `HistFactory::NormFactor` in the fit. This parameter is chosen to be the same for all channels of the measurement. In some cases, the normalization of several samples is put together in one parameter, for example for a combined signal normalization of the $W \rightarrow \mu\nu$ and the $W \rightarrow \tau\nu$ channel or a combined background normalization of all background processes assuming, that their relative normalization is correctly modeled. In the case of the combined background normalization, the backgrounds can be either treated as single histograms, or as a combined summed histogram. In the latter case, the systematic uncertainties of the single processes are summed to a combined systematic.

The systematic uncertainties are given as up and down variation H_{Up} and H_{Down} of

the nominal distribution H_0 . For each variation an individual histogram with the bin content varied accordingly is provided. The histograms are passed as input to the `HistFactory::HistoSys` class. During the fit a linear interpolation with the parameter α_p between the up and down varied histogram is carried out.

Including the uncertainty on the luminosity and the statistical errors with correlations between the bins b of the histograms this gives the following set of parameters where the indices indicate the dependence of the parameters:

- λ The luminosity parameter which varies the luminosity within the errors $\Delta\mathcal{L}$ around the nominal value \mathcal{L}_0 . It acts like a common normalization on all samples.
- γ_{cb} Bin-by-bin scale factors used for statistical uncertainties. These are nuisance parameters only entering in the error calculation of the other parameters.
- ϕ_s The product of all unconstrained normalizations ϕ_p of a sample or a set of samples.
- σ The parametrized histogram corresponding to the `HistoSys` implementing the shape variations covering the systematic uncertainties.

This leads to the following equation for the expected number of events in a given bin of the histogram:

$$\nu_{cs} = \lambda \gamma_{cb} \phi_s(\boldsymbol{\alpha}) \sigma(\boldsymbol{\alpha})$$

and the marked Poisson model

$$\mathcal{P}(n_{cb}, a_p | \phi_p, \alpha_p) = \prod_{c \in \text{channels}} \prod_{b \in \text{bins}} \text{Pois}(n_{cb} | \nu_{cb}) \cdot \text{G}(\mathcal{L}_0 | \lambda \Delta\mathcal{L}) \cdot \prod_p f_p(a_p | \alpha_p),$$

with the constraint term from auxiliary measurements $f_p(a_p | \alpha_p)$, the estimation of the histograms for the up and down variation, the Poissonian probability density function for the expected number of events $\text{Pois}(n_{cb} | \nu_{cb})$ and the Gaussian probability density function $\text{G}(\mathcal{L}_0 | \lambda \Delta\mathcal{L})$ for the variation of the luminosity. For a fixed dataset n_{cb} and fixed auxiliary measurements a_p , $\mathcal{P}(n_{cb}, a_p | \phi_p, \alpha_p)$ is the Likelihood function $L(\phi_p, \alpha_p)$ for the estimation of the normalization ϕ_p and shape parameter α_p .

The best fit value can be obtained by minimizing the Likelihood function. The minimization and an error estimation from the ROOT Minuit minimizer is implemented in `HistFactory`. Since the Minuit algorithm tends to underestimate the true errors of a parameter an Minos like approach was realized. The error is calculated for each parameter independently by fixing the parameter to a value close to the best fit value and minimizing the negative Log-Likelihood function for the remaining parameters. By varying the fixed parameter in steps and repeating the procedure the parameter value for $-\ln L = (-\ln L)_{\text{best}} + 0.5$ is searched in positive and negative direction from the best fit value. These values correspond to the positive and negative standard

errors of the parameter.

The distributions after the fit H_{fit} can be retrieved from the pre-fit distributions by applying the best fit values for the luminosity parameter λ , the normalization parameters ϕ and the shape parameters α according to

$$H_{\text{fit}} = \lambda \cdot \left[\prod_{p \in \text{norm}} \phi_p \right] \cdot \left[H_0 + \sum_{p \in \text{shape}} \alpha_P \begin{cases} H_{\text{Up}} - H_0, & \alpha_P \geq 0 \\ H_0 - H_{\text{Down}}, & \alpha_P < 0 \end{cases} \right].$$

The errors on the histogram bin content can be estimated from the pre-fit histogram errors and Gaussian error propagation of the fit parameter errors. Since the estimation of the correlation between the errors on the fit parameter is not stable for the large likelihood distribution (consecutive correlation estimations lead to changes of more than 0.5 in the correlation), the errors have to be treated as uncorrelated during the reconstruction of post-fit samples. By that, the error on the bin content is highly overestimated. This problem underlines the necessity to retrieve the branching ratio fraction from only one parameter as discussed in Section 3.7.6.

3.7.2 Asimov and Toy Datasets

In order not to bias the fitting results by tuning it to data during the framework development, Asimov and toy datasets have been produced. An Asimov dataset is a dataset which perfectly describes the Monte Carlo channels already before the fit. Such, in a correct framework, the parameters should not change from the nominal values but the errors of the parameter estimation resembles the expected errors in a fit to data. The Asimov dataset is constructed as a sum of all Monte Carlo channels. A toy dataset is a dataset, where the agreement is not perfect before the fit and the deviation of the data to Monte Carlo is constructed such, that an agreement within the errors of both distributions is achieved. It is constructed by applying variations to the content of the pure sum of all Monte Carlo channels. To include the systematic variations into the toy data, a random number is generated. The up variations scaled by the random number are added to the sum of all Monte Carlo channels for a positive random number and the down scaled variation for a negative random number, respectively. Finally the histogram is smeared by a Poisson distributed random number to factor in statistical variations.

If the fitting is repeated several times on different toy datasets, the distribution of the best guess of the fit parameter should vary around its nominal value and the width of this distribution gives the estimate for the expected error on the fit parameters. By that, it is possible to cross check the results from the Asimov datasets.

3.7.3 Input Smoothing

The low statistic MC distributions show large bin to bin fluctuations, which lead to problems in the convergence of the fit. Therefore a smoothing algorithm was applied to the multijet, $t\bar{t}$ and diboson background. For the smoothing a window of one fifth of the whole region is slid over the fitting region ($30 \text{ GeV } c^{-1} \leq p_T \leq 50 \text{ GeV } c^{-1}$ and $60 \text{ GeV } c^{-2} \leq m_T \leq 100 \text{ GeV } c^{-2}$) and a linear fit of the bin content is evaluated at the considered bins. The window is chosen to be centered around the considered bin. At the borders, where this is not possible, the width of the window is kept constant and it ranges asymmetric to the studied bin. The result of the smoothing can be found in Figure 3.11 for the distributions of the negative W^- boson and Figure A.1 for the positive W^+ boson.

The smoothing is applied before the generation of Asimov datasets, since a later smoothing would destroy the perfect agreement between data and Monte Carlo. Toy data is generated from the un-smoothed histograms and the smoothing is only applied to the Monte Carlo samples.

3.7.4 Systematic shape Variations

The generation and calibration of the data and Monte Carlo samples is affected by related uncertainties. These uncertainties are propagated to the kinematic distributions as up and down variations. Each variation corresponds to a change of the underlying parameter by plus or minus one standard deviation, respectively. The naming "up" and "down" is arbitrary and for example an "up" variation does not necessarily correspond to a positive contribution to the histogram. An overview of all systematic variations can be found in table 3.7.

Table 3.7. Overview of all systematic uncertainties on the physics modeling of the studied processes, the data reconstruction and the detector calibration. A brief description of the systematics origin is given.

Name	Source of the uncertainty
Physics Modeling	
PDF	A set of 25 variations of the eigenvectors of the Hessian approach for the particle density function uncertainty estimation.
PTW	Uncertainty on the reweighting of the W boson transverse momentum. The reweighting includes a transformation of the leading order results to higher order calculations.
XSEC DIBOSON	Cross section uncertainty of the modelled background processes. As the cross section of the signal processes is an open fit parameter, their model uncertainty is not taken into account.
XSEC TOP	

XSEC ZMUMU	
XSEC ZTAUTAU	
XSEC QCD	Uncertainty on the data driven estimation of the multijet background.
Data Reconstruction	
HR	Uncertainty from the calibration of the hadronic recoil with events from Z boson decays.
HR VARSUMET	Uncertainty from the extrapolation of the hadronic recoil from the kinematic range of the Z boson decay to the W boson decay due to the dependence of the hadronic recoil resolution on the sum of the missing transverse energy.
Detector Corrections	
MUON EXTRAP	Uncertainty related to the extrapolation of the muon transverse momentum calibration of the Z to the W boson decay.
MUON METHOD	Uncertainty from the non closure of the two methods used for the sagitta bias calibration.
MUON RESOL	Uncertainty on the estimation of the muon momentum resolution smearing the transverse momentum dependent calibration procedure.
MUON STAT	Propagation of the uncertainty due to the limited statistics of the Z boson sample used for the muon momentum calibration.
SAGITTA	Uncertainty on the sagitta bias estimation.
MUONSF TRIGGER	Uncertainty on the estimation of the muon trigger and isolation scale factor.
MUONSF RECO	Uncertainty on the estimation of the muon reconstruction scale factor.
MUON NOMSFMISS	Uncertainty due to the miss-identification of a Z event as W event due to the failed reconstruction of a decay lepton.

3.7.5 Preparation of the Shape Systematics

The uncertainties are provided in different formats, as their estimation was done in independent analysis for the different sources of uncertainties. The format has been unified for this analysis. Most systematics are retrieved by the variation of

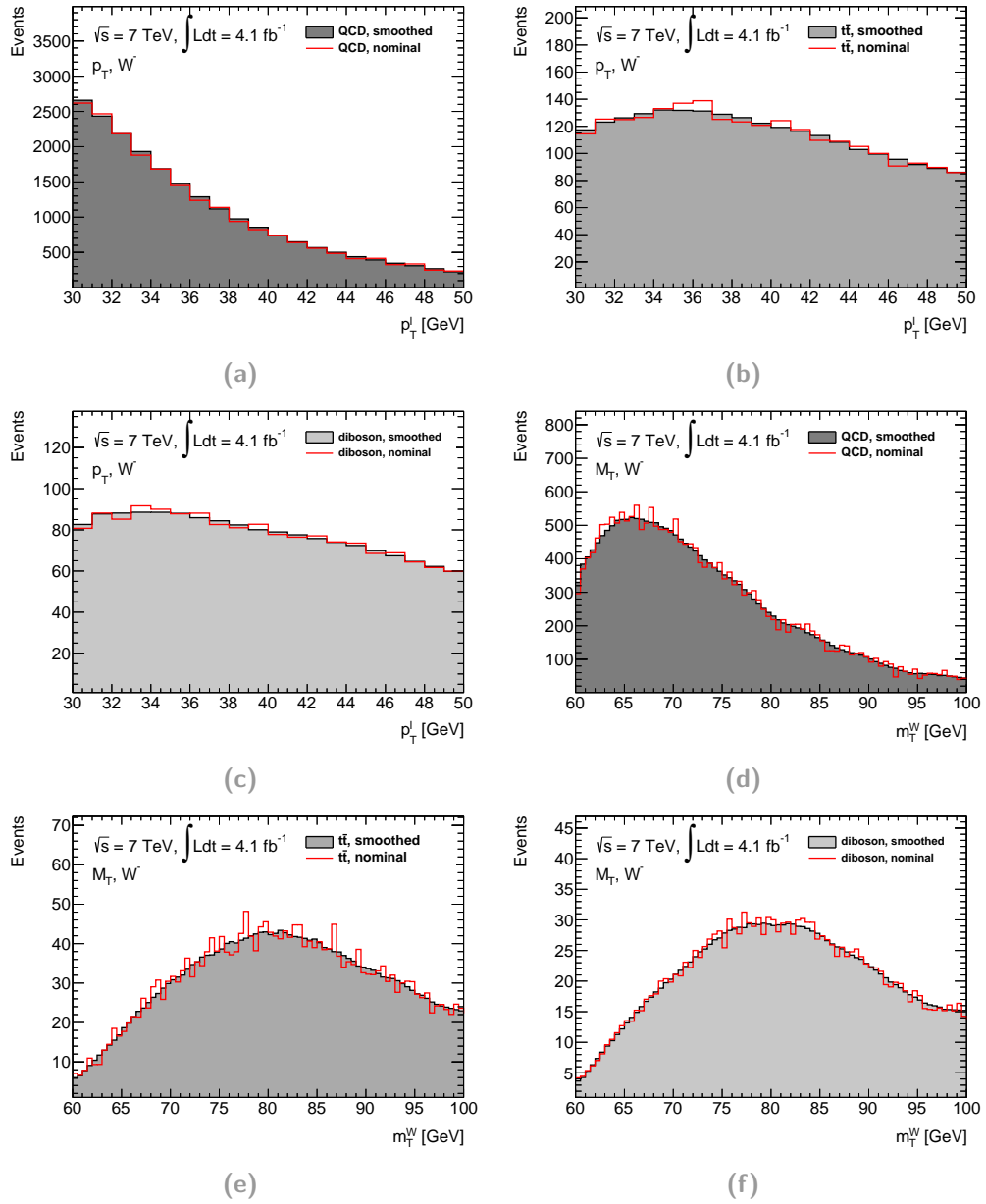


Figure 3.11. Comparison of the smoothed and original (red line) samples for the p_T (a), (b) and (c) and the m_T (d), (e) and (f) distributions for the decay of the negative W^- boson.

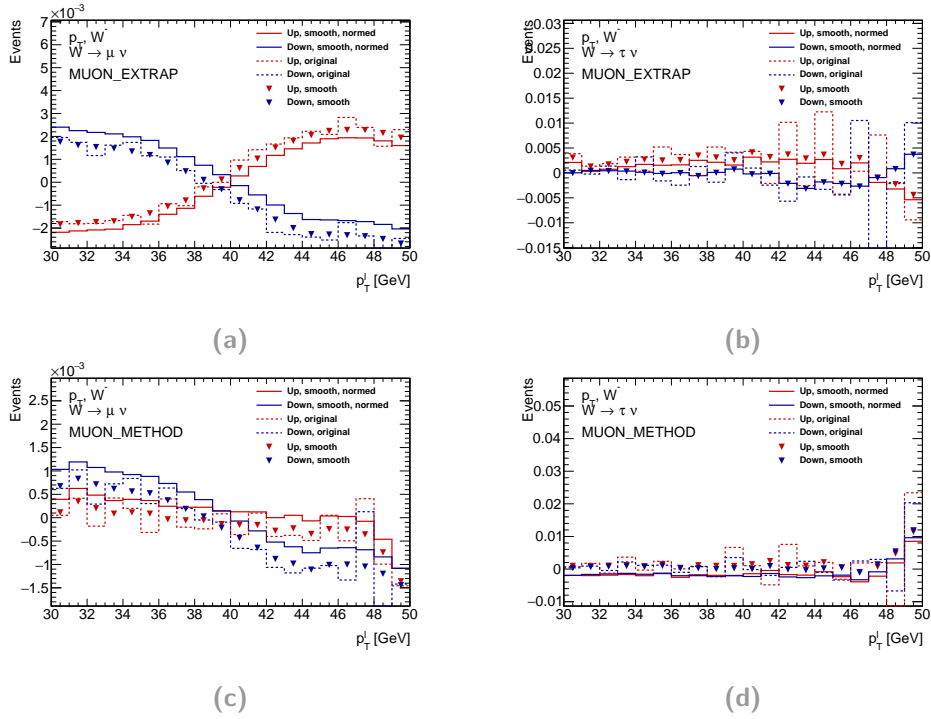


Figure 3.12. Relative shape of two of the most dominant systematics of the p_T distribution of the negative W boson decay. The $W \rightarrow \mu\nu$ decay channel is shown on the left while the $W \rightarrow \tau\nu \rightarrow \mu\nu\nu$ channel is shown on the right. The systematics are presented as they were used for the W mass measurement (dashed line), after a smoothing is applied (triangles) and after smoothing and the removal of the normalization contribution (solid line).

parameters in the reconstruction of the kinematic distributions, where some are extracted with different cuts in the event selection and reconstruction. Therefore for these systematics a nominal template with the optimized parameters and a up and down template with the varied parameters was generated. The relative deviation of the variations nominal template to the varied template is calculated. During this step, a smoothing is applied to the input templates as described for the fitting templates in Section 3.7.3. As for some uncertainties, already a relative variation is given, the smoothing is applied on this relative sample.

Shape systematics, which are provided as inclusive, relative distributions, like the PDF systematic, are distributed to the different channels according to the signal strength.

The normalization component is removed from the generated variation sample by shifting each bin entry by the fraction of the sum of the entries of all bins and the number of bins, as HistFactory only provides a implementation of shape systematics, which also change the normalization of the distribution in the range of the variations. An overview of the two most dominant shape variations apart from the PDF relative systematics, and the effect of the transformations applied during their generation is given in Figure 3.12 for the signal processes for the p_T spectrum of the negative W boson decay.

3.7.6 Approaches to Parametrize the Branching Ratio Fraction

Two different approaches are used to parametrize the change in the branching ratio fraction in one single parameter. A sophisticated choice of the parametrization allows to read the change in the branching ratio fraction from one parameter. Therefore the correlations between parameters, which tend to be poorly estimated for the large likelihood function, do not have to be propagated to the measurement. This would be for example the case if nuisance parameters could change the normalization of samples.

In general, the difference in the branching ratio fraction is given by the difference in the number of entries in the histograms of the signal process before and after the fit. The normalization free shape systematic treatment is, as discussed in the previous section, the bases for such a parametrization. In both approaches, a single parameter n_{signal} is used for the simultaneous normalization of the signal processes $W \rightarrow \mu\nu$ and $W \rightarrow \tau\nu \rightarrow \mu\nu\nu$. The background processes are treated for both approaches in three different ways. Either an individual norm factors n_i is applied to each process, the same norm n_{bckg} is applied simultaneous to all single background histograms or the single histograms are combined into one histogram and one common norm n_{comb} is applied to this.

The first approach is the easiest way to parametrize the branching ratio fraction with a single parameter. A common norm is applied to the signal processes $W \rightarrow \tau\nu \rightarrow \mu\nu\nu$ and $W \rightarrow \mu\nu$. An additional, single norm factor n_τ is applied to the process $W \rightarrow \tau\nu \rightarrow \mu\nu\nu$. This parameter accounts for the normalization difference of the two processes and therefore the branching ratio fraction is given by this parameter. The relative error on the measured branching ratio fraction is the relative error of this parameter.

The second approach for the parametrization is via a constructed shape. Therefore a shape systematic is constructed such, that the up variation adds the same number of events to the $W \rightarrow \tau\nu \rightarrow \mu\nu\nu$ sample, as it subtracts from the $W \rightarrow \mu\nu$ sample while keeping the actual relative shape the same. The down systematic is build accordingly. Such it is ensured, that each event migrated by the fit to change the branching ratio fraction is directly balanced between the two processes and not due to a mis-modeling of the background. The special shapes are shown in Figure 3.13. The difference in the branching ratio fraction is then given by the difference in the fraction of the integral of the distributions for both processes:

$$\frac{BR_{\text{Measurement}}}{BR_{\text{Theory}}} = \frac{\left(\frac{N_\tau}{N_\mu}\right)_{\text{after fit}}}{\left(\frac{N_\tau}{N_\mu}\right)_{\text{before fit}}},$$

with the integral over the fitting range of the distributions in the tau lepton and muon channel N_τ and N_μ . Since by construction only the special shape parameter

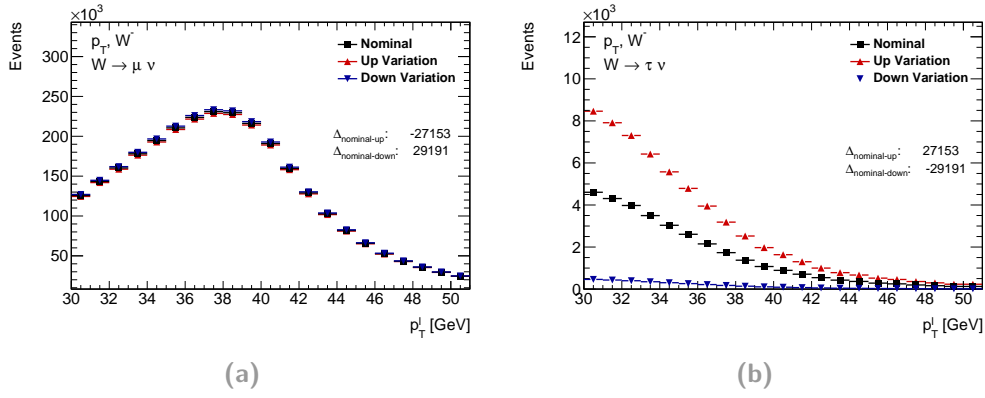


Figure 3.13. Constructed shape systematic to parametrize the variation of the branching ratio fraction for the lepton p_T distribution of the negative W boson. The comparison to the nominal histogram is displayed for the signal processes $W \rightarrow \tau \nu \rightarrow \mu \nu \nu$ (b) and $W \rightarrow \mu \nu$ (a).

α_{ratio} contributes to a change of this fraction, the error of the parameter can be directly transferred to the branching ratio fraction.

3.8 Asimov and Toy Data Results

In the following the fitting results obtained with the Asimov and Toy data are presented. These studies are performed to test the fitting framework and to obtain a first estimate on the expected error. The studies cannot provide any prediction on the measured branching ratio fraction.

The nomenclature for the different fitting configurations are discussed in Section 3.8.1 and the results from the Asimov and toy data are presented in Section 3.8.2. The stability and robustness of the fit was examined, as described in Section 3.8.3, and the fit model was tested for the ability to recover a distorted branching ratio fraction, as shown in Section 3.8.4. A final conclusion on the initial studies with a motivation for the fitting to data is given in Section 3.8.5.

3.8.1 Fitting Settings

As described in Section 3.7 the fitting was performed to the kinematic variables m_T and p_T independently for the decay of the positive and negative W boson.

Two different parameterizations for the change in the branching ratio fraction have been used. One is described as 'norm' and uses an independent normalization for the process $W \rightarrow \tau \nu \rightarrow \mu \nu \nu$ and one which implements the fraction change as a shape parameter, called 'ratio', as the ratio of the two processes is changed by this implementation without a possible migration from the background processes.

The backgrounds are treated in three different ways. The first possibility is an independent treatment of all background processes, labeled 'single'. The second option

Table 3.8. Overview of the nomenclature of the studied fitting configurations.

Name	Description
kinematic variables	
p_T	transverse momentum of the charged lepton
m_T	reconstructed transverse component of the mass of the W boson
fitting approach	
norm	branching ratio fraction parametrization as individual norm for $W \rightarrow \tau\nu \rightarrow \mu\nu\nu$
ratio	branching ratio fraction parametrization as shape systematics adding one event to the muon sample while subtracting one from the tau lepton sample and vice versa
background treatment	
single	individual histogram and individual norm for each background process
combined	individual histogram and common norm for each background process
summed	summed histogram and common norm for all background process

is to keep the individual background histograms, but apply a common normalization to all backgrounds, called 'combined' in the following. The 'summed' possibility describes the summation of all background processes to a summed histogram. In that case the contributions to the systematic variations are summed to retrieve a systematic for the summed background.

An overview of the different settings and their naming is presented in Table 3.8.

3.8.2 Fitting Results

The fitting was performed with Asimov samples and all different settings displayed in Table 3.8. Additionally the statistical error was estimated by fitting without the systematic uncertainties.

The toy samples have only been used to verify the results of the non extrapolated samples. Again the statistical error was estimated by a fit without shape systematics. The change in the branching ration fraction is transfered to the branching ratio of process $W \rightarrow \tau\nu\mu\nu\nu$. The values obtained for the branching ratio are given in Figure 3.14 and an overview compared to the branching ratio fraction world average stated in PDG [29] is given in Figure 3.15 and Figure 3.16 for Asimov and toy data, respectively. The results show a good agreement between the error estimation with Asimov and toy data. This underlines the validity of the fitting model and a sufficiently accurate generation of the toy data.

kinematic variable	fitting approach	background treatment	asimov	asimov (stat only)	toy	toy (stat only)
m_T	ratio	combined	$0.185^{+0.028}_{-0.030}$	$0.185^{+0.010}_{-0.010}$	$0.214^{+0.030}_{-0.027}$ (± 0.024)	$0.185^{+0.010}_{-0.010}$ (± 0.000)
m_T	ratio	summed	$0.185^{+0.028}_{-0.024}$	$0.185^{+0.011}_{-0.011}$	$0.197^{+0.026}_{-0.024}$ (± 0.026)	$0.185^{+0.010}_{-0.010}$ (± 0.000)
m_T	ratio	single	$0.185^{+0.061}_{-0.064}$	$0.185^{+0.043}_{-0.043}$	$0.225^{+0.063}_{-0.059}$ (± 0.034)	$0.185^{+0.049}_{-0.043}$ (± 0.000)
m_T	norm	combined	$0.185^{+0.029}_{-0.031}$	$0.185^{+0.011}_{-0.011}$	$0.218^{+0.034}_{-0.031}$ (± 0.022)	$0.192^{+0.011}_{-0.011}$ (± 0.001)
m_T	norm	summed	$0.185^{+0.036}_{-0.030}$	$0.185^{+0.011}_{-0.011}$	$0.199^{+0.031}_{-0.030}$ (± 0.027)	$0.192^{+0.011}_{-0.011}$ (± 0.001)
m_T	norm	single	$0.185^{+0.066}_{-0.069}$	$0.185^{+0.045}_{-0.044}$	$0.233^{+0.085}_{-0.077}$ (± 0.034)	$0.195^{+0.069}_{-0.045}$ (± 0.004)
p_T	ratio	combined	$0.185^{+0.023}_{-0.024}$	$0.185^{+0.008}_{-0.008}$	$0.190^{+0.024}_{-0.024}$ (± 0.023)	$0.185^{+0.009}_{-0.009}$ (± 0.000)
p_T	ratio	summed	$0.185^{+0.023}_{-0.023}$	$0.185^{+0.008}_{-0.008}$	$0.187^{+0.022}_{-0.021}$ (± 0.022)	$0.185^{+0.009}_{-0.009}$ (± 0.000)
p_T	ratio	single	$0.185^{+0.081}_{-0.085}$	$0.185^{+0.046}_{-0.047}$	$0.208^{+0.079}_{-0.069}$ (± 0.055)	$0.185^{+0.045}_{-0.044}$ (± 0.000)
p_T	norm	combined	$0.185^{+0.026}_{-0.026}$	$0.185^{+0.009}_{-0.009}$	$0.191^{+0.025}_{-0.025}$ (± 0.023)	$0.185^{+0.009}_{-0.009}$ (± 0.000)
p_T	norm	summed	$0.185^{+0.023}_{-0.023}$	$0.185^{+0.009}_{-0.009}$	$0.190^{+0.021}_{-0.021}$ (± 0.024)	$0.185^{+0.009}_{-0.009}$ (± 0.000)
p_T	norm	single	$0.185^{+0.113}_{-0.117}$	$0.185^{+0.059}_{-0.059}$	$0.214^{+0.111}_{-0.096}$ (± 0.071)	$0.189^{+0.057}_{-0.054}$ (± 0.002)

Figure 3.14. Overview of the branching ratios for the different fitting configurations. For the toy samples, the mean of the values for the single fittings is displayed along with the RMS of the distribution of all branching ratio fractions in brackets.

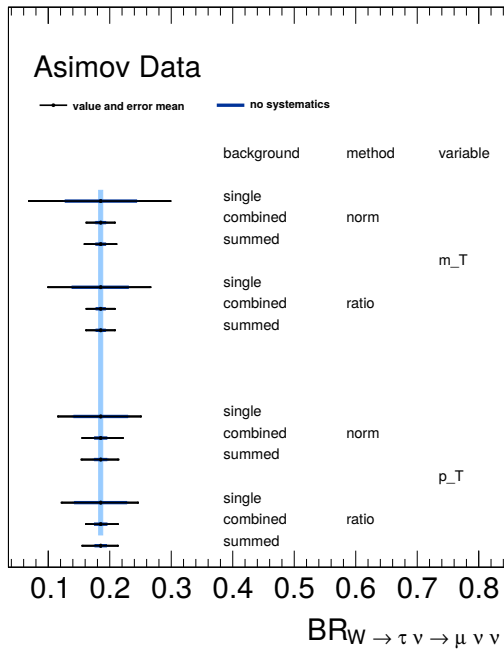


Figure 3.15. Reconstructed branching ratio from the fit to Asimov data. The world average value taken from PDG with its error band is displayed in light blue.

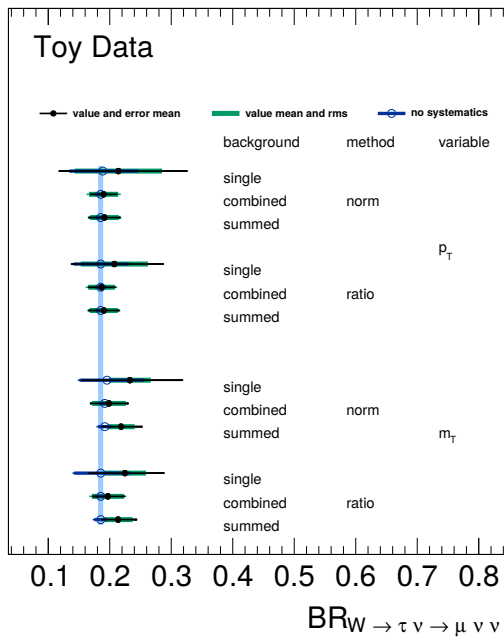


Figure 3.16. Reconstructed branching ratio from the fit to toy data. The world average value taken from PDG with its error band is displayed in light blue.

The comparison of the two kinematic variables shows, that smaller errors are achieved for the fit to the transverse momentum distribution. The better convergence of the fit to the p_T spectrum, most likely due to a more accurate systematics modeling, is also underlined by the smaller deviation from the world average in the fit to toy data.

The error of the fit to the distribution with single backgrounds is much larger than the fit to distributions with a combined or summed background. As the QCD background has a similar shape as the tauonic W boson decay and the $t\bar{t}$ and diboson background mimic the muonic W boson decay, they impose a large error on the branching ratio fraction. A combined background in contrast has a substantial different shape than both decay channels and therefore the influence on the branching ratio fraction is reduced. The evidence for this behavior can be seen in Figure 3.17. This plot shows the impact of the variation of a single fit parameter on the parameter which describes the change of the branching ratio fraction. To determine the impact of a fit parameter on the parameter of interest, the parameter was fixed to the limits of its estimated Minos error and the fitting was repeated. The now obtained values of the parameter of interest are displays as the error bars in Figure 3.17. The impact of the fit parameters for the fit to the single background (Figure 3.17a) highlights the largest contribution of the QCD background normalization to the error of the normalization of the tauonic W boson decay spectrum. The normalization of the summed background sample in contrast (Figure 3.17b) only shows a minor impact on the parameter of interest.

Both background treatments identify the PDF systematic as the nuisance parameter with the highest impact. This implies that a reduction of the theoretical PDF uncertainty will significantly boost the sensitivity of this measurement.

The huge Minos errors computed for the single measurements cannot be fully reproduced with the toy data. 200 samples have been created, each with the toy data varied within the uncertainty of the Monte Carlo generated data. The mean of all measurements reproduces the error of the single fitting on Asimov data. The RMS of the distribution of the mean values from the fit in contrast is smaller (green band in Figure 3.16). This effect is only significant for the fit to the single background.

A comparison of the two branching ratio fraction parameterizations does not show a large difference in the Minos error. A trend to slightly smaller errors (1 – 2%) is observed for the parametrization as shape systematic. This is expected, as a migration of background events to only one of the samples is suppress by this method. The agreement highlights, that both methods can be used in further studies and the two options give a possibility for a cross-check of the results and offer the access to the estimation of a error related to the parameterizations. This will become necessary

when higher precision results are obtained.

3.8.3 Fit Stability

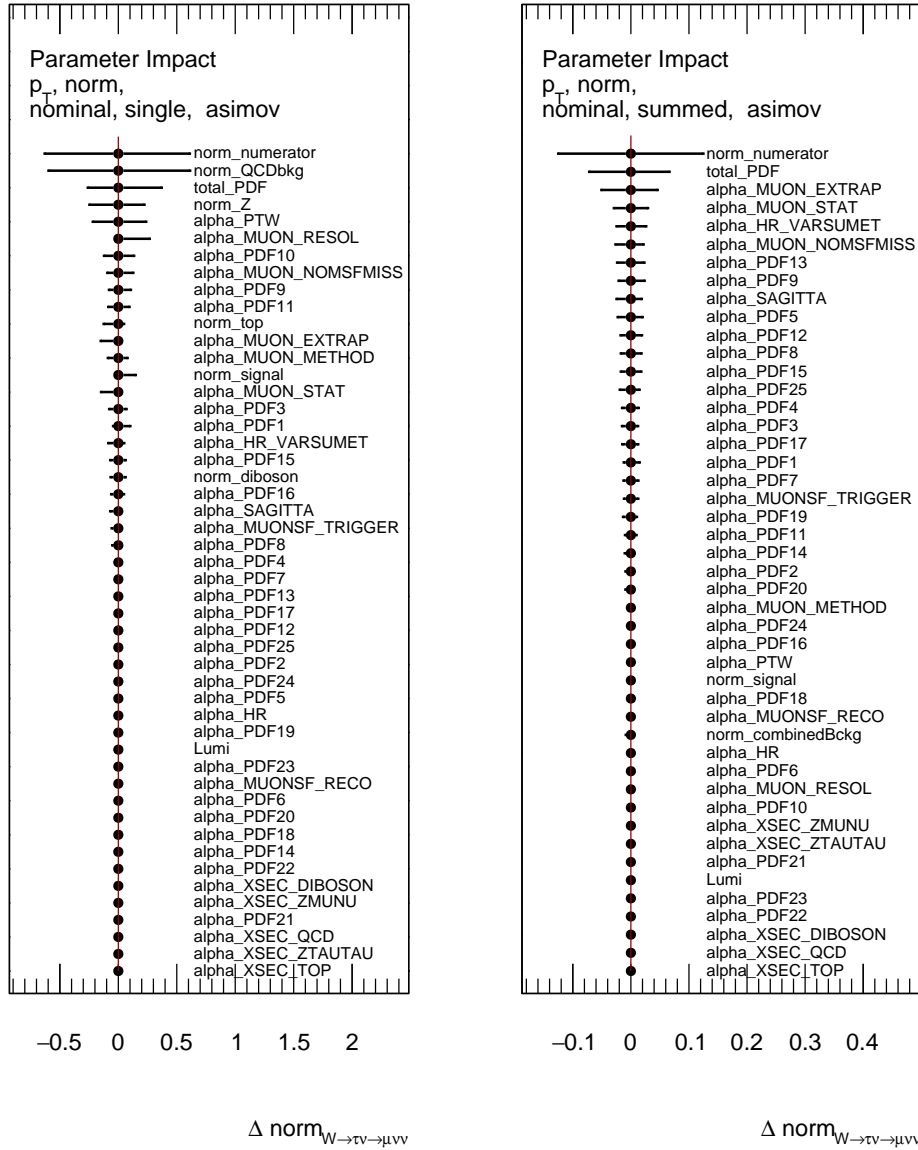
To test the stability of the fit, the convergence for different start values of the parameter of interest was tested. As the HistFactory framework does not allow to change the start value of a shape parameter this study could only be performed for the parametrization as normalization.

The start value range $[0, 3]$ was uniformly divided in 25 samples and the range of the expected fit results $[0.5, 1.5]$ was covered by additional 25 samples. Figure 3.18 shows the result for two configurations of the p_T distribution. All tested configurations for both kinematic distributions can be found in the appendix in Figure A.2 and Figure A.3. The comparison of the two settings shows a larger fluctuation of the treatment as single background compared to the combined background. This disfavors this single background method. All distributions of the combined background show a constant central value and error size over the full range of starting values. Therefore the fit result is not expected to be biased by the choice of a starting value.

3.8.4 Fit Closure

A second study to evaluate the ability of the fit model to recover a branching ratio change was conducted. During the summation of the Monte Carlo samples to create the Asimov dataset, the distribution of the muonic and tauonic W boson decay have been scaled to shift a fixed number of events from one decay channel to the other. This scaling is expected to be corrected by the fit. A comparison of a distribution before and after the fit can be seen in Figure 3.19. It is visible, that the induced branching ratio fraction change in pre-fit distributions shows an excess in the kinematic region of the tauonic decay, while a lack is observed in the muonic decay region. After the fit this is recovered to a perfect agreement, as expected for Asimov data.

To compare the different settings, the measured branching ratio change was plotted against the expected branching ratio change induced in the generated data. The result for two examples can be found in Figure 3.20, while all studied configurations are displayed in the appendix in Figure A.4 and Figure A.5. A linear fit to the data is expected to have unity as slope and a vanishing intercept. The results show, that the single background method again shows the worst results. The ratio parametrization as shape systematic leads to the smallest deviations from the perfect agreement, as this method is constructed to recover the induced parameter change and contributions from the background are less likely.



(a)

(b)

Figure 3.17. Impact of the change of a fit parameter within its error bounds on the parameter describing the branching ratio fraction change. The error bounds show the best guess of the branching ratio fraction parameter if a single fit parameter is varied to the limits of its error band. The top entry shows the total error for comparison. Normalization parameters start with 'norm' while the parameters of the shape systematics are named starting with 'alpha'

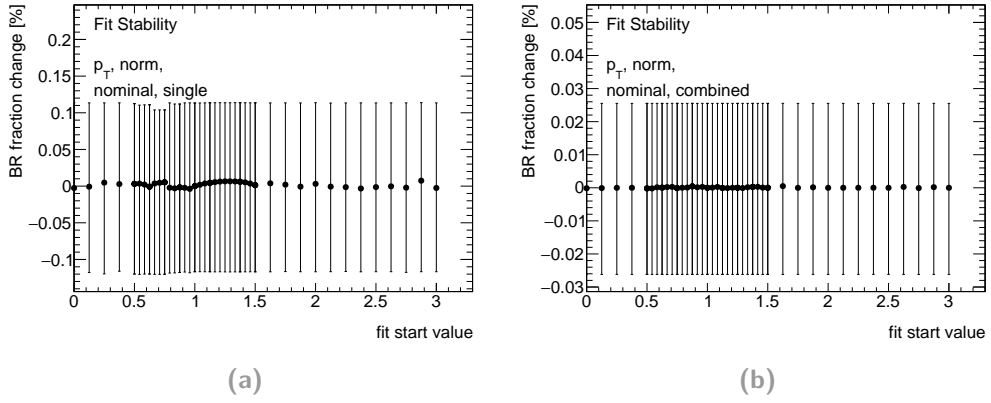


Figure 3.18. Stability of the fit to the p_T distribution.

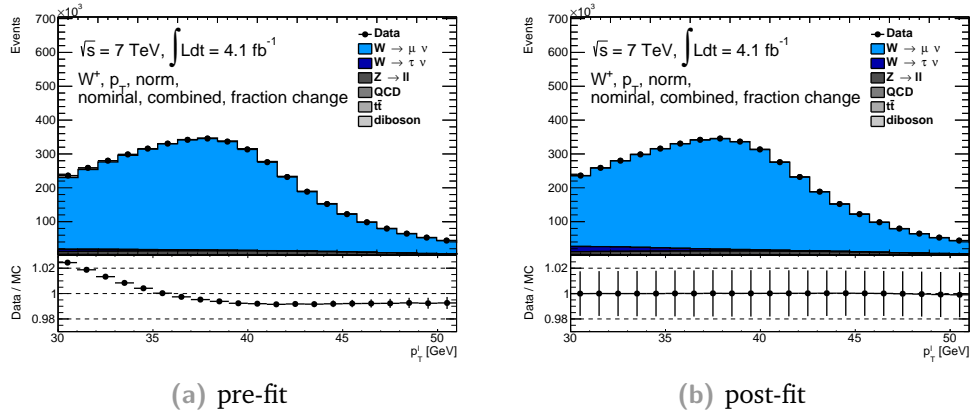


Figure 3.19. Data and Monte Carlo agreement before and after the fit. The induced branching ratio fraction change has been completely recovered, as visible in the fraction plot. The large errors after the fit originate in the treatment of the fit parameter errors as uncorrelated, since a correlation could not be stably estimated.

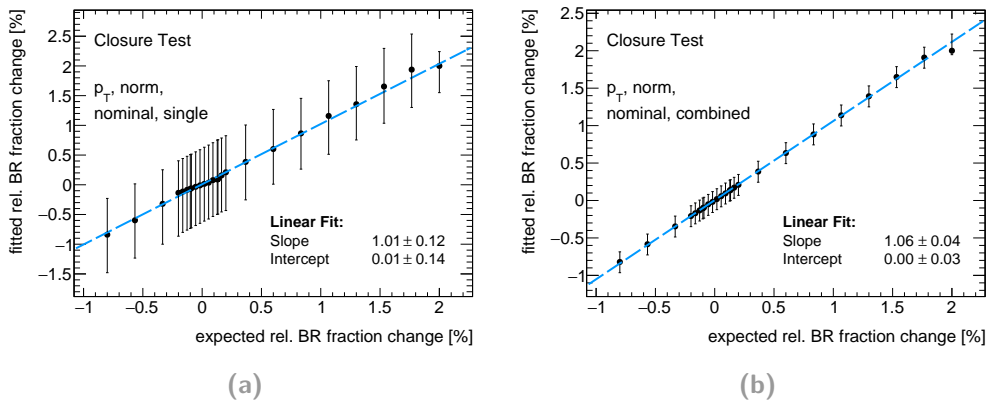


Figure 3.20. Ability of the fit to recover an induced change of the branching ratio fraction.

3.8.5 Conclusion

The studies on Asimov and toy data have shown that the independent fit of all background normalization leads to large errors and moreover does not allow for a stable estimation of the branching ratio fraction. Therefore this background treatment was not used in the fit to data. The treatment as a combined or summed background does not lead to significantly different results in the performed study. The two different parameterizations of the branching ratio fraction have shown similar results. Therefore they are both used in the fit to data.

For the fit to data, which is only preformed in the non extended range, a relative uncertainty on the measured branching ratio fraction of 12 – 15 % is expected from the estimation with Asimov data. This is not yet competitive with the world average measurements, but possibilities for a sensitivity increase are discussed in Section 3.10. This feasibility study therefore encourages for further studies in the ATLAS collaboration using the template fit method to measure the tauon contribution to the W decay muon signal.

3.9 Measurement Result

After the framework is validated on Asimov and Toy datasets, the fitting was performed on the p_T and m_T distribution for a combined and summed background treatment. The statistical errors are estimated by a fit without consideration of the systematic variations. The result of the fitting is shown in Figure 3.21 and Figure 3.22. A branching ratio $BR(W \rightarrow \tau\nu \rightarrow \mu\nu\nu) = 0.228^{+0.024(0.010)}_{-0.023(0.010)}$ was achieved as the best fit value. The values in brackets indicate the statistical errors. As expected from the previous considerations, the relative errors are in the range of 13 % to 19 % and dominated by the theoretical uncertainty. As the error is not compatible with the world average of 0.1853 ± 0.0033 with an relative error 1.8 %, further studies have been performed to show possibilities for an sensitivity increase (Section 3.10). Except for the fit to the m_T distribution with the summed background treatment, the one σ errorbands of the current best fit value for the branching ratio fraction and the fitting result of this thesis overlap. The tension in the m_T distribution is due to a pull from the first data points in the fitting range, which favor a higher contribution from the tauonic decay channel. The pre- and post-fit data and Monte Carlo agreement is shown in Figure 3.23. Due to the large bin-to-bin fluctuations in the data and Monte Carlo agreement, the values are not statistically significant. The data generally shows a trend to a higher contribution of the tauonic decay channel than predicted by the current world average value, which needs to be resolved on future studies with improved systematic and statistical errors.

kinematic variable	fitting approach	background treatment	result
m_T	ratio	combined	$0.210^{+0.027(0.010)}_{-0.026(0.010)}$
m_T	ratio	summed	$0.228^{+0.024(0.010)}_{-0.023(0.010)}$
m_T	norm	combined	$0.211^{+0.029(0.011)}_{-0.029(0.011)}$
m_T	norm	summed	$0.231^{+0.031(0.011)}_{-0.029(0.011)}$
p_T	ratio	combined	$0.207^{+0.025(0.009)}_{-0.026(0.008)}$
p_T	ratio	summed	$0.185^{+0.031(0.009)}_{-0.026(0.008)}$
p_T	norm	combined	$0.207^{+0.027(0.009)}_{-0.027(0.009)}$
p_T	norm	summed	$0.183^{+0.034(0.009)}_{-0.024(0.009)}$

Figure 3.21. Values of the reconstructed branching ratio fraction. The values in brackets are the statistical errors. The current best fit for the branching ratio fraction is 0.1853 ± 0.0033 [29].

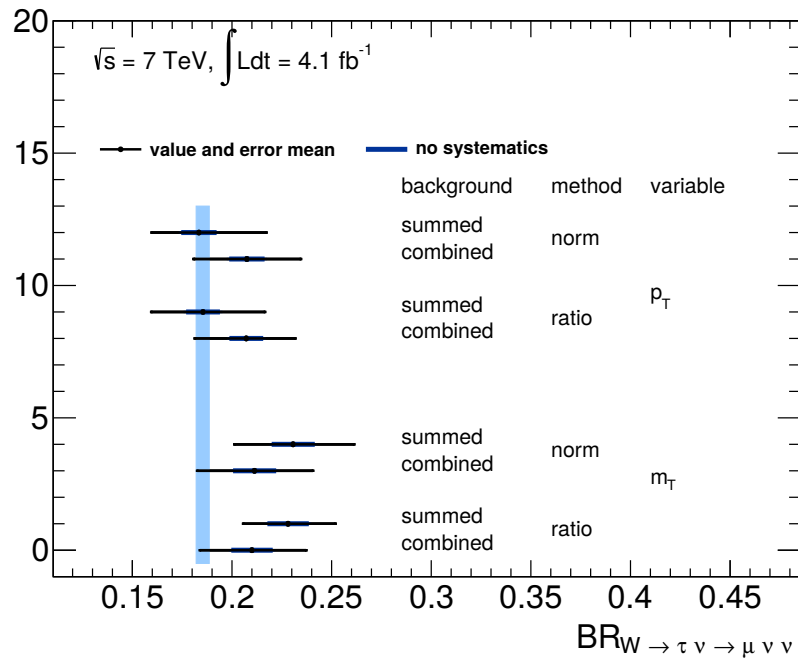


Figure 3.22. Overview of the reconstructed branching ratios.

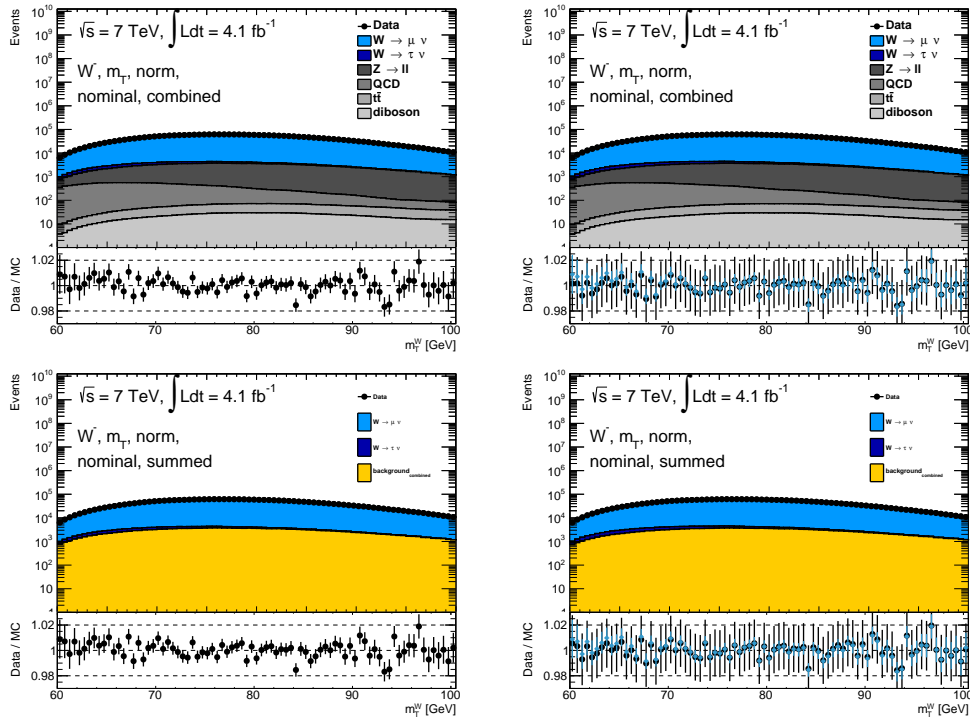


Figure 3.23. Pre- (left) and post-fit (right) distributions for the m_T distribution of the negative W boson decay. The blue points in the post-fit distribution ration plot show the pre-fit ratio.

3.10 Extrapolation of the Fitting Range

One possibility to gain more sensitivity in the fit, is the expansion of the fitting range to softer distributions. In the event selection of the W mass measurement, which data and well understood systematics are the base for this study, a cut to $p_T^l > 30$ GeV and $m_T > 60$ GeV was applied. As visible in Figure 3.10, the kinematic distribution of the tauon decay channel peaks at lower values. Such an extension to $p_T^l > 20$ GeV and $m_T > 40$ GeV is expected to increase the sensitivity. A further extension is not possible due to the trigger requirement during the data taking. The nominal distributions could be easily retrieved by re-running the selection framework. An overview of the extrapolated distributions is shown in Figure 3.24. The peak for the $W \rightarrow \tau\nu \rightarrow \mu\nu\nu$ channel is now clearly resolved. Also the peaking multijet background at even softer values is included in the distributions. This gives discrimination power for this background process over the tauonic W decay channel. The direct comparison of the extrapolated and non-extrapolated signal processes of the p_T^l distribution of the negative W boson decay is shown in Figure 3.25. Due to the relaxed m_T cut, the p_T^l distribution contains slightly more events in the nominal range as well.

The systematic shape variations could not be determined from scratch in this feasibility study, as they have been estimated by various collaborators and could not be brought together in a reasonable time. Therefore a quadratic extrapolation, with half

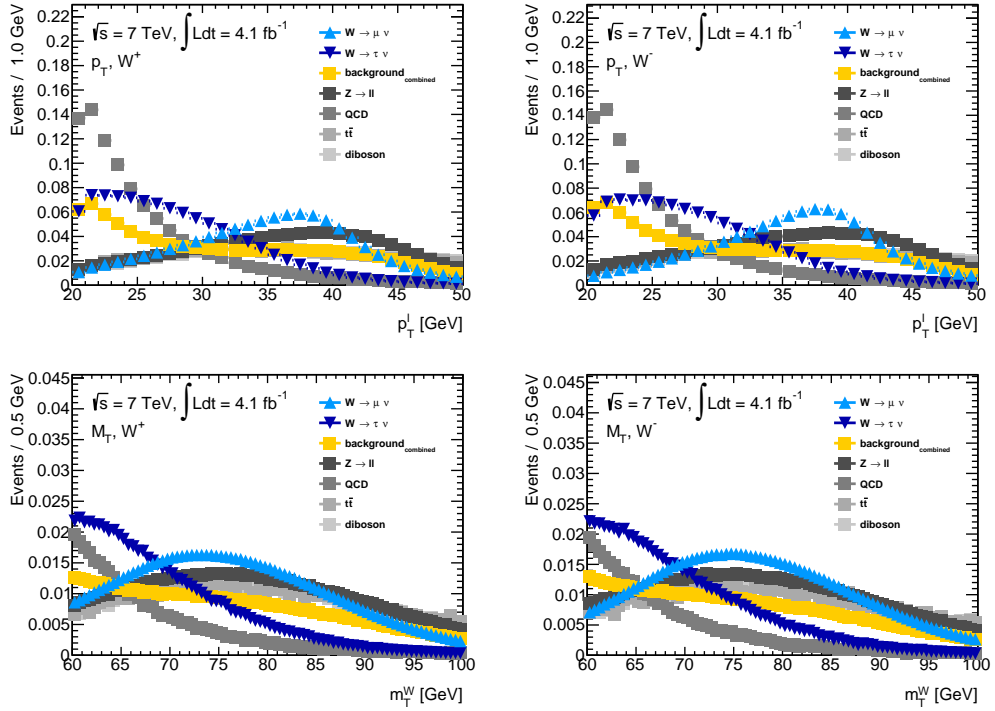


Figure 3.24. Normalized extrapolated distributions of the signal and background processes for the transverse momentum (top row) and the transverse mass (bottom row) of the W^+ (left column) and W^- (right column) decay. The background processes are shown as single processes and as the sum of all.

of the nominal systematic as basis, was performed on the smoothed distributions. After the extrapolation, the normalization procedure was applied again to avoid bias to the branching ratio fraction. The extrapolation of the two dominant shapes for the signal processes of the $W^- p_T^l$ distribution is shown in Figure 3.26.

The extension of the fitting range to softer kinematics is expected to reduce the error on the extracted branching ratio fraction. For the m_T distribution an extension from 60 GeV to 50 GeV was studied. For a further extension, the fit did not converge any more, as the distributions only have low statistics. This convergence problem might be related to the cubical extrapolation of the systematics, which tend to diverge and dominate in the soft kinematic range. An overview on the cut applied during the sample processing and the fitting can be found in Table 3.9.

For the p_T distribution, two extensions have been studied. One from 30 GeV to 20 GeV and an intermediate step at 25 GeV.

The extended samples have been produced for all configurations with the variable selection $40 \text{ GeV} < m_T < 100 \text{ GeV}$ and $20 \text{ GeV} < p_T < 50 \text{ GeV}$. The more strict cuts are only applied to the fitting range but the underlying data is produced in the fully extended range. The normalization of the shape systematics is calculated for each fitting range individually.

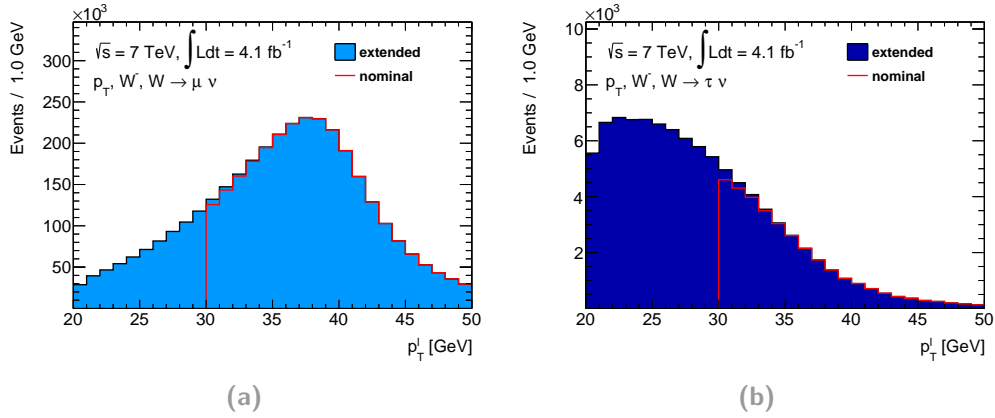


Figure 3.25. Comparison of the extrapolated and nominal p_T^l distribution for the decays $W^- \rightarrow \mu^- \nu$ and $W^- \rightarrow \tau^- \nu \rightarrow \mu^- \nu \nu$.

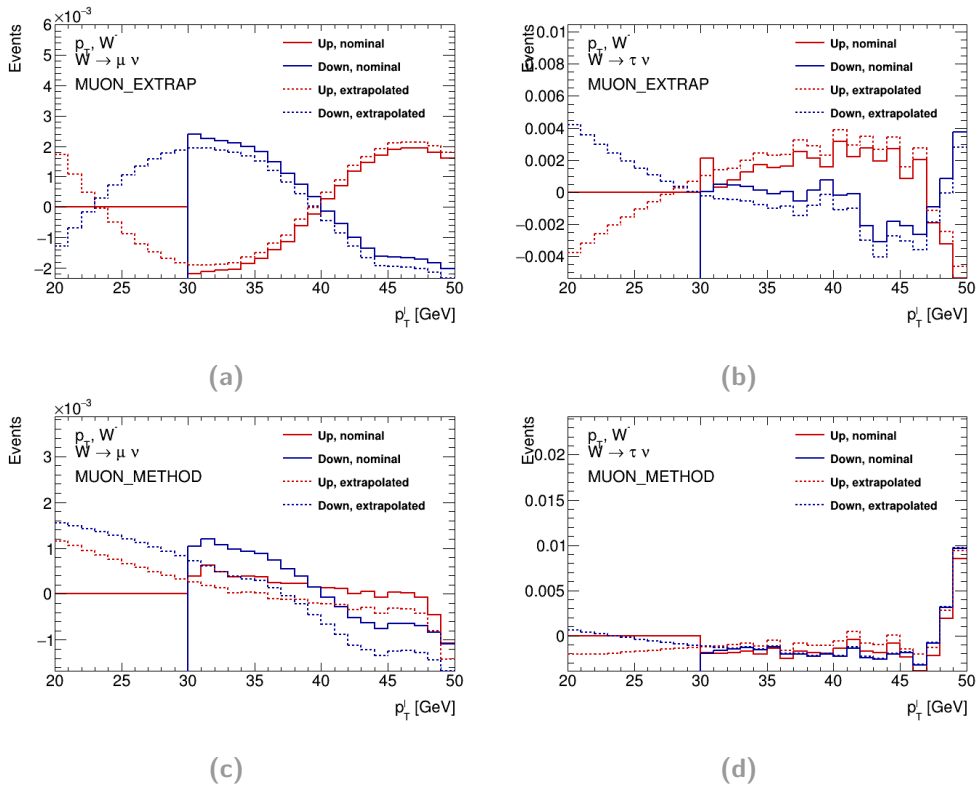


Figure 3.26. Relative shape two of the most dominant extrapolated systematics for the p_T distribution of the negative W boson decay. The $W \rightarrow \mu \nu$ decay channel is shown on the left while the $w \rightarrow \tau \nu \rightarrow \mu \nu \nu$ channel is shown on the right.

Table 3.9. Overview of the nomenclature of the studied fitting configurations.

Name	Description		
		extrapolation	
	variable	selection range [GeV]	fitting range [GeV]
nominal	p_T	[30, 50]	[30, 50]
	m_T	[60, 100]	[60, 100]
extrapolated 1	p_T	[20, 50]	[20, 50]
	m_T	[40, 100]	[50, 100]
extrapolated 2	p_T	[20, 50]	[25, 50]

An overview of the results is shown in Figure 3.28 and the values of all fittings are presented in Figure 3.27. The extension of the fitting range shows a reduction of the error by $\approx 8\%$ in for the largest extension in both kinematic variables and a $\approx 4\%$ reduction in the intermediate range used for the p_T distributions. As the shape systematics are not studied in detail for the extensions and only a quadratic extrapolation is used, the values can only serve as a estimate for the possible sensitivity. The perspective to a 4% error found in this study for an extension of the fitting range motivates future work within the ATLAS collaboration for a competitive measurement of the branching ratio fraction.

3.11 Summary and Outlook

This work provides a first measurement of the branching ratio fraction $BR(W \rightarrow \tau\nu \rightarrow \mu\nu\nu)/BR(W \rightarrow \mu\nu)$ with LHC data. A template fit approach was used to estimate the contribution of the single W boson decay channels to the inclusively measured data. The branching ratio was evaluated to $BR(W \rightarrow \tau\nu \rightarrow \mu\nu\nu) = 0.228_{-0.023(0.010)}^{+0.024(0.010)}$ in this measurement. A possible improvement of the relative measurement to 4% with an extension of the fitting range makes this measurement a competitive study with a possible impact on the world average. Therefore, the work is carried on within the ATLAS collaboration combined with an effort on the re-analysis of the W mass measurement in 7 TeV proton-proton collision data. More precise parton density function and an extension of all systematics to the extrapolated fitting range are expected to boost the significance of the measurement within the next year.

kinematic variable	fitting approach	extrapolation	background treatment	asimov	asimov (stat only)	toy	toy (stat only)
m_T	ratio	nominal	combined	$0.185^{+0.028}_{-0.030}$	$0.185^{+0.010}_{-0.010}$	$0.214^{+0.030}_{-0.027}$	$0.185^{+0.010}_{-0.010}$ (± 0.000)
m_T	ratio	nominal	summed	$0.185^{+0.028}_{-0.024}$	$0.185^{+0.011}_{-0.011}$	$0.197^{+0.026}_{-0.024}$	$0.185^{+0.010}_{-0.010}$ (± 0.000)
m_T	ratio	nominal	single	$0.185^{+0.061}_{-0.042}$	$0.185^{+0.043}_{-0.043}$	$0.225^{+0.063}_{-0.053}$	$0.185^{+0.049}_{-0.048}$ (± 0.000)
m_T	ratio	extrapolated 1	combined	$0.185^{+0.007}_{-0.006}$	$0.185^{+0.006}_{-0.006}$		
m_T	ratio	extrapolated 1	summed	$0.185^{+0.007}_{-0.006}$	$0.185^{+0.003}_{-0.003}$		
m_T	ratio	extrapolated 1	single	$0.185^{+0.008}_{-0.007}$	$0.185^{+0.009}_{-0.009}$		
m_T	norm	nominal	combined	$0.185^{+0.029}_{-0.031}$	$0.185^{+0.011}_{-0.011}$	$0.218^{+0.034}_{-0.031}$ (± 0.022)	$0.192^{+0.011}_{-0.011}$ (± 0.001)
m_T	norm	nominal	summed	$0.185^{+0.036}_{-0.030}$	$0.185^{+0.011}_{-0.011}$	$0.199^{+0.031}_{-0.030}$ (± 0.027)	$0.192^{+0.011}_{-0.011}$ (± 0.001)
m_T	norm	nominal	single	$0.185^{+0.066}_{-0.069}$	$0.185^{+0.045}_{-0.044}$	$0.233^{+0.085}_{-0.077}$ (± 0.034)	$0.195^{+0.060}_{-0.045}$ (± 0.004)
m_T	norm	extrapolated 1	combined	$0.185^{+0.012}_{-0.013}$	$0.185^{+0.005}_{-0.005}$		
m_T	norm	extrapolated 1	summed	$0.185^{+0.013}_{-0.012}$	$0.185^{+0.005}_{-0.005}$		
m_T	norm	extrapolated 1	single	$0.185^{+0.014}_{-0.014}$	$0.185^{+0.006}_{-0.006}$		
p_T	ratio	nominal	combined	$0.185^{+0.023}_{-0.024}$	$0.185^{+0.008}_{-0.008}$	$0.190^{+0.024}_{-0.024}$ (± 0.023)	$0.185^{+0.009}_{-0.009}$ (± 0.000)
p_T	ratio	nominal	summed	$0.185^{+0.023}_{-0.023}$	$0.185^{+0.008}_{-0.008}$	$0.187^{+0.022}_{-0.021}$ (± 0.022)	$0.185^{+0.009}_{-0.009}$ (± 0.000)
p_T	ratio	nominal	single	$0.185^{+0.081}_{-0.085}$	$0.185^{+0.046}_{-0.047}$	$0.208^{+0.079}_{-0.069}$ (± 0.055)	$0.185^{+0.045}_{-0.044}$ (± 0.000)
p_T	ratio	extrapolated 1	combined	$0.185^{+0.009}_{-0.007}$	$0.185^{+0.002}_{-0.002}$		
p_T	ratio	extrapolated 1	summed	$0.185^{+0.011}_{-0.009}$	$0.185^{+0.002}_{-0.002}$		
p_T	ratio	extrapolated 1	single	$0.185^{+0.012}_{-0.009}$	$0.185^{+0.004}_{-0.004}$		
p_T	ratio	extrapolated 2	combined	$0.185^{+0.011}_{-0.010}$	$0.185^{+0.003}_{-0.003}$		
p_T	ratio	extrapolated 2	summed	$0.185^{+0.006}_{-0.006}$	$0.185^{+0.006}_{-0.006}$		
p_T	ratio	extrapolated 2	single	$0.185^{+0.037}_{-0.031}$	$0.185^{+0.018}_{-0.016}$		
p_T	norm	nominal	combined	$0.185^{+0.026}_{-0.026}$	$0.185^{+0.009}_{-0.009}$	$0.191^{+0.025}_{-0.025}$ (± 0.023)	$0.185^{+0.009}_{-0.009}$ (± 0.000)
p_T	norm	nominal	summed	$0.185^{+0.023}_{-0.023}$	$0.185^{+0.009}_{-0.009}$	$0.190^{+0.021}_{-0.021}$ (± 0.024)	$0.185^{+0.009}_{-0.009}$ (± 0.000)
p_T	norm	nominal	single	$0.185^{+0.113}_{-0.117}$	$0.185^{+0.059}_{-0.059}$	$0.214^{+0.111}_{-0.096}$ (± 0.071)	$0.189^{+0.057}_{-0.054}$ (± 0.002)
p_T	norm	extrapolated 1	combined	$0.185^{+0.015}_{-0.015}$	$0.185^{+0.004}_{-0.004}$		
p_T	norm	extrapolated 1	summed	$0.185^{+0.018}_{-0.019}$	$0.185^{+0.004}_{-0.004}$		
p_T	norm	extrapolated 1	single	$0.185^{+0.018}_{-0.018}$	$0.185^{+0.006}_{-0.006}$		
p_T	norm	extrapolated 2	combined	$0.185^{+0.020}_{-0.020}$	$0.185^{+0.005}_{-0.005}$		
p_T	norm	extrapolated 2	summed	$0.185^{+0.016}_{-0.016}$	$0.185^{+0.005}_{-0.005}$		
p_T	norm	extrapolated 2	single	$0.185^{+0.028}_{-0.028}$	$0.185^{+0.014}_{-0.014}$		

Figure 3.27. Overview of the branching ratio fractions for the different fitting configurations. For the toy samples, the mean of values for the single fittings is displayed along with the RMS for the branching ratio fraction distribution in brackets.

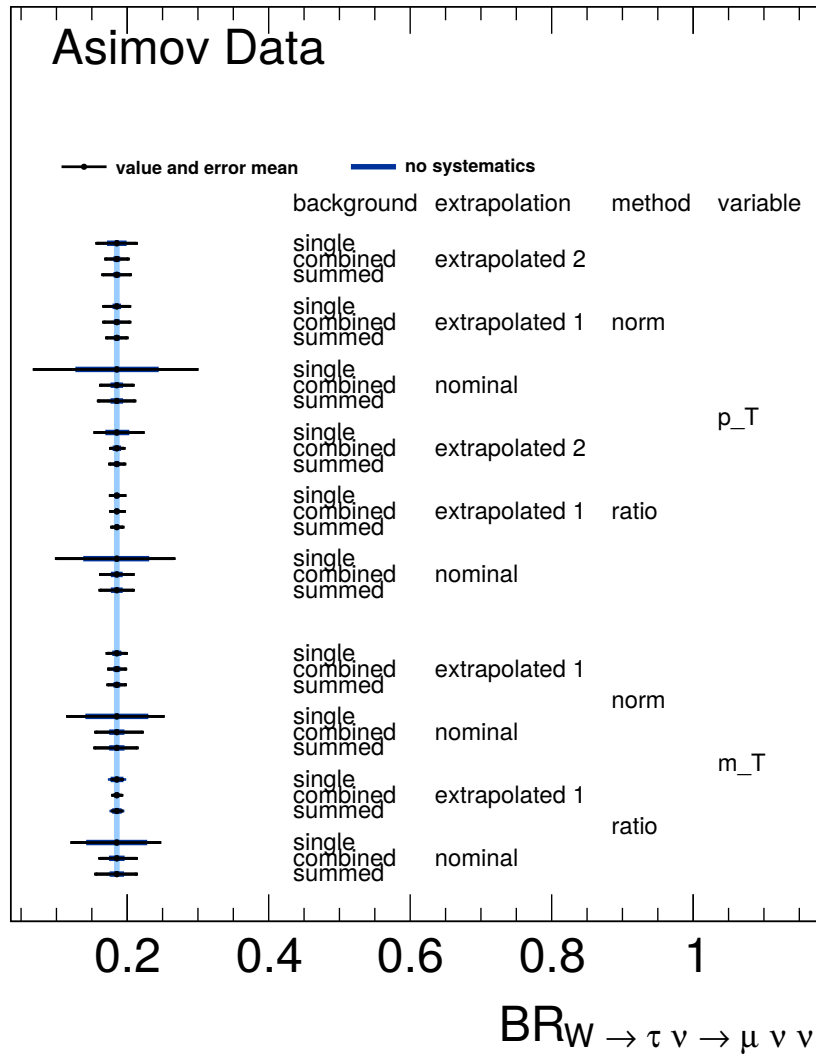


Figure 3.28. Reconstructed branching ratios from the fit to Asimov data. The world average value taken from PDG with its error band is displayed in light blue.

Micromegas Drift Panels for the ATLAS NSW Upgrade

This chapter presents the development of a drift panel production facility for the ATLAS New Small Wheel (NSW) upgrade. This detector development aims for the replacement of the first muon chambers in forward direction to prepare for the expected hit rates in the era of high luminosity LHC after 2025. As one of the detector technologies for the upgrade, the micro pattern gas detectors Micromegas have been chosen. A description of the detection principle is given in Section 4.1. An overview on the planned upgrade activity and the mechanical implementation of the Micromegas technology is explained in Section 4.2 along with studies on the used components in sight of long term stability. The setup of a production facility for high planar structures as cathode panels for large scale Micromegas detectors is explained in Section 4.4 and the production procedure is described in Section 4.5. The developed and implemented quality control methods are presented in Section 4.6 together with the results from the whole production in Section 4.6. A final outlook on the progressing upgrade project is shown in Section 4.7, along with studies on reasons for observed high voltage instabilities.

4.1 Micromegas Detectors

Micromegas belong to the group of micro pattern gas detectors. Traversing charged particles ionizes a gas and by amplification of the charge from the primary ionization a signal is induced on a readout geometry, allowing for the spatial signal reconstruction. The feature of Micromegas detectors, which makes them suitable for high rates, is the confinement of the amplification region to a geometrical small space, featuring short signal and dead times.

An overview on multiple scattering in a material, the ionization of matter and the transport and amplification of generated electrons in a gas is given in Section 4.1.1, Section 4.1.2, Section 4.1.3 and Section 4.1.4, respectively. The layout of a Micromegas detector and its performance are presented in Section 4.1.5 and Section 4.1.6.

4.1.1 Multiple Scattering

When passing through matter, charged particles get deflected in the electric field of the atoms. This leads to a distraction from the original particle path. For many scatterings, the overall scattering angle θ and particle displacement y can be described by the theory of Molière [72]. Considering only the, more probable, small angle scatterings, Gaussian distributions are found according to the central

limit theorem. 98% of the angular distribution can be estimated by the Gaussian approximation, where the RMS width in the projected plane $\theta_0 = 1/\sqrt{2}\theta_{\text{space}}^{\text{RMS}}$ is given by

$$\theta_0 = \frac{13.6 \text{ MeV}}{\beta c p} z \sqrt{\frac{x}{X_0}} \left[1 + 0.088 \ln \left(\frac{x z^2}{X_0 \beta^2} \right) \right],$$

with the the particle momentum p , the relativistic parameter $\beta = v/c$, the charge number z , the thickness x and radiation length X_0 of the material [73]. The radiation length is defined as the length where a massive particle losses a fraction $1/e$ of its initial energy. This is equal to $7/9$ of the mean free path of pair production for high-energetic photons. Taking correlations between the displacement and scattering angle into account the parameters can be estimated for a single event using two normal distributed random number z_1 and z_2 [29]

$$y_{\text{plane}} = z_1 x \theta_0 / \sqrt{12} + z_2 x \theta_0 / 2$$

$$\theta_{\text{plane}} = z_2 \theta_0.$$

4.1.2 Ionization

The interaction of radiation with matter is substantially different for massive and massless particles (photons). While massive particle loose only part of their energy by scattering processes along their path, photons can be completely absorbed in the ionization process. Therefore the two particle classes are treated independent in the following.

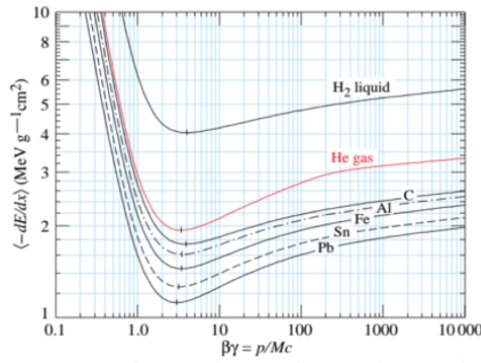
4.1.2 Massive Charged Particles

Massive particles lose energy in scatterings with the atoms or molecules of the matter along their path. A single energy loss, as a statistical process, cannot be predicted but the expected energy loss dE along a path element dx can be calculated by the Bethe equation for a particle energy range from $\beta\gamma = 0.2$ to $\beta\gamma = 10^4$:

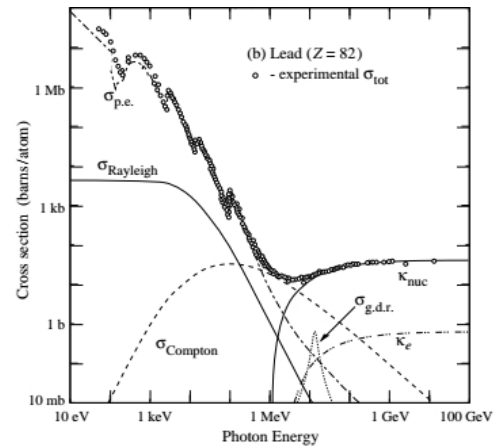
$$-\frac{dE}{dx} = k \rho \frac{Z}{A} \frac{z^2}{\beta^2} \left(\ln \left(\frac{2m_e c^2 \beta^2 \gamma^2 W_{\text{max}}}{I^2} \right) - 2\beta^2 \right),$$

with

k	$0, 1535 \frac{\text{MeVcm}^2}{\text{g}}$	z	particle charge in units of the elementary charge
m_e	electron mass	β	relativistic parameter $\beta = \frac{v}{c}$
ρ	material density	γ	relativistic parameter $\gamma = \frac{1}{\sqrt{1-\beta^2}}$
Z	atomic number of the material	I	average ionization potential



(a)



(b)

Figure 4.1. Shape of the Bethe equation (a) for the particle passage through different matter and the cross sections for photon interactions (b). $\sigma_{\text{p.e.}}$ corresponds to the photo electric effect, σ_{Compton} to Compton scattering and κ_{nuc} and κ_e to pair production in the nucleus or electron field. The contributions from Rayleigh scattering (σ_{Rayleigh}) and photonuclear interactions ($\sigma_{\text{g.d.r.}}$) are not further discussed as they either do not ionize the material or are only from interest for large atomic numbers. [29].

A atomic mass of the material W_{max} maximal possible energy transfer.

The shape of the Bethe equation is shown in Figure 4.1a. The minimal ionization capability for $\beta\gamma \approx 3$ and the slow raise afterwards is visible. The linear dependence of the Bethe equation on the atomic number and the inverse dependence on the ionization potential make noble gases an ideal medium for ionization detectors. As the cheapest of those, Argon is widely used. For minimal ionizing particles, roughly 100 electron ion pairs are expected per centimeter path length [74]. This amount of charge is by far too little to be detected with standard readout electronics. Such a charge amplification is necessary in the detector.

Electrons cannot be described by the standard form of the Bethe equation, as they are, as light particles, deflected in the atomic electric fields and radiate Bremsstrahlung.

4.1.2 Photons

Photon with low energies up to a few MeV ionize matter via the photo electric effect. The photon is absorbed by an electron in the atomic shell. The difference of the photon energy and the electron's binding energy is carried as kinetic energy of the electron. Due to the high interaction cross section of electrons with matter, the primary electron loses the kinetic energy in the vicinity of its creation by further ionization.

Photons with an energy of a few MeV mainly ionize by Compton scattering. In the interaction of the photon with an electron of the atomic shell, part of the energy is used to free the electron and part is transferred as kinetic energy to the electron. A photon with the remaining energy of the initial photon is created. Such after the

ionization a photon is still present and can further interact.

Above 1.022 MeV, double the rest mass of an electron, pair production starts to play a role. An electron-positron-pair is created from the energy of the photon. This process is not possible in vacuum, as part of the photon momentum has to be balanced either by a nucleus or an electron from the atomic shell. An overview of all relevant processes for the interaction of photons with matter is presented in Figure 4.1b.

4.1.3 Electron Transport in Gases

If no electric field is applied, the generated electron-ion-pairs recombine, as they are attracted by their opposite charge. Therefore the charges need to be separated by an electric field in the gaseous detector. Charged particles drift with a constant velocity in an electric field, as the velocity increase due to the acceleration in the electric field is balanced by elastic scatterings with gas atoms. The mean free path between to collision is proportional to the temperature and inverse proportional to the pressure $\lambda \propto T/P$. Figure 4.2a shows the dependence of the electron drift velocity on the electric field for different gas compositions. Of special interest is the comparison of argon and argon with different admixtures. The drift velocity for a mixture is larger than for pure argon, as the electrons are cooled by additional complex molecules and their velocities are shifted to the Ramsauer-Townsend minimum. For a certain electron momentum, the electron wave function shows a positive quantum mechanical interference in the gas, leading to a reduced interaction cross section [74].

In contrast to electrons, ions show a much smaller drift velocity which depends on the ratio E/P . Due to their larger mass they interact more with the surrounding gas atoms leading to up to a factor thousand smaller drift velocity. As moving particles induce a current on a conductor, the main measured signal in gas detectors originates from the ion drift. To reach a high rate capability it is desired to keep the ion drift distance before recombination short.

Besides the desired motion along the electric field lines, charged particles diffuse in all dimensions due to the thermal motion. The radial width of the diffusion is given by

$$\sigma = \sqrt{6Dt},$$

with the diffusion coefficient $D \propto \lambda$ and the drift time t . An overview of the diffusion RMS in the component parallel and transverse to the electric field can be found in Figure 4.2b. The charge diffusion during the drift is the limiting factor in the spatial resolution of gaseous particle detectors.

The comparison of different admixtures in Figure 4.2 shows the strong dependence of the operational parameters on the gas composition. Such it is crucial to avoid gas contaminations for example from the degassing of detector material or a remnant of ambient humidity in the detector.

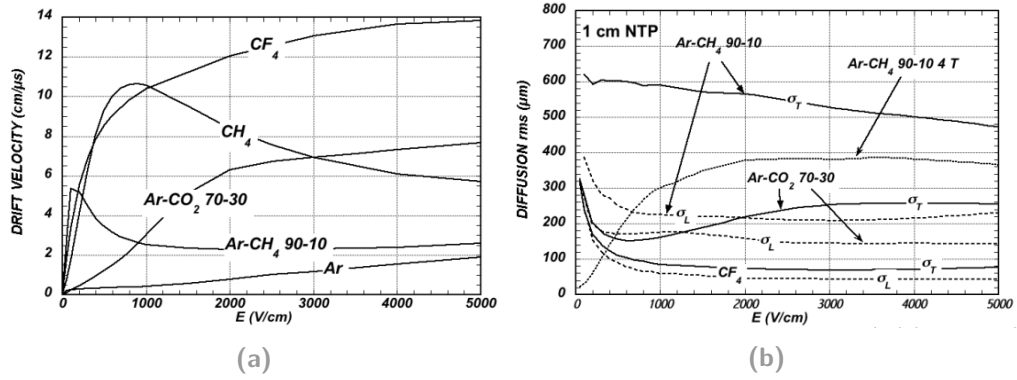


Figure 4.2. Drift velocity (a) and RMS of the diffusion along (σ_L) (dashed lines) and transverse (σ_T) to the electric field (b). The data was calculated with the MAGBOLZ framework [29, 75].

4.1.4 Gas Amplification

As the number of charges from the primary ionization (≈ 100) is too small to generate a measurable signal, the process of gas amplification is widely used in particle detectors. If the electron gains enough energy between two collisions for further ionization, an avalanche with an exponentially increase in the number of charges N forms

$$N = N_0 \exp(\alpha x),$$

where N_0 is the number of charges before the traversal of a distance x in a high electric field. The first Townsend coefficient $\alpha = 1/\lambda$ gives the probability of an ionization within a unit length. The amplification breaks down if the Raether limit for the number of charges of $N \approx 10^8$ is reached as, due to the localized large number of charges, a conducting plasma is formed [76].

With the number of generated electrons in the avalanche, also the probability for the excitation of gas atoms increases. Since argon has comparable high excitation levels, the emitted photons can free electrons from other material. Especially, an excitation level of argon matches the ionization energy of copper, which is widely used in gaseous detector for example as cathode material. To avoid fake signals from electrons created by the photons, a quenching component is mixed to the detector gas. Complex molecules, as CO₂, absorb the photons and transition via rotational degrees of freedom without the emission of further radiation into their ground state.

4.1.5 Layout of Micromegas Detectors

The basic principle of Micromegas (MICRO MESH Gaseous Structure) detectors is the separation of the ionization in the so-called drift region and the charge amplification region. The layout of a Micromegas detector is shown in Figure 4.3. The gas volume, typically filled with a mixture of argon and CO₂ in a ratio of 93 : 7, is divided with by a micro mesh. In the ≈ 5 mm thick drift region typically an electric field of 600 V cm^{-1} is applied. The thickness of the region is a trade-off between

the generation of more primary electrons within a larger volume and the worse resolution due to the increasing diffusion with the larger drift distance. Separated by a stainless steel mesh with a wire thickness of around $30\ \mu\text{m}$ and a wire periodicity of $100\ \mu\text{m}$ the amplification region with a field of more than $40\ \text{kV cm}^{-1}$ attaches to the drift region. Due to the high field gradient over the mesh, the electrons are guided through the holes and the mesh appears transparent to them [77].

The distance between the mesh and the readout structure has to be precise to a few micrometer, to guarantee a homogeneous electric field and therefore a constant amplification gain. Two approaches are widely used to achieve that. Either the stretched mesh is directly embedded in pillars made from standard PCB coverlay (bulk Micromegas) or the tensioned mesh is glued to a stiff structure and placed on top of those pillars (floating mesh Micromegas). The latter approach is used especially for large area detectors, as the floating closure of the amplification gap by the mesh allows for a re-opening and cleaning after the assembly, Even small dust grains or contaminations by solvents locally lower the breakdown voltage below the detector operation voltage and make the detector inoperable.

The presented detector geometry leads to an amplification gain of more than 10^4 [78] which brings the total number of generated charges for incident particles with high ionization capability, as α particles, over the Raether limit and leads to the formation of a conducting plasma channel between the mesh and the readout structure [79]. To cut this process, the electric field needs to be lowered in the amplification region. The global lowering of the supply voltage generating the field would make the whole detector inefficient and is therefore unfavored. To achieve a localized field reduction, the in a PCB embedded, copper readout strips are topped by congruent high resistive strips with a resistivity of several $\text{M}\Omega\ \text{cm}^{-1}$ on a thin insulator. The generated charges collected on the resistive strips slowly spreads to the outside where a common potential is applied to all strips. During the slow spread, the charge forms an electric field opposed to the amplification field reducing the effective field strength and leading to a break down of the discharge. The spreading signal on the resistive strips induces a signal in the copper readout strips which can be amplified and process with standard electronics.

4.1.6 Performance of Micromegas detectors

To give an impression on the performance of Micromegas detectors, specially in sight of the ATLAS New Small Wheel Upgrade, the results obtained with a prototype detector of $0.5\ \text{m}^2$ active area are presented in the following. The total detector consists of 4 layers of independent Micromegas detectors. Each layer contains 1024 strips with a pitch of $415\ \mu\text{m}$ and a width of $300\ \mu\text{m}$. The detector has a trapezoidal shape to allow for an integration in a disc like structure in the forward direction of the ATLAS detector. Two of the four readout layers have strips parallel to the long side of the trapezoidal to reconstruct the azimuthal precision coordinate in

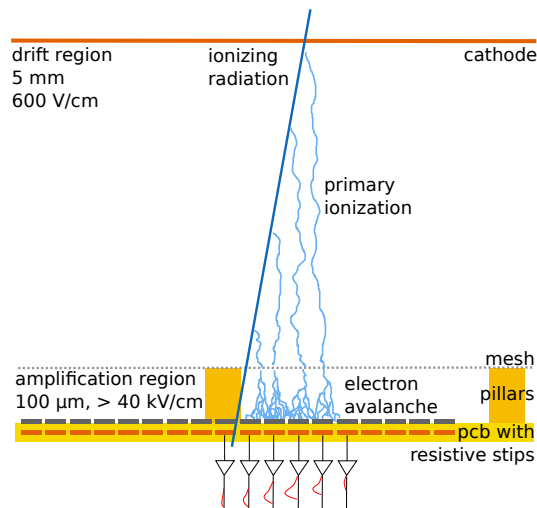


Figure 4.3. Basic structure of a Micromegas detector and schematic sketch of the electron path after the primary ionization and in the avalanche creation in the amplification region. The expected signal is shown by the red lines on the output lines of the strips amplifier. The increasing signal height to the cluster center and later signal arrival due to the longer drift time is indicated. Neighboring strips without a direct electron collection also see a signal induced by the electron and ion movement and the cross talk between the strips.

the detector. The radial coordinate can be reconstructed from the remaining two layers which have a strip inclination of $\pm 1.5^\circ$ with respect to the precision strips. A detailed overview of the detector design is given in [80] and the similar design of the quadruplet chamber for the NSW upgrade will be described in Section 4.2.1.

The typical event shape of one layer is shown in Figure 4.4. The data was taken during a beam time at the MAMI B accelerator facility at Johannes Gutenberg-University Mainz [81] providing an electron beam with an energy of 855 MeV. The readout was done with the APV25 chip [82] configured and read via the RD51 scalable readout system [83]. The figure shows in the upper right corner the charge, coded in the color scale, measured in 25 time bins of 25 ns each for all strips with a signal. Neighboring strips with a charge above the noise threshold, determined in the readout software [84], are defined as one cluster which corresponds to the interaction of one beam particle in the gas volume. For perpendicular incident particles a Gaussian charge spread, originating in the charge diffusion, can be observed in the spatial coordinate. The hit position can be reconstructed from the weighted mean of the strip charges at the time bin of the maximum charge with sub-strip precision.

The time dependence of the signal for all affected strips is shown in the lower right part of Figure 4.4. A quick charge rise and a longer signal tail can be observed. The signal duration is defined by the ion drift time to the mesh. The negative undershoot after the signal is an artefact from the signal shaping in the readout chip.

Using the other detector layers as reference, the efficiency of the prototype detector was estimated with cosmic muons. A track is considered as reconstructed, if a hit is

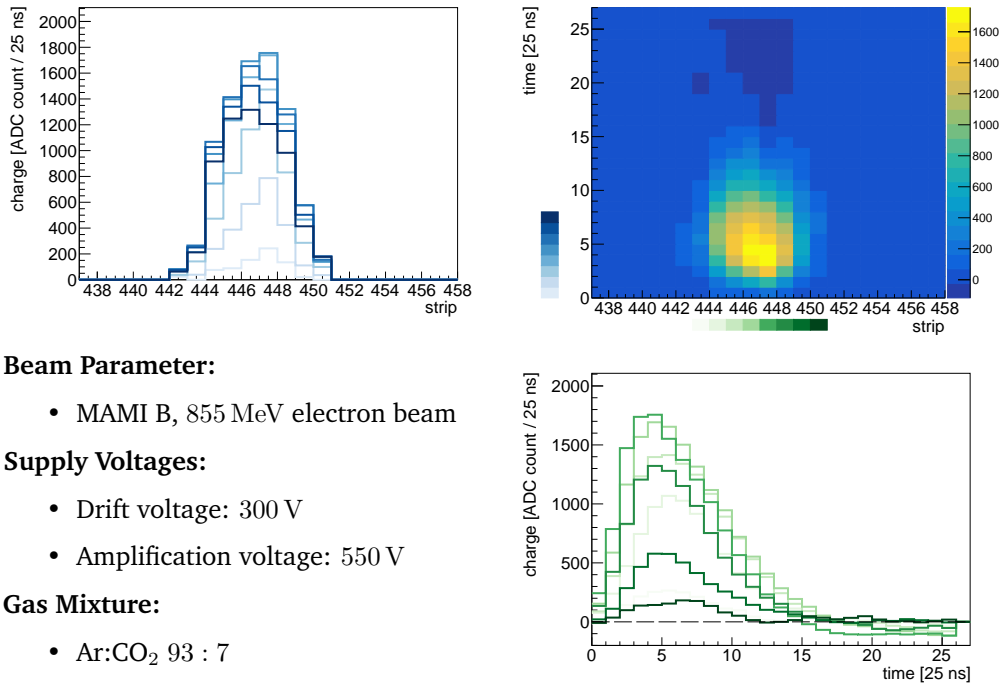


Figure 4.4. Typical event shape of a Micromegas detector with the APV 25 readout. The upper right corner shows the evolution of the event shape in all strips of the cluster over the time. The measured charge in ADC counts is color coded. Projections of the time slice are shown in the lower right and of the strips in the upper left plot. The color coding of the bins corresponding to the slices is indicated at the axis of the 2D plot. The operational parameter where the data was taken are displayed in the lower left quarter.

detected within 2.5 mm of the extrapolated track from single hits in the other detector layers. A raise in the efficiency with the amplification voltage can be observed in Figure 4.5a. A saturation behavior is observed for an amplification voltage above 580 V. Figure 4.5b shows the reconstructed efficiency in dependence of the strips. The flat distribution above 95% underlies the efficiency homogeneity over the full active area.

The prototype detector's spatial resolution is shown in Figure 4.6. The measurement was done with the MAMI B electron beam. The resolution of the precision coordinate can be measured from the hit position difference in the first two layers with parallel strips. A value of $88 \mu\text{m}$ was obtained. The resolution of the perpendicular radial coordinate, reconstructed from the two inclined layer, was measured by the comparison of the hit position in the prototype detector with a second Micromegas detector with two dimensional readout serving as reference chamber [85]. As multiple scattering and beam divergence corrected value, 2.3 mm was measured for the radial coordinate.

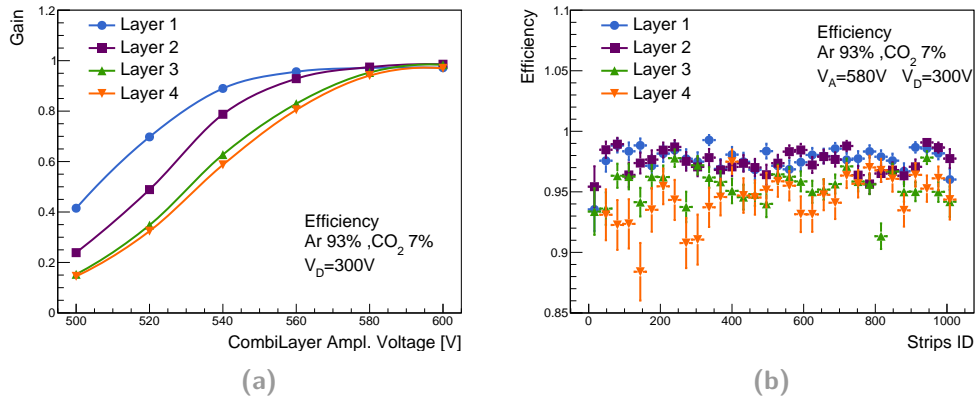


Figure 4.5. Reconstruction efficiency in dependence of the amplification voltage (a) and the strip number (b) for the four Micromegas layer of prototype detector for the ATLAS New Small Wheel Upgrade. [80]

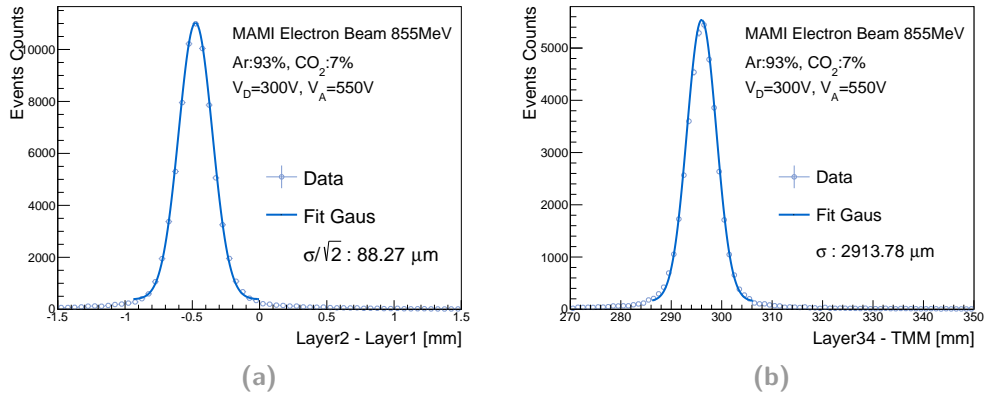


Figure 4.6. Resolution estimation for the prototype detector. For the precision coordinate (a) the difference between the reconstructed hit position in the first two detector layers is used to obtain the spatial detector resolution from the width of the distribution. The radial coordinate, reconstructed from the layers with inclined strips, is compared to an external reference chamber (TMM). The width of the distribution has to be corrected for the multiple scattering and the beam divergence to get the pure detector resolution [80].

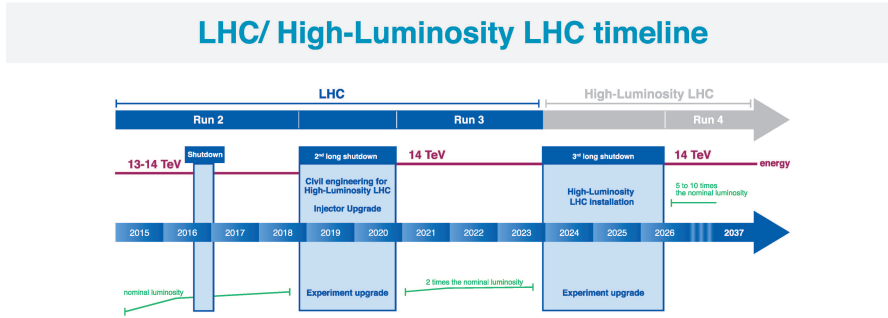


Figure 4.7. Schedule of the LHC accelerator. The discussed upgrade will be installed in the long shutdown (LS) 2 and enable the ATLAS detector for an efficient data taking in view of the high luminosity LHC in Run 4. [86]

4.2 The ATLAS New Small Wheel Upgrade

With the upgrade of the LHC accelerator to the high luminosity LHC after 2025, the instantaneous luminosity is expected to grow by a factor of 7 to up to $7 \times 10^{34} \text{ cm}^{-2} \text{ s}^{-1}$ with an increase in the average number of bunch crossing by more than a factor of 20 to $\langle \mu \rangle = 200$. The time line of the planned LHC operation is shown in Figure 4.7. The increase in the luminosity will push the hit rates beyond the limit of the currently first muon chambers in forward direction, the Small Wheel. As it is shown in Figure 4.8a most of the level 1 trigger events in the region $1.3 < |\eta| < 2.7$ do not match with a reconstructed muon. At that stage the trigger decision was based on the chambers behind the end-cap toroid and therefore is strongly biased by hadrons produced in the material of the end-cap toroid. To overcome the high fake trigger rate the chambers at the point of the Small Wheel need to be included in the level 1 trigger decision. A better spatial resolution in the radial coordinate is needed to fulfill this task at the expected high rates.

A second limiting factor is coming from the degeneration of the currently used monitored drift tubes. The efficiency of a single tube decreases linearly with the hit rate in the chamber. The reconstruction efficiency of a full chamber does not degenerate as strong as the single tube efficiency, as several tubes are used for the hit reconstruction. As it can be seen in Figure 4.8b, a steep efficiency loss is expected for tube hit rates higher than 300 kHz at the maximum design luminosity of the LHC of $2 \times 10^{34} \text{ cm}^{-2} \text{ s}^{-1}$.

The high rate environment and the fake trigger problematic impose two main requirements on the detectors for the New Small Wheel, which should replace the current Small Wheel. Assuming a four layer detector concept, the spatial resolution in the azimuthal η coordinate should be better than $100 \mu\text{m}$ to keep the tracking resolution of the MDT chambers. The spatial resolution in the radial coordinate ϕ should be in the range of 1 – 2 mm to ensure the linking in the combined inner detector and

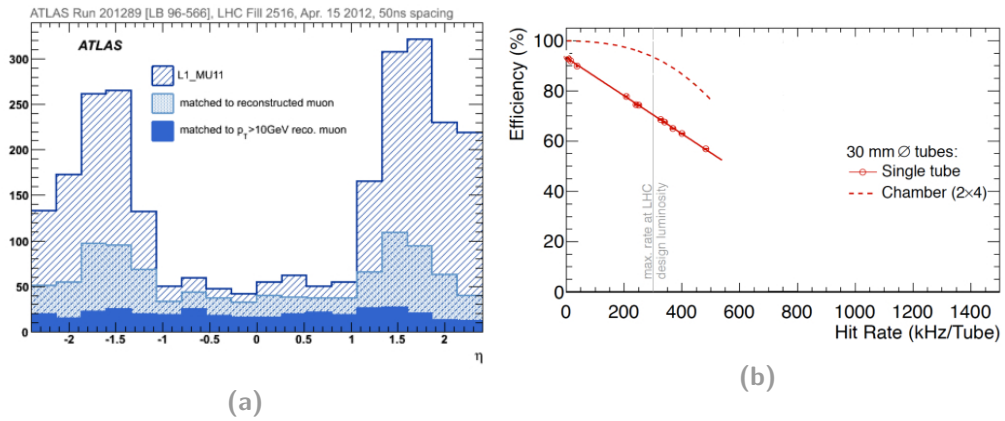


Figure 4.8. ATLAS level 1 trigger rate (a) The high fake trigger rate without the match of a reconstructed muon is visible in the region of the Small Wheel ($1.3 < |\eta| < 2.7$). The degeneration of the MDTs for a single tube and a full chamber is displayed in (b). As not all tubes are required for an efficient track reconstruction in the chamber, the chamber efficiency does not linearly depend on the hit rate, but shows a steep drop beyond the LHC design luminosity [87].

muon system reconstruction. Furthermore the hit reconstruction efficiency should be larger than 97% for muons with momenta greater than 10 GeV.

The detector geometry of the New Small Wheel is shown in Figure 4.9. The full disk is formed by 16 wedges in two geometries, where the smaller wedges cover the gap between the larger ones. The size of the wedges comes from the requirement to geometrically match the next muon detector station in ATLAS. The wedges are segmented again into two chamber geometries, as a production as a single piece is mechanically impossible.

To achieve the NSW specifications, the combination of two detector technologies was decided. [87]. Detectors of the small-strip Thin Gap Chamber (sTGC) technology are used for the trigger purpose while Micromegas detectors are used for tracking. Two quadruplets of each detector technology are stacked in each wedge. The sTGC quadruplets form the outsides of that stack to maximize the lever arm in the fast reconstruction during the trigger decision taking.

The wedge segmentation chosen for the Micromegas technology is shown on the left of Figure 4.9. The geometry called SM2 is build in a German collaboration and the production and quality control of drift panels (mechanical structures including the detector cathode) is described in the following.

The sTGC detector design is shown in Figure 4.10a. As Micromegas detectors, sTGC detectors are planar gas detectors. The gas amplification of the primary charge, generated in the 2.8 mm drift region, happens in the high electric field near wires placed in the middle of the gas volume. The $50 \mu\text{m}$ diameter gold coated tungsten wires, perpendicular to the parallel sides of the trapezoidal detector geometry, have a distance of 1.8 mm and always five wires are grouped in the readout for the deter-

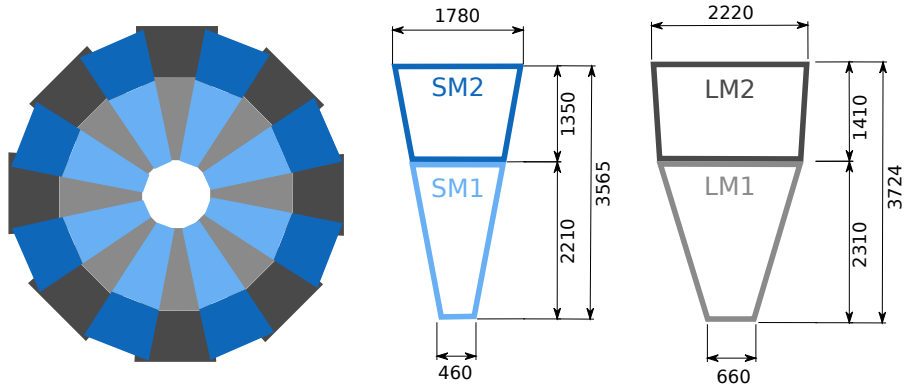


Figure 4.9. Schematical view of the NSW layout. The full disc is formed by two types of overlapping wedges indicated in gray and blue. The dimension of the Micromegas chamber geometries with their ATLAS naming are displayed in the right part of the sketch in units of millimeter.

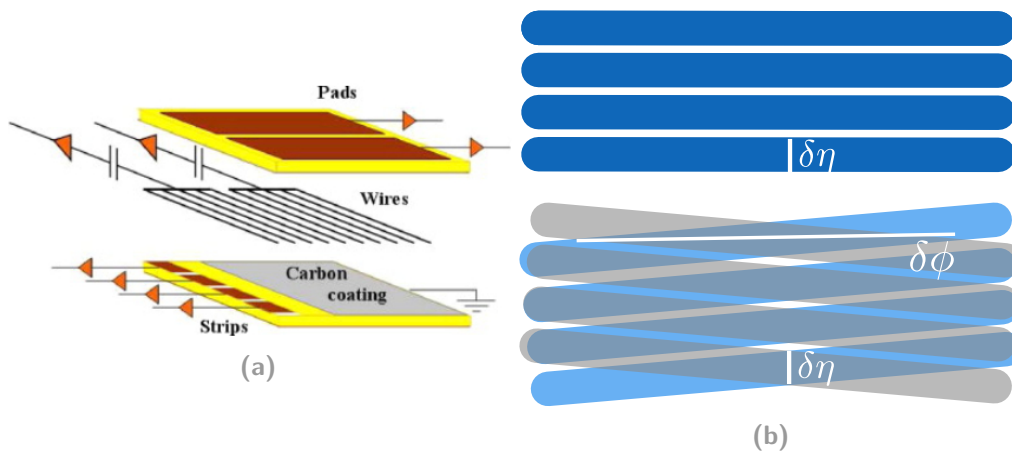


Figure 4.10. Layout of the New Small Wheel sTGC chambers (a) [87]. The reconstruction of the precision η and radial coordinate ϕ in the Micromegas chambers is shown in (b). From inclined layers (lower part) both coordinates can be reconstructed. The corresponding geometrical resolutions $\delta\eta$ and $\delta\phi$ are indicated by the white lines.

mination of the radial coordinate where less precision is required.

Cathode planes on both sides of the gas volume are coated with a high resistive ($100 \text{ k}\Omega \text{ cm}^{-2}$) graphite-epoxy mixture on a $100 \mu\text{m}$ thick insulator layer. One cathode is segmented into large pads, whose signal is used to define the region of interest for a further readout in the trigger process. The other cathode is split into 3.2 mm pitch strips, parallel to the parallel sides of the trapezoidal chamber. The precision coordinate η can be reconstructed with a resolution better than $150 \mu\text{m}$ with the given readout geometry.

4.2.1 Micromegas Quadruplet Layout

The working principle of Micromegas detectors was discussed in detail in Section 4.1. In the following their implementation in a quadruplet for the ATLAS New Small

Wheel Upgrade will be described.

An overview of the main components forming the quadruplet is shown in Figure 4.11. The four gas volumes are enclosed between sandwich structures of aluminum honeycomb surrounded by a frame of extruded aluminum bars and covered by a 0.5 mm thick FR4 board. The FR4 boards are either plain material on the detector outside, coated with a uniform $17\mu\text{m}$ thick copper cathode as upper closure of the Micromegas drift volume or composite layer structures as readout boards. The readout boards are made of FR4 where the $300\mu\text{m}$ wide copper strips with a pitch of $425\mu\text{m}$ are chemically etched from the $17\mu\text{m}$ thick copper coating. A $50\mu\text{m}$ thick Kapton[®] foil supporting the $180\mu\text{m}$ wide and $\approx 15\mu\text{m}$ thick, screen printed, resistive strips is glued with a $25\mu\text{m}$ layer of Akaflex[®] onto the readout strips. All resistive strips are connected at the side to supply the detector amplification voltage. Additionally, the resistive pattern has interconnections between the single strips to enhance the charge spread and cover for broken resistive strips. The $0.2\text{mm} \times 1.2\text{mm}$ pillars are lithographically etched from a $128\mu\text{m}$ Pyralux[®] double-layer.

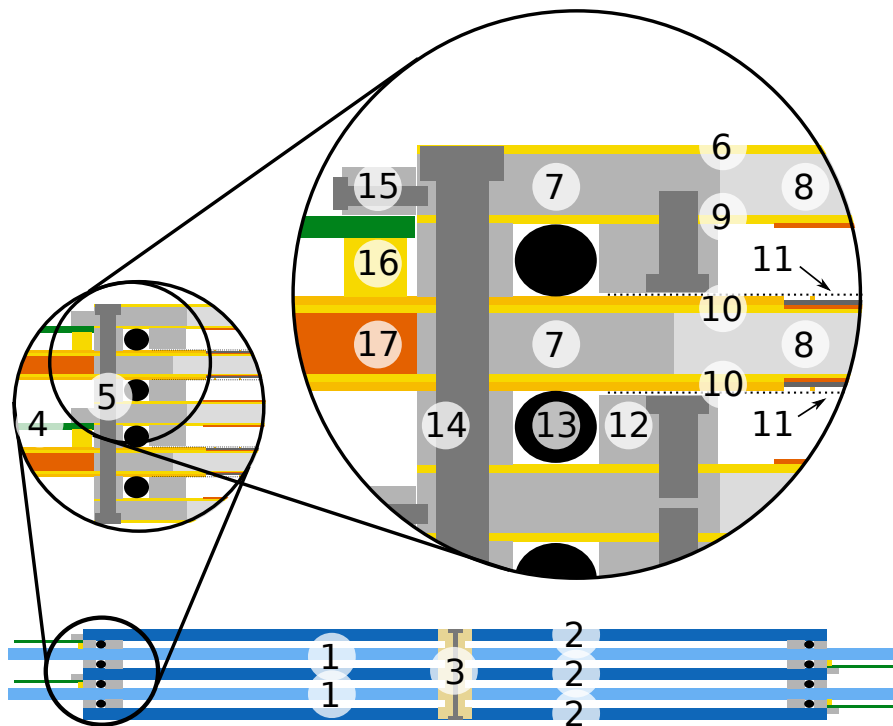
The readout strips in the first two layers are parallel to the long side of the trapezoidal detector and such measure the precision coordinate. The strips in the third and fourth layer are inclined by $\pm 1.5^\circ$. As illustrated in Figure 4.10b this allows for an additional determination of the precision coordinate and furthermore for the reconstruction of the radial coordinate with less, but sufficient precision. This readout principle was proven to fulfill the requirement for the ATLAS New Small Wheel upgrade, as presented in Section 4.1.6.

The minimal inclination of the third and fourth layer allows to route the signals, as for the first two layers, to the periphery of the readout boards on the side of the trapezoidal. The readout boards are wider than the drift boards allowing for the placement of the readout electric boards on the side. An integrated cooling channel in the protrude part of the readout panels ensures the heat transport away from the electronics. The electronics board is connected by a flexible zebra connector with six rows of embedded wires. The necessary pressure is applied to the connector by a compression bar, a dedicated bar with brass cams, mounted to the frame of the drift panel.

The drift panel is kept at a constant distance of 5 mm from the readout panel by a gas gap frame. An EPDM o-ring is placed in the space between the gas gap frame and the mesh frame. The mesh frame, where the stretched stainless steel micro-mesh with $30\mu\text{m}$ wire diameter and $100\mu\text{m}$ wire pitch is glued to, is screwed and glued onto the drift panel.

The quadruplet is hold together by M5 screws penetrating every $\approx 10\text{cm}$ through the panel frames and the gas gap frame. Additionally, the quadruplet is confined by six interconnections in the active area. The panels are reinforced by PEEK disc at these points and PEEK extensions are screwed onto the drift panels reaching in the gas volume to establish the gas tightness at the interconnection points.

On the two parallel sides, thin copper coated connections are screwed into the



- | | | |
|-----------------------|----------------------|--------------------------|
| 1 readout panel | 2 drift panel | 3 interconnection |
| 4 readout electronics | 5 fixation screw | 6 outer skin board |
| 7 panel frame | 8 aluminum honeycomb | 9 cathode board |
| 10 electronics board | 11 micro-mesh | 12 mesh frame |
| 13 o-ring | 14 gas gap frame | 15 zebra compression bar |
| 16 zebra connector | 17 cooling channel | |

Figure 4.11. Schematic cross section of a Micromegas quadruplet. The sketch is not to scale.

frames of the panel to unify the chamber grounding. It requires, that all electrical conducting components inside a panel have to be connected to propagate the ground potential.

4.2.2 Drift Panels Mechanical Design

An overview of the mechanical design of the ATLAS New Small Wheel drift panels is shown in Figure 4.12. As it can be seen from the quadruplet cross section in Figure 4.11, two different types of drift panels are necessary. One type, where only one side implements a cathode as closure of the Micromegas drift region and one side forms the detector outside, called outer drift panel, and one where both sides implement cathode surfaces, called central drift panel. For the total production of the NSW, including two spare quadruplets, 68 outer and 34 central panels have been produced.

The production of bare panels will be described in the following. A bare panel is the plain sandwich structure, without any peripheral structure, as the frames for the mesh gluing or holes for the assembly. The assembly holes and the mounting of further parts is done in the ATLAS NSW collaboration at the production facility at Ludwig-Maximilians-University Munich. This scheme eases the production, as no glue can penetrate through holes and no alignment between holes in the several components is necessary.

The panels are constructed as sandwich structures of the FR4 boards as outer surfaces and an aluminum frame with aluminum honeycomb as stiffening element in the middle. The honeycomb provides the mechanical stability of the panel while contributing only little to the material budget. This reduces the multiple scattering of particles in the inactive detector material. The 9 mm wide honeycomb cells are formed by 0.1 mm thick aluminum walls.

The outer dimensions of the finished panel are given by the outline of the frame constructed from extruded aluminum profiles. The panels have a height of 1350 mm a length of 1689.3 mm and 1188.9 mm on the long and short side of the trapezoid, respectively. The design thickness of the panels is 11.33 mm, consisting of two 0.5 mm FR4 sheets on the panel outside, the 10 mm thick aluminum bars, the 10.1 mm thick honeycomb sheets and a glue gap. The honeycomb is thicker than the frames, to allow to extend into the glue gap, as the thin walls of the honeycomb cells do not provide a large gluing surface.

The FR4 surface, either plain material in the case of the chamber outside or coated with a copper cathode, is split vertical into three single boards. The production of a single, full size sheet is due to technical limitations not possible. The single boards are separated by a 0.4 mm wide gap, which is filled with glue to ensure the gas tightness of the surface and a smooth transition between the single boards, which is crucial for an efficient sealing with the o-ring at the panel periphery.

The raw FR4 boards are ≈ 15 mm wider than the final panel to catch the spilling redundant glue. The protrude part is cut after the panel is cured.

The gap between the three single boards is reinforced by internal bars. All aluminum bars are extruded with grooves on the gluing surface to enlarge the contact area. Hollow channels are implemented, where possible in the bars, to reduce the weight and the material budget contributing to multiple scattering. While the internal frames are almost completely hollow, only a small hollow gap is possible for the frames of the surrounding frame. Towards the panel outside M5 clearance holes for the quadruplet assembly screws have to be drilled and towards the panel inside threads for the mounting of the mesh frame have be cut into the panel frame. A cross-section of the frames, showing their internal structure is give in section C-C and section D-D in Figure 4.12 for the bars of the panel frame and the internal bars, respectively.

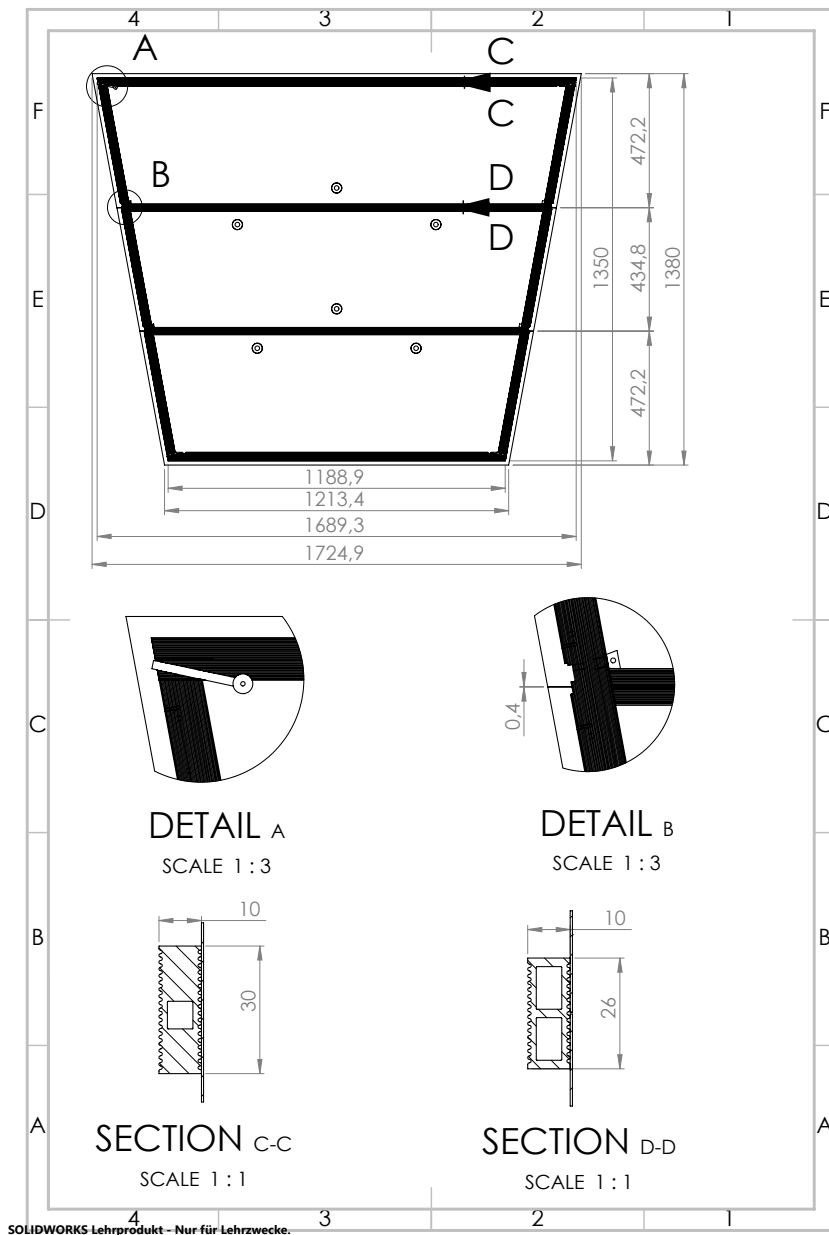


Figure 4.12. Mechanical drawing of the drift panel layout. To catch redundant glue during the gluing, the FR4 boards exceed the pure geometry of the final panel which outer dimensions are given by the bars. The surface is split vertically into three individual PCBs which are aligned with a gap of 0.4 mm. The bars appear black, because the surface grooves are not resolved in the sketch. Detail A shows the positioning of the gas distribution and detail B the high voltage feed-through also serving as confinement of the internal bars during the gluing. A cross-section, revealing the internal structure of the bars can be seen in section C-C for the outer frame and section D-D for the internal bars.

Several components have to be included into the panel structure. Six PEEK disks as a reinforcement of the quadruplet interconnections screws, preventing a blowup of the chamber with the overpressure during operation are included, as visible in Figure 4.12. The position was optimized to minimize the panel blowup deformation. Due to the later drilling of all assembly holes the positioning of these parts has only loose position requirements of $\approx \pm 5$ mm.

For the gas distribution a manifold is included in the panel corners routing a gas line from the inside to the cathode surface(s) of the panel. The positioning of the manifold is realized as a shape fit with a cutout in the top and bottom frames to enforce the correct position of the gas output line to the panel surface. Later, a perforated aluminum pipe parallel to the long and short panel side is mounted serving as gas input and output, respectively. At the transition point of the gas distribution and the hollow part of the frame, an aluminum reinforcement piece is glued into the frame. The distribution of the high voltage line to the cathode surface is implemented in the panels as well. 3D printed feed-throughs are included in the panel frame, guiding the cables from the side toward the cathode surface. In the later processing steps, the cathode segments of the three FR4 sheets are connected by soldering. Redundancy in the HV supply is achieved, by including feed-throughs at all connections of the internal bars with the outer frames. Thus two connections per cathode surface are provided for central panels and four for outer panels. The feed-throughs are stuck into holes in the outer frame and the part expanding into the panel center is shaped such, that it exactly fits to the internal frames and confines them in the trapezoidal shape of the outer frame during the gluing process, ensuring their correct alignment.

4.2.3 Drift Panel Specifications

The efficient operation of the Micromegas quadruplets imposes several challenging requirements on the production of the bare drift panels. In the following an overview on the specifications along with a brief description of the method for the implementation and quality control is presented.

The most demanding limit of the production is the requirement on the flatness and planarity. This comes from the need of a uniform amplification gap height in the Micromegas detector. As the mesh is attached to a frame screwed to the drift panels, deviations in the drift panel geometry translate to fluctuation in the amplification gap. The deviation of the panel surface from an ideal plane and the fluctuations in the panel thickness have to be less than $\pm 110 \mu\text{m}$ in total, translating to a RMS of the distribution of all deviations of less than $37 \mu\text{m}$.

To achieve this requirement, the FR4 surfaces are sucked to a vacuum table with a precision surface during the production. The RMS of the vacuum table flatness is required to be less than $27 \mu\text{m}$ in the fiducial area. To achieve the thickness uniformity, the vacuum tables holding the two FR4 surfaces of a panel during the

gluing are supported on precise distance pieces.

Not only the quality of the FR4 surfaces, but also the relative alignment of all components in the panel is important for the proper operation. The outer dimensions, formed by the panel's aluminum frame, are the reference for the alignment during later production steps, as the drilling of the assembly holes. To match the active cathode area with the readout area an alignment of the single FR4 sheets of better than $200\ \mu\text{m}$ relative to each other and relative to the aluminum frame is necessary. As the side frames of the panel host compression bars for the zebra readout connectors and the proper compression of those connectors is essential for a reliable connection of the contact pad on the readout panel and the readout electronics board, the lateral and vertical position of the side frames in the panel is important. The relative positioning of the FR4 boards and the aluminum bars forming the frame is guaranteed by an external alignment frame which provides contact points for the placement of the components. The vertical bar positioning is ensured by a well defined glue gap.

As the detector outside acts as Faraday cage for the electric fields inside, the electrical continuity of all metal parts has to be ensured over the full detector lifetime. Therefore the aluminum bars are produced with an Alodine[®] coating which enhances the surface conductivity and avoids a connection loss due to oxidation. Furthermore, not only contact interfaces are used between all internal metallic parts, but each connection is as well supported by a conducting silver paint guarded with a layer of epoxy glue.

In order to avoid gas pollutions which degenerate the detector performance the gas tightness of the quadruplet has to be ensured. The limit of the ATLAS collaboration for the gas loss is $10 \times 10^{-5}\ \text{bar L s}^{-1}$, also coming from safety requirements on the air quality around gas detectors.

For the drift panels this concerns the junction between the single FR4 boards and the surface quality at the panel periphery, where the o-ring seals the chamber. For that reason, a well defined gap of $400\ \mu\text{m}$ between the single boards is implemented. The sealing of that gap with epoxy glue not only enhance the gas tightness towards the panel inside, which is already well established by the internal aluminum frame behind the junction, but also creates a smooth transition between the boards at the o-ring position.

4.3 Material Irradiation Studies

The high radiation rates in the ATLAS detector lead to an aging of the detector components. It has to be ensured, that the radiation damage does not influence the detector performance. The New Small Wheel upgrade uses two components,

Table 4.2. Neutron flux at the irradiation positions of the TRIGA Mark II reactor. The conversion to the fast neutron flux and the 1 MeV equivalent is taken from [89]

	neutron flux (100 kW)	neutron flux (1 kW)
thermal flux	$0.7 \times 10^{12} \text{ cm}^{-2} \text{ s}^{-1}$	$0.7 \times 10^{10} \text{ cm}^{-2} \text{ s}^{-1}$
fast neutrons	$2.1 \times 10^{11} \text{ cm}^{-2} \text{ s}^{-1}$	$2.1 \times 10^9 \text{ cm}^{-2} \text{ s}^{-1}$
1 MeV equivalent	$2.2 \times 10^{11} \text{ cm}^{-2} \text{ s}^{-1}$	$2.2 \times 10^9 \text{ cm}^{-2} \text{ s}^{-1}$

which have not been used in high rate particle detectors before. The first component is the zebra connector, which transfers the signals from the readout board to the readout electronics. The used FG-6 connector from COMPELMA has 6 rows of $30 \mu\text{m}$ gold plated brass wires with $50 \mu\text{m}$ pitch embedded in a silicone bar. A connection is established over the embedded wires by compression of the connector between contact pads on both ends of the wire.

The second novel component is the choice of the o-ring. As in total four o-rings have to be compressed in a quadruplet, a soft (20 shore A) EPDM o-ring from Angst+Pfister with an internal foam structure was selected.

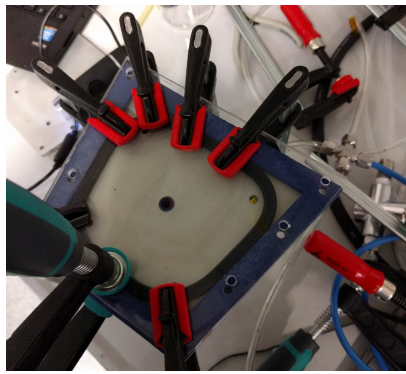
The TRIGA Mark II reactor at Johannes Gutenberg-University Mainz [88] provides a pneumatic post system for neutron irradiation in the reactor core. The neutron flux in the reactor is given in Table 4.2. The simulated neutron flux of in the ATLAS CSC region, the hottest region of the New Small Wheel, is $3.4 \times 10^4 \text{ cm}^{-2} \text{ s}^{-1}$. The expected flux for 10 years of operation was accumulated in the reactor in 30 min of operation at 1 kW reactor power with a safety factor of 1.2.

Limited by the space in the irradiation facility, five zebra connector samples and two o-ring ropes for a small test stand have been investigated.

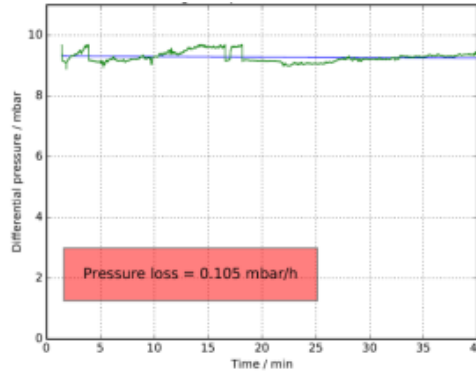
The zebra connector was checked before and after the irradiation with a special tester board. The board has the same geometry for the compression and the contact pads as the New Small Wheel quadruplet. The contact between opposite pads is indicated by a LED. A full connectivity was achieved for all tested zebra connector samples. As also a visual inspection did not show any material degeneration, no evidence for a harmful aging under neutron irradiation was found.

The o-ring samples have been tested in a small gas test stand (Figure 4.13a) which has the same corner geometry as the ATLAS New Small Wheel SM2 geometry. A gas tightness test with the pressure drop method described in Section 4.6.5 showed a pressure loss well below the ATLAS limit of 1 mbar h^{-1} . The result for one test sample can be found in Figure 4.13b.

As an additional study the size and number of pores in the compressed surface of the o-ring was investigated. The soft EPDM o-ring consists of a foam structure and therefore

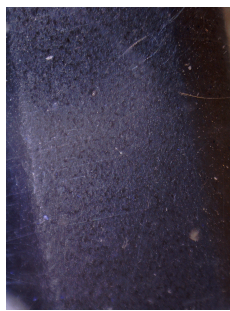


(a)

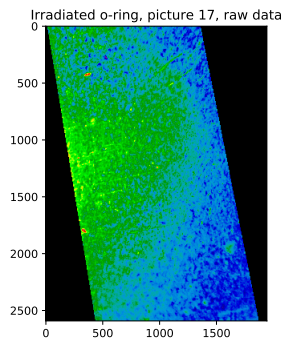


(b)

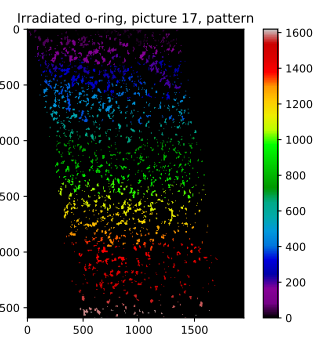
Figure 4.13. Setup for the tightness measurement of irradiated o-rings (a) and result of a irradiated sample (b).



(a)



(b)



(c)

Figure 4.14. Analysis scheme of the o-ring foam structure. The picture of the compressed o-ring (a) was decomposed in a single color value (b). The color code in this picture is the color value in the range $[0, 255]$. The darker spots which do not touch the surface are identified and combined in clusters (c). Each identified cluster is encoded in a different color, starting from the top left corner and moving row by row to the lower right corner.

potentially open channels into the gas volume can be formed by the connection of pores. A picture was taken with a digital microscope through the top Plexiglas plate of the gas tightness test stand. The picture was cut to the compressed surface, decomposed in the single RGB channels and the blue channel was investigated, as it showed the clearest pore identification. The color noise was corrected by a Gaussian filter with three pixel standard deviation. The pattern of the pores was identified as spots where the color value is by 10 units smaller than the value of a Gaussian filter with width $\sigma = 75$ around the pixel. Neighboring pixels have been combined as one cluster representing one pore. The analysis principle is shown in Figure 4.14. The result of the analysis is presented in Figure 4.15. It is visible, that slightly more, but smaller pores are detected after the irradiation. As the change is not significant and the tightness of the samples was confirmed this test does not predict any aging problems for the o-ring under neutron irradiation.

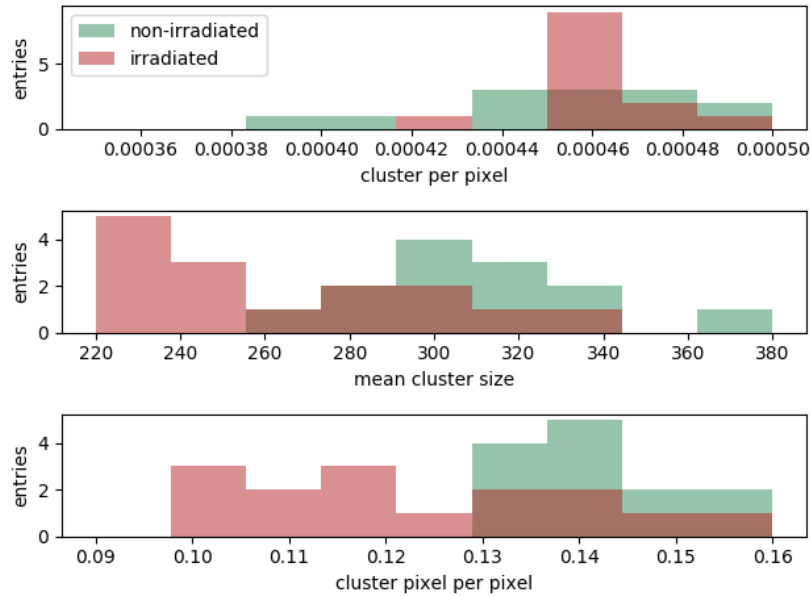


Figure 4.15. Result of the cluster analysis for pores in the surface of the compressed o-ring. The results are normalized to the total number of clusters in the compressed surface to correct for a different picture detail.

4.4 Production Infrastructure

The following section describes the infrastructure used for the production of the NSW drift panels. The whole production facility was planned and realized, the production was ramped up and the total manufacturing was monitored within the scope of this work.

A basic overview on the lab infrastructure and the available resources is given in Section 4.4.1. The construction of the necessary tooling for the production, as the precision surface vacuum tables and an alignment system for the components of the drift panel is described in Section 4.4.2 and Section 4.4.3, respectively.

4.4.1 Lab Infrastructure

The production was set up in the PRISMA Detector Lab at Johannes Gutenberg-University Mainz [90] which is optimized for the construction of (large scale) micro-pattern gas detectors [91]. An overview of the lab is shown in Figure 4.16. The lab includes a 2.5 m × 1.8 m high planarity granite table inside a 3 m × 4 m ISO class 5/6 laminar flow tent. The granite table provides a surface planarity of $\pm 14 \mu\text{m}$ (DIN 876 0) over the full surface and is such well suited as a base for the construction of the precision vacuum tables and the planarity and thickness measurements of the finished panels.

For these measurements a 3D positioning system with a laser distance sensor (MicroEpsilon OptoNCDT 2300) is mounted on top of the granite table. The area inside the measurement system is 1.42 m × 2 m. A detailed overview on the performance of

the measurement system and the measurement strategy is given in Section 4.6.4.

Considering the high surface planarity requirements, a dust reduced working area for the panel gluing is preferential. Therefore the laminar flow box was extended by a tent whose roof is closed by a plastic foil. At the transition of the laminar flow box towards the extension tent the floor-length curtain was replaced by half-length separator foil. A complete opening was discarded, as it would allow for more back-flow from the extension into the laminar flow tent, risking contaminations.

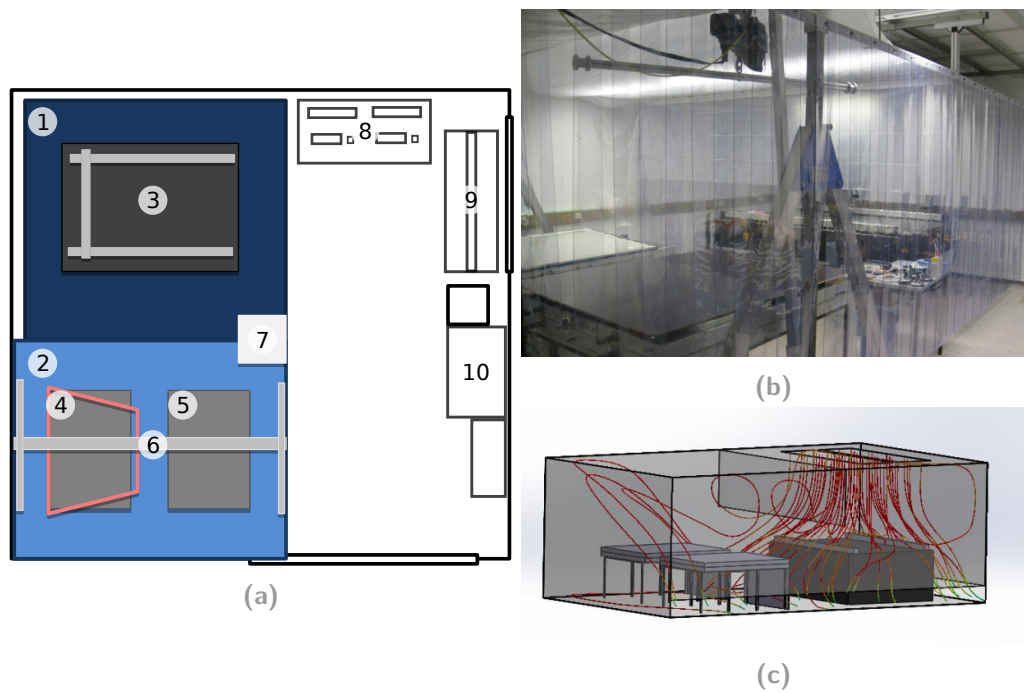
The air flow in the combined system was simulated with SolidWorks. The simulation result is shown in Figure 4.16c. A turbulent spread of the clean air from the filter directly above the vacuum table surface is visible. To suppress a circular airflow traversing under the vacuum tables and later raising at the wall to pass the table surface, the table side facing towards the laminar flow tent was closed with a cover. The density of particles smaller than $0.5\ \mu\text{m}$ was reduced to 2% of the particle density outside the extension by this approach.

The two vacuum tables for the panel gluing are placed in the tent extension under a crane with a speed controlled motor to ease the lifting of the second vacuum table during the panel closure. One of the vacuum tables is equipped with an alignment frame for the positioning of the components during the panel assembly.

A small tooling table is placed between the two clean areas at the outside wall. Such it can be reached from all areas and new equipment can be put in place without entering the clean area.

A setup for the gas tightness test is included in the lab outside the clean areas. The design of the test stand and the measurement procedure will be presented in Section 4.6.5.

It was found, that the FR4 sheets expand with a change in humidity more than $100\ \mu\text{m m}^{-1}$ per 20% humidity change. This makes the proper alignment and stable sucking to the vacuum tables impossible, as the single sided copper clad cathode boards show a strong wavy structure due to the constraint of the non-expanding copper. Therefore a humidity controlled storage box was built and placed under one of the vacuum tables. The humidity was set to 45% relative humidity, a bit less than the nominal 50% relative humidity from the board conditioning in industry to reach the nominal value by the humidity absorption during the gluing. The humidity stabilization was reached with a constant humidity device and four container of PRO SORB silica gel for a quick stabilization after the opening of the box.



- | | | | | | |
|----|-------------------|---|------------------|---|--------------------|
| 1 | laminar flow tent | 2 | tent extension | 3 | granite table |
| 4 | vacuum table 1 | 5 | vacuum table 2 | 6 | crane |
| 7 | tooling table | 8 | computer station | 9 | gas tightness test |
| 10 | storage | | | | |

Figure 4.16. Overview sketch of the lab infrastructure (a) and picture of the dust reduced area for the panel production (b). The simulation of the air flow in the tent extension proves the spread of the clean air over the vacuum tables (c).

4.4.2 Vacuum Table Construction

To achieve the required surface planarity, the flexible FR4 boards are sucked to precision surface vacuum tables. These vacuum tables are, as the panels, built as sandwich structures of a flexible outer skin and a stiffening aluminum honeycomb and frame in the middle. 1 mm thick aluminum plates are used as outer skin. The width of 1400 mm is adapted to fit inside the 1420 mm gap between the bars of the positioning system on the granite table. The length of the plate is chosen as 1800 mm to fit the full drift panel well.

The gluing is performed as a two-step process, where the latest glued side is the later precision side. For each gluing step, the aluminum sheets are sucked to the granite table. As the table does not provide vacuum holes, a thin plastic grid is placed between the granite surface and the aluminum sheet, creating channels where the air can be evacuated to the short sides of the aluminum sheet. A fly screen was found to be a suitable and cheap mesh for that purpose. Tests with metallic meshes have shown worse results, as the metal tends to get irreversible dents when handled in that large size.

At the long sides, the mesh is cut a few millimeter shorter than the aluminum sheet to avoid fibers sticking out of the sealing tape creating leakage channels. At the short sides the mesh is exceeding the aluminum sheet. A foil cover with a connection to a vacuum pump is sealed towards the aluminum plate and the granite table on both sides. For a better gas distribution towards the sheet, a line of fleece tissue is placed along the junction (see Figure 4.17).

The pressure at the vacuum pump was regulated to create between 100 mbar and 200 mbar under pressure with respect to atmospheric pressure. This results in a force of ≈ 35 kN on the aluminum surface which presses it towards the granite table and transfers its flatness. To keep the flatness of the finished vacuum table, it is crucial not to introduce further stress to the components during the final gluing step, which leads to a deformation as soon as the constraint is removed.

To obtain the desired mechanical strength of the vacuum table, a 80 mm high aluminum honeycomb with 9 mm cell width is glued to the outer sheets. The gas tightness toward the outside is guaranteed by a 40 mm wide aluminum frame, where handles and a vacuum junction to the inside are fixed on the short sides. The frame is miter cut. Such the single bars stabilize their position relative to each other when pressure from the outside is applied and the frame can be fixed with a lashing strap during the gluing.

To reduce the gravitational sag of the vacuum table, as it is turned over and supported only on twelve distance pieces during the gluing of the drift panel, an additional aluminum bar is placed in the center in the final design of the vacuum tables. It is glued with brackets toward the outer frame.

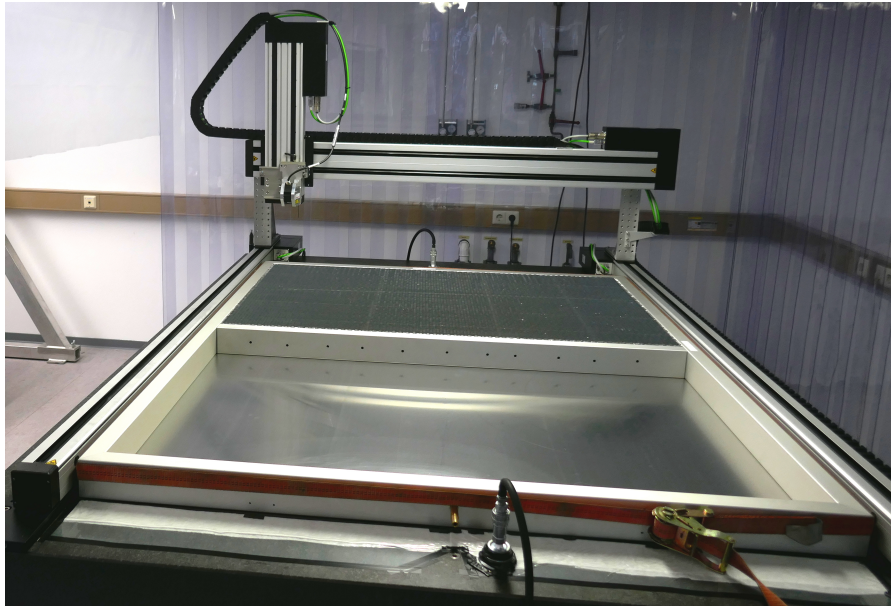


Figure 4.17. Picture from the vacuum table gluing process. The frame, fixed by a lashing strap, is placed on a aluminum plate sucked to the granite table. The vacuum connection with a distribution along the full front side is visible. The internal bar is, as well as the honeycomb sheet, perforated with 6 mm diameter holes to allow for a faster evacuation of the completed vacuum table.

The impact of the internal bar on the reduction of the gravitational sag is shown in Figure 4.18. While the measurement in 4.18a was done with a vacuum table without internal bar supported on six distance pieces, the other two measurements have been done with a vacuum table with internal bar. Figure 4.18b shows, that even though the vacuum table is not supported at in the middle of the long side any more, the total bending deviation goes down by more than 10%. Figure 4.18c shows a measurement where the table was supported on the same points as during the gluing process, when the two halves of the panel are closed.

The internal bar, as well as the honeycomb are perforated horizontally with 6 mm diameter holes to ease the evacuation of the vacuum table inside. The honeycomb walls itself are micro-perforated, but the total gas throughput is small compared to the 6 mm channels.

During the first gluing step, the aluminum bars and the honeycomb pieces are glued with Araldite® 2011 to the first aluminum sheet sucked to the granite table. A weight of ≈ 100 kg is applied uniformly on top of the open vacuum table, to compensate for internal stress and bending of the honeycomb. After the curing of the glue, the half-table is removed from the granite table and a new aluminum sheet is sucked to the granite table. A uniform glue layer of at least 0.4 mm is applied to the surface. The glue gap compensates for deviations in the planarity of the first half of the vacuum table. These can either appear due to height variations of the components, or an internal stress introduced when the honeycomb sheets have been evened

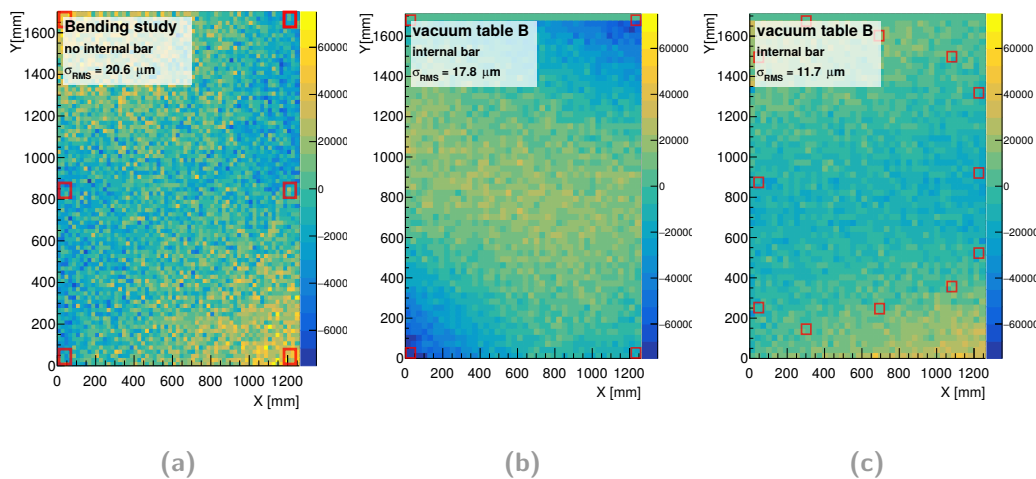


Figure 4.18. Comparison of the gravitational sag of a vacuum table with and without internal bar. The deformation of the vacuum table surface is shown for a table only supported at the positions indicated by the red boxes.

during the first gluing step. To avoid the later effect in the second gluing, the weight applied to the vacuum table to press it into the second glue layer is reduced to ≈ 20 kg after half an hour of curing time, so while the glue stays liquid.

After the curing the planarity is measured with the laser distance sensor, following the procedure described in Section 4.6.4. The planarity in the fiducial area of the panel surface is estimated for the two possible orientations of the trapezoidal shape. The optimal position is chosen and a $100 \text{ mm} \times 100 \text{ mm}$ grid of 2 mm diameter holes to suck the FR4 sheets to the vacuum table is drilled. As the FR4 expands with humidity which leads to a wave structure in the single sided copper clad cathode boards an additional ring of holes, 30 mm from the panel border, with a hole distance of 30 mm was drilled into the vacuum table surface, to enhance the cross section for the evacuation of potentially leaking air.

4.4.2 Vacuum Table Planarity

In total six vacuum tables have been constructed whereof three fulfilled the requirements for the ATLAS production. The other tables have been either used as support under the tables used for the gluing or as a work table for raw material quality control measurements.

The three vacuum tables are labeled A, B and C, whereby the labeling follows the production order. Tables A and B have been produced in 2015 and were used for the production of NSW prototype panels. Table C was produced in 2016 as a result of an observed thickness variation in the panels due to the gravitational sag of the top vacuum table during the gluing. Therefore the internal bar, was introduced in

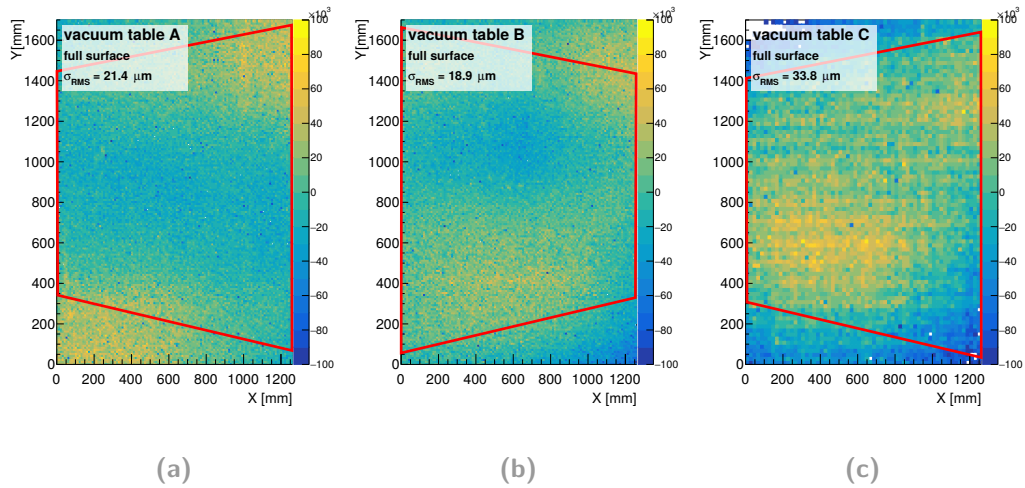


Figure 4.19. Planarity scans of the vacuum tables. The chosen panel orientation, fixed by the drilling pattern of the vacuum holes is indicated by the red trapezoid.

Table 4.3. Planarity result of the constructed vacuum tables. Table A and B have been already used for the construction of prototype panels in 2015 and table C was built in 2016 with the reinforced internal structure. The planarity for the full surface and the two possible orientations of the trapezoidal detector geometry is shown.

	full surface	fiducial area 1	fiducial area 2
vacuum table A	21.4 μm	19.3 μm	19.6 μm
vacuum table B	18.9 μm	16.8 μm	19.1 μm
vacuum table C	33.8 μm	24.1 μm	26.4 μm

vacuum table C.

The planarity scans of the three vacuum tables is shown in Figure 4.19. Here the planarity is evaluated for the full table area and the chosen panel orientation is indicated by a red contour. An overview of the planarity for the two possible drift panel orientations is shown in Table 4.3.

As table B provides the best surface planarity, the alignment frame, as reference for the positioning of the panel components, was mounted to it and it was used over the full production, referred to as vacuum table 1 in the description of the production procedure. Table A was replaced as second gluing table after the prototype production by table C and was kept as spare. Even though the planarity of table C is slightly worse than the planarity of table B when measured laying on the granite table, the reduced gravitational sag when only supported on distance pieces results in a better production quality using this table. This table is named vacuum table 2 in the following.

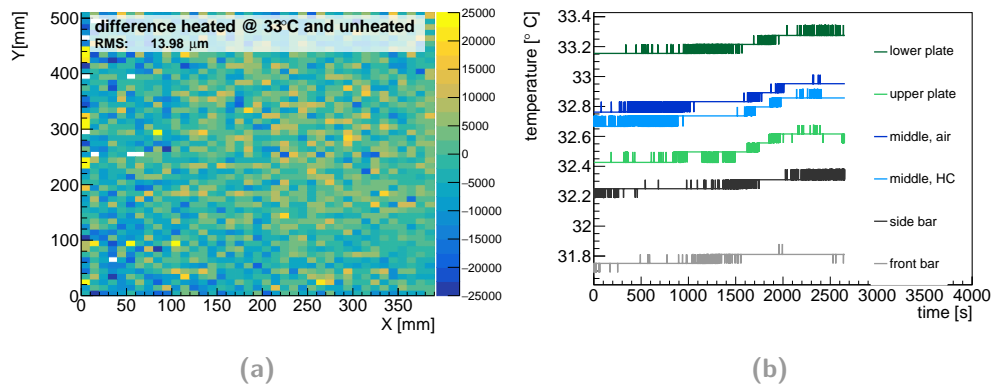


Figure 4.20. Change in the surface planarity deviation from an ideal plane (a) and temperature distribution inside the vacuum table (b). The fluctuations in the temperature measurement come from the limited resolution of the temperature sensor DS18B20.

4.4.2 Vacuum Table Temperature Deformation

The air conditioning of the production facility was only established in summer 2016, after the prototype production and the setup of the main infrastructure. Therefore the impact of a temperature change on the vacuum table planarity was investigated. A small scale 500 mm × 390 mm model, keeping the aspect ratio of the real size vacuum tables, was constructed.

The model was built from the same material as the real size tables and 6 temperature sensors have been included. One at a long (labeled side) and one at a short (labeled front) bar, one in the geometrical middle attached to the honeycomb (HC) wall and one floating the air at the same point. A sensor was coupled to the inside of each aluminum plate cover.

Heating wires have been attached to the outside of the vacuum table model and the table was placed on a thermal insulator on the granite table surface. The table sides with been wrapped with bubble foil for thermal insulation.

The non-planar difference of the models surface structure at room temperature (22 °C) and heated to 33 °C is shown in Figure 4.20a. As only point to point variations and no global structure can be seen in this study and the total heat distribution is constant within 1 °C a uniform temperature change in the vacuum tables can be concluded. As the tables are purely build from aluminum, no internal stress due to a different expansion of different material compositions is expected. This study also shows, that a longer time storage without temperature control is possible.

4.4.3 Alignment System

As emphasized in the previous sections, reference points for the alignment of the panel components have to be provided during the gluing. Therefore a system of a frame, glued onto the vacuum table, and thereto referenced attachments, called fingers, with a point contact to the component to be aligned, has been designed. A picture of a finger is shown in Figure 4.21a. The contact points for the FR4 boards

and the panel's aluminum frame, as well as the contact surface to the alignment frame are the crucial features of these parts which are produced with tight allowance. As the FR4 boards are flexible, reference points are foreseen at least every 400 mm. A larger density of reference points on the inclined sides is necessary due to the segmentation in three FR4 boards. Each board is referenced with two points.

The mechanical drawings of the parts, as they have been handed for the production can be found in the appendix in Section A.2.1. Changes to the design, implementing the experience from the beginning of the production will be discussed in the following. A sketch of the alignment system mounted to a vacuum table can be found in Figure 4.22.

It can be seen, that the alignment frame exceeds the dimensions of the vacuum table on the long sides. This became necessary as the vacuum table size was limited by the space inside the positioning system for the planarity scans on the granite table. The parallel reference frames have been implemented as T-section to gain mechanical strength. An additional advantage is, that screws penetrating the vertical part can fix the distance to the vacuum table side and such stabilize the alignment frame inclination during the mounting.

The single frames of the alignment system have been referenced towards each other during the gluing with a gauge in the size of the panel dimensions. The fingers have been mounted to the frames and opposite frames were connected via metal strings stretched with tension locks, to push the reference point of the fingers against the gauge. The procedure is displayed in Figure 4.21b. In that way, manufacturing allowances are evened as the same point is taken a reference during the assembly of the frame and the panel gluing. A unique position on the frame is assigned for each finger during the frame mounting and the position is preserved over the full production. Attachments for the corners of the frame have been produced to ease the mounting procedure.

Several changes to the initial design of the alignment system have been implemented. The first change is the concept of the alignment of the parts on the two vacuum tables. While the initial idea foresaw the mounting of an individual frame on each vacuum table and the relative alignment of the two frames by precision pins, the concept was simplified to the use of a single alignment frame keeping more space between the vacuum tables to observe the closing procedure. The half panel, glued in the first construction step and transferred to the second vacuum table, is reference to three special fingers touching the panel frame. For that purpose these fingers have been thinned down to fit between the vacuum tables and not to touch spilled out glue from the first gluing step at the FR4- frame junction.

An additional adaption is the shortening of the back of the fingers to allow for the placement of the additional frame of a vacuum bag used in first gluing step. Initially, it was foreseen to press only the aluminum frame of the panel into the glue

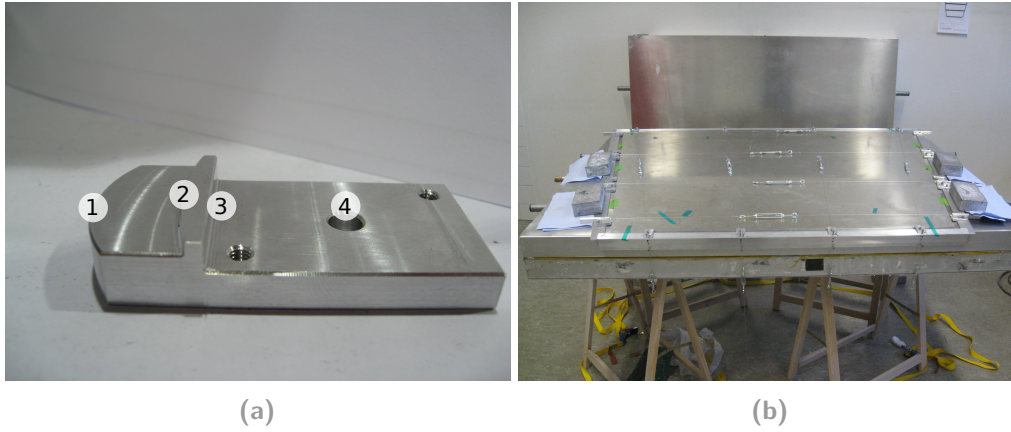


Figure 4.21. Picture of a alignment finger (a). The contact point for the panel’s FR4 boards (2) and the frame (1) are marked. The finger is reference toward the frame at surface (2) and mounted to it with an M5 plastic screw in hole (4).The mounting of the alignment frame with help of the gauge can be seen in (b).

with attachments mounted to the fingers and keep the honeycomb floating. First gluing studies revealed an internal deformation of the honeycomb which needs to be corrected by external pressure to meet the mechanical requirements of the panel. Therefore the gauge from the vacuum frame mounting is placed on top the full panel under the vacuum bag foil. The alignment fingers have been thinned by 2 mm not to stick out over the height of the half panel. Otherwise the gauge might lay on the fingers and no pressure would be distributed to the panel.

4.5 Drift Panel Production

In the following sections, an overview on the drift panel production is given. The production is explained from the point of the mechanical requirements. A detailed step-by-step description of the production procedure can be found in the construction manual, which is attached in the appendix in Section A.2.2.

For quality assurance a check list is followed and the gluing process is documented. The provided templates can be found in the appendix in Section A.2.4 and Section A.2.5.

The gluing of the panel is a two step process. In the first step, the panel’s internal infrastructure is glued with the epoxy glue Araldite® 2011 to the first FR4 layer as described in Section 4.5.1. In the second step, presented in Section 4.5.2, the grounding connections for the metallic internal parts are established and the sandwich is closed with the second FR4 side. As the FR4 boards exceed the later panel dimensions to catch abundant, spilled out glue, the protrude part has to be cut and afterwards the gap between the single boards has to be sealed for the assurance of the chamber gas tightness. The steps for the panel finalization are described in Section 4.5.3. The whole production procedure was developed in the scope of this

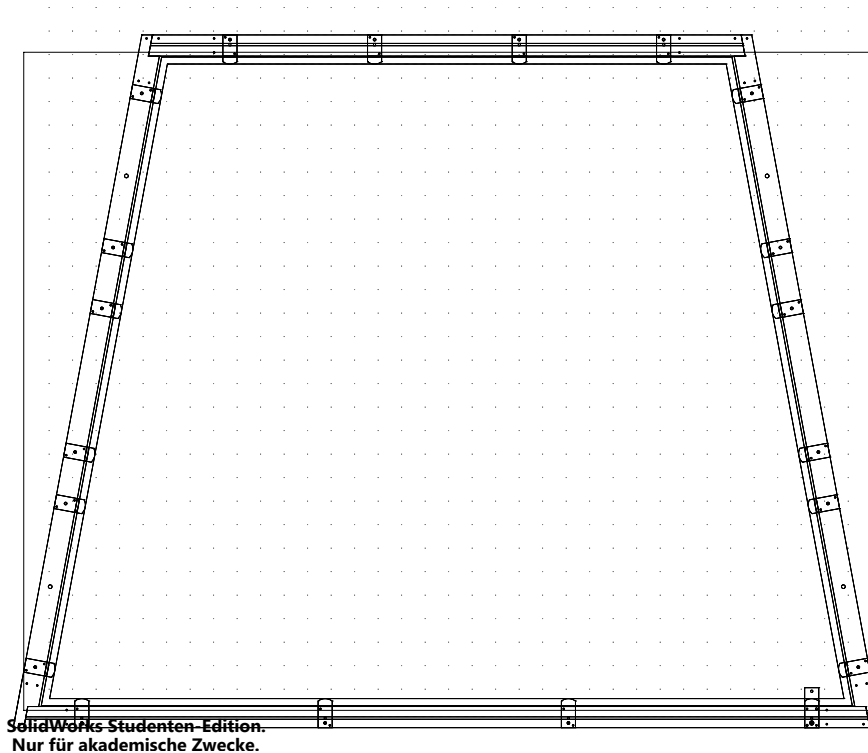


Figure 4.22. Sketch of the alignment frame on top of the vacuum table. The gauge with the outer dimensions of the panel frame is placed inside the frame.

thesis. The description in the following sections aims to present the idea behind major details as background information to the construction manual to allow for a resumption of the production if more material is need.

During the learning phase of the production team, a delamination was found on the surface glued on the second day. This can occur due to a inhomogeneous spread of the glue or local thickness variations in the half panel, which enlarge the glue gap at other points. A repair procedure for delaminated spots was developed and is presented in Section 4.5.4.

During the description of the production procedure, it will be referred to several kinds of adhesive tapes. An overview of the naming used in the description and the tape specifications is given in Table 4.4

4.5.1 First Production Step

The most stringent requirement for the NSW drift panels is the average flatness of less than $37\ \mu\text{m}$. The same limit is set for the panel's thickness variation. To achieve the flatness, the FR4 surfaces are sucked to the precision surface of a vacuum table, whose construction was explained in Section 4.4.2.

To guarantee the thickness specification, it has to be ensured, that the panel's internal structure, the honeycomb and the aluminum bars, does not have protrude parts. As

Table 4.4. Overview of the different adhesive tapes used during the drift panel gluing. If different width are available for one kind of tape, the value is specified before the tape name where important in the explanations in the text.

Name	width [mm]	thickness [μm]	description
green tape	6, 12	89	polyester tape, removable without traces
brown tape	6, 9, 12	64	polyamide tape, flexible but stable against compression
copper tape	25	50	copper foil with an acrylic glue layer
insulating tape	15	/	flexible tape, well suited for vacuum sealing where no stable tape thickness is required

the parts might have an internal stress, which leads to deformations, they have to be pushed down during the gluing process. Therefore a vacuum bag with a frame laying on the alignment frame is applied on top of the components. To protect the foil of the vacuum bag from the sharp edges of the panel parts, the gauge used for the alignment frame gluing, is placed on top of the half panel. It has to be ensured, that the gauge lays on the panel components and cannot touch the alignment finger's top surface.

The vacuum foil is supported by a stable polystyrene foam, which is higher on top of the gauge than over the alignment fingers to apply pressure to the panel edges. The full setup is shown as a cross section in Figure 4.23.

The pressure was tuned to have a pressure gradient over the vacuum bag and the vacuum table. 300 mbar depression compared to atmospheric pressure have been applied to the vacuum table. This value is sufficient to suck the FR4 board reliable. Lower values have been discarded to reduce the mechanical stress on the vacuum table. Inside the vacuum bag, 150 mbar below atmospheric pressure have been applied. The value was found to be sufficient to flatten the components and a remaining pressure difference of 150 mbar to the vacuum table safely attaches the FR4 boards.

The panels are sealed at the border toward the vacuum table with a layer of the brown tape, which provides a high flexibility to follow the contours while being able to be removed without major traces.

The quality of the internal parts is checked during a dry run of the assembly. All parts are placed on the FR4 boards already sucked to vacuum table 1 and the relative height deviation of the components to each other is controlled by the light-gap method with a 500 mm straight-edge as reference. If no deviations are found the

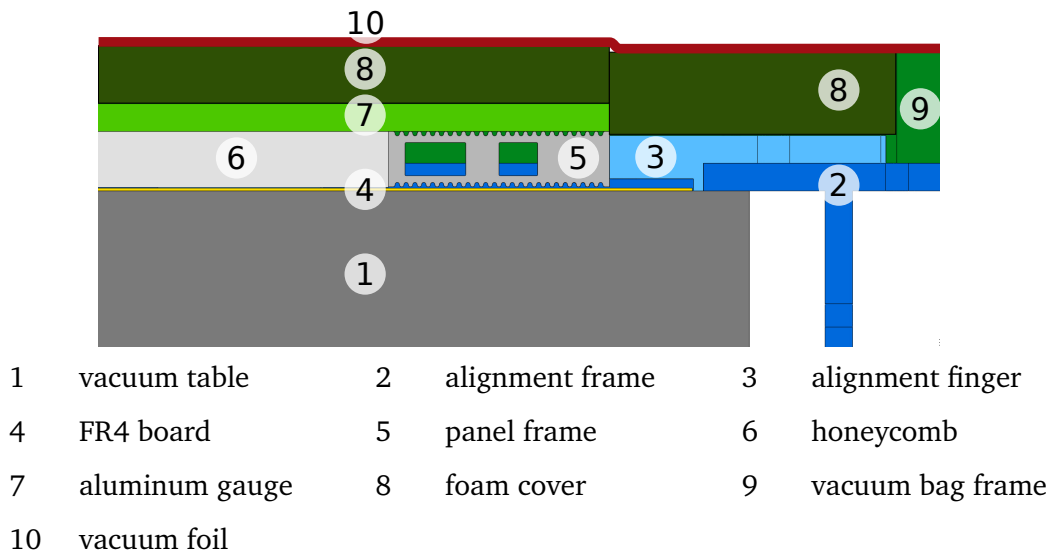


Figure 4.23. Cross section of a the mechanical model at the end of the first gluing step. The panel frame and the honeycomb are glued to a FR4 board layer sucked to the vacuum table. The frame and the FR4 board are reference towards the alignment finger. The half panel is topped with the aluminum gauge, used for the vacuum frame alignment. A vacuum foil attached to a frame at the outside. For an ideal pressure distribution a layer of stable polystyrene foam is applied under the vacuum foil.

final assembly with glue can be executed.

The strict allowances require working in a clean environment. The extension of the laminar flow tent provides a sufficient clean environment if a cleaning is ensured before each assembly step. Persons working on the production have to wear a clean room coat, a hairnet and gloves to avoid pollution. All surfaces have to be cleaned with an anti static adhesive roller directly before placing components or spreading glue.

Before the first placement of the components for the test assembly, they are cleaned with isopropyl alcohol to remove contaminations from the production. As the final degreasing all gluing surfaces are treated with acetone directly before the gluing.

The relative alignment of the internal components is ensured by the contact points of the fingers attached to the alignment frame. While in principle three contact points would be sufficient to constrain the alignment of the components, an over constrained situation was implemented. As the FR4 boards are flexible and tend to elongate by humidity absorption, more contact points are chosen to define a line along the board's edge. Initially two lines are used for the alignment of two edges of the first board. The smallest board is placed first, as the other boards would need to be moved over it's final position leading to a possible pollution of that spot. The

board positioning is checked by placing the fingers at the third side. If a non-contact is observed, the board has to be checked and the dimensions have to be corrected. The fourth board side is the side facing towards the next board. Here two short pieces of $400\mu\text{m}$ wire are placed at the edge of the board. The next board is aligned towards these wires and the fingers at one inclined side. Two short wire pieces are used instead of a single long wire, as the board flexibility might lead to a distortion of the board's outer dimensions, which would be propagated to the components alignment if the positioning is constrained over the full side. The fingers at the second side are placed for the alignment and board dimension confirmation after the actual positioning. The wires are kept in place and the gap between the board is sealed for vacuum tightness and against a glue spill out by a line of 6 mm brown tape.

The last board is placed in the same procedure. The fingers on the top side of the frame are placed as a check of the total board alignment and the dimensions are adjusted if necessary. For outer panels the cathode side is glued in the first step, as a better attachment of the components is expected since they are pressed into the glue. During the second gluing step, the glue gap is well defined by distance pieces and such an inhomogeneous glue spread can lead to unglued spots.

The panel frame is designed in a self stabilizing way. The side frames press the top and bottom frame against the reference points. The side frames itself are stabilized by the trapezoidal cut of the internal bars which are fixed from the long side by the form-fit high voltage feed-throughs anchored in holes of the side frame. A lateral movement of the top and bottom bar is prevented by a gluing connection with fast curing cyanoacrylate glue at the edge to the FR4 surface during the gluing process. Two layers of 6 mm green tape are applied every $\approx 15\text{ cm}$ to the gluing surface of the bars to ensure a well defined glue gap and the centering of the frame in the sandwich.

The honeycomb sheets were cut in advance to fit inside the foreseen space. It has to be ensured during the gluing, that a connection of at least one honeycomb cell wall can be connected to each frame to establish the grounding connection in the second gluing step. A gap larger than 5 mm between the honeycomb and the aluminum bars should be avoided for stability reasons.

The interconnections are placed inside cutouts in the honeycomb sheets. Their position can be checked with the shine through copper pattern of the cathode facing towards the vacuum table. As they are larger than the later drilled holes, their positioning is not crucial and a shift in the range of $\pm 5\text{ mm}$ is tolerable.

The gas feed-through connector in contrast have to be positioned precisely, as the hole drilled into the cathode surface has to match the connector outlet. The cylindrical manifold is referenced to a form-fit cutout in the frame and fixed in place with



Figure 4.24. Gluing tools used during the construction. A spill of the glue over the sides of the aluminum bars is avoided by the dedicated gluing tool (a). The thickness of the glue layer on the FR4 boards is fixed by wires, bend over the edge of a spatula (b).

additional cyanoacrylate glue during the gluing. The connector pipe is embedded in a cutout, which is sealed with clay towards the panel side.

The holes in the gas connector and the high voltage feed-through have to be protected from invading glue. Small pieces of the brown tape are applied to the holes. Additionally a glue spread inside the cutout for the high voltage connection circuit board at the side frame has to be protected from glue. Fitting teflon pieces are attached with clay into the cutout.

Special tools have been developed to ensure a well defined glue layer without unglued spots. The aluminum bars for the panel frame contain 0.8 mm grooves to enhance the gluing surface. Glue has to be distributed into the grooves, as the glue thickness of 0.2 mm for the first gluing step and 0.4 mm for the second gluing step is not sufficient to fill the full groove. To avoid a glue spilling over the bar's side surfaces, a gluing tool sliding along these surfaces is used, as shown in Figure 4.24a. The gluing tool has 0.8 mm wide contact surface with the bar gluing side to avoid a tilt of the tool.

For a uniform glue layer on the FR4 surface, spatulas with distance wires with the diameter of the desired glue thickness are used. The wires are routed around the spatula edge and fixed at holes in the spatula. In contrast to a standard toothed spatula, this ensures the constant glue thickness independent of the spatula tilt.

4.5.2 Second Production Step

The second production step starts after a curing time of ≈ 24 h after the first gluing. A quality control of the first gluing step has to be performed before the production can be continued. As a first step, the light-gap method is used to spot protruding parts on the surface of the half panel still sucked to vacuum table 1. If outliers are

found the salient material has to be ground or scratched off.

The thickness of the half panel is measured at 20 points along the panel edge with a micrometer screw during the transfer to vacuum table 2. The values have to be in the range of [10.43 mm, 10.83 mm]. If a lower thickness is measured, more glue has to be applied to the concerning spots. In the case of a larger thickness the panel needs to be thinned to ensure the final total panel thickness.

The grounding connection to all internal parts has to be ensured before the panel closing. Therefore, at least one grounding flag is established between the honeycomb sheets and each surrounding bar. A cell wall of the honeycomb is bend to touch the bar and the connection is fixed with cyanoacrylate glue. The honeycomb-bar-junction is covered with a conducting silver paint, which is sealed with the epoxy glue Araldite® 2012, which cures within 5 min. The paint guarded by the epoxy glue is applied to the junction of the parts of the gas distribution piece and the frame as well.

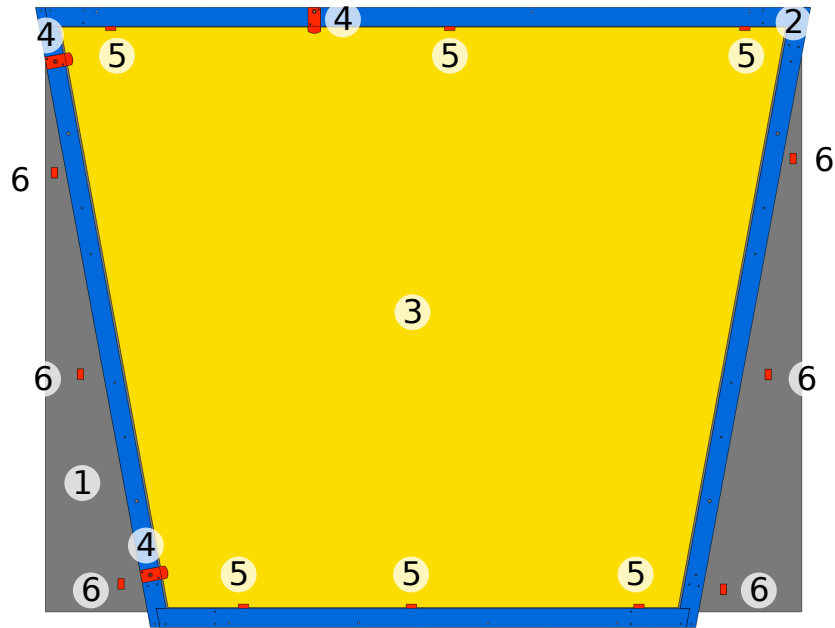
The two main challenges of the second gluing step are the relative positioning of the half panel from the first gluing step to the new FR4 surface and the uniform panel thickness.

The half panel is transferred and sucked to vacuum table 2. The junction between the FR4 and the vacuum table surface is sealed again with a line of 12 mm brown tape. As this fixes the panel to the vacuum table, which has to be lifted off after the whole panel is cured, a 0.4 mm diameter wire is attached next to the FR4 edge on the vacuum table. By pulling the wire, the gluing connection is broken and the vacuum table is deattached from the panel. Since the direct access to the panel is blocked by distance pieces on the inclined trapezoidal sides, the wire needs to be routed back along the side on top of the tape.

A new set of FR4 boards is positioned and sucked to vacuum table 1 as during the first construction step. Three special, thinner finger, with only one contact point for the panel frame are mounted to vacuum table 1 at the positions indicated in Figure 4.25. These three contact points define the position of the half panel sucked to vacuum table 2 relative to the FR4 layer sucked to vacuum table 1. Metal ropes tightened by tension locks are attached to vacuum table 2 to pull the half panel against the reference points.

The panel thickness is defined by brass distance pieces placed between the vacuum tables. The positioning of the distance pieces on the parallel sides can be seen in Figure 4.25. The contact of the distance pieces to vacuum table 2 is monitored. A electrical circuit is closed as soon as the distance pieces touch the upper vacuum table and the a LED lights up. Therefore the distance pieces are insulated from the lower vacuum table.

Due to the limited vacuum table size, the distance pieces cannot be placed directly on the vacuum table surface. Therefore they are enclosed in between the FR4 surfaces



- | | | | | | |
|---|-----------------------------|---|---|---|--|
| 1 | vacuum table 1 | 2 | alignment frame | 3 | FR4 boards |
| 4 | thin alignment fin-
gers | 5 | distance pieces be-
tween FR4 boards | 6 | distance piece on vac-
uum table surfaces |

Figure 4.25. Placement of the thinned alignment fingers as reference for the half panel on vacuum table 2 and placement of the distance pieces.

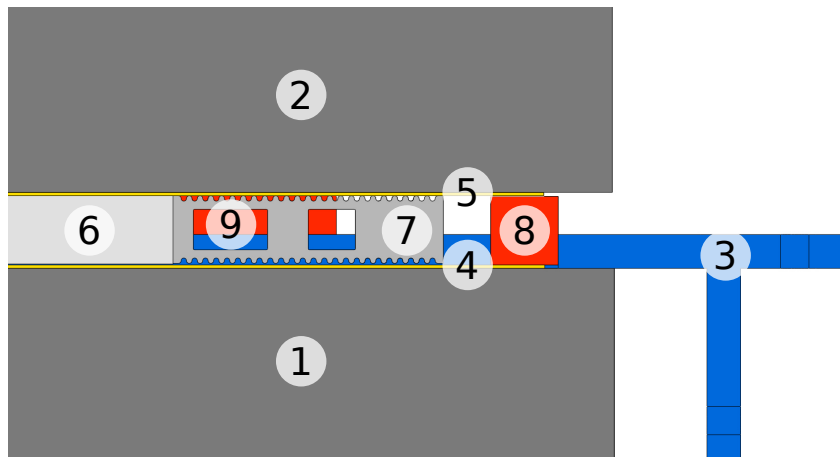
as it is shown in the cross section of the assembly in Figure 4.26. To retrieve the contact feed-back via the LED monitoring system a layer of copper tape is applied on the protrude surface of FR4 layer on vacuum table 2. The thickness of the copper tape and the brown tape for the vacuum sealing is encountered in the height of the distance pieces placed between FR4 surfaces.

4.5.3 Panel Finalization

After the gluing of the panel is finished an extensive quality control, described in Section 4.6.2, and final mechanical work follows.

The first step is the cutting of the projection FR4. As this is a dust intensive work, the panel is carried to a dedicated lab and the person involved in the cutting procedure have to wear an overall and a full face box respirator, where the face shield also serves as protection from fly around swarfs. The panel itself is protected by a foil cover from contamination.

The cutting is done with a thin plate on a low speed angle grinder. The cut side of the panel is clamped between two aluminum bars. These bars confine the panel to avoid a delamination due to mechanical forces during the cutting and the top bar serves as guidance of the angle grinder. The blade is guided with an inclination pointing towards the bar clamped 1 – 2 mm inside the panel. This ensures, that no



1	vacuum table 1	2	vacuum table 2	3	alignment frame
4	FR4 side 1	5	FR4 side 2	6	honeycomb
7	panel frame	8	distance piece between FR4 boards	9	distance piece on vacuum table surfaces

Figure 4.26. Cross section of a the mechanical model at the end of the second gluing step. Vacuum table 2, carrying the half panel from the first gluing step is supported in distance pieces.

material can stick out over the frames any more and that the machine can be guided safely without the danger of slipping off and damaging the panel side.

After the cutting, the panel sides are cleaned carefully from spill out glue and remnants of the sealing clay. A flat panel contour is important, as additional parts, as the zebra compression bar are mounted there.

The last mechanical work on the panel is the sealing of the gap between the single FR4 boards. Therefore a line of green tape is applied to each side of the gap serving as protection for the panel. Fast curing Araldite[®] 2012 is pressed with a perpendicular positioned syringe into the gap. The glue is flattened with a spatula on the tape which has the removed before the glue starts hardening. After a short curing time, when the glue is not yet completely hardener, the remaining glue part in the height of the tape is cut of with a sharp blade. If the correct moment in the curing process is caught, the cutting work with low force, while the glue does not stick to the blade.

4.5.4 Delamination Repair Procedure

During the start of the production phase and the training of the contributing people, some insufficient gluing processes, resulting in delamination on the second gluing side occurred. The problem was traced back to two problems related to the glue spreading. The most obvious reason is a non-uniform glue layer on the second gluing day. The problem was addressed by the construction of a more rigid spatula,

avoiding a bending of the material in the glue gap between the wires and additional training.

A second problem, also resulting in an increased thickness of the panel, was origin in a too generous spread of the glue on the panel frames in the first gluing step. The glue is pushed out to the panel side and was touching the top surface of the alignment fingers used for the positioning of the half panel during the closure in the second step. Therefore the fingers have been thinned in the front part and the glue spread on the bars was monitored more carefully.

A repair procedure was developed to inject glue into the panel at delaminated spots. The idea of the procedure is to inject glue through the panel surface and ensure the surface flatness by sucking the panel to a vacuum table with the glued side facing down. The holes are closed by a layer of brown tape, which is also used as a gasket at the panel vacuum table border. In the case where additional infrastructure, as the mesh frame, was already mounted to the panel surface, a small vacuum table was used at the delaminated area and the rest for the panel was supported by distance pieces.

1.2 mm holes are drilled in a grid of 20 mm × 20 mm through the delaminated surface protected by green tape. A pneumatic glue dispensing setup was built. The compressed air is pulsed with a Festo magnet valve MHE3 in reverse operation to the glue in a syringe with a short 0.84 mm needle. The driving signal of the valve is generated by the signal generator ELV UPG 100 and transformed to the valve's power consumption by a solid state relay CMX60D5. The experience showed that 150 – 200 cycles of a 27 Hz signal which opens the valve for 13 ms inject enough glue to fill three quarters of a honeycomb cell. As the glue is injected from the delaminated side, it has to be ensured that it will flow back when the panel is flipped over to be sucked to the vacuum table. To allow for a better glue flow, the symmetry of the glue sunk to the bottom of the cell is broken by turning the panel for ≈ 5 min in vertical position before placing it on the vacuum table.

To ensure a flat surface when attaching the panel to the vacuum table, glue spill is removed with the green tape and fins from the drilling are removed with a flat scraper before the holes are sealed with the brown tape.

After the curing the holes on a cathode surface are inspected with a microscope and if air bubble enclosures are found, which might lead to a leakage to the inside of the panel they are sealed with a drop of glue formed by a single cycle of the glue dispenser. After the sealing, the protrude part of the glue drop is cut off with a sharp blade and the repaired surface is flattened by wet sanding with sandpaper of grain size 800.

4.6 Quality Control Methods

This section describes the quality control methods and results of the ATLAS New Small Wheel drift panel construction. In Section 4.6.1 a brief introduction to the database structure and the interface developed for the database management is given. Section 4.6.2 focuses on the quality control of the panel raw material and Section 4.6.3 on the quality control of the finished panels. Two panel control methods, namely the flatness scans and the gas tightness measurements are discussed in more detail in Section 4.6.4 and Section 4.6.5, respectively.

4.6.1 Database and Interface

The New Small Wheel Upgrade is an international project, which requires the tracking of the numerous components and the necessity to commonly store and save the quality control results. Therefore two database, hosted at CERN are implemented. The tracking database hosts the information on the location of parts. A parenting is applied to components integrate in assemblies.

The central database stores the results from the quality control of all components down to the level of single parts. This allows to trace back problems in the final detector or subcomponents.

An independent database was developed at the construction site, which interfaces both databases at CERN. The standalone system allowed for a flexible development unconstrained from the status of the central databases. The outline for the development was the idea to create a platform independent framework, which works without a network connection and features the parallel work on several machines. Therefore a python Kivy [92] GUI was implemented with a sqlite back-end. A sqlite database is stored in a file on the local machine. For the exchange between several machines, a export method to a sqlite file in a cloud storage was set up. During the export the changes are merged according to the latest data update.

The GUI main panel (see Figure 4.27) is divided in a navigation panel on the left and an overview of the available material of the selected type structured by their production status. The interface provides the possibility to retrieve data from the logistics database and export parentings of the assembled parts. The measurement results can be exported to the central database and an overview of all panel quality control measurements as well as a collection of all measurement related to each panel can be created (example in the appendix in A.2.6). The quality control measurement of the raw material and the panels can be entered and analyzed from the interface. A detailed description on the functionality of the database interface is given the database manual attached in the appendix in Section A.2.3.

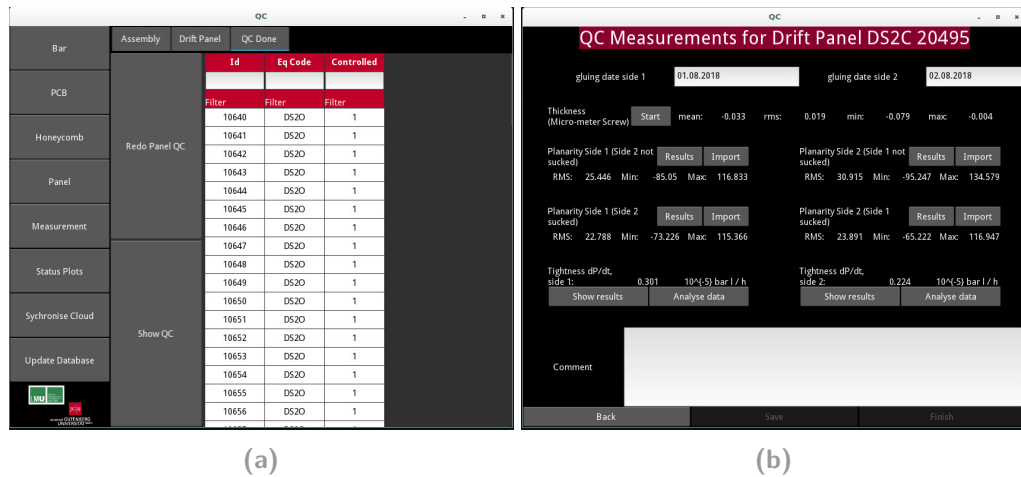


Figure 4.27. Screenshots of the GUI interface to the local database. The main panel is shown in (a) and the panel for the input of the panel quality control measurements in (b).

4.6.2 Raw Material Quality Control

To guarantee the bare drift panel quality, the raw material has to undergo an extensive quality control. The small components as the gas inlet, the interconnection reinforcement piece and the HV feed-through are produced by partners in the collaboration and are checked on a sampling base for the geometrical dimensions. The gas inlet is checked for tightness after the gluing of the gas pipe to the cylindrical manifold by applying ≈ 5 bar overpressure and observing for leaking bubbles in a bath of pure water.

The large components, produced in industry, are checked piece by piece and the quality control results are stored in the database. In the following an overview of the implemented quality control methods and results for all checked materials is provided. As the in plane dimension of the material are implicitly checked during the construction by the referencing in the surrounding alignment frame, the values of interest for the quality control are the material thickness to guaranty the panel thickness and planarity. An overview of the thickness specifications and their impact in the panel geometry is shown in Figure 4.28. The possible thickness variations give the motivation for the larger glue gap in the second gluing step.

4.6.2 Board Quality Control

The thickness of the boards is measured with a micrometer screw (measurement error: $4 \mu\text{m}$) at 20 points uniformly distributed along the border of the boards. As for some boards the copper extends until the edge, the deviation to the nominal value (0.538 mm on copper and 0.52 mm on bare FR4) is stored for a better comparison. The distribution of the measurement values of all measurements is shown in Figure 4.29a. The maximal measured deviation from the nominal thickness is less than half of the value of the specification. This allows to relax the requirements on

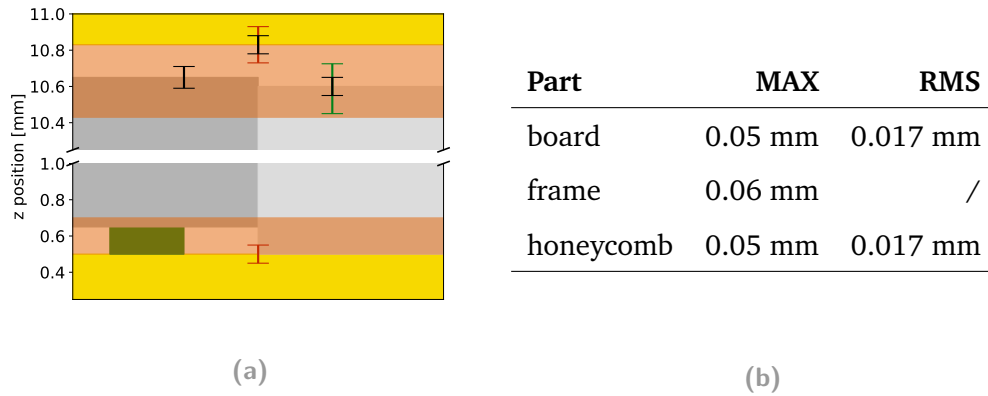


Figure 4.28. ATLAS New Small Wheel specifications of the drift panel parts (b) and their impact on the panel production procedure (a). The plot shows a panel cross section with the boards indicated in yellow, the frames in gray and the honeycomb in light gray. The frames are supported on a $150\mu\text{m}$ double layer of green tape to center them in the panel. The impact of the part's thickness variations is indicated in the second glue gap (top), where due to the confinement of the panel height by the vacuum table distance, a sufficient glue thickness is necessary. The possible variation of the lower board is transferred to the upper glue gap. The thickness of the glue layers is indicated by the orange area. As the variation of the boards was found to be only half of the required value, the acceptance criteria for the honeycomb pieces could be relaxed to $+0.125\text{ mm}$ and -0.15 mm , indicated by the green arrow bars.

the other components, like the honeycomb, while still achieving the same drift panel quality.

4.6.2 Honeycomb Quality Control

The thickness of the honeycomb sheets was measured in a grid of $10\text{ mm} \times 10\text{ mm}$ with a depth micrometer (measurement error: $10\mu\text{m}$). The rest of the tool is pressed on the walls of the honeycomb sheet laying on a flat surface and the probe is stuck through the cells to the supporting surface. It has to be ensured, that the honeycomb sheet is pressed against the surface at the measured position to avoid an influence of the honeycomb bending on the measurement. The bending is corrected by the vacuum bag during the construction.

An overview of all measurements is shown in Figure 4.29b. The distribution is clearly peaking at the nominal thickness of 10.1 mm a second peak at values around 9.9 mm is most likely due to a mis-calibration of the measurement tool during the data taking.

4.6.2 Frame Quality Control

The thickness of the frames is controlled by a template test. The schematic test is shown in Figure 4.30a. The template has the bridge like shape and is slid over the frame. Two templates, each with a gap of exactly the frame height at the specification limits ($(10.00 \pm 0.06)\text{ mm}$) are available. The electrical contact between the template and the frame is monitored with an ohmmeter. The lower limit template

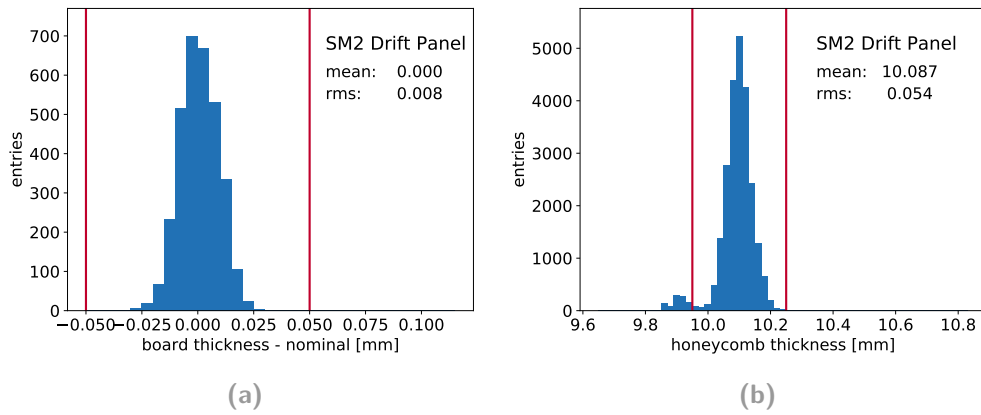


Figure 4.29. Overview for all measured values for the board (a) and honeycomb (b) quality control. The specification limits are indicated by the red lines, where in case of the honeycomb thickness measurement the relaxed values are chosen.

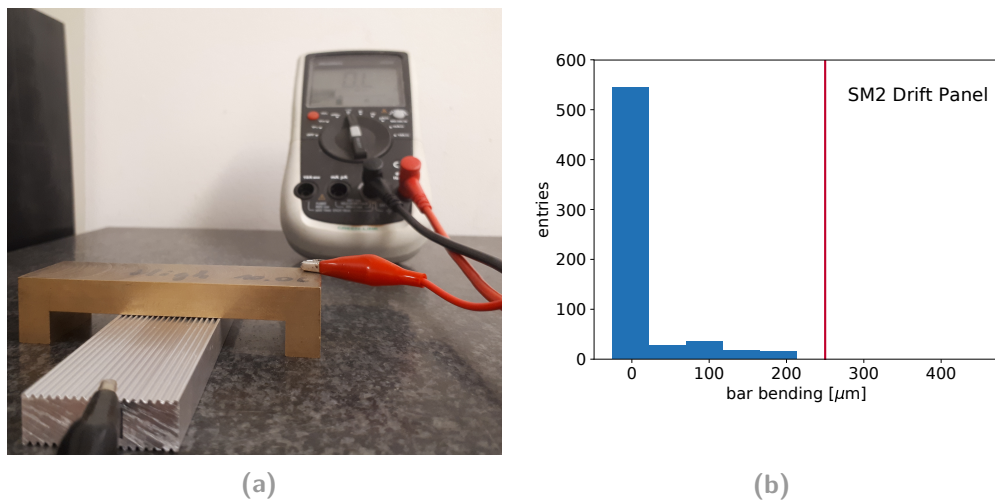


Figure 4.30. Picture of the principle of the frame thickness quality control (a) and result of the frame bending test (b).

should show a permanent contact, while the upper limit template should never show a contact. All frames passed the template test.

Additionally, the in-plane bending of the frame was monitored. As frames define the shape of the final panel, a distortion would be translated. Therefore the frames are placed in both orientations with the thin side down on a precise surface and the potential gap between the frame and the surface and the frame is mapped with a thickness gauge in steps of $50\ \mu\text{m}$. The result is shown in Figure 4.30b. It is visible, that all frames are below the limit of $250\ \mu\text{m}$ and most bars do not show any bending.

4.6.3 Drift Panel Quality Control

The ATLAS New Small Wheel collaboration poses several requirements on the bare drift panels. The maximal allowed thickness and planarity deviation is $\pm 110\ \mu\text{m}$ ($RMS < 37\ \mu\text{m}$) and the pressure loss on the panel surface has to be less than

$1 \times 10^{-5} \text{ bar L h}^{-1}$ at 3 mbar overpressure.

To test the panels for these requirements, an extensive measurement campaign has been conducted. The thickness variation and the planarity are scanned with a laser triangulation sensor mounted to the positioning system on the high planarity granite table. Each side of the panel is measured twice, once sucked to the granite table and once floating on the table. As the panel is sucked to the table, its downside follows the table surface. Therefore deviations on the top panel surface originate in a thickness variation. The floating measurement in contrast examines the pure panel planarity including deformations due to internal stress. An overview of the measurement principle, a characterization of the measurement system and a discussion of the production results is given in Section 4.6.4.

The absolute panel thickness cannot be estimated from the scan of the sucked panel, as the panel has to be placed on a plastic mesh for the vacuum distribution, leading to an unknown contribution to the thickness. As a calibration leads to propagating errors worsening the measurement resolution, a different approach was chosen to measure the panel's absolute thickness. Like for the board quality control, a measurement is taken along the panel periphery at 24 points with a micrometer screw. The result of the measurement for the full production is shown in Figure 4.31.

The plots show that most of the panels fulfill the requirements. Panels with larger deviations mainly occurred during the learning phase at the production start. These panels show a larger thickness at the long side, with an excess toward the corner facing to reference fingers in the second gluing step. It was found that redundant glue from the first construction day, forming a solid bulge at the frame side sits on the top of the alignment finger. By thinning the alignment finger, the problem could be solved.

The gas tightness of the panels is measured with a dedicated setup. The measurement setup and the results are presented in Section 4.6.5

4.6.4 Planarity Measurements

The measurement system is mounted on a granite table with a surface planarity better than $14 \mu\text{m}$ (DIN 876 0) as shown in Figure 4.32. The positioning system consists of two parallel Y -axis parallel to the long side of the table which are operated in gantry mode and carry the X -axis as a bridge. The Z -axis is mounted to the bridge and holds the laser triangulation sensor for the surface planarity measurement. The system provides a repeatability of $20 \mu\text{m}$ in all axes.

While the Y movement range is sufficiently large for the measurement of the drift panel geometry, the movement in X is limited by the space between the support rails (1420 mm) and the width of the Z axis to 1260 mm. To extend the range to measure the full panel surface a mount which allows for a sensor displacement of 80 mm in

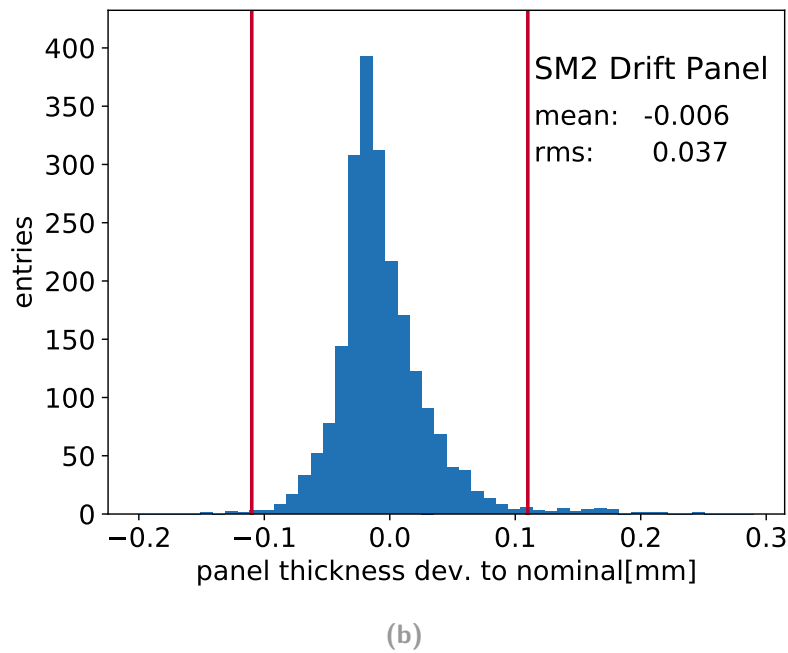
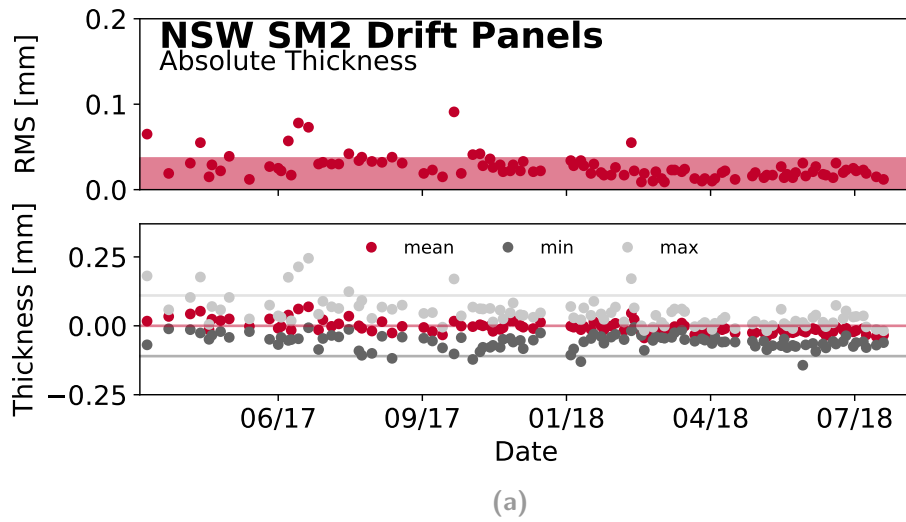


Figure 4.31. Result of the panels absolute thickness. (a) shows the thickness of each panel, sorted by the production date. The limits for the absolute deviation is indicated by the gray lines in the lower plot, while the required region of the RMS values is shaded in red. (a) is a histogram of all single measurements.

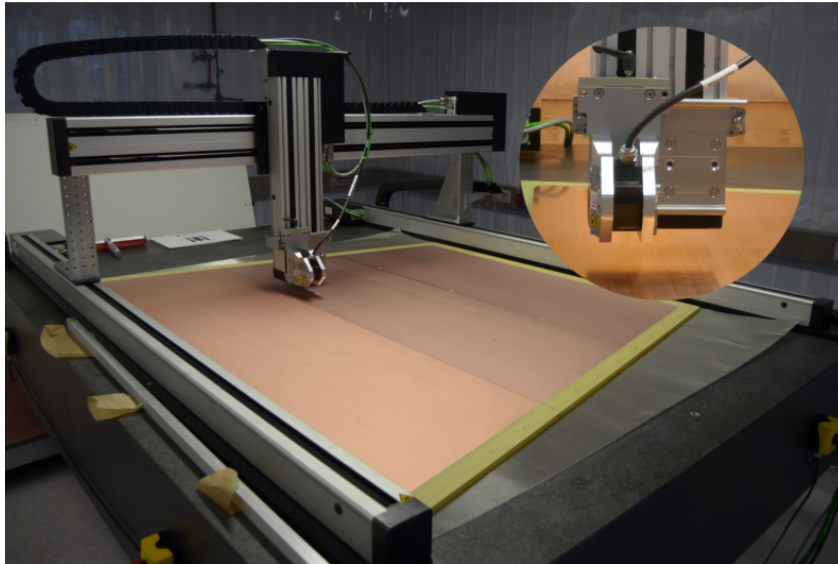


Figure 4.32. 3D positioning system mounted on the granite table. The laser triangulation sensor is mounted to the vertical axis of the system (detail).

X was attached. The final scan of the full surface is composed of two individual scans of both sensor positions. In the overlap region of the scans, the average of both is calculated.

4.6.4 Measurement Strategy

The measurements are taken in a grid of $20\text{ mm} \times 20\text{ mm}$. The positioning system moves to the measured point and after a waiting time of 500 ms to stabilize vibrations from the movement, ≈ 200 values are taken at 20 kHz readout rate. The average of the single measurement give the value for the distance of the workpiece to the laser sensor.

An overview on the analysis procedure of the scans is give in Figure 4.33 using the measurement of vacuum table B as example. As the distance from the workpiece to the sensor is recorded, the measurement is biased by a displacement of the laser sensor due to a mechanical deformation of the positioning system. The main source is the gravitational sag of the bridge with an amplitude of $\approx 500\mu\text{m}$, which is superposed by oscillations along the Y axis due to the mechanical support of the mandrel carrying the bridge. These effects are corrected by subtracting a reference measurement of the granite table surface from the measurement of the workpiece. To extract the planarity from the difference of the measurements, the deviation to a fitted plane is calculated. If no parallelism of the plane to the granite table surface is required during the fit, the pure planarity of the workpiece's top surface is measured. This procedure is used for the planarity measurement of the vacuum tables, as their thickness is not ensured to be uniform by construction.

For the measurement of the panel planarity and thickness deviation, the plane is

confined to be parallel to the granite table surface. Thus the measurement states the deviation to the ideal case of flat panel with parallel surfaces.

4.6.4 Characterization of the Measurement System

To characterize the measurement system and to estimate its stability, all reference scans of the granite table have been analyzed. The first study is the examination of the oscillations during the data taking at a single point. A typical oscillation structure is shown in Figure 4.34a. The pattern comes from the vibrations of the machine and the constant position adjustment of the servomotor. It can be described by the product of a cosine with an exponential decay. The measurement value v in dependence of the time t is given by

$$v(t) = A \exp(-t/t_{\text{decay}}) \cos(t/t_{\text{oszi}} + \phi) + v_0,$$

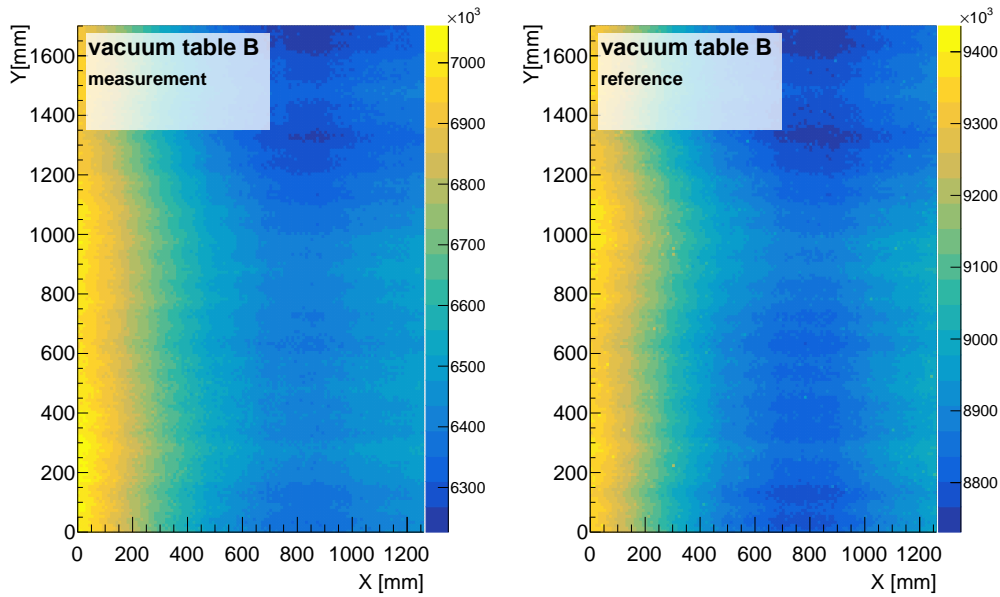
with the amplitude A , the decay constant t_{decay} , the periodicity t_{oszi} , an arbitrary phase ϕ encountered for the start of the data taking with respect to the oscillation pattern and a constant offset v_0 , which could be seen as the measurement value at this point of the scan.

The evolution of amplitude, the decay time and the periodicity of the oscillations is shown in Figure 4.34. The measurements have been stopped for a renovation of the lab in summer 2016. During that time an air conditioning system was installed, to stabilize the temperature to ± 1 °C. No change was observed in the oscillation pattern after the renovation and no significant overall time dependence can be observed.

The second study performed on the granite table reference runs is the direct comparison of single runs. As the granite table surface can be considered as stable, the RMS of the difference of two reference runs give the single point resolution of the measurement system.

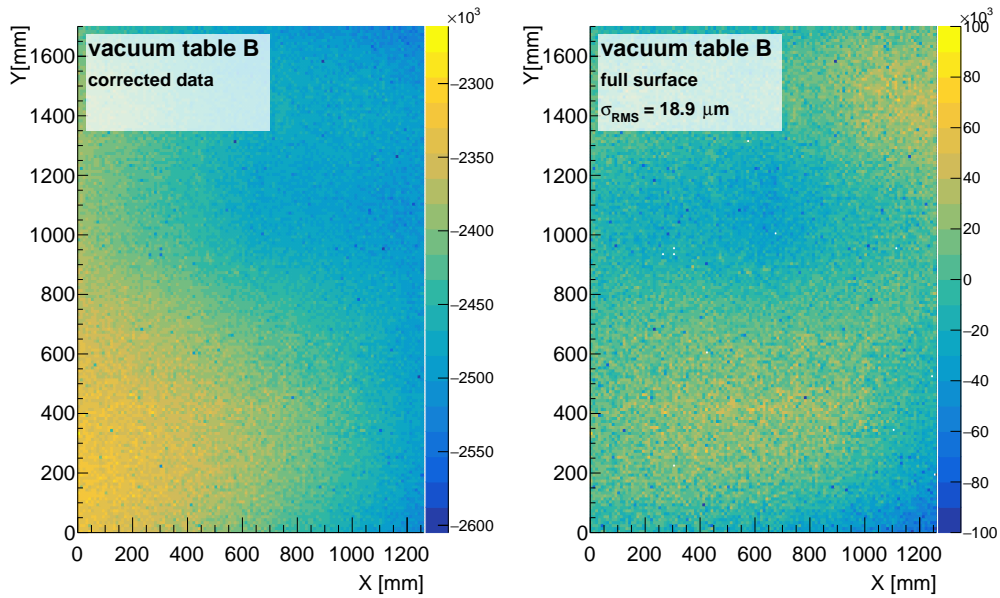
A comparison of all reference runs is presented in Figure 4.35a. The comparison is grouped in three phases. During the first phase, the shift-able sensor mount was not yet installed. Phase 2 covers the time of the vacuum table and prototype panel construction. The production of the series drift panels falls in phase 3. It is visible, that the RMS gets larger the more time lays between the measurements. This effect is most pronounced during the production phase, as, in contrast to phase 1, the temperature was stabilized and in contrast to phase 1 and 2 all infrastructural work on the setup of the production facility was finished and no external disturbances occurred any more. Therefore also larger deviations occur for short time differences in the first two phases.

The dependence of the RMS on the time between runs is shown in Figure 4.35b for the last phase. A clear worsening of the resolution is visible for large time periods between the single runs. The ideal resolution of $\approx 5 \mu\text{m}$ found for the difference



(a)

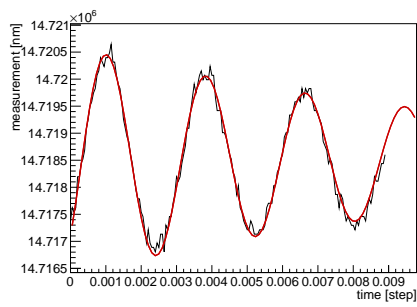
(b)



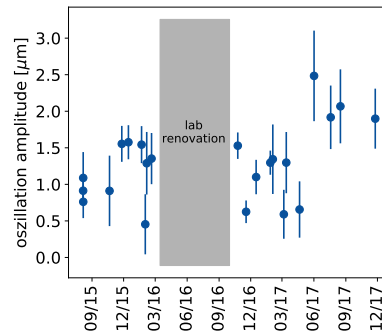
(c)

(d)

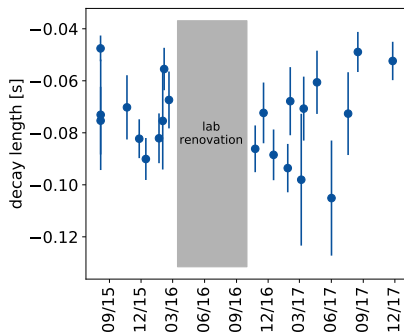
Figure 4.33. Overview of the measurement principle. A reference run (b) is subtracted from the measurement (a) to encounter for deformations of the measurement system. The deviation of the difference (c) to a fitted plane gives the planarity measurement (d). The measurement values encoded in the color scale are the workpiece's distance to the laser sensor in nanometer.



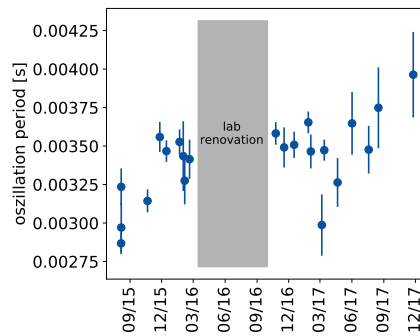
(a)



(b)



(c)



(d)

Figure 4.34. Oscillation of the sensor measurement. The time evolution over the single measurements recorded with laser sensor is shown in (a). The mean of the distribution of the three main fit parameters for each run is plotted in (b-d).

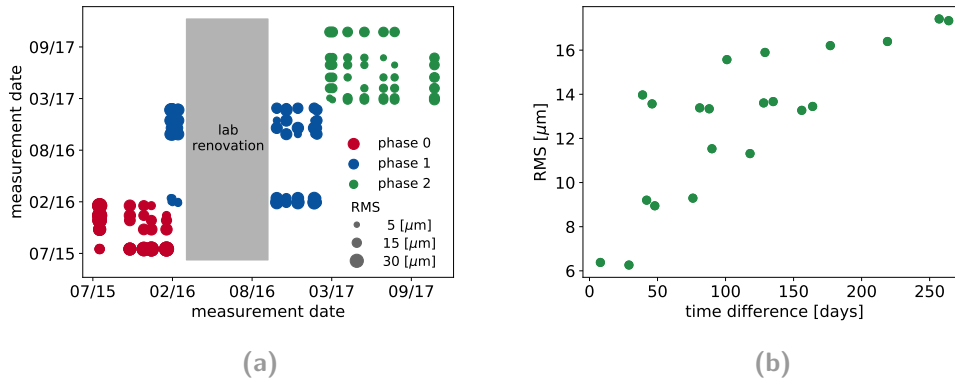


Figure 4.35. Comparison of granite table reference measurement for the full project time. (a) shows RMS of the difference of two measurements. The value is encoded in the point size. The measurements are grouped by different project phases. Phase 1 are measurements with an old sensor mount. Phase 2 are the measurement with the new sensor mount during the vacuum table and prototype panel construction. Phase 3 is the period of the ATLAS New Small Wheel drift panel production. The dependence of the RMS on the time difference between the measurements is shown in (b) for the production phase.

of scans performed on the same day can only be achieved if the time difference between the single runs is less than one month. This underlies the importance of regular reference runs.

4.6.4 Production Results

An overview of the planarity of all produced panels is presented in Figure 4.36. The overview histogram shows that more than 95% of the panels fulfill the requirements on the thickness variation, estimated with the planarity scan of the panel sucked to the granite table. As it is visible in the time dependence of the results shown in Figure 4.37, most panels which lay outside the specifications are produced in the first third of the production, suffering from the learning phase. The panel with a high thickness deviations are the panels, which show the problems in the measurement of the absolute thickness. As explained, the source of the problem is the hardened redundant glue sitting on the alignment fingers during the second gluing. These panels suffered as well from unglued spot and have been repaired following the procedure described in Section 4.5.4.

Despite the few panels with large RMS the time series of the quality control shows, that the production was running smooth, without major issues in the second half. The consideration of the minimum and maximum value in the lower plots of Figure 4.37 shows more points close or slightly over the specifications than the distribution of the RMS values. This is not of major concern, as the results have not been corrected for the resolution of the measurement system. As single values, the minimum and maximum value are biased by the measurement system resolution of $> 5 \mu\text{m}$, which

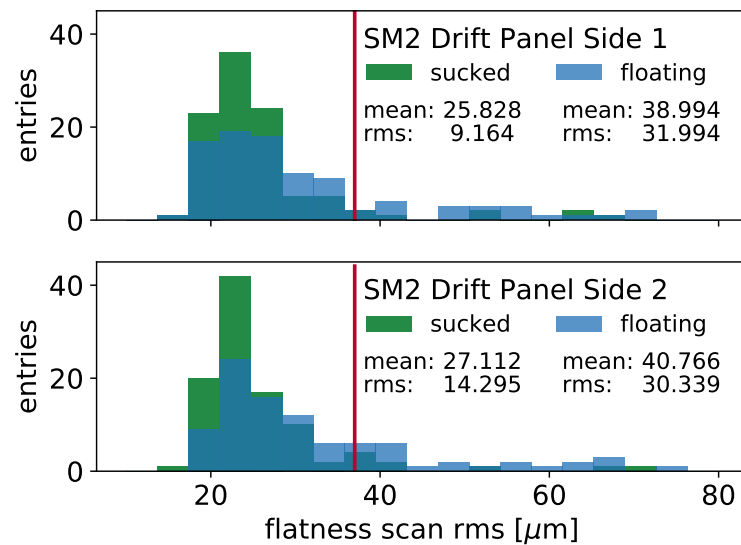
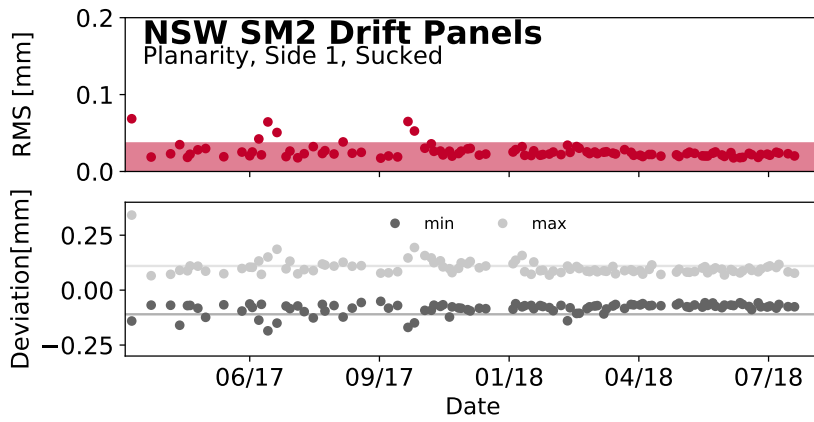


Figure 4.36. Histogram of the results of the planarity scan for all produced panels. The results for the first and second gluing side are presented in the upper and lower histogram, respectively. The ATLAS New Small Wheel collaboration limit for the RMS is indicated by the red line.

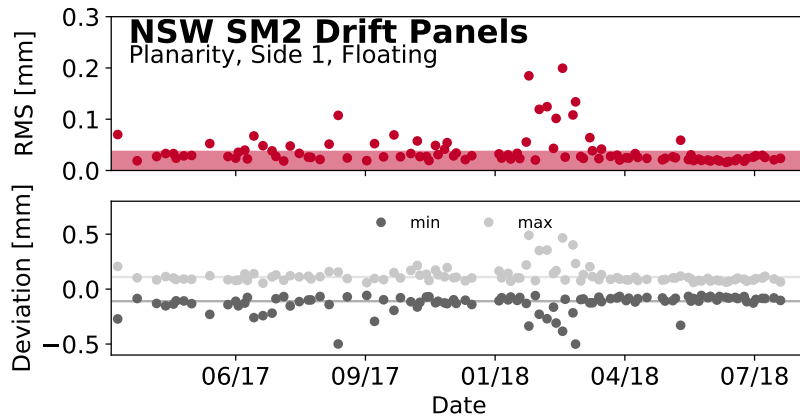
translates to a 1 % effect at the acceptance limit.

The planarity measurement of the panels floating on the granite table shows several excesses over the specification. The deviations are, besides the already known issues from the sucked measurement, only found for outer panels. The reason for that was found in the expansion of the bare FR4 skins. As discussed, FR4 expands under the absorption of humidity. The copper coating of the cathode boards prevents a humidity absorption in the subjacent FR4 in the cathode side of the panels. As the detector outside is, by design for a cost reduction, not protected by copper, the full surface can absorb water. The single sided expansion of the panel surface imposes a bowl shape structure to the panel, as shown in Figure 4.38. The plots shows a scan of both sides of an outer panel. The distance to the laser sensor is encoded in the color scheme of the histogram filling. Therefore, lower values correspond to a bending of the panel towards the sensor. The panel is bending toward the cathode side, as the opposite outer side expands.

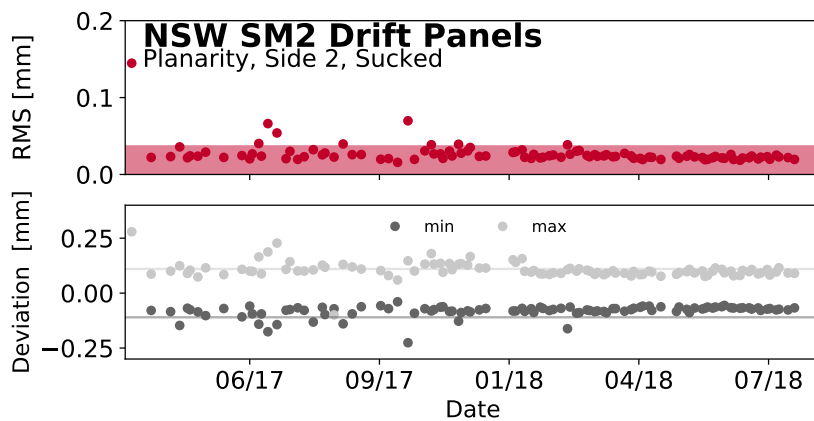
This effect can be corrected with little force, as the effect is not visible in the sucked measurement. Therefore it can be safely assumed that the effect will be corrected once the panel is confined by the 50 assembly screws on the panel periphery and the six interconnection in the active area during the quadruplet assembly and the deviation is no reason for a rejection of the panels.



(a)



(b)



(c)

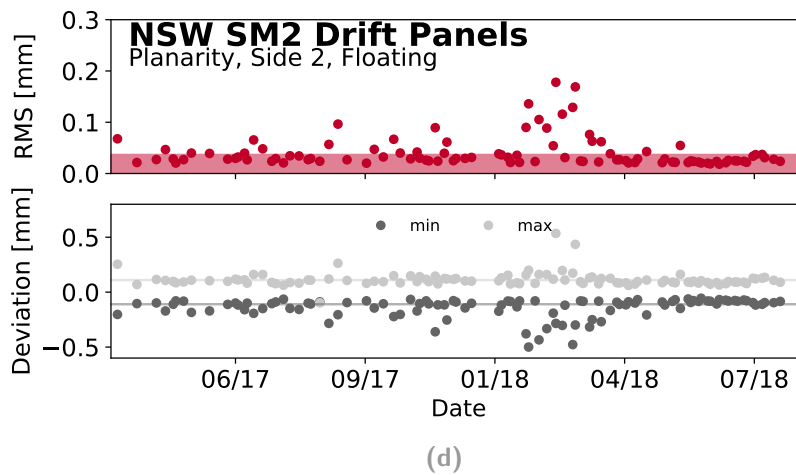


Figure 4.37. Results of the planarity measurement for both sides of all panels. The results from the measurement of the panel sucked to the granite table for the thickness variation estimation and the measurement of the panel floating on the granite table surface are shown. The upper plot for each setting displays the RMS of the distribution where the allowed range is indicated by the shaded red area. The lower plot shows the minimal and maximal values, where the corresponding limits are indicated by a solid line.

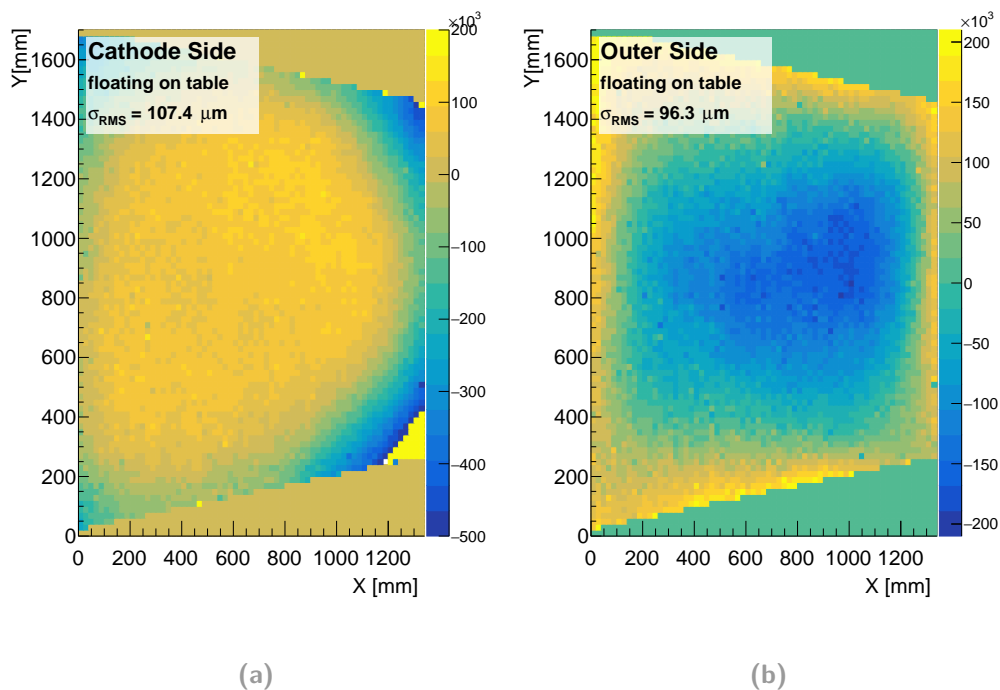


Figure 4.38. Planarity scan of an outer panel floating on the granite table. The bowl shape induced by the expansion of the bare FR4 outer skins is clearly visible. The color scale of the histogram represents the distance to the laser triangulation sensor in nanometer. The yellow area at the small side of the panel in (a), corresponds to an area, where the panel surface lays outside the sensor range.

4.6.5 Gas Tightness Measurement

The tightness of the final quadruplets is essential to avoid a contamination of the gas mixture by permeating air. A change in the gas composition can lead to a degeneration of the detector performance and a potential damage due to the depositions. Therefore the tightness of the components needs to be tested. For the drift panels this requires, that the cathode surface needs to be tight and well fitting to the o-ring gasket. A possible weakness is the gap between the single board. Therefore this gap is sealed with glue. A dedicated test stand was designed, where the pressure drop inside a gas gap to a reference back-end, simulating a readout panel, is measured. The mechanical design of the test stand is described in Section 4.6.5.1. The measurement principle is explained in Section 4.6.5.2 and a calibration procedure for the volume expansion due to a bending of the panel surface with overpressure is presented in Section 4.6.5.3 followed by a estimation of the measurement error in Section 4.6.5.4. In Section 4.6.5.5 the tightness results for all produced drift panels are shown.

4.6.5 Mechanical Design of the Test Stand

To check the tightness of a bare drift panel, a gas volume in the geometry of the quadruplet has been confined on top of the cathode surface. This volume is enclosed by an EPDM o-ring to ensure the gas tightness. In the quadruplet, the o-ring is confined in a groove between the mesh and the gas gap frame, which are screwed to the drift panel.

As the mounting holes will be drilled on a CNC machine at the Munich construction site, the option to mount the frames is not possible after the production in Mainz. Therefore a back-end, which host the frames was build from a panel glued for test purposes. The tightness of the back-end is ensured by a generous spread of glue over the gap between the single boards. Therefore a pressure loss in the gas gap comes from imperfections on the panel under test.

The back-end, which also hosts the connection for the gas inlet and the pressure monitoring, is fixed on a stand, build of extruded aluminum profiles. The construction drawing of the stand can be seen in Figure 4.39a.

The back-end is slightly inclined, such that the panel under test leans against it. Like that the panel, which is supported on rails on the down side (Figure 4.39b), is stable on the test stand, even without a fixation.

The panel has to be pressed against the back-end to compress the o-ring and establish it's tightening. Since also the holes for the assembly screws are not yet machined in the bare panel, this option cannot be used to close the gas gap. Therefore the stand was equipped with quick release clamps (Figure 4.39c). This does not only provide the necessary pressure for the o-ring compression, but also allows for a quick exchange of the tested panel.

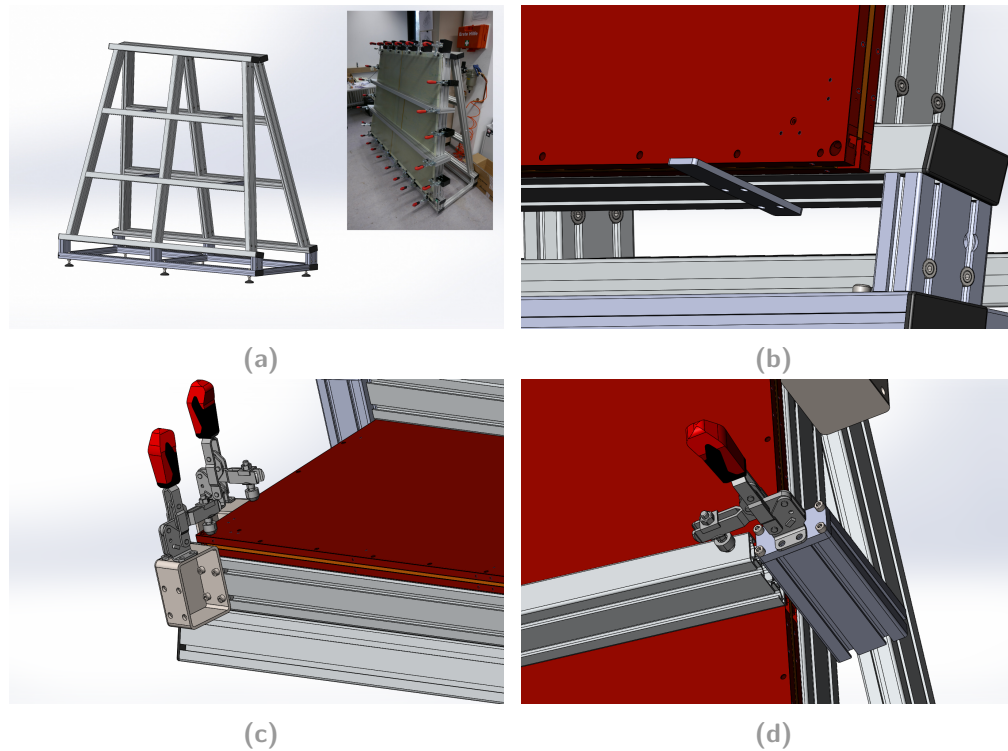


Figure 4.39. Design of the gas test stand. The frame support structure (a), the support for the attached panel (b), the clamping of the panel sandwich (c) and the bar preventing the panel blow up (d) are shown.

To avoid a deformation of the sandwich, the back structure of the stand was built from 80 mm thick bars and a set of two bars was clamped to the front of the panel (Figure 4.39d). This confines the panel deformation sufficient to rule out a damage of the panel's internal structure. In a quadruplet, this confinement is ensured by the six interconnections. A residual volume expansion is corrected in the analysis of the gas test data, as described in Section 4.6.5.3.

4.6.5 Measurement Principle

The measurement principle of the gas tightness is the evaluation of the pressure drop inside the gas volume starting at 3 mbar overpressure. Figure 4.40 shows a sketch of the setup used to perform the gas tightness measurements. The test stand is connected to a pressured nitrogen bottle. As start condition and during the mounting of the panel to the test stand, valve 3 is opened to keep the gas volume at atmospheric pressure. This valve is closed and the connection to the compressed nitrogen is opened through valve 1 and 2. The flow to the panel is limited to 10 l h^{-1} to slowly build up the pressure in the volume. A branch of the gas input line is rested in a bubbler. 3 cm water level over the gas outlet in the water require 3 mbar overpressure, before the gas bubbles can emerge from the gas line. The beginning bubbles in the water are a sign that the desired overpressure is reached in the input line can be closed. Besides the leaking gas in the bubbler stops a further pressure raise in the gas volume, such acting as safety valve.

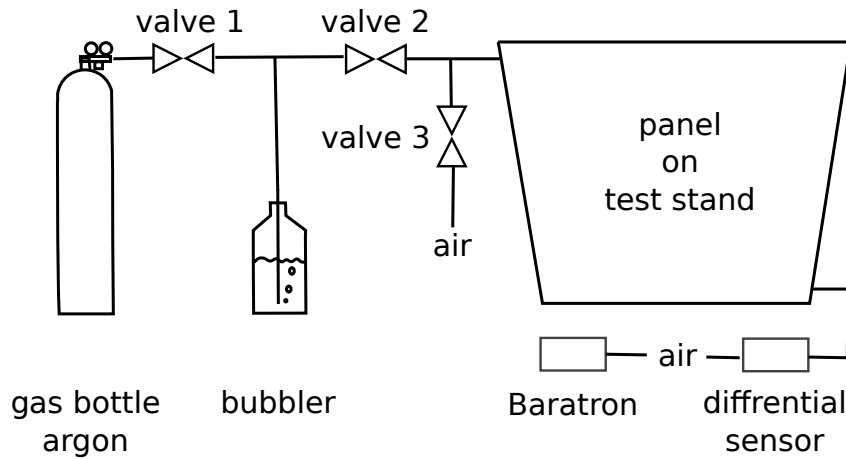


Figure 4.40. Sketch of the setup used for the drift panel gas tightness measurement.

The pressure drop in the panel is recorded with a digital differential pressure sensor HCLA12X5EU to measure the pressure difference to atmospheric pressure. The atmospheric pressure is recorded during the test with a MKS Baratron[®] 690A17TRB. Additionally the temperature inside the gas volume is monitored by five uniformly distributed digital temperature sensor of the type DS18B20

The differential pressure measurement relative to atmospheric provides a direct correction for the influence of atmospheric pressure changes, as it can be assumed in a first approximation that they are directly transferred over the flexibility of the panel surface into the gas volume. Residual effects are taken into account in the measurement error, as discussed in Section 4.6.5.4. The measurement of the atmospheric pressure is necessary to convert the differential to an absolute pressure for the application of the ideal gas law. Using this, the gas leak, as a loss of gas molecules nk , can be described as:

$$nk = \frac{pV}{T},$$

with the pressure p being the value of the differential sensor plus the atmospheric pressure measured at the beginning of the measurement, the gas volume V and the temperature T , measured as the average value of all five temperature sensors. The volume V consist of the geometrical volume $V_0 = 9.991$ for a gas gap between a perfectly flat panel and a volume expansion dV due to the blow up with overpressure. The volume expansion estimation is described in Section 4.6.5.3.

The particle loss is fitted with an exponential decay I_a . To state the volume loss per time at 3 mbar overpressure the slope is evaluated at this pressure value.

4.6.5 Calibration for Volume Expansion

Even though the panel surface is confined by two aluminum bars clamped to the top, a significant blow up is measured. This effect was estimated with a test panel during

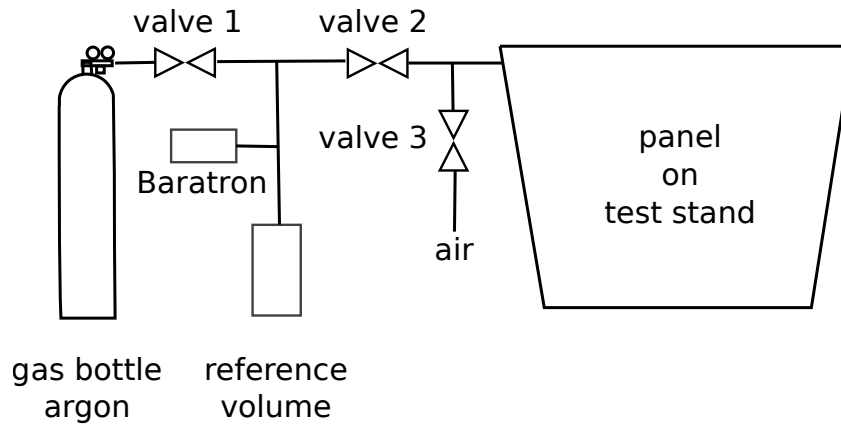


Figure 4.41. Sketch of the setup used for the volume expansion calibration of the drift panel gas tightness measurement.

the prototype construction. The result is shown in Figure 4.42a. The deformation was measured in the middle of the panel for a panel with and without confinement of a external bar. The plot shows that the panel deforms $\approx 0.7 \text{ mm mbar}^{-1}$. The bars on the panel surface reduce the effect to 0.1 mm mbar^{-1} , which is not expected to harm the panel structure. Still, the induced volume expansion is not negligible and need to be calibrated.

As the geometrical shape of the expansion cannot be easily estimated due to the bar confinement, a calibration measurement was performed. A sketch of the setup used for the volume expansion calibration is given in Figure 4.41. A $V_{ref} = 4.03 \text{ l}$ reference volume was filled with a fixed pressure p_1 . The pressure is recorded with the Baratron[®], as it provides a high accuracy over a large pressure range. A valve to the panel volume is opened and the pressure p_2 after a stable equilibrium is established is recorded again. As the measurement does not take a long time, atmospheric pressure and temperature changes can be neglected. Furthermore it is assumed, that the gas loss due to a leakage is negligible. This results in the equilibrium equation

$$p_1 V_{ref} = p_2 (V_{ref} + V_0 + dV),$$

which can be solved for the volume change dV . Plotting the volume change against the overpressure in the panel, a calibration curve is taken. This was done with a combined linear fit to the data of two different panels tested with the described procedure. The fitting range was chosen between 1 mbar and 4 mbar overpressure, as below 1 mbar a change in the slope is observed. With raising pressure, the volume expands first more, as the panel is pressed against the bars. After the contact is established, the bars slow down the further expansion. The result is shown in Figure 4.42b.

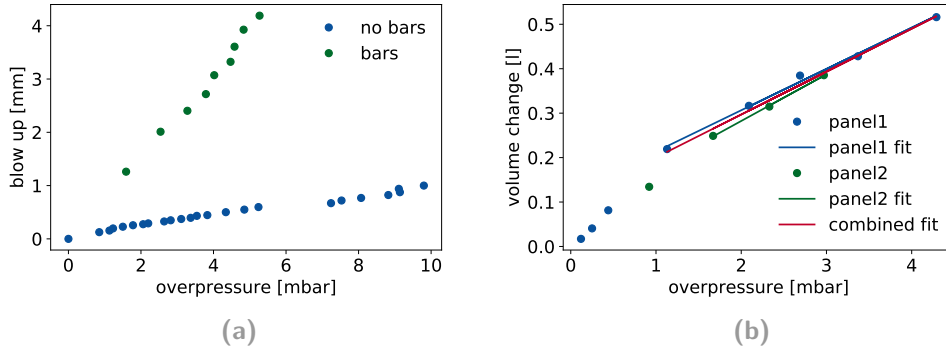


Figure 4.42. The comparison of the deformation of the panel with overpressure with and without confining bars on the panel (a) underlines the necessity of a calibration for the volume expansion (b).

4.6.5 Error Estimation

To estimate the error of the correction procedure for temperature and pressure changes a long term measurement was performed. The gas volume was closed at atmospheric pressure. Pressure changes now can only occur due to the change of the ambient conditions. The data recorded with the differential pressure sensor is shown in Figure 4.43a and the change of the atmospheric pressure is given in Figure 4.43c. The atmospheric pressure raise of 6 mbar over the full measurement period is not visible in the differential data. This underlines that the atmospheric pressure change is directly transferred to the gas volume with the panel itself acting as membrane. The differential pressure data shows a oscillatory pattern with ≈ 2 h time period. The same pattern is found in the temperature distribution shown in Figure 4.43b. The temperature changes are induced by the cycles of the air conditioning system. The residual deviation of the gas loss nk is shown in Figure 4.43d. The width of the distribution of $0.018 \times 10^{-3} \text{ Pa m}^3 \text{ K}^{-1}$ is taken as error on the gas loss in the analysis of the pressure drop data.

4.6.5 Production Results

An example for a gas tightness measurement is shown in Figure 4.44a. In the upper plot, the gas loss pV/T is shown together with the experimental fit. The plot in the middle shows the deviation of the data to the fit. A good agreement is found within the error bars. As comparison, the recorded temperature is shown in the lower plot. No significant residual effect from temperature changes on the gas loss distribution can be observed.

An overview of all results from the production is given in Figure 4.44b. It shows, that the ATLAS collaboration limit for gaseous detectors of 10^{-5} vol/min is reached for all panels and the result is stable over the full production period.

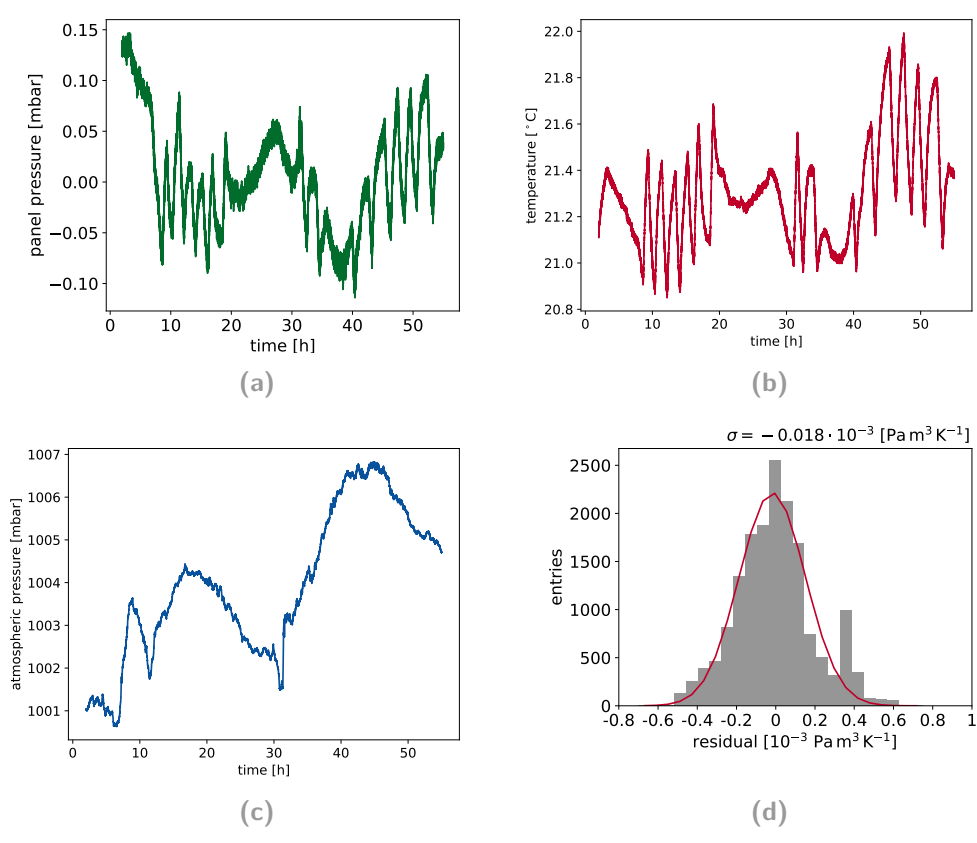


Figure 4.43. Error estimation of the gas tightness measurement. The pressure inside a closed panel volume (a) was corrected for the temperature change (b). The change of the atmospheric pressure (c) is supposed to be corrected by the differential measurement. The difference to a flat distribution after the correction is binned in a histogram (d). The width of the distribution gives the error on the data after the correction procedure.

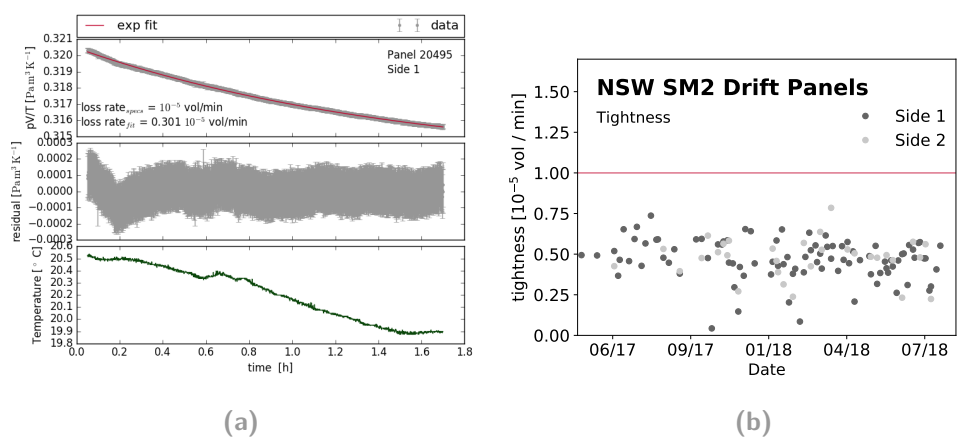


Figure 4.44. Gas tightness measurement for the last produced panel (a). The evolution of the results over the full production (b) underlines the stable quality well below the limit of the ATLAS collaboration indicated by the red line.

4.7 Project Perspective

At the time of the finalization of this thesis, the production of the New Small Wheel components in the other production sites is still ongoing. Roughly one quarter of the quadruplet assembly is finalized and ready for the integration with the already finished New Small Wheel support structure.

The so far build detectors show few stability issues. A high spark rate, sometimes hindering the ramp up to the nominal voltage affects few high voltage sectors per module. The behavior was significantly improved after a revision of the cleaning procedure before assembly. All panels are now washed and the readout panels are polished and dried at low humidity before the assembly. As still some sectors with random sparks occur and the breakdown of few sectors was observed after an operation time of several weeks, further material studies have been carried out.

Possible sources for the detector instability are inhomogeneities in the gas composition or the surface planarity. Degassing studies have been conducted for the detector material (Section 4.7.1) and the impact of sparks on the readout board surface was investigated (Section 4.7.2).

4.7.1 Degassing Studies

To study the degassing of components used in the detector construction a mass spectrometer, provided by the PRISMA Detector Lab at JGU Mainz [90], was used. The mass spectrometer setup is shown in Figure 4.45. The Pfeiffer Vacuum PrismaPlus[®] QMG 220 with a mass range of 1 – 200 u was used for the test. The gas remnants in a vacuum are ionized by an electron gun in front of a quadrupole magnet. The quadrupole frequency is adjusted, that only ions with a fixed ratio of their mass and charge m/z can pass. By scanning the frequency, the whole mass range can be explored. The charges passing the quadrupole can be detected. In the simplest case a Faraday cup is used to measure the created charge. For a higher sensitivity, a secondary electron multiplier (SEM) was used during the measurements.

The mass spectrometer setup provides two possibilities for a sample feeding. Samples can be placed in a recipient to test their direct degassing in vacuum. Via a needle valve a sample from a gas line can be fed as well into the spectrometer to analyze gas compositions.

4.7.1 Data Analysis

An example for mass spectrometer data is given in Figure 4.46. The scan over the mass range was performed in several sequences to check the device stability. The region of the mass peak at $m/z = 18$ u, which corresponds to water, is shown. The mass spectrometer provides a sub atomic mass unit resolution. The peak shows a slightly asymmetric shape, which shifts to lower values with a longer operation time. To correct for this effect, the signal strength of a certain integer m/z ratio was

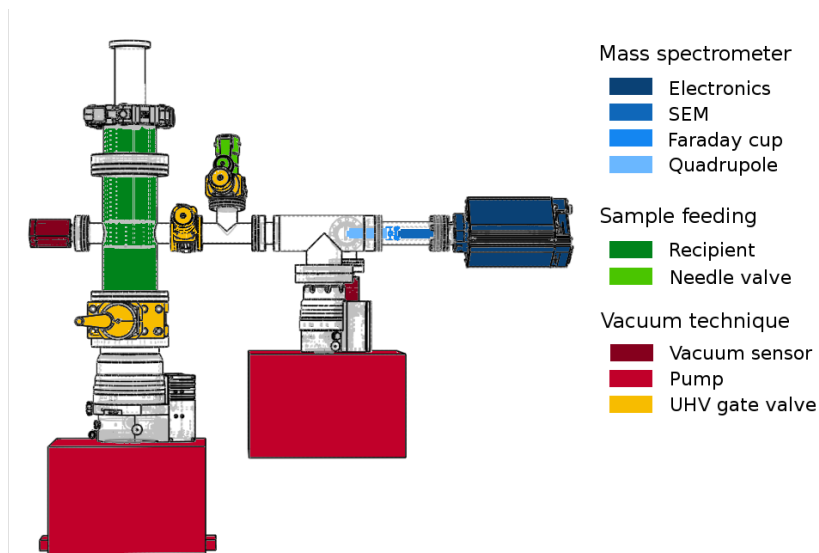


Figure 4.45. Schematical drawing of the mass spectrometer setup. The mechanical drawing was provided by [90]

estimated by summing all measurement in a peak until 10 % of the peak maximum or a change in the slope indicating the raise of the next peak, is observed.

4.7.1 Results

Several materials used in the detector construction have been investigated for their degassing. In general, plastic components and glues tend to higher degassing. For the New Small Wheel Micromegas, this included the epoxy glues used for the construction, the readout board, which host the resistive strip as a polymer embedded carbon resistor and the glue of the capton tape, which is used for passivations. Two versions of the readout board have been investigated. One samples was polished to even the surface. This is expected to reduce the sparking in the detector as superior parts creating a higher electric field are evened. For the epoxy glues and the capton tape, the tested amount corresponds to the estimated material budget in the detector. An overview of the samples can be found in Table 4.5

An overview of the degassing of all samples is shown in Figure 4.47. All samples show the highest contribution from water at $m/z = 18$ u. The highest degassing is observed for the capton tape. This samples shows, as the only one, a long tail exceeding the mass range of the mass spectrometer. This is most likely due to long polymer chain in the glue surface of the tape. This glue surface is only exposed to gas when the tape is applied to the mesh for passivation. When glued to a solid surface, only the sides of the glue layer are open to the gas volume and significant less degassing is expected. The slower curing epoxy glue Araldite® 2011 shows a higher degassing rate than the faster curing Araldite® 2012. As the single samples have been created in a single gluing step, the result is not fully conclusive. The

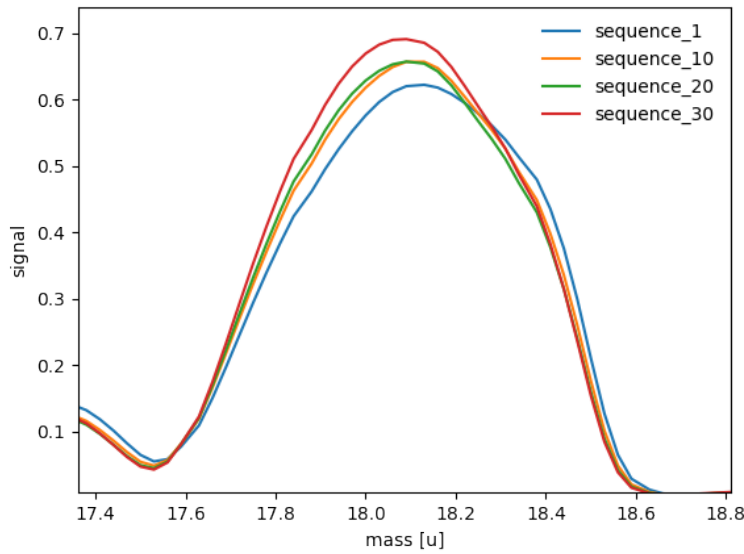


Figure 4.46. Evolution of the peak shape over several measurement sequences.

degassing is expected to depend on the mixing ratio of the two components of the glue. A longer study with different mixing ratios could verify the result.

No difference is observed between the degassing of the polished and unpolished readout board. This shows, that the destruction of the bonded resistive surface does not increase a material degassing. The small sample of the readout board shows much less degassing compared to the other samples, but one has to keep in mind, that while the other sample correspond to the total material budget exposed to the gas volume in the detector, the readout board sample only corresponds to 0.1 % of the total active area. Thus the readout board is expected to be main source for gas impurities.

The measurements do not allow to conclude for the chemical composition of the degassing. Organic compounds fragment during the ionization in the mass spectrometer. To identify single compositions from the fragmentation process, manifested in the peak ratios at the different mass values, the original compounds have to be known and a spectra of the single components has to be compared to the measurement.

The readout boards have been measured once after the receipt and a storage at normal air and once after 1.5 weeks storage in dry air (5 %RH). After the drying, not only the water pollution was reduced by almost one order of magnitude, but also the contribution from all other components. This hints, that water acts as a catalyst or carrier for degassing of the readout board components. The measurement comparison is shown in the appendix in Figure A.10.

The epoxy glue and capton tape samples have been tested as well for the degassing in gas stream of argon. The samples have been flushed with a flux of 3 L h^{-1} , as

Table 4.5. Samples investigated in the mass spectrometer.

Sample	Amount
Araldite® 2011	8.1 g
Araldite® 2012	9.1 g
Capton tape	2.8 g
Readout board polished	5 × 5 cm ²
Readout board unpolished	5 × 5 cm ²

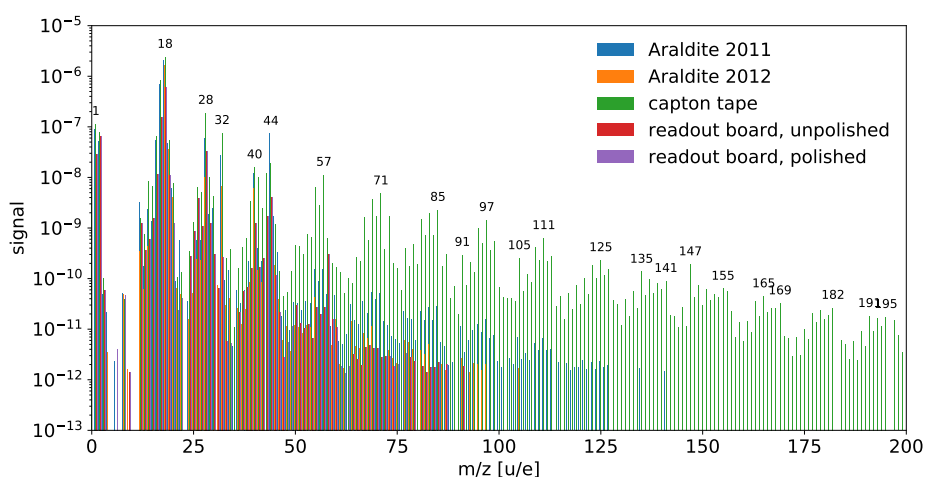


Figure 4.47. Outgassing results for the tested components. For a better visualization, the contributions of the single samples are plotted next to each other in around the integer mass value.

during the detector operation, and half of the gas flow was directed into the mass spectrometer via the needle valve. No contribution of the sample degassing could be found in the argon. This shows, that no impact on the detector performance is expected from these components. To investigate the impact on the gas quality from the full readout board surface, a extraction of the gas after flushing the detector would be necessary.

4.7.2 Sparking impacts

The formation of sparks in the detector might lead to a degeneration of the resistive strip surface by polymerization of the material. To investigate the effect samples of an polished and unpolished readout board have been exposed to sparks. The tests have been conducted in an argon atmosphere and at air, as the detector is powered at air during the assembly to check for the cleanliness.

The sparks have been created with two setups, shown in Figure 4.48. To mimic the detector operation, a calendered micromesh (wire diameter: 30 μm, pitch: 100 μm)

was glued to a metallic frame and powered with high voltage, limiting the current to $2\mu\text{A}$. The mesh was not fully stretched during the gluing to allow for a bending toward the middle of the surface and induce sparks at this point of lowest distance. To avoid a surface contact of the loose mesh, a capton foil with a 3 mm hole was placed between the readout board and the mesh.

As a second test at higher currents, the readout board surface was exposed to sparks from an arc lighter. One electrode of the lighter was electrically connected to the resistive surface while the other electrode was placed over the board surface.

Microscopic pictures of the impact of the sparks on the resistive surface can be found in Figure 4.49. In general, less growth of structures on the unpolished surface was found, compared to the polished surface. In a comparison of the surfaces, it becomes visible, that the unpolished board has a reflecting smooth surface, while the polished surface shows scratches from the polishing and appears opaque. The destruction of the bonded resistive layer might favor the formation of growing structures.

Figure 4.49a shows a structure widely found on the polished surface after treatment with arcs from the lighter in an argon atmosphere. Small round structures grow on the strip surface. The stand off of the structure can be better seen in the comparison of the illumination from four directions. A rough structure of the growing parts was visible, not resolved in the picture. By comparison with a mesh wire, the size of the structure was estimated to $\approx 10\mu\text{m}$.

A longer exposure with the lighter leads to a big polymerization completely destroying the resistive strip surface (Figure 4.49b). The biggest comparable structure on the unpolished board is shown in Figure 4.49c. A porous bump exceeds the strip surface by $\approx 10\mu\text{m}$. The surface of the bump shows evidence for the formation of a glass phase.

A similar effect was observed at few spots under the mesh. An example is shown in Figure 4.49d. A whitish, shining layer formed on top of the resistive strip. No evidence for a significant height build-up was observed for this layer.

The trace from sparks on the unpolished board was found as lines pointing toward the board edge. A white deposit is observed on the strips along the path of the spark and the strips get harmed at the board edge (Figure 4.49e and 4.49f). The high currents and voltage build ups at the edge even lead to a damage on the pillars and the FR4 of the board.

The studies on the spark resistance of readout boards have shown a trend to a higher spark tolerance of unpolished strips. While a growth of various small structure was observed when treated with the arcs from the lighter on the polished surface, only a whitish, glass like deposit without significant height was observed on unpolished strips. As the study was limited by the little available material, a more detailed, systematic study within the ATLAS New Small Wheel Micromegas is advisable

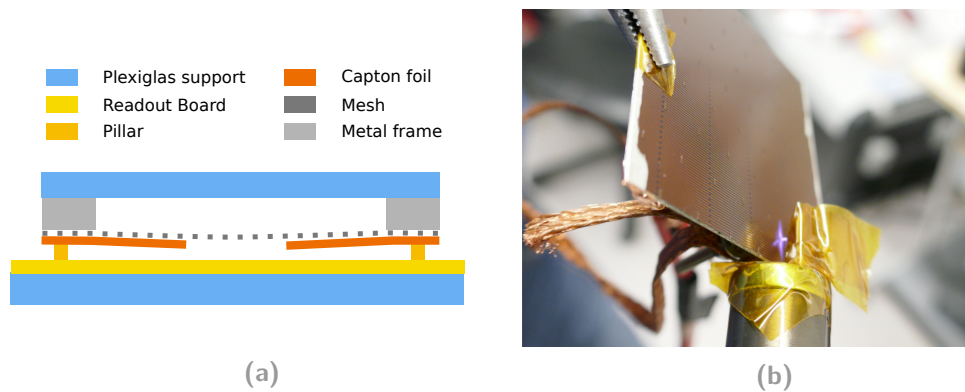


Figure 4.48. Setup for the spark creation on the readout board surface. The setup to investigate a situation as in the detector is shown in (a). An arc lighter was used to check for the impact of sparks with a higher current (b).

to understand a possible risk and origin of sparks in voltage breakdowns in the detectors.

4.8 Summary and Outlook

This chapter presented the production of Micromegas drift panels for the ATLAS New Small Wheel Upgrade. The requested amount of detector component was delivered to the collaboration well in time with a full production yield. The developed production procedures have been transferred to other construction sites as well. The method for the board cutting and the sealing between the single boards was adapted by other construction sites. The established repair strategy for unglued or delaminated areas was collaboration wide approved as repair procedure. Besides the sole production of the detector components, input to the full upgrade program could be provided by the material irradiation studies, the experience exchange in the design and quality control working groups and the results on the component degassing and spark resistance.

Besides the benefits for the ATLAS collaboration, this work sets several pioneering aspects for developments in the Detector lab of the excellence cluster PRISMA⁺. The developed production procedure for large scale, high planarity detector components can be adapted for future projects. This does not only include the experience in the gluing process, but also the production of tooling, as the vacuum tables. The shape of a vacuum table as a base for a planar detector construction is only limited by the size of the granite table. The handling of the vacuum tables in the extension of the laminar flow box manifested to be highly profitable for the production. The setup of the clean area extension and the crane was highly appreciated by the following user of the detector lab and stays as a permanent lab infrastructure.

The project's sustainability does not only include the mechanical work, but also the established measurement procedures. The analysis strategy for planarity scans was defined and the measurement system properties have been evaluated. A setup and

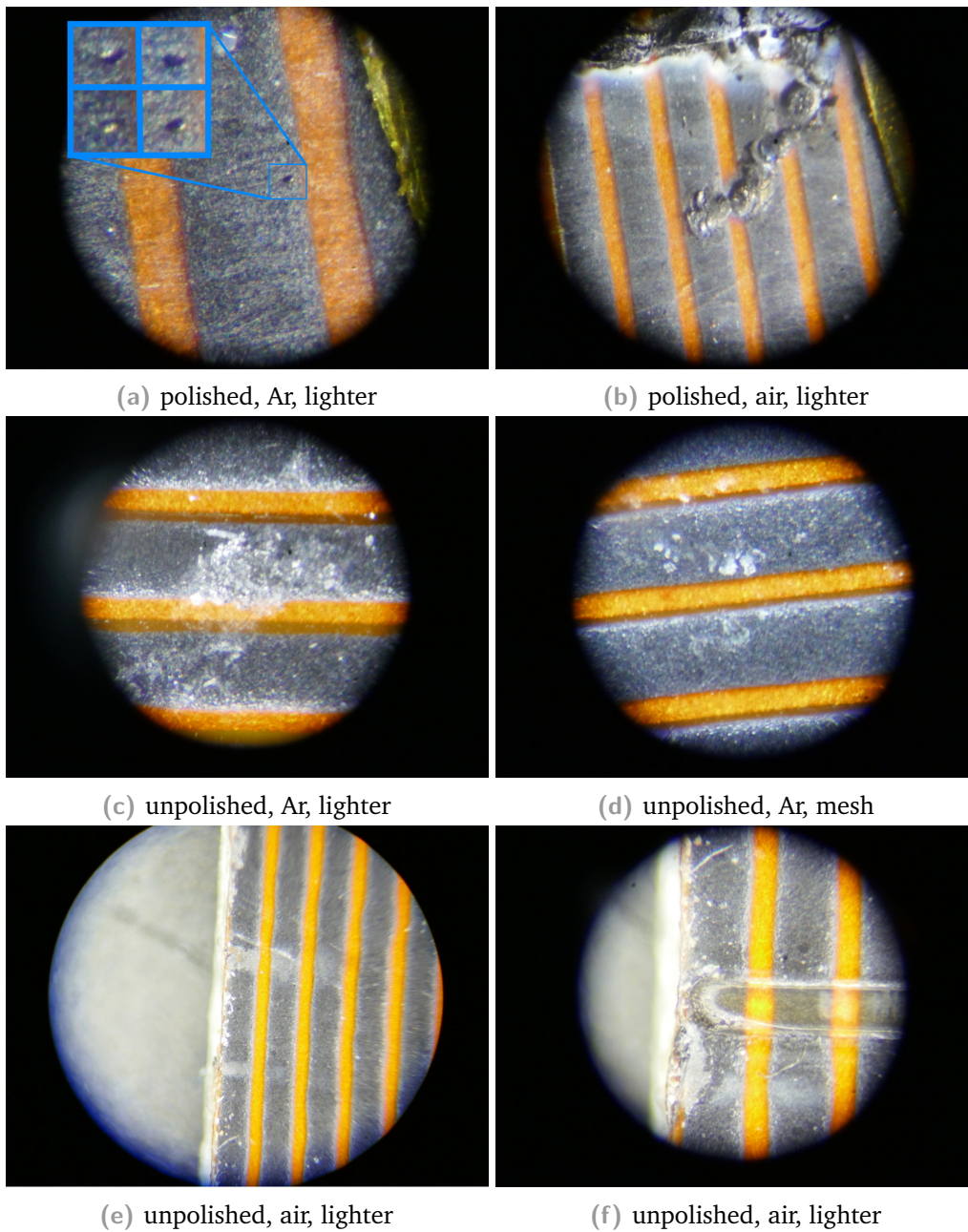


Figure 4.49. Microscopic picture of the impact of the sparks on the resistive surface of the readout boards. Whether the test was performed on a polished or unpolished board, in a argon atmosphere or at air and if the lighter or the mesh setup was used in indicated in the caption of the single pictures.

calibration procedure for gas tightness measurements has been tested. The degassing studies, have not only been the first measurement with the mass spectrometer, but also resulted in a flexible analysis framework for a measurement comparison and interpretation. Motivated by the achieved results, profound studies on material degassing are planned in the near future. This will not only include studies on the humidity intake of construction materials, but also aims for the transfer of degassing measurements to an impact on the detector performance. Therefore the gas composition in a temperature and pressure stabilized gas detector under operation will be measured.

Conclusion

As a first part, this thesis showed a first measurement of the branching ratio fraction $BR(W \rightarrow \tau\nu \rightarrow \mu\nu\nu)/BR(W \rightarrow \mu\nu)$ with a template fit method based on $\sqrt{s} = 7$ TeV proton-proton collision data. This data, with the well studied systematic variations from the measurement of the W mass, formed an ideal base for the development and implementation of the fraction fit method with a MINOS error estimation and leads to best fit value of $BR(W \rightarrow \tau\nu \rightarrow \mu\nu\nu) = 0.228^{+0.024(0.010)}_{-0.023(0.010)}$. Two different parametrization of the branching ratio fraction have been investigated. In the first approach, the ratio fraction is parametrized by a normalization applied to the two signal samples and in individual norm only applied to the tauonic decay channel. In the second approach, the ratio fraction is parameterized by a shape systematic scaling the normalization of one signal process up, while scaling the normalization of the second process down and vice versa. Both approaches showed identical results and can be used redundant in future measurements.

Different approaches have been studied for the background treatment as well. The studies have shown, that a single treatment of each background process does not have enough discrimination power in the fit. The combination of the background process in a single norm or as a single summed process have provided similar results and should both be considered for future studies.

The study was shown to be dominated by systematic uncertainties, mainly the uncertainty on the parton density function entering the modeling of the physics process and the systematics on the reconstruction of the muons in the detector.

A possible improvement to a 4% uncertainty could be motivated for an extension of the kinematic range of the fitting distributions. With this perspective, the study is carried on within the ATLAS collaboration in the context of a reanalysis of the W mass measurement with improved parton density functions.

As second part of the thesis, the construction of detector components for the ATLAS New Small Wheel upgrade was presented. The work on that topic started in 2015 with the setup of the production infrastructure and the production of the necessary tooling. Precision vacuum tables have been assembled for the alignment of the detector components. The construction site in Mainz was qualified as ATLAS production site in autumn 2015 and the production readiness review was passed in spring 2017. In the mean time, the detector design was finalized with the New Small Wheel Micromegas Construction Working Group, the construction of prototype panels was performed and the quality control methods and data handling were defined not only for the local production, but also in view of the whole collaboration.

The first third of the mass production starting in spring 2017 was leaded and the full

production was accompanied as expert in the scope of this work. The production of 102 detector components was finished late summer 2018 as, with a large distance, the first construction site in the collaboration. The quality control results show a production yield of 90 %. Components not fulfilling the requirement have been produced in the learning phases at the beginning of the production and after the hand over of the production supervision. As no spare material was foreseen from the collaboration, a repair mechanism was developed to recover structures with a weak gluing. The repair was successfully conducted and all panels have been accepted for the further assembly.

Several material studies have been performed for the New Small Wheel detector. The radiation hardness of components was proven by a neutron irradiation at the Mainz TRIGA reactor. Furthermore the degassing of construction materials was investigated as problems with the high voltage stability of the assembled detectors appeared throughout the whole collaboration. The readout board was identified as the main source of gas pollution.

The impact of sparks created in the instable high voltage situation on the readout board surface was studied. While a short term treatment with sparks in a setting resembling the current limit during the detector operation only showed a surface coating of the readout board without a harmful height buildup, the treatment with higher intensity sparks lead to a growth of instable, porous structures on the readout board, weakening and possibly polluting the detector. A future long term study needs to show if these structure can also occur after a long term exposure in the limited current situation.

A.1 Branching Ratio Fraction Determination

A.1.1 Smoothing Results

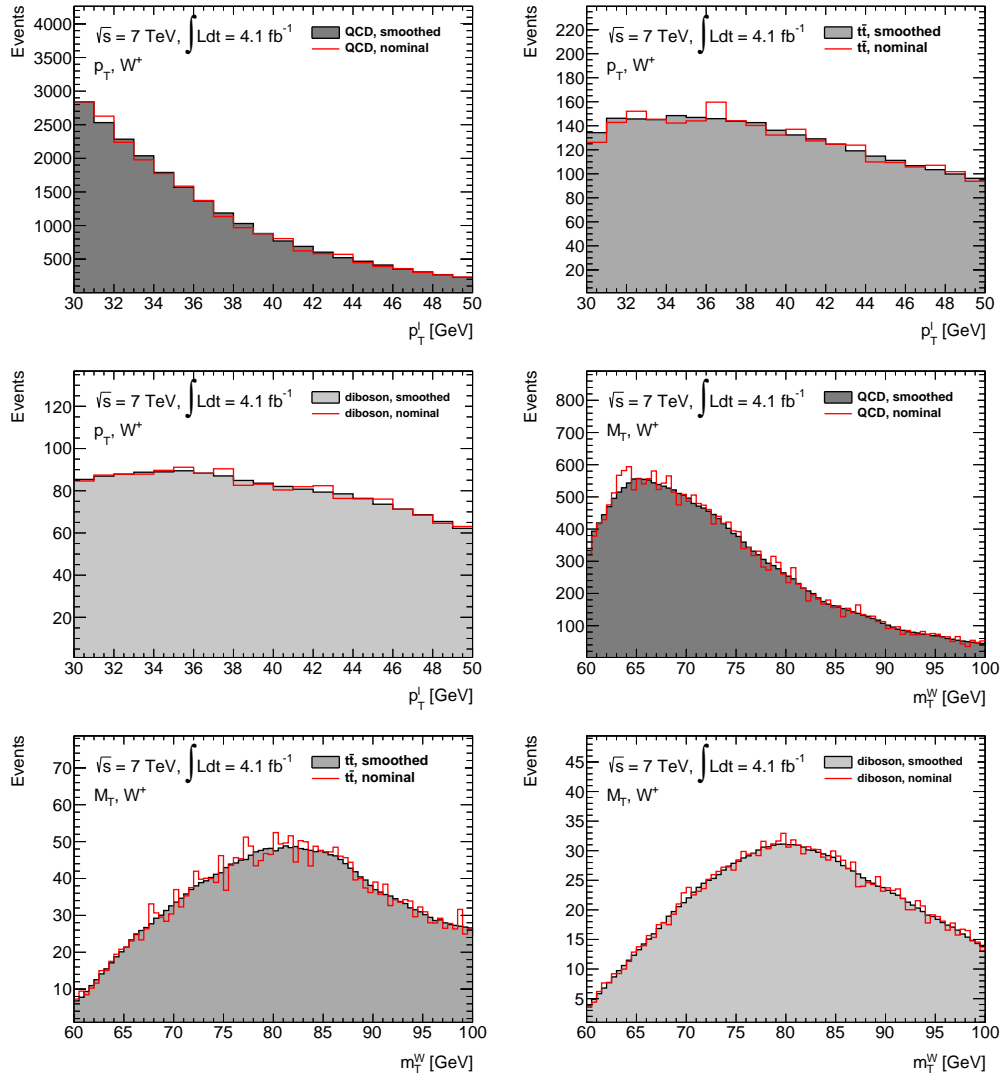


Figure A.1. Comparison of the smoothed and original (red line) samples for the p_T (a), (b) and (c) and the m_T (d), (e) and (f) distributions for the decay of the negative W^+ boson.

A.1.2 Fit Stability

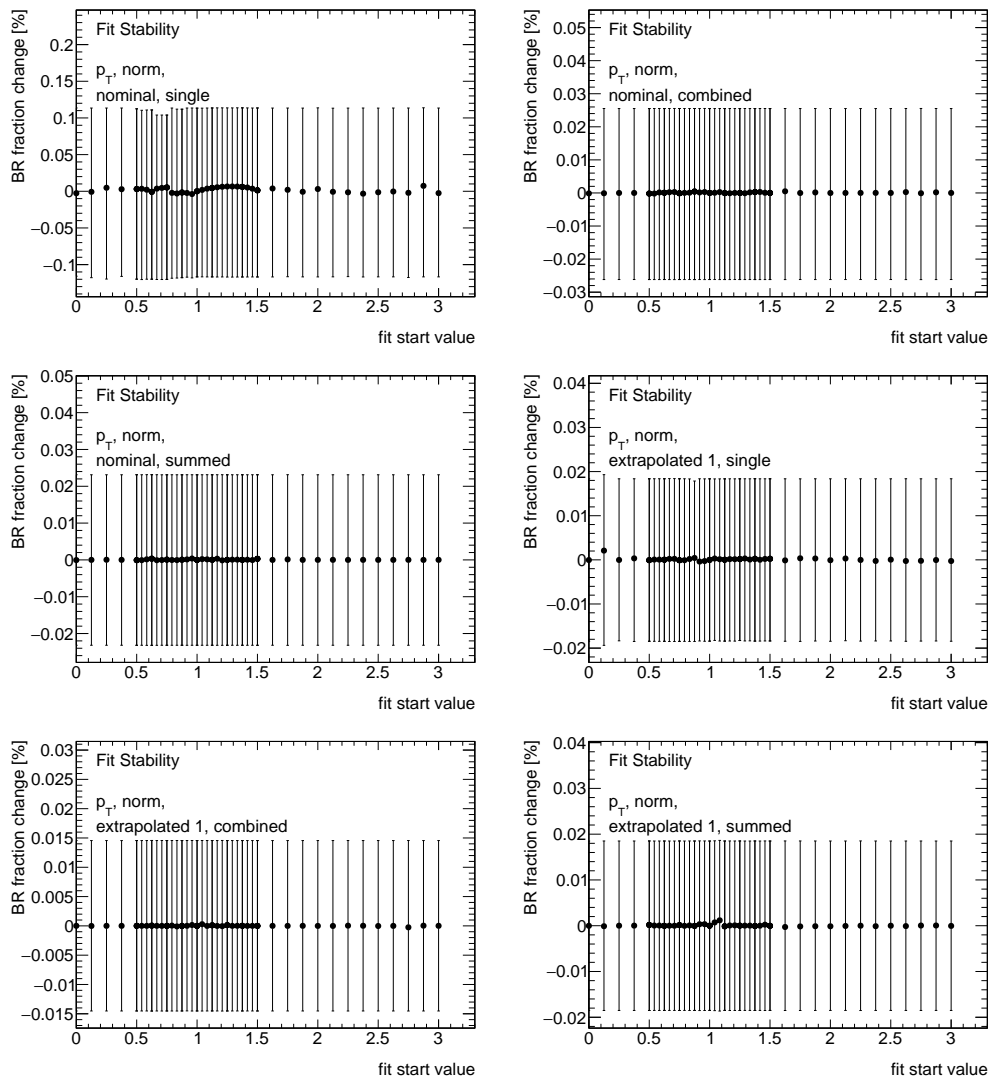


Figure A.2. Stability of the fit to the p_T distribution.

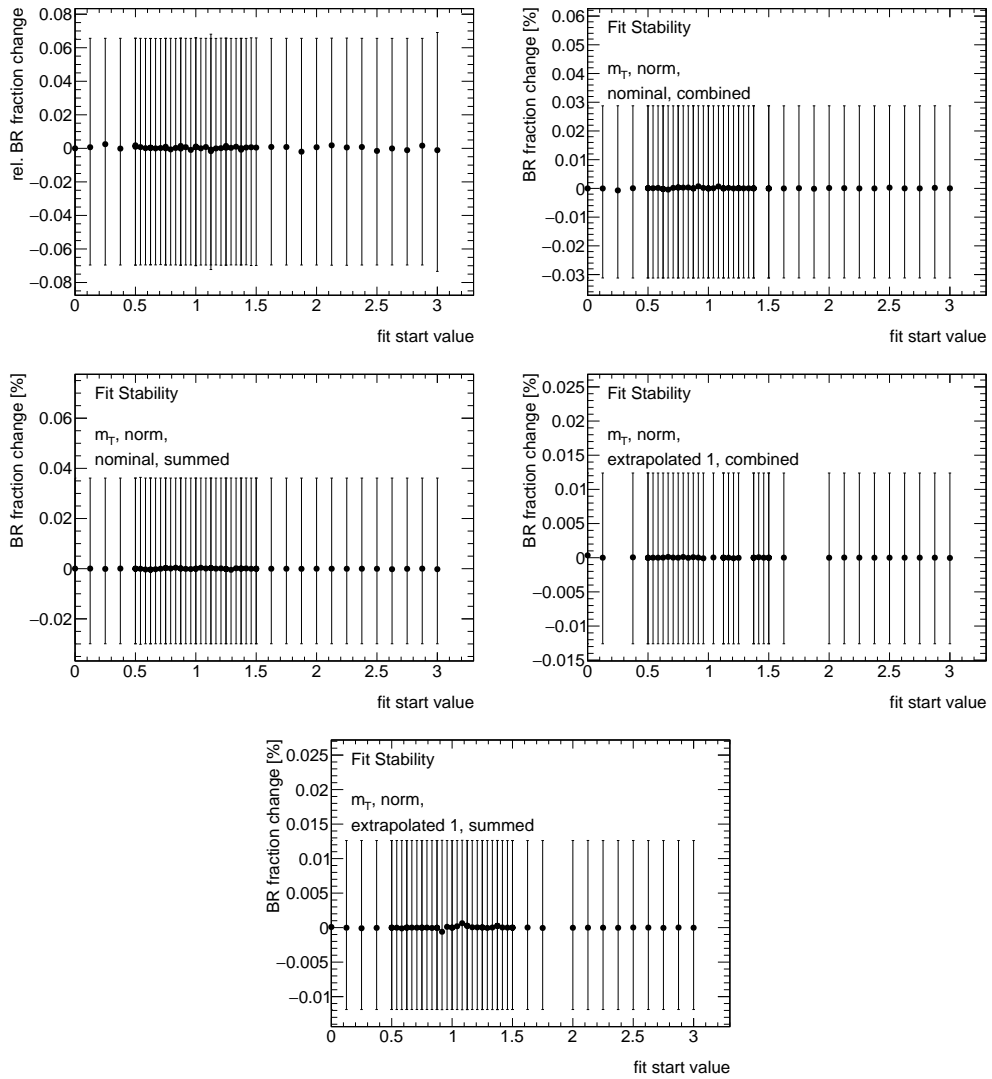


Figure A.3. Stability of the fit to the m_T distribution.

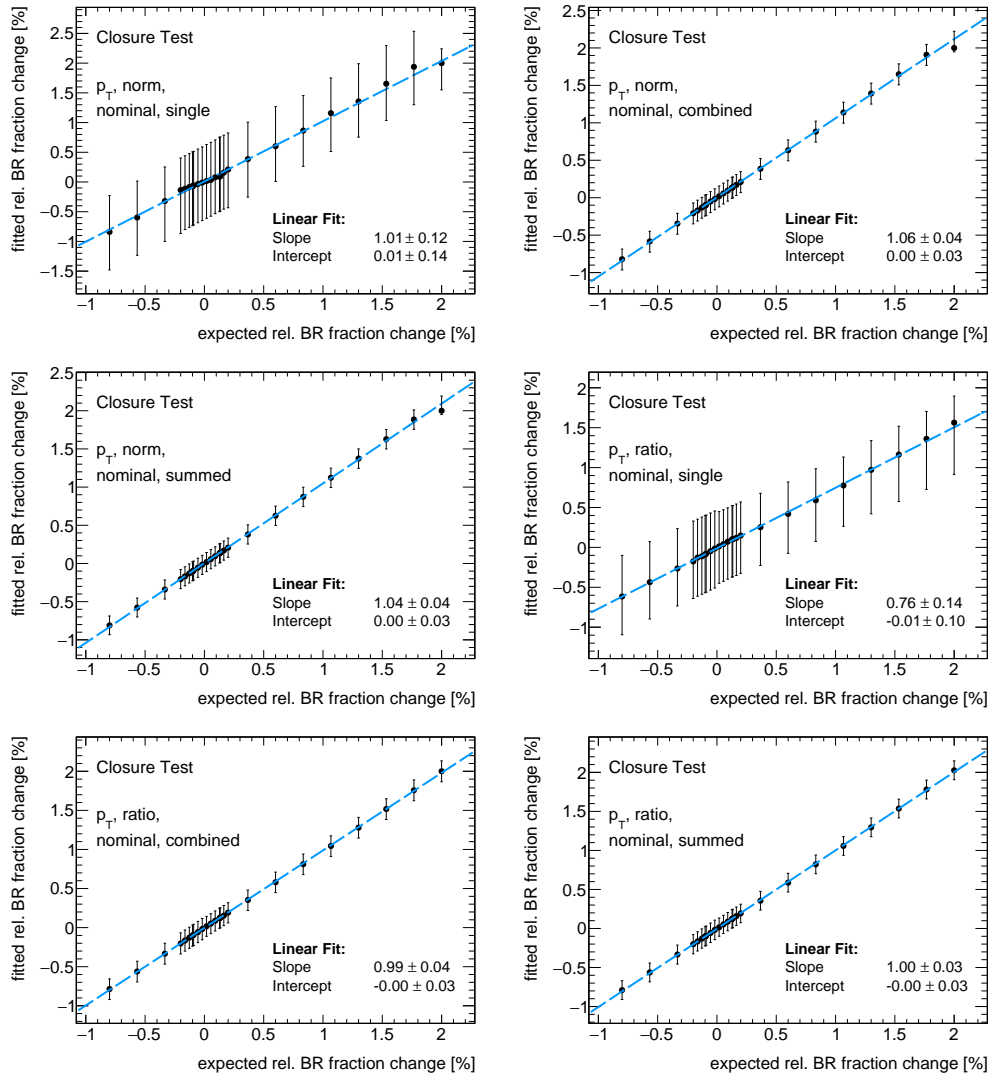


Figure A.4. Closure of the fit to the p_T distribution.

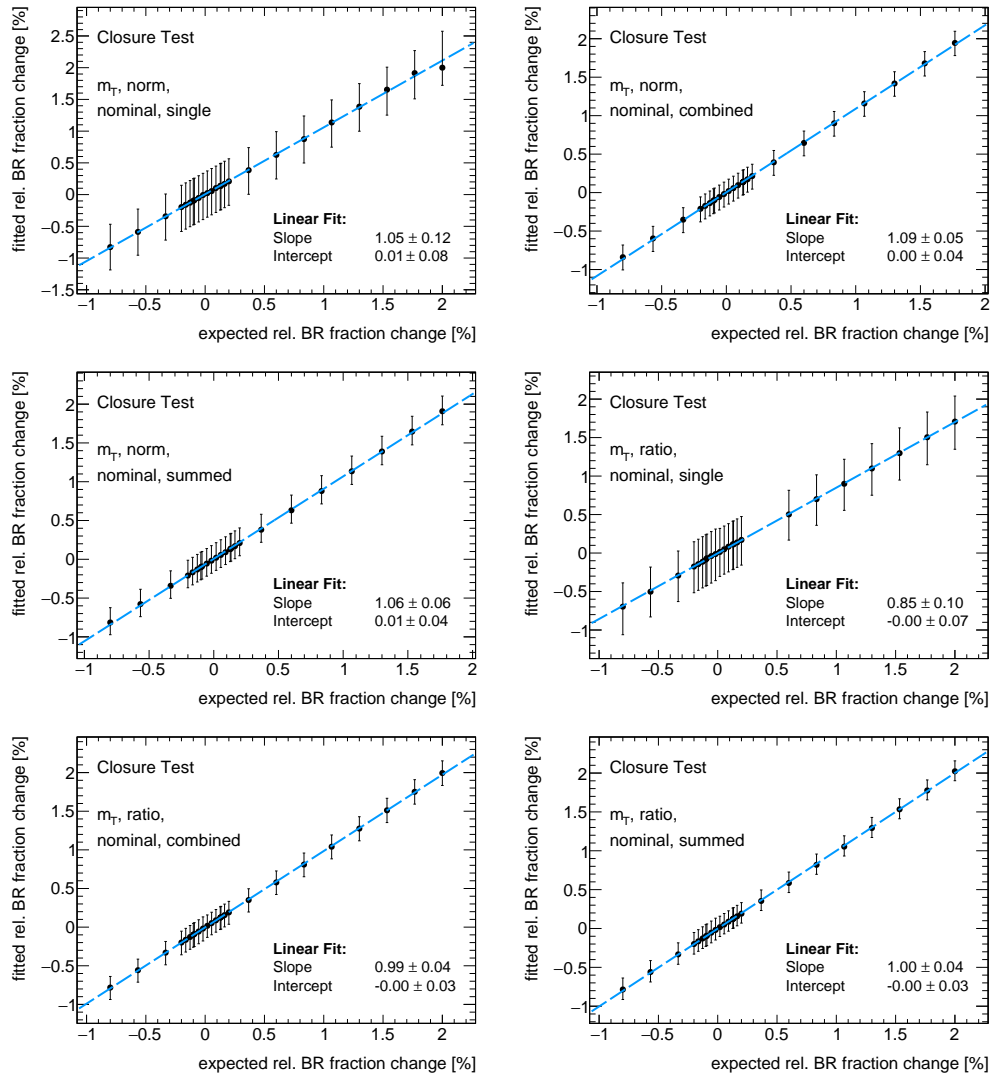


Figure A.5. Closure of the fit to the m_T distribution.

A.1.3 Fitting Results

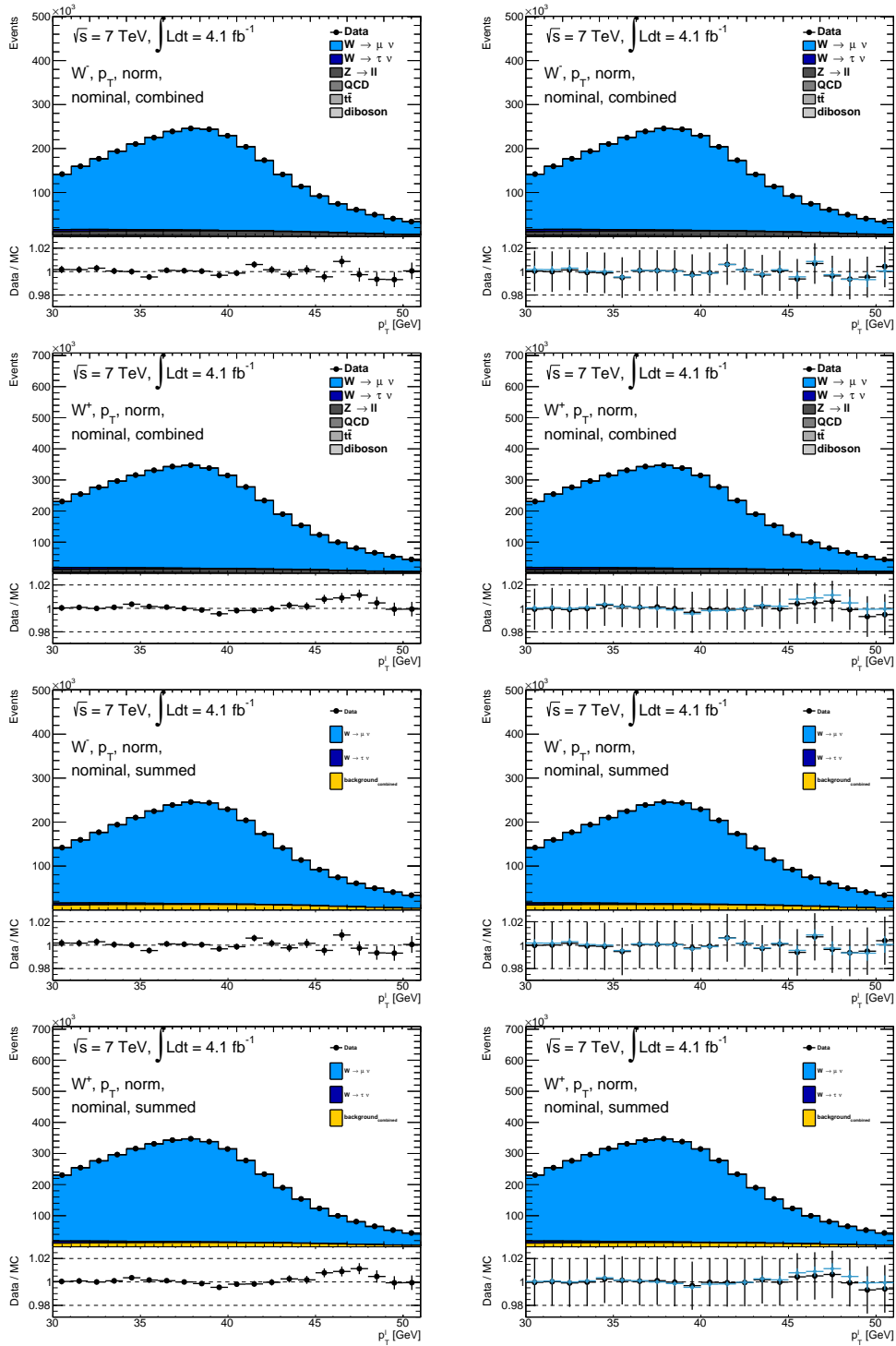


Figure A.6. Pre- and post-fit distributions for the norm fitting approach to the p_T distributions.

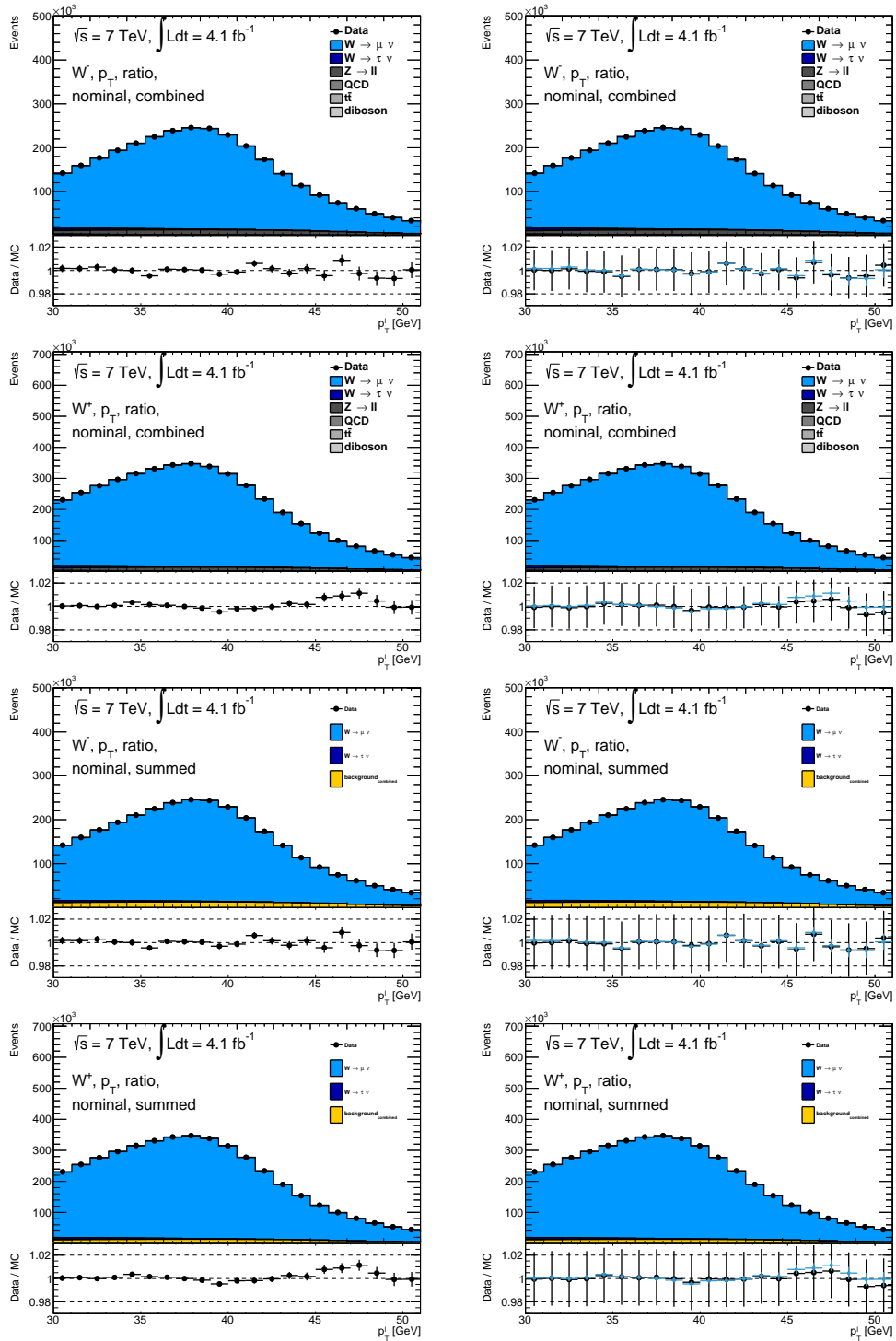


Figure A.7. Pre- and post-fit distributions for the ratio fitting approach to the p_T distributions.

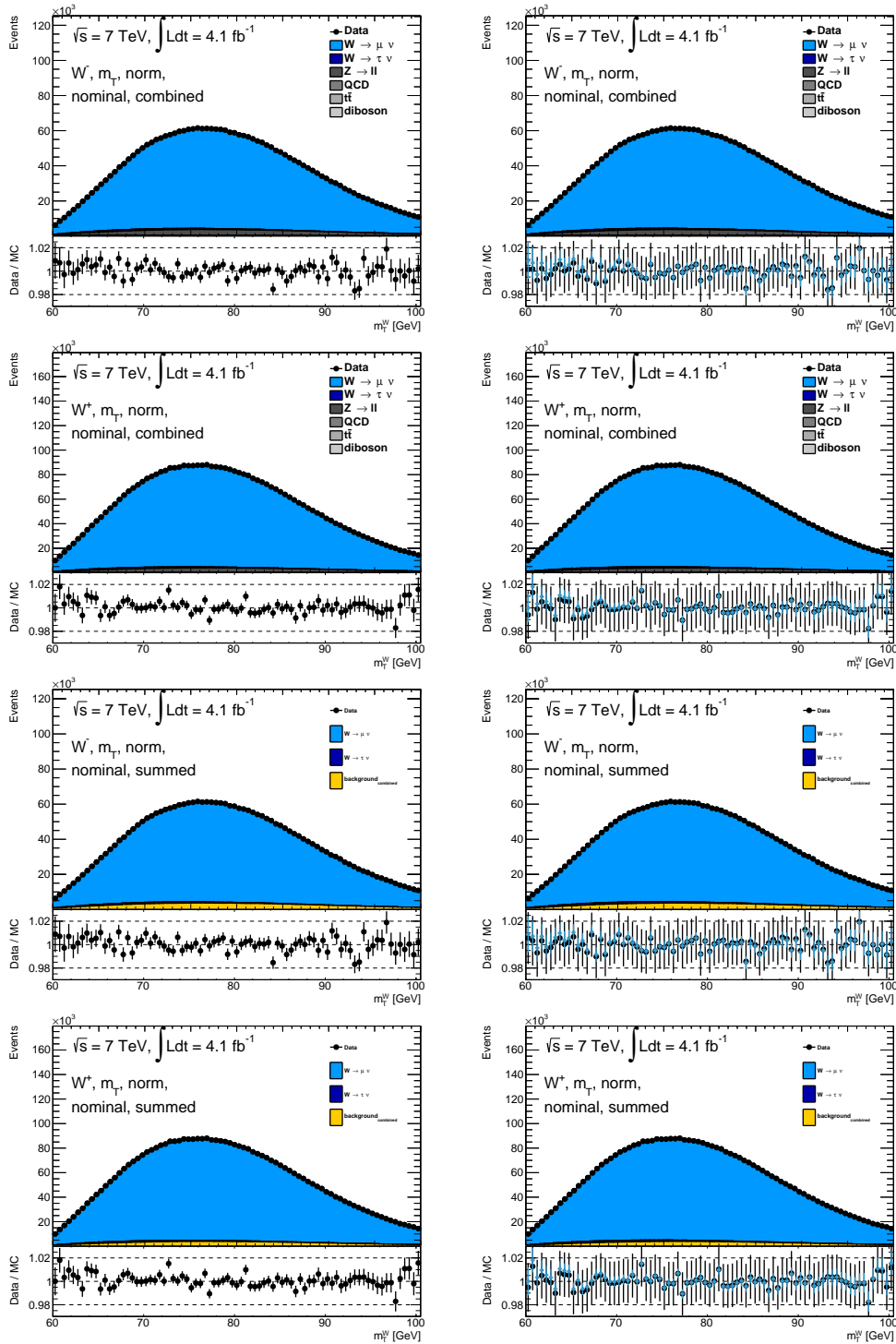


Figure A.8. Pre- and post-fit distributions for the norm fitting approach to the m_T distributions.

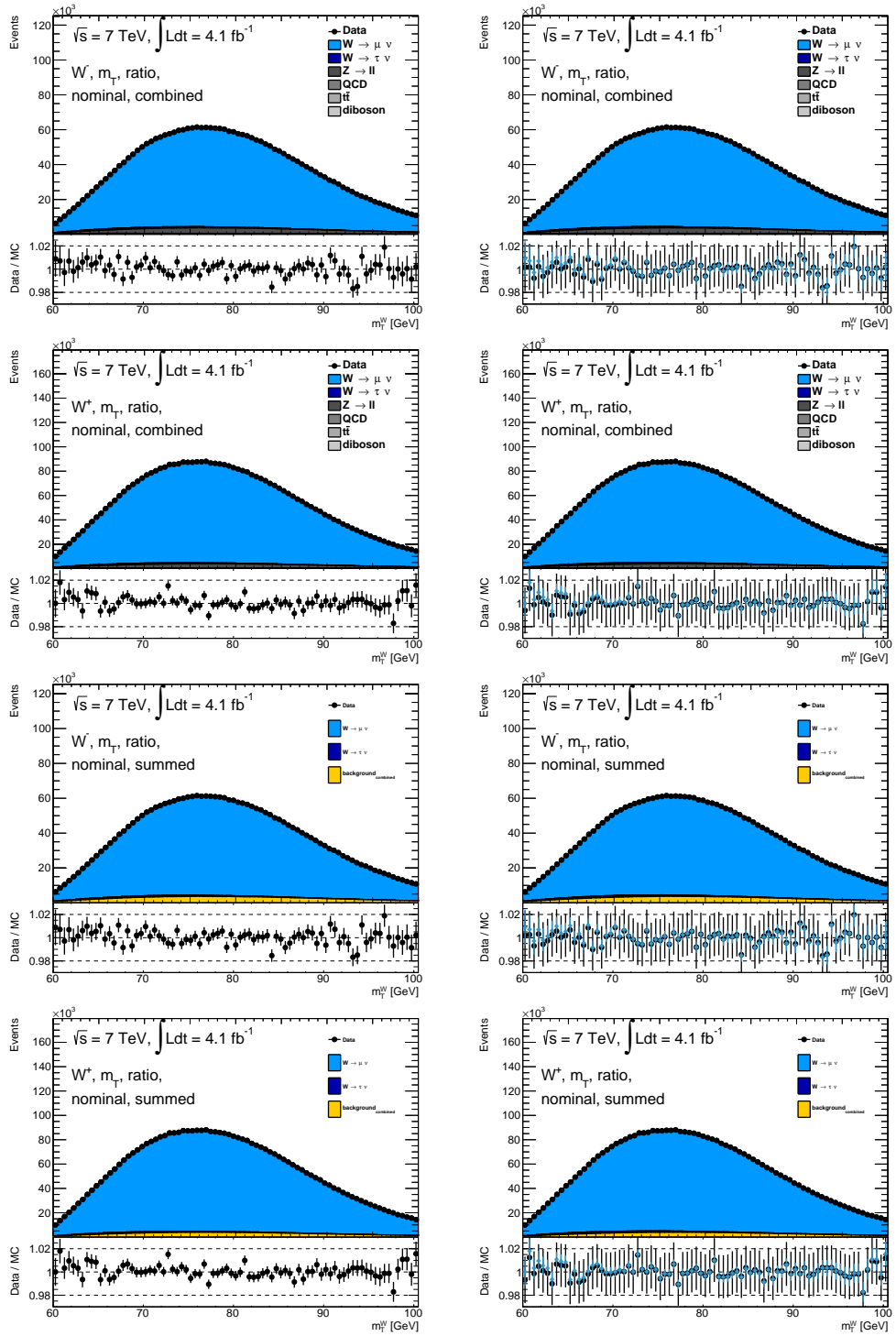
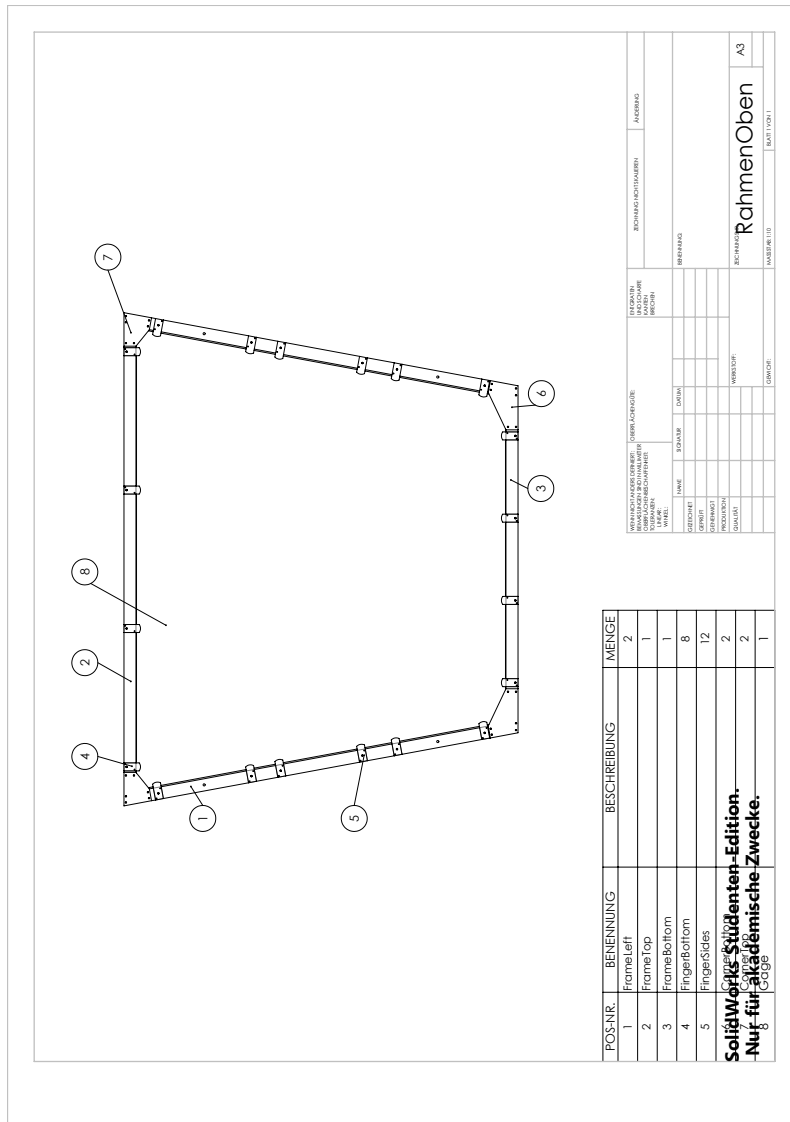


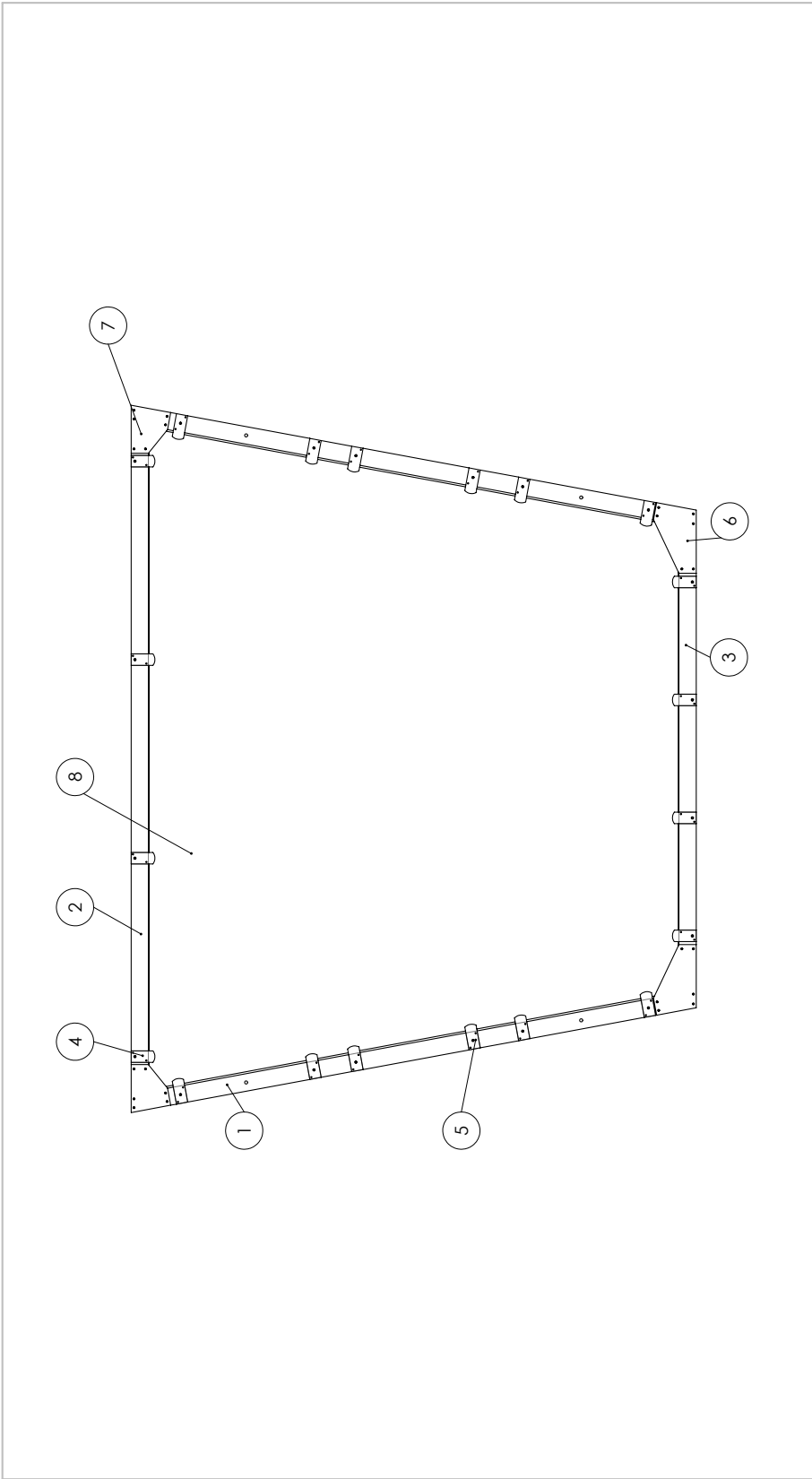
Figure A.9. Pre- and post-fit distributions for the ratio fitting approach to the m_T distributions.

A.2 NSW Drift Panel Construction

A.2.1 Alignment Frame Drawings

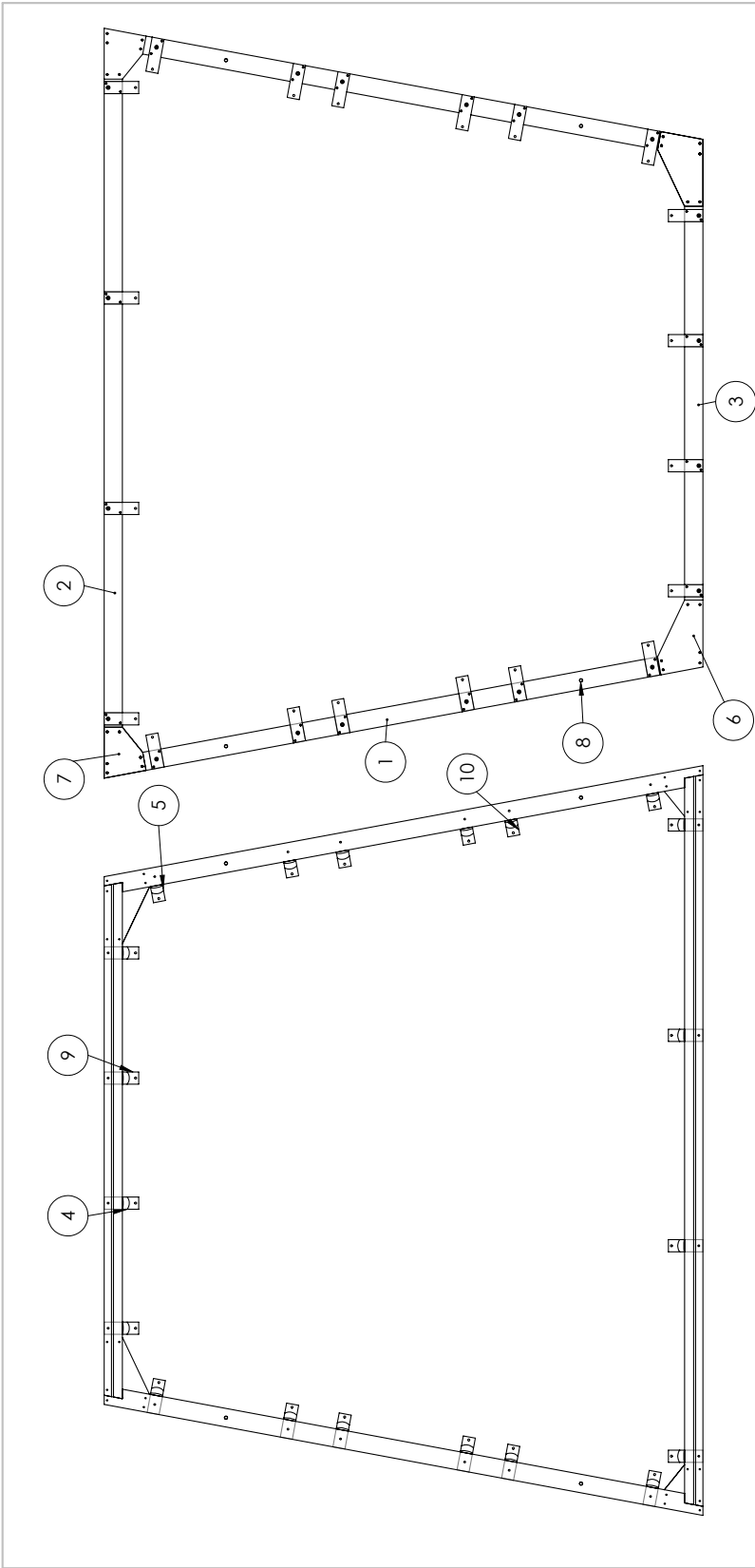
On the next pages, the mechanical drawings of the alignment are presented, as they have been send to the producing company. Some changes have been implemented in the use of the positioning system during the production, which are discussed in Section 4.4.3.





POS-NR.	BENENNUNG	BESCHREIBUNG	MENGE
1	FrameLeft		2
2	FrameTop		1
3	FrameBottom		1
4	FingerBottom		8
5	FingerSides		12
SolidWorks Studenten-Edition.			
Nur für akademische Zwecke.			
8			

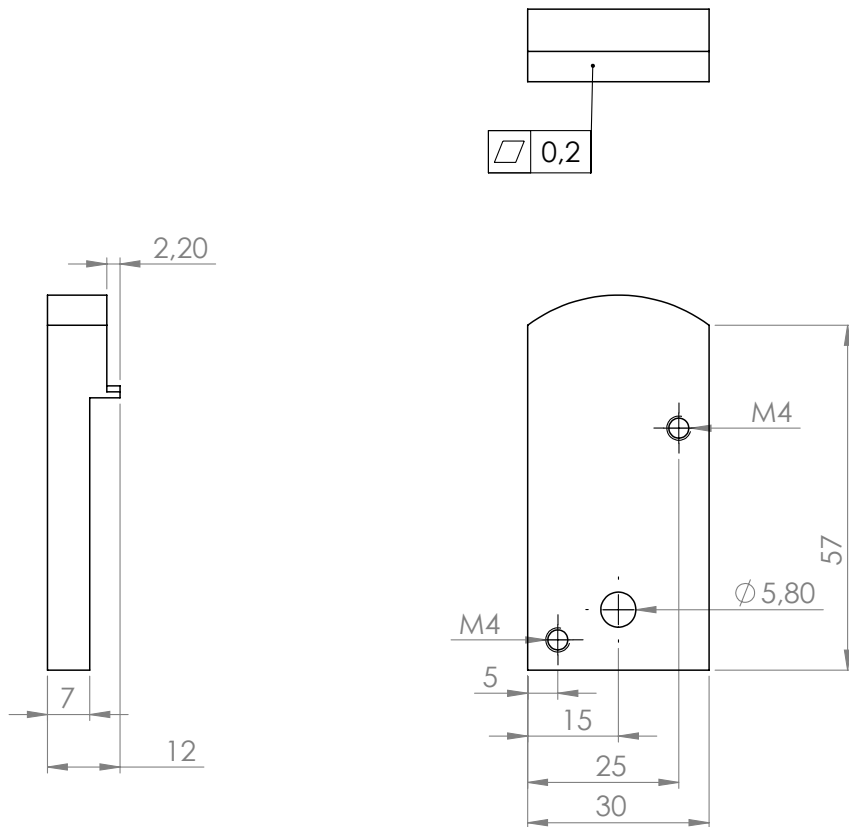
WENN NICHT ANDERS DREHMER: BEWASSUNGSER SIND IN MILLIMETER ANGABEN LINEAR- WINKEL	OBERFLÄCHENGÜTE:	ENTGRATEN UND SCHARFE KANTEN BRUCHEN	ZEICHNUNG NICHTSÄLERN	ÄNDERUNG
NAME	SIGNATUR	DA TUM	BENENNUNG:	
GEZEICHNET				
GEPRÜFT				
GENEHMIGT				
PRODUKTION				
QUALITÄT		WERKSTOFF:		
		GEWICHT:		
			ZEICHNUNGS-	A3
			MASSSTAB: 1:10	BLATT VON 1
			RahmenOben	



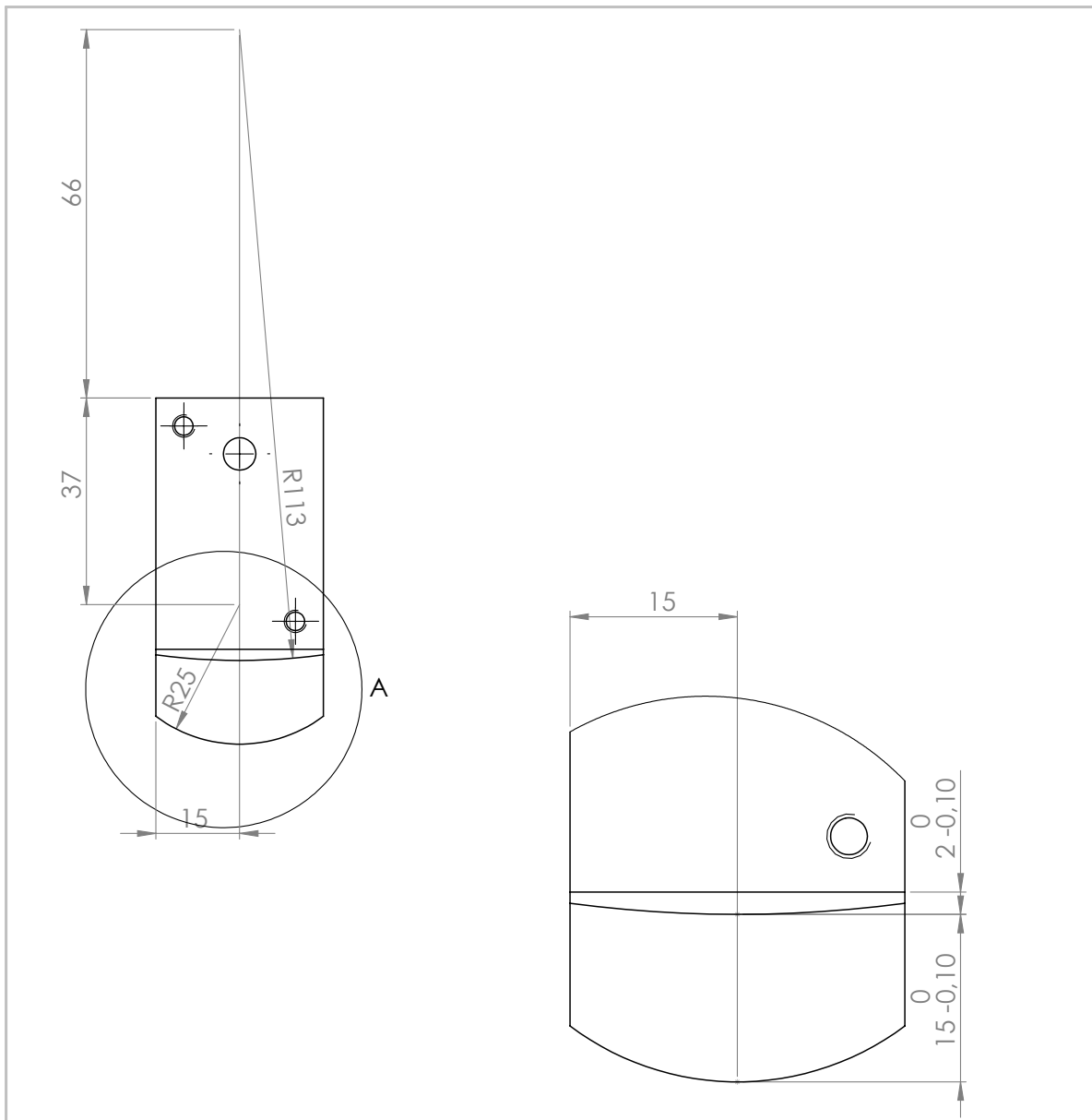
POS-NR.	BENENNUNG	BESCHREIBUNG	MENGE
1	FrameLeft		2
2	FrameTop		1
3	FrameBottom		1
4	FingerBottom		8
5	FingerSides		12
6	CornerBottom		2
7	CornerTop		2
8	Pin		4
10	SolidWorks Studenten - Edition. Nur für akademische Zwecke.		8
			12

WENN NICHT ANDERS DREHNER: BEWÄSSIGTER SIND IN MILLIMETER ANGEBEN. WINKEL:	OBERFLÄCHENGÜTE:	ENTGRATEN UND SCHÄRFE KANTEN BRUCHEN	ZEICHNUNG NICHT SKALIEREN	ÄNDERUNG
GEZEICHNET	SIGNATUR	NAME	BENENNUNG:	
GEPRÜFT	DAITUM	DATE		
GENEHMIGT				
PRODUKTION		WERKSTOFF:		
QUALITÄT				
			ZEICHNUNGS RahmenUnten	
			MASSSTAB: 1:10	
			BLATT 1 VON 1	

SolidWorks Studenten - Edition.
Nur für akademische Zwecke.

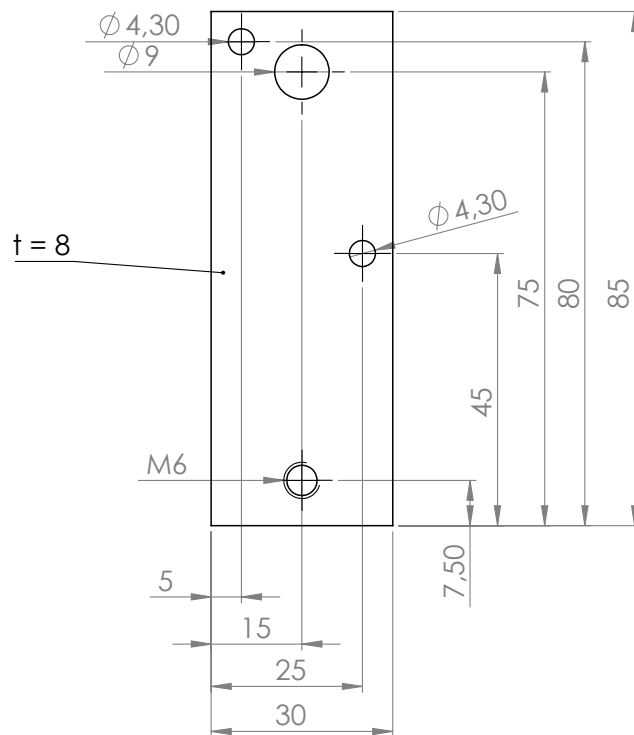


WENN NICHT ANDERS DEFINIERT: BEMASSUNGEN SIND IN MILLIMETER OBERFLÄCHENBESCHAFFENHEIT: TOLERANZEN: LINEAR: WINKEL:		OBERFLÄCHENGÜTE:		ENTGRATEN UND SCHARFE KANTEN BRECHEN		ZEICHNUNG NICHT SKALIEREN		ÄNDERUNG	
NAME	SIGNATUR	DATUM				BENENNUNG:			
GEZEICHNET						ZEICHNUNGSNR. FingerBottom			
GEPRÜFT									
GENEHMIGT									
PRODUKTION									
QUALITÄT	SolidWorks Studenten-Edition. Nur für akademische Zwecke. <small>WERKSTOFF:</small> Aluminium							A4	
				GEWICHT:		MASSSTAB:1:1	BLATT 1 VON 2		

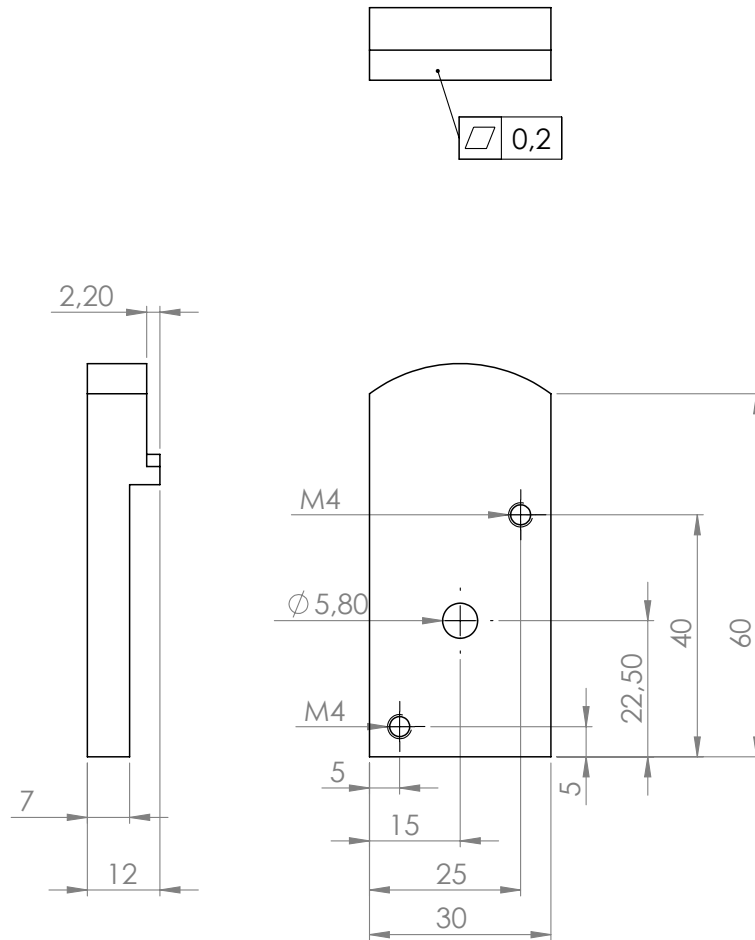


A (2 : 1)
enge Toleranz am Scheitelpunkt benötigt

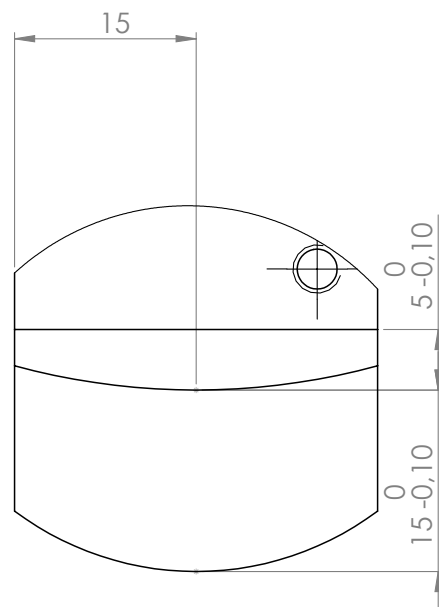
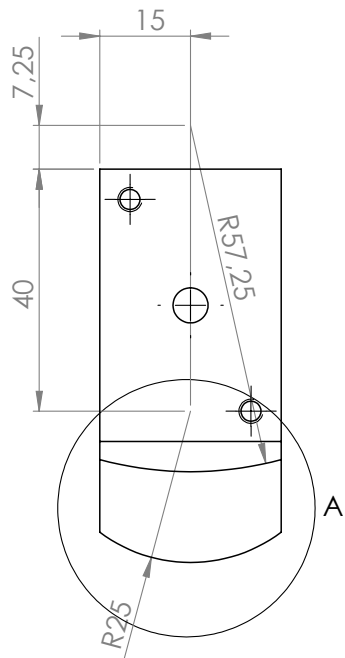
WENN NICHT ANDERS DEFINIERT: BEMASSUNGEN SIND IN MILLIMETER OBERFLÄCHENBESCHAFFENHEIT: TOLERANZEN: LINEAR: WINKEL:		OBERFLÄCHENGÜTE:		ENTGRATEN UND SCHARFE KANTEN BRECHEN		ZEICHNUNG NICHT SKALIEREN		ÄNDERUNG	
NAME	SIGNATUR	DATUM				BENENNUNG:			
GEZEICHNET						ZEICHNUNGSNR. FingerBottom			
GEPRÜFT									
GENEHMIGT									
PRODUKTION	SolidWorks Studenten-Edition.					MASSSTAB:1:1			
QUALITÄT	Nur für akademische Zwecke. Aluminium								
					GEWICHT:	BLATT 2 VON 2		A4	



WENN NICHT ANDERS DEFINIERT: BEMASSUNGEN SIND IN MILLIMETER OBERFLÄCHENBESCHAFFENHEIT: TOLERANZEN: LINEAR: WINKEL:		OBERFLÄCHENGÜTE:		ENTGRATEN UND SCHARFE KANTEN BRECHEN		ZEICHNUNG NICHT SKALIEREN		ÄNDERUNG	
NAME	SIGNATUR	DATUM				BENENNUNG:			
GEZEICHNET									
GEPRÜFT									
GENEHMIGT									
PRODUKTION	SolidWorks Studenten-Edition.								
QUALITÄT	Nur für akademische Zwecke.								
					WEICHSTOFF: Aluminium	ZEICHNUNGSNR. FingerBottomPressurePlate			
					GEWICHT:	MASSSTAB:1:1		BLATT 1 VON 1	



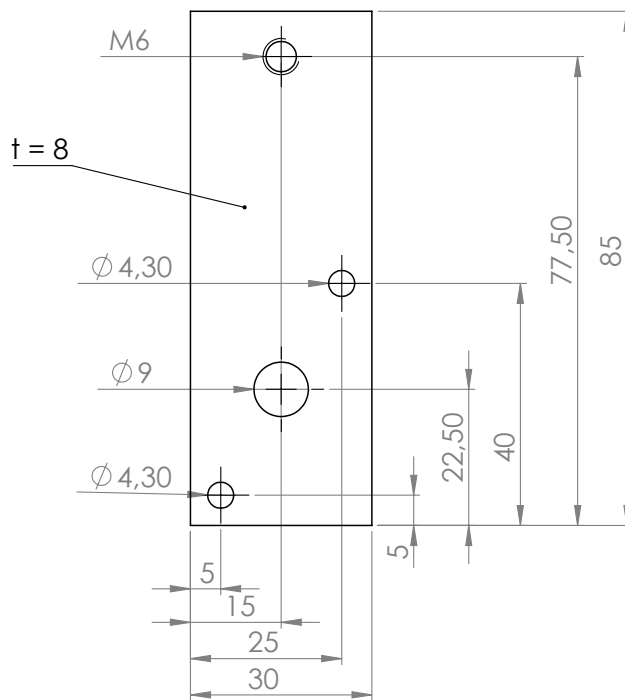
WENN NICHT ANDERS DEFINIERT: BEMASSUNGEN SIND IN MILLIMETER OBERFLÄCHENBESCHAFFENHEIT: TOLERANZEN: LINEAR: WINKEL:		OBERFLÄCHENGÜTE:		ENTGRATEN UND SCHARFE KANTEN BRECHEN		ZEICHNUNG NICHT SKALIEREN		ÄNDERUNG	
NAME	SIGNATUR	DATUM				BENENNUNG:			
GEZEICHNET						SolidWorks Studenten-Edition. Nur für akademische Zwecke. <small>WERKSTOFF:</small> Aluminium			
GEPRÜFT									
GENEHMIGT									
PRODUKTION									
QUALITÄT						ZEICHNUNGSNR.	FingerSides		A4
					GEWICHT:	MASSSTAB:1:1	BLATT 1 VON 2		



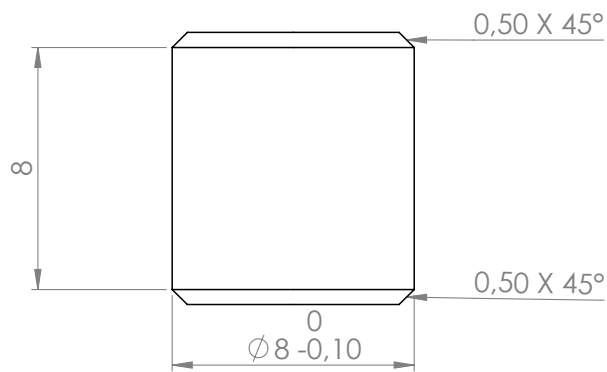
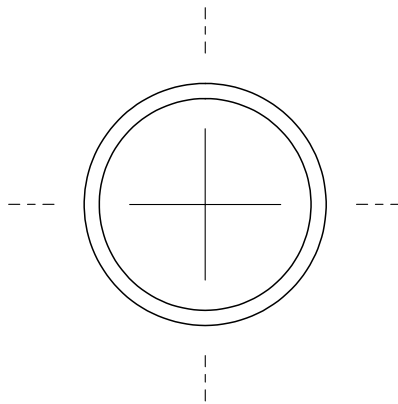
A (2 : 1)

enge Toleranz am Scheitelpunkt benötigt

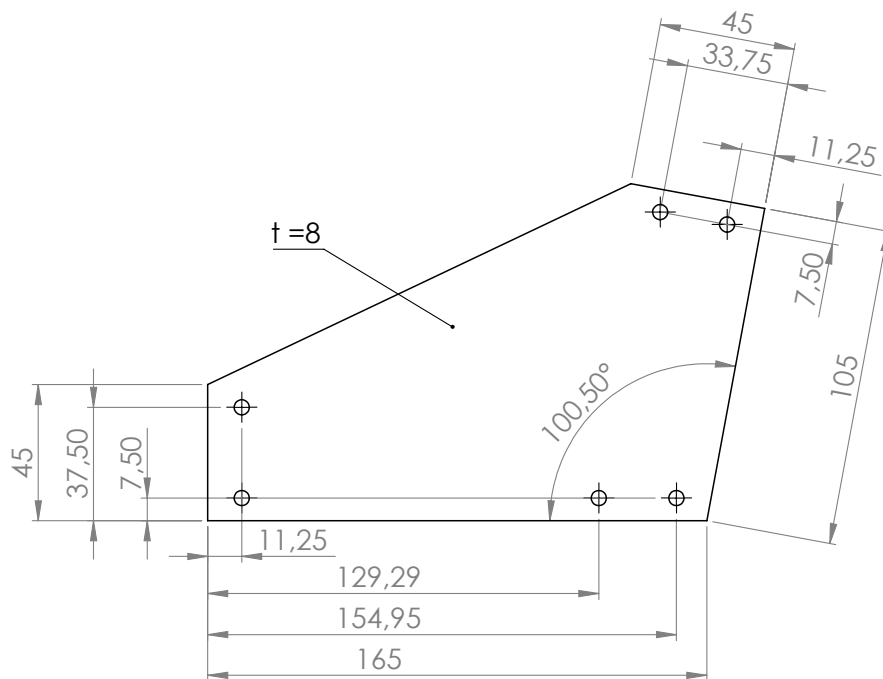
WENN NICHT ANDERS DEFINIERT: BEMASSUNGEN SIND IN MILLIMETER OBERFLÄCHENBESCHAFFENHEIT: TOLERANZEN: LINEAR: WINKEL:		OBERFLÄCHENGÜTE:		ENTGRATEN UND SCHARFE KANTEN BRECHEN		ZEICHNUNG NICHT SKALIEREN		ÄNDERUNG	
NAME	SIGNATUR	DATUM				BENENNUNG:			
GEZEICHNET						SolidWorks Studenten-Edition. Nur für akademische Zwecke. <small>WERKSTOFF:</small> Aluminium			
GEPRÜFT									
GENEHMIGT									
PRODUKTION						ZEICHNUNGSNR.	FingerSides		A4
QUALITÄT						MASSSTAB:1:1	BLATT 2 VON 2		
					GEWICHT:				



WENN NICHT ANDERS DEFINIERT: BEMASSUNGEN SIND IN MILLIMETER OBERFLÄCHENBESCHAFFENHEIT: TOLERANZEN: LINEAR: WINKEL:		OBERFLÄCHENGÜTE:		ENTGRATEN UND SCHARFE KANTEN BRECHEN		ZEICHNUNG NICHT SKALIEREN		ÄNDERUNG	
NAME		SIGNATUR		DATUM		BENENNUNG:			
GEZEICHNET		GEPRÜFT		GENEHMIGT		SolidWorks Studenten-Edition. Nur für akademische Zwecke. FingerSidesPressurePlate			
PRODUKTION		QUALITÄT		WERKSTOFF: Aluminium					
				GEWICHT:		MASSTAB:1:1		BLATT 1 VON 1	



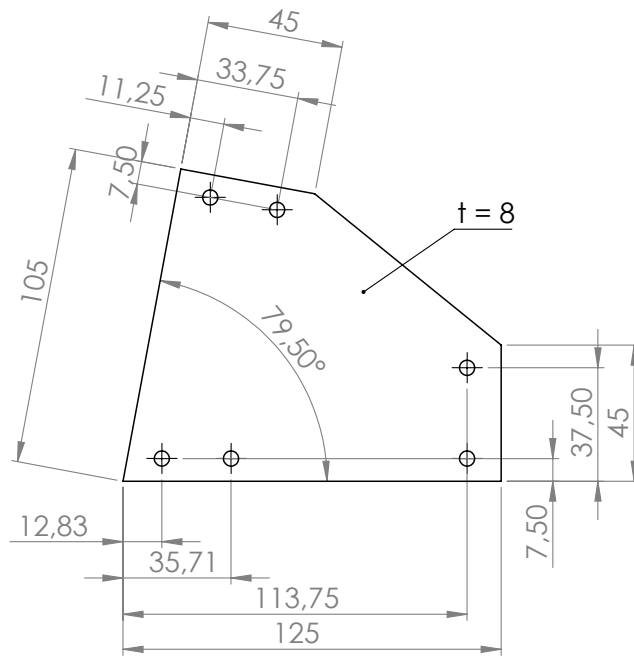
WENN NICHT ANDERS DEFINIERT: BEMASSUNGEN SIND IN MILLIMETER OBERFLÄCHENBESCHAFFENHEIT: TOLERANZEN: LINEAR: WINKEL:		OBERFLÄCHENGÜTE:		ENTGRATEN UND SCHARFE KANTEN BRECHEN		ZEICHNUNG NICHT SKALIEREN		ÄNDERUNG	
NAME		SIGNATUR		DATUM		BENENNUNG:			
GEZEICHNET		GEPRÜFT		GENEHMIGT		SolidWorks Studenten-Edition. Nur für akademische Zwecke. <small>WERKSTOFF:</small> Edelstahl			
PRODUKTION		QUALITÄT		ZEICHNUNGSNR.					
				GEWICHT:		MASSSTAB:5:1		BLATT 1 VON 1	



Durchmesser aller Bohrungen: 5 mm

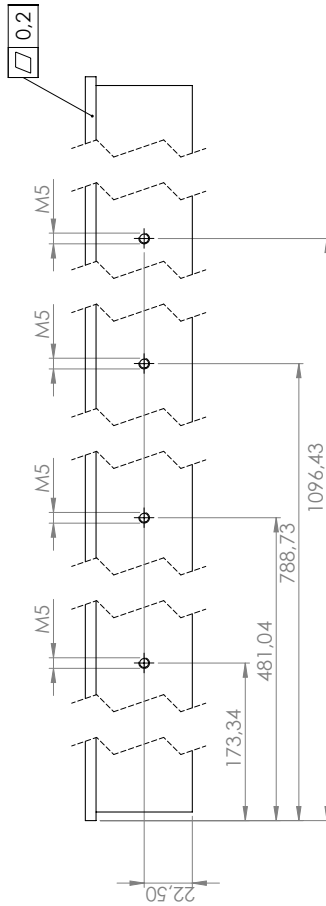
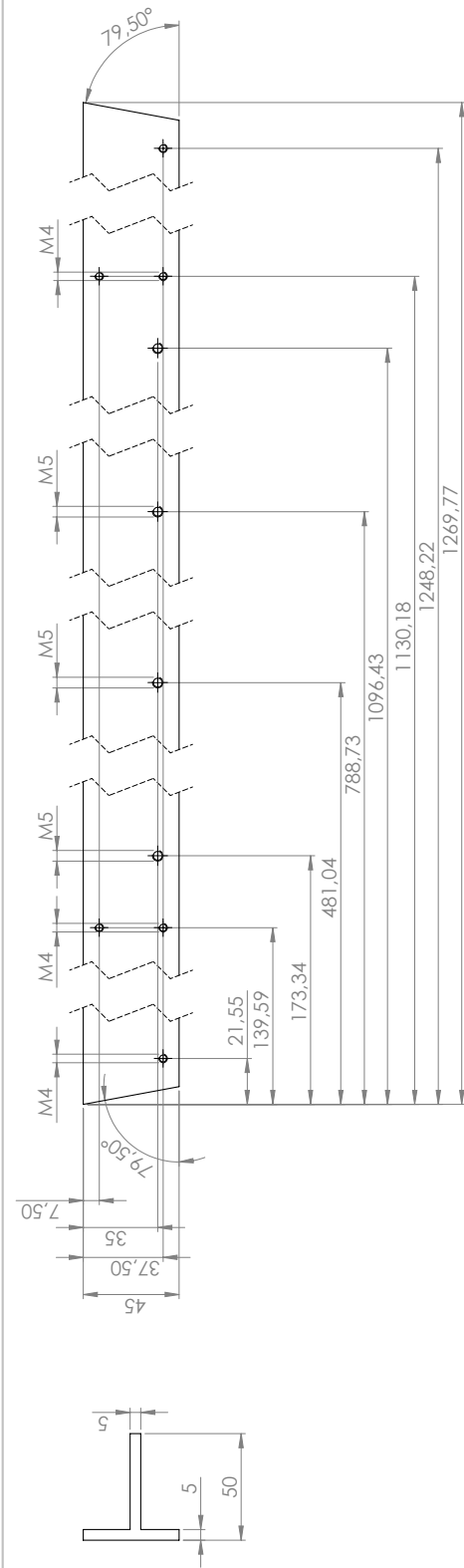
WENN NICHT ANDERS DEFINIERT: BEMASSUNGEN SIND IN MILLIMETER OBERFLÄCHENBESCHAFFENHEIT: TOLERANZEN: LINEAR: WINKEL:		OBERFLÄCHENGÜTE:		ENTGRATEN UND SCHARFE KANTEN BRECHEN		ZEICHNUNG NICHT SKALIEREN		ÄNDERUNG	
NAME		SIGNATUR		DATUM		BENENNUNG:			
GEZEICHNET		SIGNATUR		DATUM		ZEICHNUNGSNR. CornerBottom			
GEPRÜFT		SIGNATUR		DATUM					
GENEHMIGT		SIGNATUR		DATUM					
PRODUKTION		SIGNATUR		DATUM					
QUALITÄT		Werkstoff: Aluminium		GEWICHT:		MASSSTAB:1:2		BLATT 1 VON 1	

SolidWorks Studenten-Edition.
Nur für akademische Zwecke.



Durchmesser aller Bohrungen: 5 mm

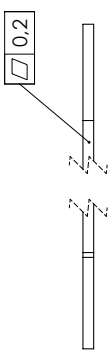
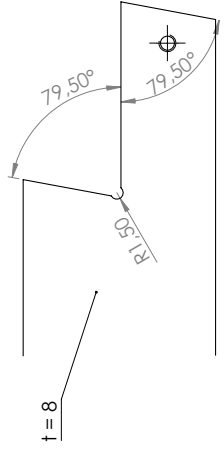
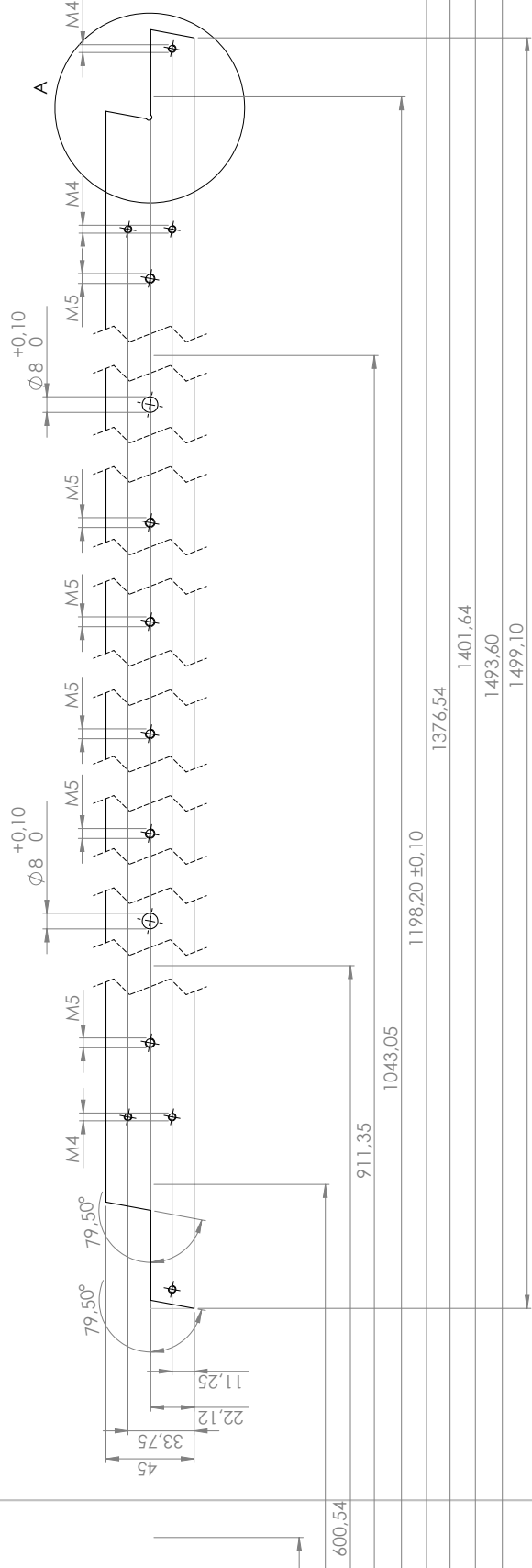
WENN NICHT ANDERS DEFINIERT: BEMASSUNGEN SIND IN MILLIMETER OBERFLÄCHENBESCHAFFENHEIT: TOLERANZEN: LINEAR: WINKEL:		OBERFLÄCHENGÜTE:		ENTGRATEN UND SCHARFE KANTEN BRECHEN		ZEICHNUNG NICHT SKALIEREN		ÄNDERUNG	
NAME		SIGNATUR		DATUM		BENENNUNG:			
GEZEICHNET		GEPRÜFT		GENEHMIGT		ZEICHNUNGSNR. CornerTop			
PRODUKTION		QUALITÄT		WERKSTOFF: Aluminium					
GEWICHT:		MASSSTAB:1:2		BLATT 1 VON 1					



WENN NICHT ANDERS DREHWEISE ANGEZEIGT, SIND ALLE DIMENSIONEN IN MILLIMETER ANZUGENOMMEN.		ZEHNUNG NICHT SKALIEREN		ÄNDERUNG	
OBERFLÄCHENGÜTE:		ENTGRATEN UND SCHÄRFE			
FUNKTIONELLE BESCHREIBUNG:		KANTEN			
WINKEL:		RÄUMLICH			
NAME	SIGNATUR	DATEI	BENENNUNG:		
GEZEICHNET					
GEPRÜFT					
GENÜHMIGT					
PRODUKTION					
QUALITÄT					
WERKSTOFF: Aluminium			ZEHNUNG: FrameBottom		
GEWICHT:			MASSTAB: 1:2		
			BLATT VON 1		
			A3		

**SolidWorks Studenten-Edition.
Nur für akademische Zwecke.**

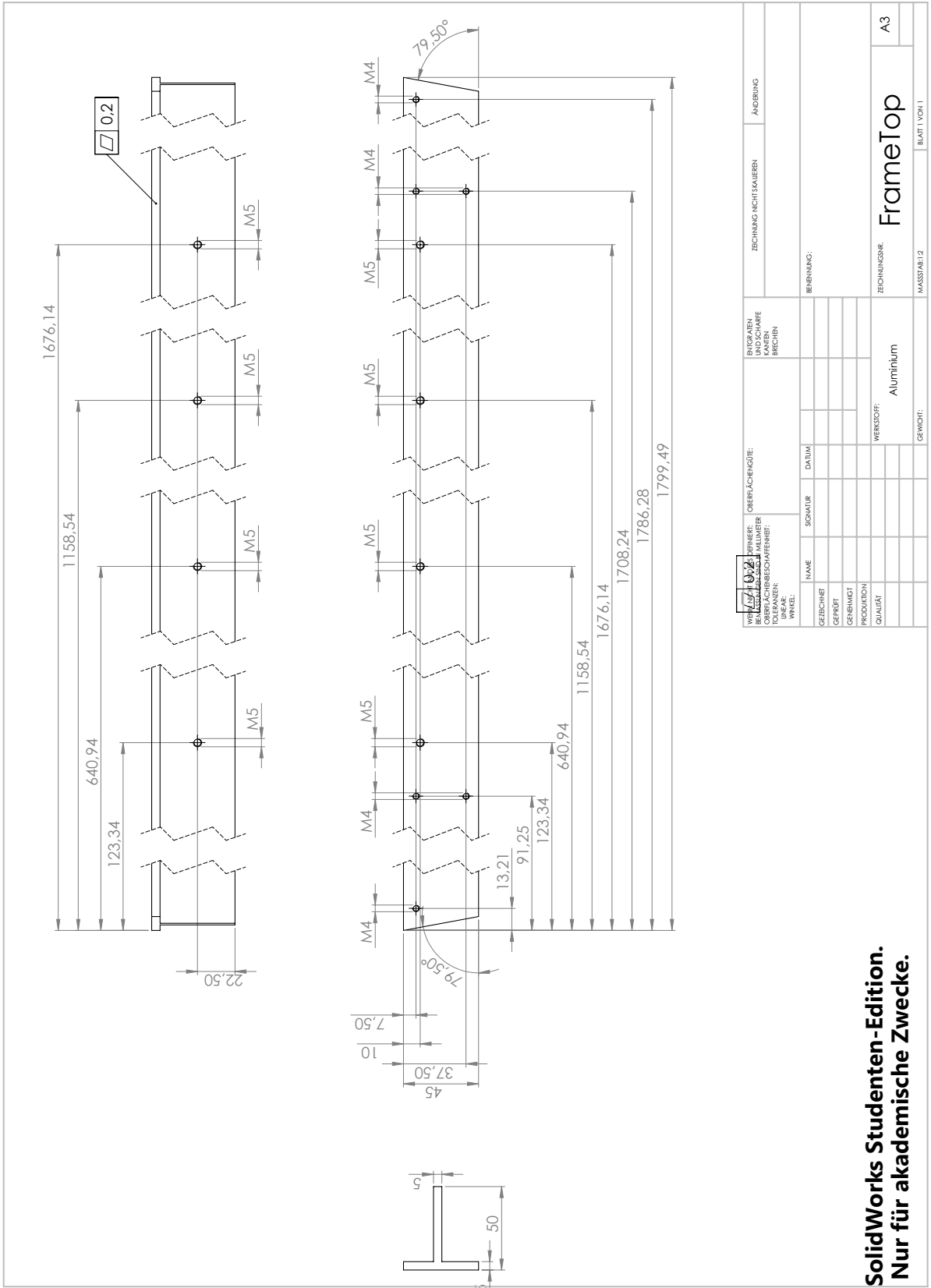
Toleranz der horizontalen Ausrichtung der 8mm Bohrungen: 0.1 zur präzisen Kanten (obern in Draufsicht ht)



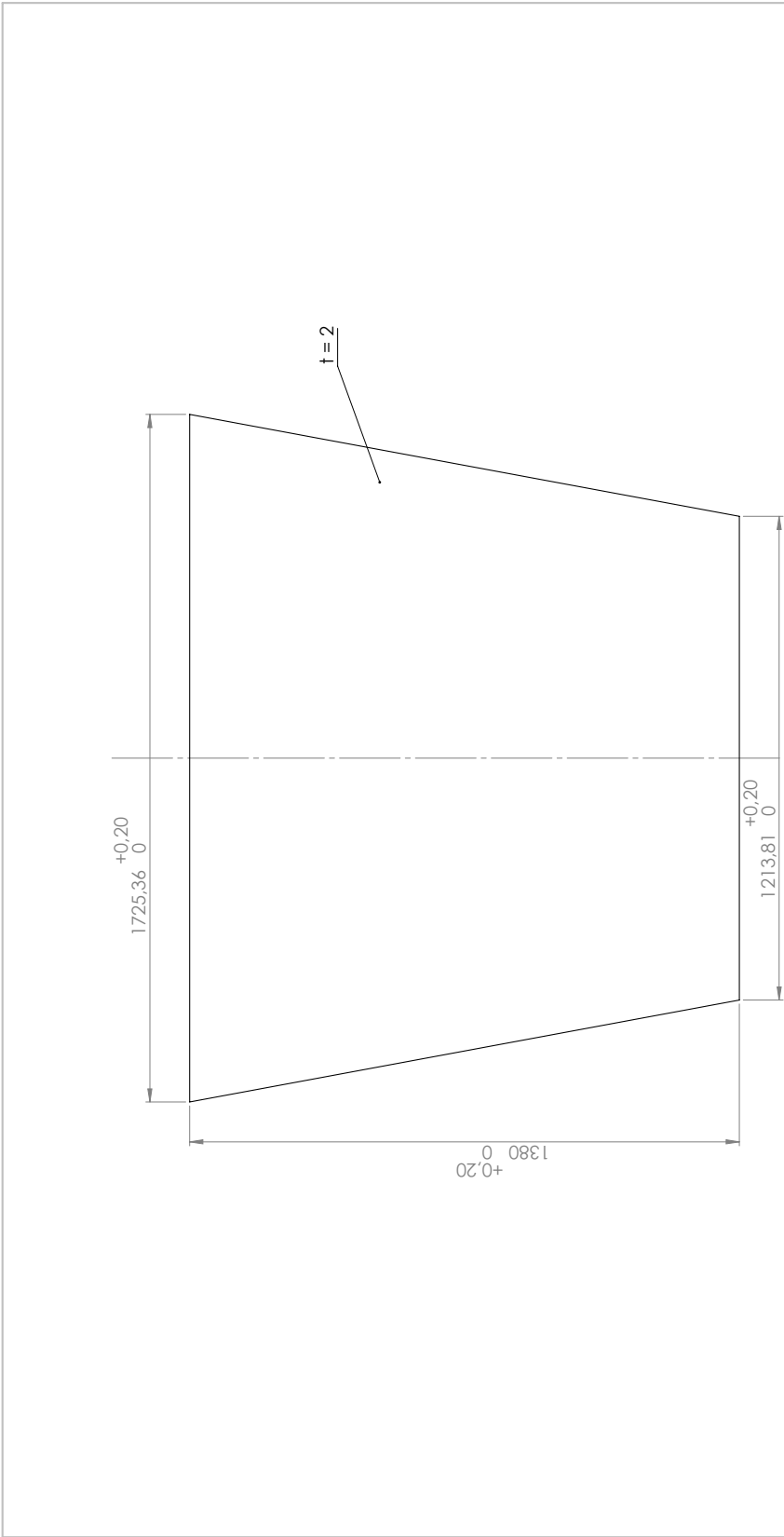
A (1 : 1)

WENN NICHT ANDERS DREHMER: BEWASSUNGEN SIND IN MILLIMETER ANGEBEN WINKEL:		OBERFLÄCHENGÜTE:		ENTGRATEN UND SCHARFE KANTEN ABRUCHEN		ZEHNUNG NICHTSALBERN		ÄNDERUNG	
GEZEICHNET	NAME	SIGNATUR	DATEUM						
GEPROBT									
GENEHMIGT									
PRODUKTION									
QUALITÄT									
				WERKSTOFF: Aluminium		ZEHNUNGSSUR: FrameLeft		A3	
				GEWICHT:		MASSSTAB: 1:2		BLATT VON: 1	

SolidWorks Studenten-Edition.
Nur für akademische Zwecke.



SolidWorks Studenten-Edition. Nur für akademische Zwecke.



alle Flächen an Außenseite (Höhe 2 mm) mit Ebenheit 0.2

WENN NICHT ANDERS DREHMER: BESMASSUNGEN SIND IN MILLIMETER		OBERFLÄCHENGÜTE:		ENTWERFEN		ZEICHNUNG NICHTSULESEN		ÄNDERUNG	
OBERFLÄCHENBESCHAFENHEIT:				UNDSCHWARZE					
TOLERANZEN:				STRICHEN					
WINKEL:									
GEZEICHNET	NAME	SIGNATUR	DATUM	BENENNUNG:					
GEPROBT									
GENÜHMIGT									
PRODUKTION				WERKSTOFF:					
QUALITÄT				ZEICHNUNGSUR:					
				Gage					
				A3					
				MASSTAB: 1:10					
				BLATT VON 1					

**SolidWorks Studenten-Edition.
Nur für akademische Zwecke.**

A.2.2 SM2 Drift Panel Construction Manual

SM2 Driftpanel Construction Manual for the Mainz Construction Site



Last modified: 16/05/2017

Contents

1	Introduction	2
2	Part arrival and Quality control	2
2.1	Labeling of the parts in the database	2
2.2	PCB	4
2.3	Extruded aluminum bars	5
2.4	Honeycomb	6
3	First Construction Day	7
3.1	Beforehand preparations	7
3.2	First day overview	7
3.3	Required material	7
3.4	Preparation of the Stiff-backs	8
3.5	Test Alignment	9
3.6	Gluing of first side	10
4	Second construction day	12
4.1	Preparations and Test Alignment	12
4.2	Second day gluing	15
5	Panel Dismantling and QC	16
5.1	PCB Cutting	16
5.2	PCB Gap Sealing	17
5.3	Panel Quality control	18

1 Introduction

This document provides a manual for the construction of drift panels for the the ATLAS NSW Upgrade. The construction steps for the production site at the Johannes Gutenberg University Mainz are described here.

The constructed drift panels have a trapezoidal shape with a long side of 1698.93 mm, a short side of 1188.87 mm and a height of 1350 mm. The panels are built as a sandwich structure. The outer surface are three 0.5 mm FR4 sheets on each side, particular with an etched copper coating as cathode. The panel is stiffened by a 10 mm high frame of extruded aluminum profiles and a 10.1 mm micro-perforated aluminum honeycomb.

The construction takes place in the PRISMA Detetor Lab in Staudingerweg 9 00-121. The lab is equipped with an automatic 3D positioning system (CMM) with a laser distance sensor on a precision granite table for the flatness measurement of the panels and an laminar flow box to provide clean conditions.

The laminar flow box has an extension for the construction of the drift panels in a dust reduced environment. To achieve the required average surface planarity of 37 μm in the drift panel construction two precision aluminum vacuum tables have been constructed, both with an average planarity better than 25 μm . They are placed in the flow box extension under a crane to support their transport during the sandwich construction. The setup is shown in Fig. 1.

The construction process is structured as follows:

Most parts are delivered from CERN as raw material which has to be cut in shape. The material will be prepared for the gluing and a quality control (QC) is performed after the delivery and machining. The PCBs have a border of ≈ 15 mm to the outer side. This prevents the glue to flow around the border of the PCB. The redundant material will be cut after the gluing.

The extruded aluminum bars are delivered as long bars. The will be cut by an external company to the shape necessary for the panel construction.

The honeycomb is delivered in large sheet. It will be cut with a template before the construction.

The construction itself takes place on two days. The first day the honeycomb and the extruded bars are glued to one layer of PCBs. The second day an electrical contact between all metallic parts glued at the first day is ensured and the sandwich is closed with the second side of PCBs.

The manual structures as follows:

First the necessary steps for the quality control of the processed raw material are discussed. Next the working steps for the construction at the two days is described. In each section first the needed materials are stated and afterward the working procedure is explained in detail.

2 Part arrival and Quality control

2.1 Labeling of the parts in the database

All parts are registered in a database. Two different databases are installed at CERN. The logistics database to keep track of the parts location and the central

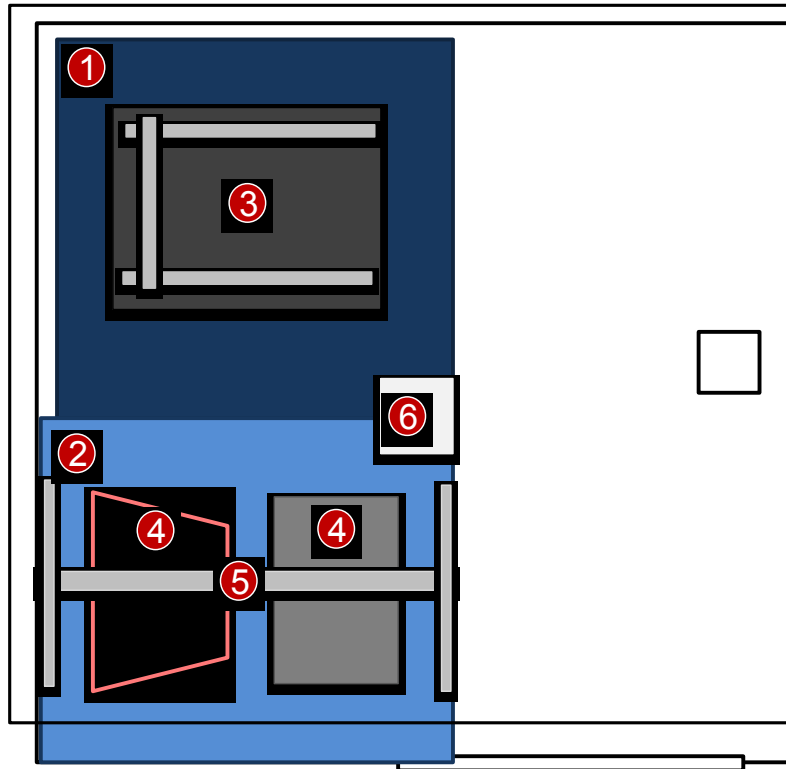


Figure 1: Overview of the infrastructure of the lab. Inside the laminar flow box (1) the granite table with the CMM measurement system is placed. The panel construction is done in the extension of the flow box (3) on the vacuum tables. The vacuum table on the left side has an alignment frame mounted and is called vacuum table 1 (the other one vacuum table 2 respectively) in the following. A crane (5) is used to handle the vacuum table. Between the flow box and it's extension, a table for the preparation of the tools is placed.

Table 1: Equipment types in the database

FDRI	frame type 2.1 (outer frame)
FDII	frame type 2.2 (inner frame)
HOCL	honeycomb raw material
HCS6	cut honeycomb small
HCS7	cut honeycomb middle
HCS8	cut honeycomb large
BOS6	outer skin board small
BOS7	outer skin board middle
BOS8	outer skin board large
BDS6	cathode board small
BDS7	cathode board middle
BDS8	cathode board large
DS2O	outer drift panel
DS2C	central drift panel

database for the storage of the quality control results. At the construction site, one database which exports to both databases at CERN is installed.

In the database, all parts are identified by a global, unique Id. To refer to the different parts, each item is described as well by a four digit equipment type. A list of all the relevant equipment types is given in table 1. For the interaction with this database a python GUI is implemented. Different views for each item in the construction are implemented to be selected on the left side. For each item, tabs showing the material in different stages of the construction are given. The workflow structures as follows: To import the items from the logistics database, a .csv file is created via the webinterface (<http://atlas-project-nsw-log.web.cern.ch/atlas-project-nsw-log/LOG.php?page=overview>) and imported to the local database via the *Update Database* button.

Before a panel can be build, the quality control has to be performed on the parts used in the panel. During the panel construction, the parts are linked to the panel referred by their id. In this stage, only parts with a finished quality control are available. After the linking is finished, the parenting has to be written to a file for the export to the logistics database before the quality control of the panel can be started.

A detailed overview on the database handling can be found in a dedicated database manual.

2.2 PCB

There are six different kinds of PCB formats used in the construction. Each surface of a panel consist of three PCB sheets. Two different kind of surfaces exist. The cathode surface with a etched copper layer facing the inside of the detector and a surface forming the outside of the chamber. This surface is of plain FR4 without any copper coating.

The PCBs are unpacked on the arrival, registered in the local database and checked by a visual inspection. It is necessary to check for a straight cut on the outside and the completeness and cleanness of the copper surface. If dust or

changes in the color can be found on the copper surface the electrical contact of the spot has to be examined. Areas with no electrical contact or salient material cannot be accepted and the PCB shall be rejected.

For the further quality control of the PCB the thickness is measured at the border of the PCB at 20 uniformly distributed points.

The minimum thickness should be more than 0.45 mm and the maximum thickness less than 0.55 mm. All measured values are entered in the local database. After the quality control, the PCBs are stored in a humidity controlled storage box in the lab to avoid an elongation with humidity absorption.

2.3 Extruded aluminum bars

There are aluminum bars in two different width. 30 mm wide bars are used outer frame of the panel. 26 mm wide bars are used as internal bar at the junctions between two PCB sheets.

After the bars are cut in a company, the quality control is performed. The results of the inspection are entered to the local database.

The quality check is performed on the vacuum table in the basement.

Quality Check	Description	Limits
visual inspection	The bar is checked by eye for scratches and cuts and material which sticks out.	Rejected if material stick out of nominal shape.
vertical bending	The bar is put on the vacuum table next to a ruler with one small side facing down. The gap between the bar and the granite table is measured with precision gauges in steps of 50 μm and sizes and position of the largest gap is recorded in the database. Afterwards the bar is rotated and the check is redone for the other side.	max gap 0.2 mm
thickness	The control of the thickness of the bar is performed with a limbo test. Two precision brass gauges are used in combination with an Ohmmeter. The gauges are slid on a plastic foil on the vacuum table over the bar. One gauge defines the minimum thickness and should always have electric contact with the bar. The other one defines the maximum thickness and should never have contact with the bar.	check for constant electric contact/non-contact minimum gauge height: 9.94 mm maximum gauge height: 10.06 mm

After the registration in the database and the quality check the bars are put in

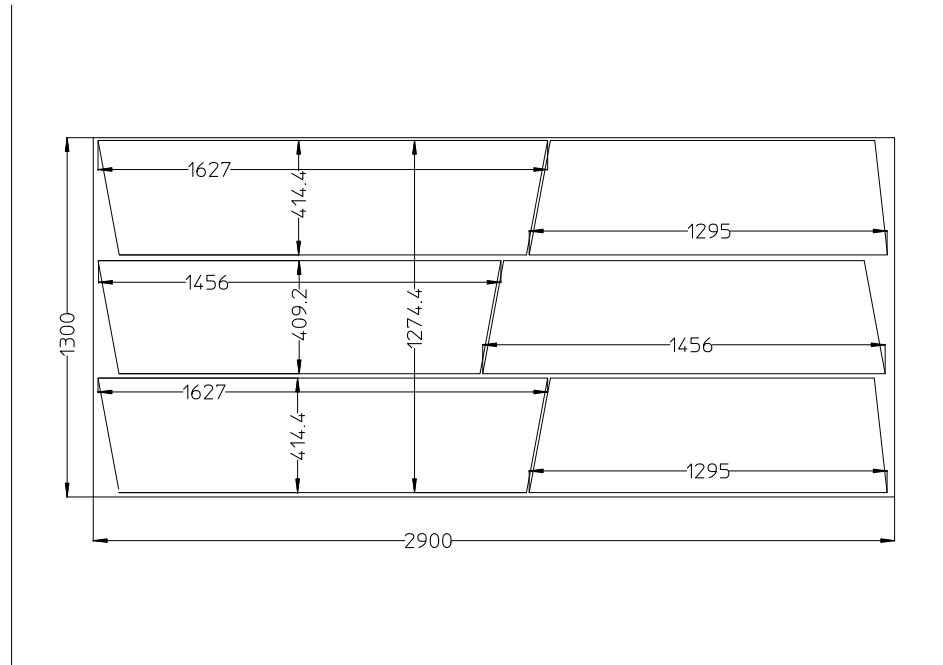


Figure 2: Cutting scheme for the honeycomb. Sheets for 2 Drift Panels can be cut from one raw sheet of honeycomb.

the shelf in the basement storage sorted by the different sizes.

2.4 Honeycomb

All sheet of honeycomb are cut to size for the assembly of the panel. For each panel three pieces of honeycomb with three different sizes are necessary. The big raw sheets are put to an table and the metal templates for the cutting are placed on top. The outer dimensions of the template are cut with an angle grinder with a thin disc in the honeycomb. The cutting follows the cutting scheme in Fig 2.

For the quality control the thickness of each cut piece is measured with a depth gauge. Therefore the Honeycomb is flushed with compressed air and put to the granite table in the laminar flow box. The honeycomb is pressed down with the measurement tool to the granite table during the measurement and the thickness is measured in a grid of $20 \times 20 \text{ cm}^2$. The values are stored in the local database. The limit for the maximum value is 10.3 mm and the minimum value 9.9 mm.

3 First Construction Day

3.1 Beforehand preparations

As preparation of the gluing, the interconnection reinforcements, the HV-feedtrough and the gas connectors have to be cleaned in an isopropyl ultrasonic bath (20 min).

Additionally, the gas connectors have to be glued and tested for tightness. The gas pipe has to be screwed and glued into the disk like connector to the panel gas pipe. Therefore a thin layer of Araldite 2012 is applied to the thread of the pipe. To avoid the glue to ooze out to much, only the grooves of the thread should be filled. The gas pipe is screwed 5 mm into the disk like piece. The screwing depth has to be check by measuring the salient lenght of the pipe (58 mm).

After the curing of the glue (over night) the thightness has to be tested. Therefore a special compressed air pistol with a M5 connector exists. The M5 connector is screwed into the end of the gas pipe. While pressing rubber plates on the holes in the disk like connector and holding the glued junction in a bowl with distilled water 2 bar overpressure are applied and the gluing is observed for leaking air bubbles.

3.2 First day overview

On the first construction day, the preparation of the materials and the gluing of the honeycomb and the extruded aluminum frames to the PCBs is performed. As starting point, the two vacuum tables are laying next to each other and the surface of the vacuum table without alignment frame is covered by a wooden plate on styrodur support for protection. At the first day, this vacuum table serves as a table used for the preparation of the material.

All materials have to be flushed with compressed air and cleaned with an isopropyl soaked tissue before they are moved to the construction area in the extension of the laminar flow box.

During all work, gloves, a clean room coat and a hairnet should be worn, on one hand to avoid the spread of dirt and grease from the skin to the parts and on the other hand to protect from the cleaning agents and the glue.

For all works at both construction days, where the large PCBs, or the work-piece is handled two people are necessary.

3.3 Required material

In the following list the material, excluding the fixed infrastructure in the lab, which is needed for the construction on the first day is mentioned. The list is ordered by the chronology the material is needed:

- One PCB foil of each size
- One piece of each size of honeycomb
- Complete aluminum frame
- 6 interconnection reinforcements
- 4 HV feed-through s

- 4 assembled gas connector pieces

The necessary tools for the first day gluing is listed below:

- Cleaning tissue
- Isopropyl
- Acetone
- Capton tape (65 μm thick, 6 mm and 12 mm wide, brownish tape)
- Electrical insulation tape (black tape)
- Vacuum tape (black clay-like tape)
- Clay for gas pipe sealing
- M5 screws to close gas pipe
- Marker + distance tool for marking
- Araldite 2011
- Glue mixing bowl, spatula (0.2 mm wires) and balance
- Frame gluing tool

In the construction it is aimed for an uniform layer of 200 μm glue. This can be either achieved by a standard toothed spatula with 400 μm teeth. The experience showed, that the metal teeth of a spatula are likely to deattach tape from the PCBs. Better results have been achieved with a flat spatula, where every few centimeter a 200 μm wire is routed through holes in the spatula close to the edge. The wire is routed around the edge of the spatula and the two ends of the wire are fixed with a knot. Like this, the thickness of the glue is also independent of the angle of the spatula to the glue surface. In the following the single steps of the production are presented in a sorted list. The procedure includes the preparation of the parts, a test alignment and the final gluing. The steps of the gluing shall be documented in the foreseen quality control sheet and a check list is followed to remember all steps.

3.4 Preparation of the Stiff-backs

1. Cover second vacuum table with protection layer and wooden plate
2. Clean surface of first vacuum table with Isopropyl
3. Check surface by sight inspection
4. Put fingers in place next to mounting position (distinct position marked by number)
5. The fingers need to be checked for glue remnants and cleaned if necessary
6. Mount fingers on the short side and one of the inclined sides of the trapezoidal

3.5 Test Alignment

1. Place PCB with copper side up on table
2. Clean upper PCB surface with isopropyl and check for remaining dust
3. Clean PCB and vacuum table surface with sticky roller
4. Place PCB with copper side down on cleaned vacuum table and fix them with the fingers
5. Check all fingers while placing them for remaining glue from the last gluing
 - (a) Put lower PCB on the vacuum table and push it against the already mounted fingers
 - (b) Place missing two fingers on the inclined side and fix them
 - (c) Successive place the remaining PCB foils, push them against the already aligned PCBs and and fingers and fix the missing fingers
6. If one finger does not fit, check the planarity of the side and the opposite side of PCB with the straight-edge and scratch redundant material with a knife or a file (careful, not to scratch the vacuum table and avoid dust under the PCB, best to move PCB out). Report on the gluing sheet.
7. Place ≈ 5 cm long $400 \mu\text{m}$ copper wire on both sides of the gap between the PCBs
8. Seal the gab between the PCBs with 6 mm capton tape
9. Pump vacuum to vacuum table 1 (-300 mbar)
10. Seal outer side of PCBs with 12 mm capton tape (successively remove and remount fingers)
11. To press on the tape, a wrinkled mylar foil can be used along the straight sides and a small FR4 piece with round corners can be used at the corners of the PCB.
12. Place the outer aluminum bars inside the alignment frame on top of PCB
13. Check if the bars fit well (no gap to reference point on fingers)
14. Place internal bars so that cuts fit to external frame
15. Place honeycomb inside and cut to length if necessary
16. Prepare grounding contact pieces with all surrounding frames by opening cells of the honeycomb
17. Place HV feed-through at the pipe in the side bars and cut the honeycomb to fit around the connector
18. Check the side bars for a bending to the inside (non contact with the fingers). If this happens, glue a thin metal contact to the inside of the bar with cyanoacrylate glue while the frame is pushed to the foreseen position. The possible positions of contact pieces can be seen in Fig 3

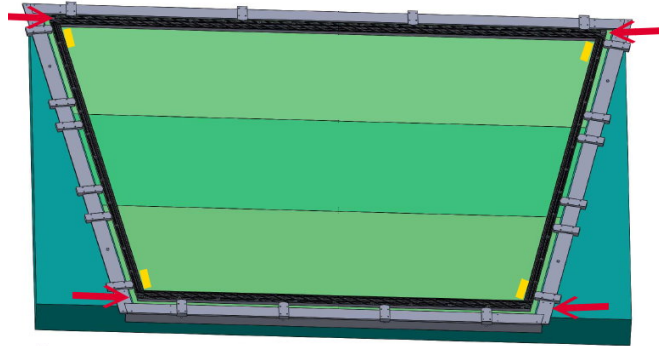


Figure 3: Possible position for contact piece in case of bend side bars (yellow) and the position of the cyanoacrylate glue drops to avoid the shift of the parallel bars (red arrow).

19. Place the interconnection reinforcement pieces in the honeycomb and check their alignment with the templates or by the footprint of the PCB (if necessary widen the holes in the honeycomb)
20. Remove honeycomb, aluminum bars and the HV feed-through and place them in the same orientation on the wooden plate
21. Seal the holes in the gas connector and the HV feed-through with round pieces of capton tape
22. Seal the groove with the gas pipe in the bar with clay from the outside

3.6 Gluing of first side

1. Apply two layers of polyester strips (6 mm wide) on bars to ensure minimum thickness of the glue.
 - (a) Every 10 cm two layer of tape perpendicular to long side of the bar
 - (b) The tape should leave a few mm of plain bar on each side for a better gluing contact to the bar
2. Clean the PCB and the frames with acetone as a final de-greasing before the gluing
3. Mark the outer line of the glue with the template (20 mm distance to the alignment frame) on the PCBs
4. Clean the PCBs with the sticky roller, to remove last dust
5. Mix Araldite 2011 (720 g, A: 400 g, B: 320 g)
6. Apply a uniform layer of glue to the PCB using the wired spatula until the contact point of the frame with the fingers

7. Apply glue with the dedicated tool to the bars to fill the grooves
8. Place bars on PCB, as for the dry assembly starting with the outer frame
9. Fix the upper and lower frame on the inclined side with a drop of cyanoacrylate glue and hardener to avoid a shift (see Fig 3)
10. Position the HV feed-through at the frame on the glue surface (Apply a thin layer of glue to the cylindrical extension going into the bar)
11. Place honeycomb inside and press into the glue
12. Apply glue to the downside of the interconnection piece
13. Position interconnection piece at the foreseen place
14. Check the interconnection position with a template and if necessary fix them by shimming with o-ring pieces toward the honeycomb
15. Bend grounding connection of honeycomb toward frame
16. Place the gas connector and check the seal on the outside of the frame cutout
17. Fill the cutout in the frame with glue and apply a 9 mm wide capton strip on top
18. Check the aluminum gauge for remaining glue from the last gluing
19. Place the trapezoidal aluminum gauge on top of the honeycomb and the bars
20. Check for well fitting at the contact point of the fingers
21. Place frame with vacuum foil on top of the alignment frame
22. Check the position of the frame and the spacer over the fingers
23. Seal the gap between the vacuum frame and the alignment frame with insulating tape
24. Apply vacuum to vacuum bag
25. Seal leakages (specially at the corner and sometimes on the top side of the vacuum table under the alignment frame) with vacuum tape
26. Check and regulate the pressure inside vacuum bag to be ≈ 100 mbar more than in vacuum table
27. Apply a small quantity of remaining glue on a tape placed near the vacuum table and write down the finish time of the gluing
28. Clean all tools which have been in contact with the glue with warm water
29. Curing time of the glue: ≈ 24 h

4 Second construction day

In the following section the construction steps, performed at the second day are described in detail. The gluing of the first day has to be dismantled, the quality of the gluing needs to be checked and the grounding connection between the honeycomb and the frame has to be ensured. Next, the piece glued on the first day is transferred to the second vacuum table and the new PCB is prepared in the alignment frame. Special, thinner, fingers are mounted at the alignment frame and after the application of the glue on the new PCB, the sandwich is closed with the work-piece on the second vacuum table.

A list of the necessary tools is given here:

- Thin pliers and small side cutter
- Ohmmeter
- Silver paint and narrow piece of PCB/plastic to apply the paint
- Glue gun with Araldite 2012
- Tissue
- Isopropyl
- Cyanoacrylate (fast curing) glue and hardener
- Sticky roller and sticky paper
- Capton tape (15 mm wide)
- Copper tape
- Distance pieces
- Double sided tape
- Marker
- Araldite 2011
- Mixing bowl and spatula (0.6 mm tooth or 0.3 mm wires)

4.1 Preparations and Test Alignment

1. Remove the wooden platen from the second vacuum table
2. Clean the surface of the vacuum table with isopropyl
3. Check glue sample on the tape for curing (glue must not be sticky or flexible any more)
4. Remove tape connection between the vacuum frame and the alignment frame
5. Disconnect vacuum connection from vacuum bag, leaving vacuum in the vacuum table

6. Remove vacuum bag
7. Remove trapezoidal pressure plate
8. Clean the plate from glue
9. Check planarity of the honeycomb with respect to the frames with straight-edge
10. If the honeycomb is not flat, use fine sandpaper to remove overhang
11. Bend the flags on the honeycomb toward the frame using the pliers. If necessary, make a small cut with the side cutter to get a movable flag of honeycomb.
12. Fix the grounding connection to the frame with fast curing glue and hardener
13. Apply a layer of silver paint from the grounding connection to the frame
14. Apply a silver line between the gas manifold, the gas pipe and the aluminium frame
15. Measure the conductivity between the frame and the honeycomb
16. Seal all silver line connections after curing with Araldite 2012
17. Unscrew the alignment fingers
18. Check the alignment fingers for sticking glue, clean them and place in the pockets at the vacuum table
19. Vent the vacuum table
20. Clean the second vacuum table with the sticky roller as described above
21. Fix a M4 screws on each end of top and bottom bar and connect the half panel with the white wire to the crane
22. Remove work-piece with the crane (slow lifting) from vacuum table 1 and place it on vacuum table 2
23. While moving the piece, remove copper wires between the PCBs and check the thickness with a micrometer screw. If the thickness is below 10.5 mm, 0.4 mm wires have to be used as distance pieces in the spatula. Otherwise 0.3 mm wires can be used.
24. Apply vacuum to vacuum table 2 (-200 mbar)
25. Seal the border of the workpiece with tape (12 mm capton tape)
 - (a) Place 0.4 mm wire under the tape next to the PCB and rout the wire to the outside of the vacuum table for later removal of the tape (route back on the included sides, because the distance pieces avoid to pull it out between the closed vacuum tables)
 - (b) Seal end of tape and wire with vacuum tape if necessary

- (c) Apply one layer of copper tape on the parallel sides at the position of the distance pieces (marked at the side of the vacuum table)
 - (d) The corners of the copper tape sitting on the vacuum table are bent over to achieve the electrical contact of the copper surface with the vacuum table
26. Check the flatness of the tape at the position of the distance pieces
27. Ensure electrical contact of the copper surface of the tape with the vacuum table surface
28. Place PCBs for the second gluing day with the cathode side up on top of the work-piece on the second vacuum table
29. Clean the PCBs and the vacuum table with the sticky roller
30. Align and suck the PCB to vacuum table 1 as in the previous gluing step
31. Apply vacuum to the vacuum table to suck the PCBs (-200 mbar)
32. Seal the border of the PCB with 12 mm capton tape, but make sure, that the tape is routed to the frame to be able to remove it when the sandwich is closed
33. Place a 0.4 mm wire under the tape next to the PCBs on the inclined side where the thin fingers for the alignment of vacuum table 2 are mounted
34. Rout the wire back to the start on top of the tape that it can be pulled to remove the wire when it is trapped behind the fingers
35. Remove fingers
36. Put the thin fingers on the inclined side facing the wall (two) and the long side (one)
37. Place distance pieces on the vacuum table surface
38. Check the monitoring system by connection the wire to vacuum table 1
39. All LEDs should light up
40. Check the open surface of both vacuum tables for remaining glue. They have to be perfectly clean, because the distance pieces are placed there.
41. Position distance pieces
 - On each side: three pieces, uniformly distributed over the full accessible length
 - Parallel sides: narrow distance pieces positioned on the PCB at the edge, three distance piece uniformly distributed over each side.
 - Attached the distance pieces on the inclined side with double sided tape to the alignment frame.
42. Flip second vacuum table with workpiece as a test and check for contact with distance pieces (check monitoring LEDs)

43. If not all LEDs light up, check in the area around the affected distance piece if the honeycomb is higher than the bars with the straight-edge. If so, flatten honeycomb with sandpaper while sucking with vacuum cleaner to avoid spread of the dust.
44. Mark the gluing area on the PCBs with the template

4.2 Second day gluing

1. Clean the PCB surface with the sticky roller
2. Mix Araldite 2011 (0.3 mm wires: 810 g, A: 450 g, B: 360 g; 0.4 mm wires: 900 g, A: 500 g, B:400 g)
3. Apply a uniform layer of Araldite 2011 to the PCBs using the wired spatula and do not exceed the marks
4. Apply glue to the bars of the half panel to fill the grooves
5. Apply glue to the top surface of the interconnection pieces.
6. Flip second vacuum table with work-piece to the first vacuum table
7. Slowly lower the second vacuum table on the last centimetres
8. Make sure to press frame of work-piece against the thin fingers while lowering the vacuum table
9. Never lift the second vacuum table after the work-piece had contact with the glue!
10. Hook tension less metal rope connected to the wall in the loop at the vacuum table
11. Tension the metal rope using the tension lock to press the frame of the work-piece against the contact point of the fingers
12. Check the LED monitoring system (some LED might light up later when the upper vacuum table sinks to the glue, press at the position of non light up LEDs)
13. Do not keep weight for longer than 30 min on top of the second vacuum table to press it into the glue.
14. Apply sample of remaining glue on tape next to the vacuum table and note finishing time
15. Drying time: 24 h

5 Panel Dismantling and QC

First the steps to dismantle the finished panel are described here:

1. Check the glue sample, if the glue is completely cured
2. Vent the top vacuum table
3. Remove the tape to the first vacuum table using the 0.4 mm wires. If intact, save the wires for the next gluing.
4. Lift the top vacuum table, turn it and place it again at the second table
5. Vent the lower vacuum table
6. Remove the tape from the lower vacuum table using the wire
7. Remove the fingers from the alignment frame
8. Check the fingers for remaining glue
9. Lift the sandwich from lower vacuum table
10. Perform the thickness QC of the panel with the micrometer screw

5.1 PCB Cutting

The cutting of the 15mm protrude PCB is done in a dedicated room in 4th floor of Staudingerweg 7. The Panels is moved there on the transport cart, supported on screws in the M4 threads on the long side of the trapezoid. As protection of the dust, a full body suit and a face mask with dust filter has to be worn.

The panel is placed horizontally on the support and the PCBs surface is covered with a foil to shield from dust. The cutting is done with an angle grinder with a thin plate. The grinder always has to be connected to the vacuum cleaner for dust protection. To avoid delamination during the cutting, metal bars are clamped on the side to be cut. An aluminum bar below the panel and an aluminum bar on top of the panel. The top bar also serves as guidance of the saw. The bar is placed inside the panel area. Such, it is ensured, that no projecting PCB is left. The cutting is done with an inclined plate of the grinder pointing toward the panel and the top bar. Such a slipping of the plate along the frame of the panel is avoided.

After both sides are cut, it has to be ensured, that no glue, is left on the bars. If remnants of glue are found, they carefully need to be scratch off with a sharp knife.

After the cutting, the panel is cleaned with a vacuum cleaner and wiped with isopropyl. In the following, a step by step introduction is given.

1. Move the panel on the transport cart to the lab. Screws (4-5) have to be attached to the holes on the long side of the panel as a stand during the transport. The panel cannot stand on the PCBs.
2. Cover the open side of the panel with the foil.
3. Move the panel to the cutting table with the foil facing down.

4. Cover the upper side with foil as well.
5. Attach one clamp to each corner and cut the corners with the angle grinder.
6. Clamp one side with the bars on above and below the panel. The upper bar, which is used as a guidance for the saw, has to be 1-2 mm inside the panel, such that the plate cuts on top of the frame right at the edge.
7. Fix the bar with 4 clamps. The clamps in the middle have to be shifted during the cutting process.
8. For the cutting, hold the angle grinder with an inclination, such that the plate is facing towards the upper bar. Like that, slipping off along the panel is avoided.
9. After the first side is cut, suck the sides with the vacuum cleaner and wipe the foil on the panel with isopropyl.
10. Turn around the panel and cut the other side with the same procedure.
11. After the cutting, scratch remaining glue on the bars with a sharp knife. It is important to scratch off all glue at the bars, because of the tight mechanical tolerances!
12. Use the multimaster with 180 sandpaper to flatten the cut. For that hold the sandpaper surface with 45° inclination on the cut edge.
13. Clean the sides of the panel with the vacuum cleaner.
14. Clean the screws in the gas inlet from the sealing clay with a brush and isopropyl.
15. Wipe the foil surface and the panel side with isopropyl.
16. Remove the top foil cover and wipe the bare panel with isopropyl.
17. Move the panel to the transport cart, with the foil surface facing to the outside.
18. Clean the foil surface with isopropyl.
19. Remove the foil.
20. Clean the panel surface with isopropyl.

5.2 PCB Gap Sealing

To ensure the gas tightness of the panel and gain a flat surface for the o-ring, the gap between the three PCBs needs to be sealed with Araldite 2012. Therefore a line of polyester tape (removable without remnants) is glued on both sides of the gap. The tape should never overlap the gap, but not be more than 0.2 mm away from the gap. The glue is pressed with a perpendicular pointing syringe into the gap between the PCBs and flattened with a spatula. The tape is immediately peeled off by pulling it to the top and slightly away from the gap. Such, a line of

glue in the height of the tape is left on the gap. After 15-20 min of curing, this line is cut with a sharp blade on the PCB surface. The glue should be cured such, that is not sticky any more, but still not completely hardened, so it can be well cut. The ideal texture is identified by the cut off line peeling of the blade and not bulking at the cut.

5.3 Panel Quality control

In the following part the quality control methods applied to the finished sandwich are described.

Quality Check	Description	Limits
Visual inspection	The panel is inspected from both sides for visual deformations. At suspect areas the straight-edge with front-lightning can be used	No deformations should be visible
Tapping test	Both sides are carefully tapped with the fingers at the full surface.	The PCB material should not be able to deform nor sound hollow.
Planarity measurement	A measurement with the laser head on the CMM is performed using a grid of $20 \times 20 \text{ cm}^2$ on each side of the panels sucked to and floating the granite table. A calibration measurement of the granite table is subtracted and the deviation to a plane is calculated	RMS of the deviation $< 37 \mu\text{m}$
Mean thickness	The thickness of the panel is measured at 20 points uniformly distribute on the border of the panel.	Expected thickness: 11.2 mm
Leakage test	The panel is mounted to the gas test stand, 3 mbar overpressure are applied and the pressure drop is recorded	Leak rate less than $10^{-5} \text{ bar l s}^{-1}$

The finished and checked panel is marked with a unique identification number, wrapped dedicated bubble foil bags and transported on dedicated cart in the storage room.

A.2.3 SM2 Drift Panel Construction Database Manual

SM2 Database Manual for the Mainz Construction Site



Last modified: 12/11/2017

Contents

1	Introduction	2
2	Installation	2
2.1	Connection to the Cloud storage	2
2.2	Requierements for the program	3
2.3	Download and configure the code	3
3	The Interface	4
3.1	Bar quality control	4
3.2	Honeycomb quality control	5
3.3	PCB quality control	5
3.4	Panel assembly	6
3.5	Panel quality control	6
3.6	CMM measurement	6
4	CMM scan	7
5	Gas tightness measurement	7
6	Export to the CERN central database	7
6.1	Script setup on lxplus	8
6.2	Raw material parenting	8
6.3	Panel Measurements export	8

1 Introduction

The materials used for the NSW construction are stored in two different databases at CERN. One database is for the tracking of the material and one for the storage of quality control measurements. A web interface for both databases can be accessed via <http://atlas-project-nsw-log.web.cern.ch/atlas-project-nsw-log/index.php>.

At the construction site an independent database framework is implemented. It is written in python with the Kivy GUI and a sqlite backend. Sqlite is chosen for the database, to be independent from connections to a server. Therefore, special care needs to be taken, if the database is used from different machines to keep all database files updated. Therefore one database file is stored in a cloud storage for the exchange and a special update method was implemented. It has to be ensured, that the update is done before and after each work.

The main machines for the work with the database are the computer in the construction lab and the tablet for the flexible raw material quality control.

For large datasets, database operations can take a some time to be executed. All methods are triggered by a button. If this button is still in state "down" (color changed), please wait for the method to finish.

In the following document, the setup and installation of the database are described for Windows and Linux and the handling of the database app and the import and export with the central databases at CERN are explained.

Data is imported and exported from and to the central database via .csv files. An interface is provided for the import of files. The export is done when the parts are assembled as a panel.

2 Installation

The setup of the database is described in the following. Several components need to be installed and configured. First the connection to the cloud for the exchange of measurements and results needs to be established. The environment for the program has to be setup and the code has to be checked out from the git repository.

2.1 Connection to the Cloud storage

As a cloud storage, Seafile as provided by JGU Mainz is used. The desktop client is already installed on the dedicated computers. If you need to install it, please follow the instructions on the web page (<https://www.rhrk.uni-kl.de/seafile/>) and make sure to install the version with the shibboleth support. To setup the desktop client, please register your user account first as described on the website (<https://www.rhrk.uni-kl.de/seafile/seafile-fuer-windows-linux-und-mac/windows-10-einrichtung-des-klient/>).

Afterward a client with the shared libraries should be shown. You will for sure have the library "NSW.SM2.MZ" and if you work with planarity scans, you also have "NSW.SM2.MZ.CMM". To add the libraries to your synchronization, right click on it and select "Synchronise" or "Ordner herunterladen", depending on your language settings. Please remember the path to the folders for the later configuration

In "NSW_SM2_MZ" there is one folder called documentation, where all manuals are stored.

2.2 Requierements for the program

To run the database app, python 2.7 (with numpy, scipy) and kivy 1.9 need to be installed. For quidance, please check <https://wiki.python.org/moin/BeginnersGuide/Download> and <https://kivy.org/docs/installation/installation.html>.

Additionally a package to display a calendar is needed. Please type

```
pip install KivyCalendar
```

in the command shell of you operating system.

2.3 Download and configure the code

To download the code from the git repository, open a command shell (on windows use the git bash coming with the git installation, it can be found under C:/Öffentlich(Public)/Git/bit-bash.exe. If it is not there, please download the git for windows portable and unpack it to there.) and type on the tablet

```
git clone /c/Users/Public/QC_App/
```

or on the linux machine in the lab type

```
git clone /opt/qc_software/QC_App/
```

Navigate to the new folder

```
cd QC_App
```

and create a folder "database" for the storage of your local version of the database

```
mkdir database
```

Now some path variables have to be set. They are loaded by the program from a config file. This config file can be found in the seafiler folder "NSW_SM2_MZ/-Documentation/config.cfg". Copy this file to the folder "QC_App" and change the variables in sharp Brackets. On the tablet an installation of Notepad++ can be found in C:/Users/Public/Notepad/. If you are working on windows, please change all path separators "/" to "\". On Windows you also have to exchange the ./ in the path of the local database with the full path

If you want to work with the CMM analysis software, set "enable" und "[flatnessAnalysis]" in the config file to "True". In that case you need to compile the analysis software (requires gcc and root). To do so change to the folder "CMM/code" and execute

```
make
```

```
make -f MakefileDiffCombined
```

```
make -f MakefilePlotter
```

Now you should be able to start the database program. Manage in the command shell in the folder "QC_App" and run

```
python mainProd.py
```

Table 1: *Equipment types in the database*

FDRI	frame type 2.1 (outer frame)
FDII	frame type 2.2 (inner frame)
HOCL	honeycomb raw material
HCS6	cut honeycomb small
HCS7	cut honeycomb middle
HCS8	cut honeycomb large
BOS6	outer skin board small
BOS7	outer skin board middle
BOS8	outer skin board large
BDS6	cathode board small
BDS7	cathode board middle
BDS8	cathode board large
DS2O	outer drift panel
DS2C	central drift panel

A window for the GUI should open now. Do not worry it takes a while to build up everything.

3 The Interface

In the following the different views of the database interface are described. The interface is divided in two parts. A button menu on the left side and a view with a table displaying the parts on the right side. This view is structured with tabs in the different stages of the parts. The tabs contain lists of the parts on the construction site. The list can be filtered by entering an value or part of a value in the text input at the top of the table.

All parts have a unique id, an MTF ID from the central tracking database and maybe an alias id from the manufacturer. The MTF ID also contains the equation code (eqCode) which specifies the type of the part. An overview can be found in table 1.

3.1 Bar quality control

Two quality checks are performed for the bars. The vertical bending with fillar gauges and the thickness check with the limbo test. Before the quality control a database id has to assigned to the bar. The range of numbers for the different bar types will be provided in an additional document to ensure the correct parenting to the raw bars in the central tracking database. The number of the bar is written on one small side of the bar. For the trapezoidal shaped bars, it should be the longer side. Next to the number, an arrow is noted pointing to one of the grooved sides.

For the bending quality control, the bar is selected in the table and the interface started with the button "Bending QC". The button "Create canvas" need to be pressed, to create a grid, which allows to mark the position of the deviation. The bar is first placed with the number facing up on the table. The gap to the table is checked with the gauges and the highest value is stored in the database.

Therefore the "Add" button next to the measured number is pressed. Now two overlapping circles appear. They can be moved with the cursor or on touch and are positioned to show the deviation. An indicator can be removed by selecting the corresponding entry in the table on the left and pressing the "delete" button. Only the deviation per site need to be registered.

The "Next" button opens the interface for the deviation of the bar turned by 180°. The deviation is entered in the same way as for the first side. Finally an interface where it needs to be selected whether the bending quality control is finished or not.

For the limbo quality control, the button "Limbo QC" has to be pressed after selecting the bar. Via drop down menus, it can be selected if the quality control is passed or not. Side one refers to the side where the arrow, marked when writing down the number on the side, points. With the next button, again the interface to enter whether the limbo quality was finished is entered. On this interface finished has to be selected, even if the other quality control (bending qc for limbo qc and vice versa) was not done yet. It only counts for one part of the quality control.

3.2 Honeycomb quality control

The honeycomb quality control is already finished and will not be described here.

3.3 PCB quality control

There are two different kinds of pcbs, which are treated differently in the database. The cathode boards are registered as single items and the outer skin boards as a group of items. For the cathode boards, the single item can be selected, chosen by its alias id which is written on the board. Attention, the alias ids are not unique for the full database, but only for one size of pcbs. Therefore also the eqCode has to taken into account.

For the outer skin boards, the group with the "eqCode" corresponding to the size of the pcb has to be selected. To store their measurement in the database, a number has to be assigned. Therefore the alias id assigned at CERN will be used. It is written on one side of the pcb. It contains three groups of numbers and digits. The first digits indicate the size of the pcb. The second group of digits groups different deliveries to CERN and the last digits a number in that batch. The last two groups are entered to the text input of the opening popup. The number groups are separated by an underscore "_". For example if "S06 S02 001" is written on the pcb, "S02_001" is entered.

The interface to enter the measured values is the same for all types of boards. The measured value is entered in the text input. If the measured side of the pcb has copper until the edge, it is measured on the copper. In the table overview of the measured values, only the deviation to the nominal value is displayed and also stored in the database to cope for the difference, if it was measured on copper or plain FR4. If a value has to be changed, it can be selected in the table and modified with the "Change Value" button. When the quality control is finished it is stored with the "Finish" button. The "Back" button moves back to the table view without declaring the part to be controlled.

3.4 Panel assembly

To track the raw material to a panel, it has to be assigned in the database. In the panel tab "Assembly", the a id for the new panel is selected. Attention, watch for the correct equation code for an outer or inner drift panel. With the buttons on the left, the GUIs to link the frames, pcbs and honeycombs are opened. When the linking is finished, the parenting has to be exported to a .csv with the "Export Parenting" button, before the quality can be done. The .csv will be stored in the folder specified in the config file (normally it should be in the seafile cloud).

3.5 Panel quality control

When the parenting for a panel is done, it appears in the "Drift panel" tab. There it can be selected and the quality control can be started.

The absolute thickness measurement is entered on a pop-up similar to the pcb quality control. A detailed description can be found there.

The gluing date for the first and second side can be entered in the first row. The date has to be formatted as dd.mm.yyyy.

The CMM flatness measurement can be analyzed via the GUI. The "Import" button allows to select the measurement. Only measurements suited for the chosen configuration are displayed. The wanted measurements and reference runs have to be selected for the left and right sensor position. After pressing the button, a pop-up opens and stays open for the time of the analysis. When the analysis is finished the rms, min and max are stored in the database and display on the GUI. A pdf with the plots can be found under the path specified in the config file in a folder named like the panel id.

The tightness measurement is also analyzed from the GUI. The "Import" button opens a file screen, where the data file has to be selected. The default path is set to the Seafiler folder for the storage of the tightness test data. When the file selection is confirmed, the fitting range has to be specified in the next window. The numbers are entered in the two text fields on the top and the input is confirmed with the "Apply" button. The fit data is highlighted in red. On the final screen, the results of the analysis are shown.

For each measurement, a comment text field is provided. They should be used to enter information on the measurement. General information on the panel, e.g. the reason for acceptance despite bad measurements, is entered to the comment field on the main panel quality control page.

When all measurements are finished the panel has to be moved to the next step in the quality control. By pressing the "Finish" button, all measurements are written to a file for the export to the central database and an overview .pdf file with all measurements of the panel is created at SeafilerFolder/panelExport/-panelOverview.

3.6 CMM measurement

The CMM measurement are tracked in the database. Via the "Measurement" button, the "CMM measurement" can be entered. The measurement name has to be completed and checked for correctness. It already shows the first digits of the current date, which is part of the measurement name. Furthermore the

additional information on the measurement has to be added.

4 CMM scan

The CMM is controlled via an labview interface on the network disk "Q11" in the folder "MMMeasurements/history". The program imCoDemo.vi has to be opened. It has to be ensured, that the green button on the CMM controller under the granite table is not blinking. If it is, the button has to be pressed.

To connect the system to the control panel, the "Power" button on the interface has to be pressed. Afterwards the two lights for "power" and "Homing needed" should light up. If they do not, reinitialize the system by pressing the "Power" button again. Afterwards the homing button has to be pressed and the sensor will move to its zero position.

To efficiently perform a scan, the speed has to be set to 50 (text field on the upper right). The range of the scan is entered in the text fields. A panel is measured twice. Once with a sensor on the left of the mount and once with the sensor on the right. To move the sensor, the screw on the top can be opened.

For the X range 0-1260 is entered for the left sensor position and 800-1260 for the right sensor position. The width is always kept at 20. All values are in millimeters. The Z position is aimed to be constant. A value where the measured surface is in the range of the sensor (green light on the top of the sensor) has to be chosen. For a panel on the granite table or the plain granite table 270 is a good value. Since always an range with the start value different of the end value has to be specified. Therefore the width has to be made larger than the difference of the start and end value, so no second value is chosen. For example 270 to 300 with a width of 100 can be chosen.

The Y range is for all values 0 to 1700 with a width of 20.

With the "Execute" button, the measurement can be started. A saving dialog opens and the measurement should be stored in the correct seafile folder. Otherwise it has to be copied to the cloud via the web interface. The measurement needs to be registered in the database.

5 Gas tightness measurement

The gas tightness measurement is recorded by a python module, which is stored in the folder "runGastest" in the git repository of the GUI. To start a measurement, navigate to this folder and enter:

```
python3 startGasTest.py FILENAME.pkl
```

As soon as the measurement is started, the values are shown in a plot as a preview. If not all 10 lines of the temperature sensor show up, the measurement has to be restarted. The option `-override` has to be used, if the output file name already exists.

6 Export to the CERN central database

Two different database exist at CERN for the storage of the measurements of all construction sites (central database) and to follow the tracking of the equipment

(logistics database). In the logistics database the parenting of the raw material and the status of the panels is recorded. All measurements are exported to the central database after the panel completion. In the following, the steps necessary to fill both databases are described. The data is exported as .txt/.csv files from the local database and uploaded via scripts to the central database from lxplus.

6.1 Script setup on lxplus

The scripts for the data import to the central can be retrieved from the git repository

```
git clone ssh://git@gitlab.cern.ch:7999/temming/
ATLAS.NSW.LOG.IMP.git
```

In the git folder, an additional folder "files" for the storage of the import data has to be created. It is recommended to delete files which are exported from this folder again to keep an overview of the files. The data for the log in is saved in an additional file secrets.py. This file is stored in the git repository of the local database interface. The file has to be copied to the base directory of the scripts.

6.2 Raw material parenting

For each panel, a .txt file with the parenting of the raw material is written to folder pathToSeafiler/panelExport/. For each panel the file, containing the panel id and the date when the panel was saved in unix time, has to be copied to the folder files in the directory of the import scripts on lxplus. After the copying, the file is moved to the folder exportedFiles to keep track which files are already uploaded. The upload on lxplus is done by

```
python parenting.py files/FILENAME —prod
```

6.3 Panel Measurements export

Three steps are necessary after the panel quality control is finished.

1. For all finished panels, the status has to be changed in the log database as soon as possible. Therefore login to the web interface and select the panel by its id in the "Display Equipment" tab. Change the status to "completed, bare", enter the current date in the appearing text field and save the changes with the button "Save changes in Input Fields".
2. When finishing the quality control of a panel, a .txt file containing the panel id in the file name with all measurement is created at SeafilerFolder/panelExport and all the plots necessary for the export are copied to this folder. The .txt file and the plots have to be copied to the files folder on lxplus. Afterwards the import to the central database is done by

```
python measurements.py files/FILENAME.txt ger
Mainz —prod
```

3. The overview .pdf file with all measurements of the panel is attached to the panel in the logistics database. The file is uploaded via the web interface. The panel is loaded on the "Display equipment" tab by its id and the dialog appearing when pushing the "Upload new Doc" button is followed.

A.2.4 SM2 Drift Panel Gluing Check List

SM2 Driftpanel Construction Checklist for the Mainz Construction Side

Last changed: 02/04/2017


First Day

- Prepare and clean vacuum tables
- Clean PCBs with isopropyl and sticky roller and place them on the vacuum table, starting on the small side
- Seal gab between the PCBs with 8 mm capton tape
- Pump vacuum to vacuum table 1 (-300 mbar)
- Seal outer side of PCBs with 12 mm capton tape
- Test assembly of bars and honeycomb
- Place HV and gas feed-through and adapt honeycomb cutting
- Place and check with the template the position of interconnection pieces
- Prepare grounding contact pieces with all surrounding frames by opening cells of the honeycomb
- Check the side bars for a bending to the inside (non contact with the fingers).
- Remove honeycomb, aluminum bars and the HV feed-through and place them in the same orientation on the wooden plate
- Seal the holes in the gas connector and the HV feed-through with round pieces of capton tape
- Apply tape shimming to the bars
- Clean the PCB and the frames with acetone, mark gluing space with the template and clean the PCBs with the sticky roller
- Mix Araldite 2011 (720 g, A: 400 g, B: 320 g)
- Apply a uniform layer of glue to the PCB using the wired spatula until the contact point of the frame with the fingers
- Apply glue with the dedicated tool to the bars to fill the grooves
- Place bars on bars, honeycomb, feed-throughs and interconnection pieces
- Place gas connector and seal the gap in the frame
- Place aluminium plate and vacuum bag
- Check and regulate pressure at vacuum bag to be ≈ 100 mbar more than in vacuum table
- Apply a small quantity of remaining glue on a tape placed near the vacuum table and write down the finish time of the gluing

Second Day

- Check for the curing of glue sample
- Prepare vacuum table 2 and remove the vacuum bag from vacuum table 1
- Check planarity of the honeycomb with respect to the frames with straight-edge
- Fix grounding contact between honeycomb, frames and gas connector
- Unscrew alignment finger and vent the vacuum table
- Move the half panel to the cleaned second vacuum table
- Measure the thickness of the panel and remove the copper wires between the PCBs during the moving
- Apply vacuum to the second vacuum table (-200 mbar)
- Seal the border of the workpiece with tape, place 0.4 mm wires under the tape
- Glue copper tape at the distance piece positions
- Check contact between vacuum table and all copper tapes
- Align cleaned PCBs on cleaned first vacuum table and seal them (copper wire on the inclined side with the thin finger)
- Put the thin fingers on the inclined side facing the wall (two) and the long side (one)
- Place distance pieces on vacuum table surface and check LED system
- Flip second vacuum table with workpiece as a test and check for contact with distance pieces (check monitoring LEDs)
- Mark gluing area with the template
- Clean the PCB surface with the sticky roller
- Mix Araldite 2011 0.3 mm wires: 810 g, A: 450 g, B: 360 g; 0.4 mm wires: 900 g, A: 500 g, B:400 g)
- Apply an uniform layer of Araldite 2011 to the PCBs using the wired spatula (0.3 mm wires) and do not exceed the marks
- Apply glue to the bars of the half panel and interconnections
- Flip second vacuum table with work-piece to the first vacuum table (slowly on the last centimetres!!!)
- Make sure to press frame of work-piece against the thin fingers while lowering the vacuum table
- Never lift the second vacuum table after the work-piece had contact with the glue!
- Hook tension less metal rope connected to the wall in the loop at the vacuum table and tension metal rope
- Check the LED monitoring system (some LED might light up later when the upper vacuum table sinks to the glue, press at the position of non light up LEDs)
- Apply sample of remaining glue on tape next to the vacuum table and note finishing time

A.2.5 SM2 Drift Panel Gluing Quality Control Sheet

SM2 Drift Panel Gluing Sheet							
Panel ID:							
Frames		Honeycomb		PCB			
Top:		Top:		Top S1:			
Top Middle:		Middle:		Middle S1:			
Bottom Middle:		Bottom:		Bottom S1:			
Bottom:				Top S2:			
Left:				Middle S2:			
Right:				Bottom S2:			
First Day							
Date:							
Team:							
Dry assembly:							
		Signature Expert		Signature Technician			
Gluing							
Glue mixed:		Glue left:		Start time:		End time	
Comments:							
Second Day							
Date:							
Team:							
Dry assembly:							
		Signature Expert		Signature Technician			
Gluing							
Glue mixed:		Glue left:		Start time:		End time	
Comments							

A.2.6 SM2 Drift Panel Quality Control Result Overview

SM2 BARE DRIFT PANEL

20MNMD52C00034
20495



GLUING DATE

Side 1 01/08/2018 Side 2 02/08/2018

RAW MATERIAL PARENTING

	FRAME		HONEYCOMB		Pcb
TOP	19557	TOP	5383	TOP S1	12948
CENTRAL TOP	9183	MIDDLE	5250	MIDDLE S1	12862
CENTRAL BOTTOM	19486	BOTTOM	5082	BOTTOM S1	12815
BOTTOM	19596			TOP S2	129472
LEFT	19611			MIDDLE S2	12861
RIGHT	19614			BOTTOM S2	12814

GENERAL COMMENTS

PANEL THICKNESS

MEAN	RMS	MIN	MAX
-33 μm	19 μm	-79 μm	-4 μm

The values are relative to the nominal thickness 10.33 mm

COMMENTS:

PANEL PLANARITY

	RMS	MIN	MAX
SIDE 1 SUCKED	24 μm	-65 μm	117 μm
SIDE 2 SUCKED	23 μm	-73 μm	115 μm
SIDE 1 FLOATING	25 μm	-85 μm	117 μm
SIDE 2 FLOATING	31 μm	-95 μm	135 μm

The values are relative to the average thickness

COMMENTS:

SIDE 1 SUCKED
SIDE 2 SUCKED
SIDE 1 FLOATING
SIDE 2 FLOATING

PANEL TIGHTNESS

SIDE 1 0.301 10^{-5} bar Ls $^{-1}$ SIDE 2 0.224 10^{-5} bar Ls $^{-1}$

COMMENTS:

SIDE 1 SUCKED
SIDE 2 SUCKED

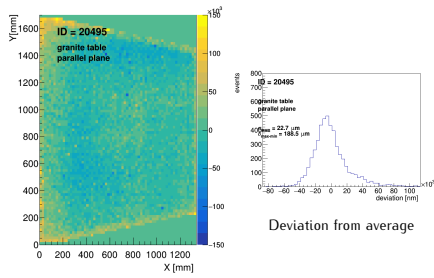
SM2 BARE DRIFT PANEL

20MNMD52C00034
20495

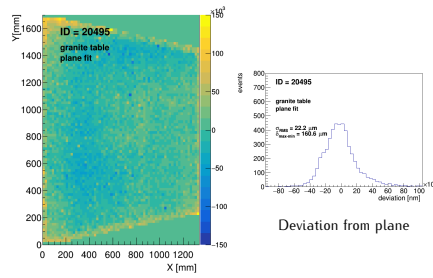


PLOTS

PANEL PLANARITY S₁ SUCKED

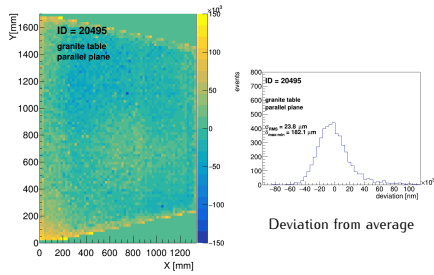


2D Deviation from average

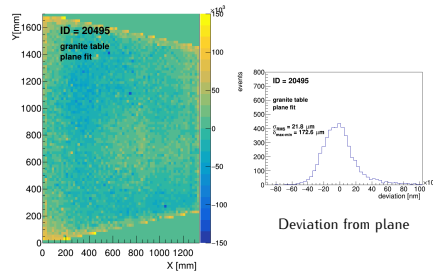


2D Deviation from plane

PANEL PLANARITY S₂ SUCKED

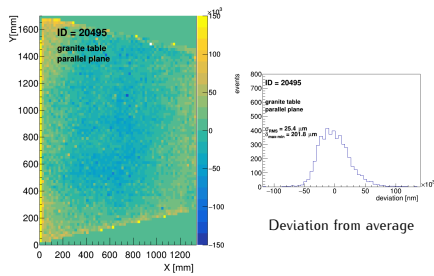


2D Deviation from average

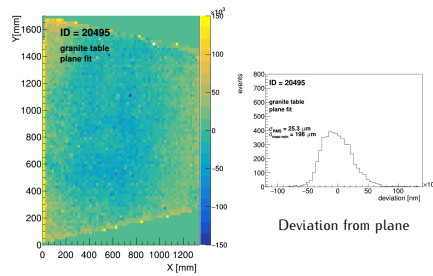


2D Deviation from plane

PANEL PLANARITY S₁ FLOATING



2D Deviation from average



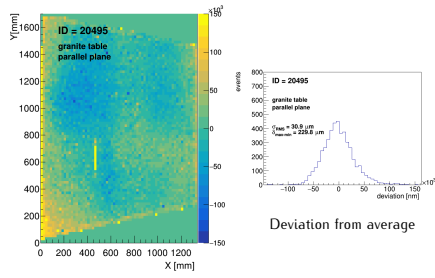
2D Deviation from plane

SM2 BARE DRIFT PANEL

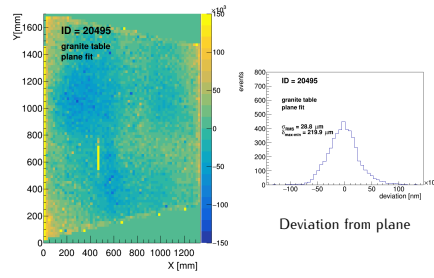
20MNMD52C00034
20495



PANEL PLANARITY S₂ FLOATING

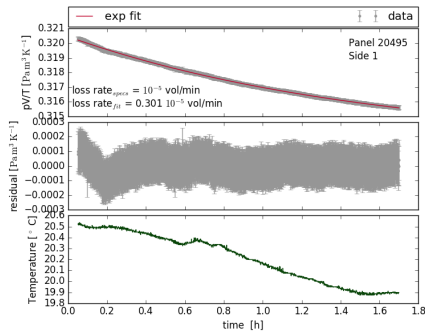


2D Deviation from average

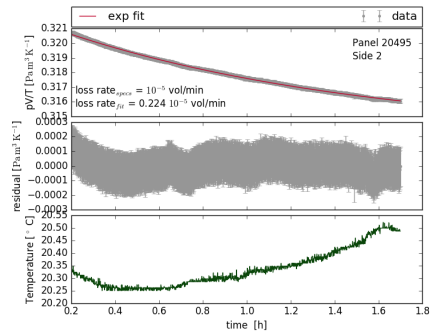


2D Deviation from plane

PANEL TIGHTNESS

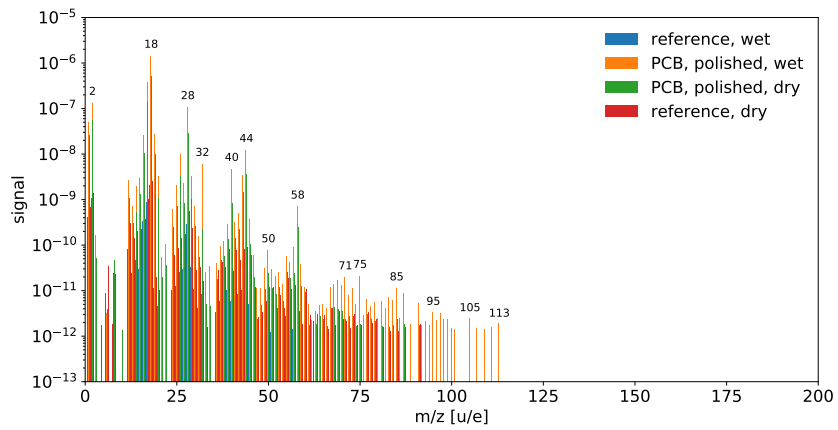


Side 1

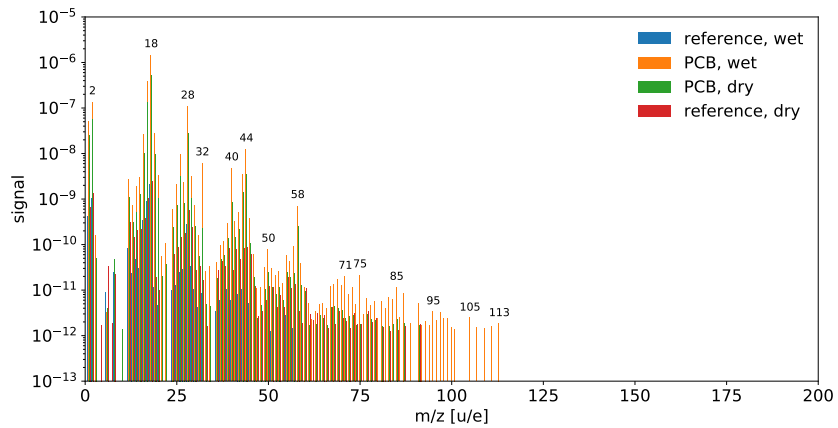


Side 2

A.2.7 Material Degassing



(a)



(b)

Figure A.10. Component outgassing before and after drying. The reference run of the empty mass spectrometer is shown as a comparison to estimate the measurement significance.

Bibliography

- [1] David J. Griffiths. Introduction to elementary particles, 2009.
- [2] Francis Halzen and Alan D. Martin. Quarks and leptons : an introductory course in modern particle physics, 1984.
- [3] M. Tanabashi et al. Review of particle physics. *Phys. Rev. D*, 98:030001, Aug 2018.
- [4] Matthias Schott and Monica Dunford. Review of single vector boson production in pp collisions at $\sqrt{s} = 7$ tev. *The European Physical Journal C*, 74(7):2916, Jul 2014.
- [5] J. J. Thomson M.A. F.R.S. XI. cathode rays. *The London, Edinburgh, and Dublin Philosophical Magazine and Journal of Science*, 44(269):293–316, 1897.
- [6] Carl D. Anderson. The positive electron. *Phys. Rev.*, 43:491–494, Mar 1933.
- [7] J. J. Aubert, U. Becker, P. J. Biggs, J. Burger, M. Chen, G. Everhart, P. Goldhagen, J. Leong, T. McCorrison, T. G. Rhoades, M. Rohde, Samuel C. C. Ting, Sau Lan Wu, and Y. Y. Lee. Experimental observation of a heavy particle *j*. *Phys. Rev. Lett.*, 33:1404–1406, Dec 1974.
- [8] J. E. Augustin, A. M. Boyarski, M. Breidenbach, F. Bulos, J. T. Dakin, G. J. Feldman, G. E. Fischer, D. Fryberger, G. Hanson, B. Jean-Marie, R. R. Larsen, V. Lüth, H. L. Lynch, D. Lyon, C. C. Morehouse, J. M. Paterson, M. L. Perl, B. Richter, P. Rapidis, R. F. Schwitters, W. M. Tanenbaum, F. Vannucci, G. S. Abrams, D. Briggs, W. Chinowsky, C. E. Friedberg, G. Goldhaber, R. J. Hollebeek, J. A. Kadyk, B. Lulu, F. Pierre, G. H. Trilling, J. S. Whitaker, J. Wiss, and J. E. Zipse. Discovery of a narrow resonance in e^+e^- annihilation. *Phys. Rev. Lett.*, 33:1406–1408, Dec 1974.
- [9] G. Arnison et al. Experimental Observation of Isolated Large Transverse Energy Electrons with Associated Missing Energy at $s^{**}(1/2) = 540$ -GeV. *Phys. Lett.*, B122:103–116, 1983. [,611(1983)].
- [10] G. Arnison et al. Experimental Observation of Lepton Pairs of Invariant Mass Around 95-GeV/c**2 at the CERN SPS Collider. *Phys. Lett.*, B126:398–410, 1983. [,7.55(1983)].

- [11] Georges Aad et al. Observation of a new particle in the search for the Standard Model Higgs boson with the ATLAS detector at the LHC. *Phys. Lett.*, B716:1–29, 2012.
- [12] Serguei Chatrchyan et al. Observation of a new boson at a mass of 125 GeV with the CMS experiment at the LHC. *Phys. Lett.*, B716:30–61, 2012.
- [13] Fabienne Marcastel. CERN’s Accelerator Complex. La chaîne des accélérateurs du CERN. Oct 2013. General Photo.
- [14] G. Aad et al. The ATLAS Experiment at the CERN Large Hadron Collider. *JINST*, 3:S08003, 2008.
- [15] The ATLAS Collaboration. Measurement of the W-boson mass in pp collisions at $\sqrt{s} = 7$ TeV with the ATLAS detector. *The European Physical Journal C*, 78(2):110, Feb 2018.
- [16] Joao Pequena. Computer generated image of the whole ATLAS detector. Mar 2008.
- [17] Joao Pequena and Paul Schaffner. An computer generated image representing how ATLAS detects particles. Jan 2013.
- [18] *ATLAS magnet system: Technical Design Report, 1*. Technical Design Report ATLAS. CERN, Geneva, 1997.
- [19] D. E. Baynham, J C Butterworth, F. S. Carr, C. Densham, E. Holtom, J. Rochford, E. F. Towndrow, Gert-Jan Luijckx, H. J. Geerinck, Y. Lefevre, and Mathijs Doets. Atlas end cap toroid magnets cryostat design, manufacture and integration at cern. *IEEE Transactions on Applied Superconductivity*, 14:522–525, 2004.
- [20] *ATLAS inner detector: Technical Design Report, 1*. Technical Design Report ATLAS. CERN, Geneva, 1997.
- [21] Joao Pequena. Computer generated image of the ATLAS inner detector. Mar 2008.
- [22] *ATLAS liquid-argon calorimeter: Technical Design Report*. Technical Design Report ATLAS. CERN, Geneva, 1996.
- [23] *ATLAS tile calorimeter: Technical Design Report*. Technical Design Report ATLAS. CERN, Geneva, 1996.
- [24] Joao Pequena. Computer Generated image of the ATLAS calorimeter. Mar 2008.
- [25] ATLAS muon spectrometer: Technical design report. 1997.

- [26] A Combination of preliminary electroweak measurements and constraints on the standard model. 2001.
- [27] Y. Amhis et al. Averages of b -hadron, c -hadron, and τ -lepton properties as of summer 2016. *Eur. Phys. J.*, C77:895, 2017. updated results and plots available at <https://hflav.web.cern.ch>.
- [28] Mathias Uhlenbrock. *Studies into the mis-identification probability of tau leptons and a measurement of the cross section ($pp \rightarrow W$) \times $BR(W \rightarrow)$ at a center-of-mass energy of $s = 7$ TeV with the ATLAS detector*. PhD thesis, Bonn U., 2015.
- [29] M. Tanabashi et al. Review of particle physics. *Phys. Rev. D*, 98:030001, Aug 2018.
- [30] ATLAS Collaboration. Improved luminosity determination in pp collisions at $\sqrt{s} = 7$ TeV using the ATLAS detector at the LHC. *Eur. Phys. J. C*, 73:2518, 2013.
- [31] ATLAS Collaboration. Topological cell clustering in the atlas calorimeters and its performance in lhc run 1. *The European Physical Journal C*, 77(7):490, Jul 2017.
- [32] ATLAS Collaboration. Measurement of the muon reconstruction performance of the ATLAS detector using 2011 and 2012 LHC proton–proton collision data. *Eur. Phys. J.*, C74(11):3130, 2014.
- [33] Paolo Nason. A New method for combining NLO QCD with shower Monte Carlo algorithms. *JHEP*, 11:040, 2004.
- [34] Stefano Frixione, Paolo Nason, and Carlo Oleari. Matching NLO QCD computations with Parton Shower simulations: the POWHEG method. *JHEP*, 11:070, 2007.
- [35] Simone Alioli, Paolo Nason, Carlo Oleari, and Emanuele Re. A general framework for implementing NLO calculations in shower Monte Carlo programs: the POWHEG BOX. *JHEP*, 06:043, 2010.
- [36] Hung-Liang Lai, Marco Guzzi, Joey Huston, Zhao Li, Pavel M. Nadolsky, Jon Pumplin, and C. P. Yuan. New parton distributions for collider physics. *Phys. Rev.*, D82:074024, 2010.
- [37] Torbjörn Sjöstrand, Stephen Mrenna, and Peter Skands. Pythia 6.4 physics and manual. *Journal of High Energy Physics*, 2006(05):026, 2006.
- [38] Torbjorn Sjostrand, Stephen Mrenna, and Peter Z. Skands. A Brief Introduction to PYTHIA 8.1. *Comput. Phys. Commun.*, 178:852–867, 2008.

- [39] J. Pumplin, D. R. Stump, J. Huston, H. L. Lai, Pavel M. Nadolsky, and W. K. Tung. New generation of parton distributions with uncertainties from global QCD analysis. *JHEP*, 07:012, 2002.
- [40] Piotr Golonka and Zbigniew Was. PHOTOS Monte Carlo: A Precision tool for QED corrections in Z and W decays. *Eur. Phys. J.*, C45:97–107, 2006.
- [41] Stefano Frixione and Bryan R. Webber. Matching nlo qcd computations and parton shower simulations. *Journal of High Energy Physics*, 2002(06):029, 2002.
- [42] Stefano Frixione, Paolo Nason, and Bryan R. Webber. Matching nlo qcd and parton showers in heavy flavour production. *Journal of High Energy Physics*, 2003(08):007, 2003.
- [43] Stefano Frixione, Eric Laenen, Patrick Motylinski, and Bryan R. Webber. Single-top production in mc@nlo. *Journal of High Energy Physics*, 2006(03):092, 2006.
- [44] Gennaro Corcella, Ian G. Knowles, Giuseppe Marchesini, Stefano Moretti, Kosuke Odagiri, Peter Richardson, Michael H. Seymour, and Bryan R. Webber. Herwig 6: an event generator for hadron emission reactions with interfering gluons (including supersymmetric processes). *Journal of High Energy Physics*, 2001(01):010, 2001.
- [45] J. M. Butterworth, J. R. Forshaw, and M. H. Seymour. Multiparton interactions in photoproduction at hermes. *Zeitschrift für Physik C: Particles and Fields*, 72(4):637, Dec 1996.
- [46] Nansi Andari, Jean-Baptiste Blanchard, Maarten Boonekamp, Stefano Camarda, Aleksandra Dimitrievska, Remie Hanna, Chris Hays, Mikhail Karnevskiy, Oleh Kivernyk, Matthias Schott, Giovanni Siragusa, Raimund Strohmer, Nenad Vranjes, Samuel Webb, and Christoph Zimmermann. Measurement of m_W with 7 TeV data: W boson mass measurement. Technical Report ATL-COM-PHYS-2014-1569, CERN, Geneva, Dec 2014.
- [47] K Bachas, M Bellomo, F Buehrer, S Camarda, A Cooper-Sarkar, J Dassoulas, R S Hickling, F Ellinghaus, C Issever, C T Jeske, D Froidevaux, L Iconomidou-Fayard, A Glazov, T Guillemin, A Kapliy, M Karnevskiy, M Klein, U Klein, J Kretzschmar, T Kono, A Lewis, K Lohwasser, M Lisovyi, T Matsushita, J Maurer, P Onyisi, E Richter-Was, E Rizvi, V Radescu, P Sommer, G Sedov, T Serre, A Schaffer, S Schmitt, J Sandler, M Shochet, J Tseng, M Vincter, M Wielers, E Yatsenko, Oleh Kivernyk, and Andrey Sapronov. Measurement and QCD Analysis of Differential Inclusive $W^\pm \rightarrow l\nu$ and $Z/\gamma^* \rightarrow ll$ Production and Leptonic Decay Cross Sections with ATLAS: Analysis STDM-2012-20: W and Z inclusive

cross section with 2011 data. Technical Report ATL-COM-PHYS-2013-217, CERN, Geneva, Feb 2012.

- [48] Georges Aad et al. Measurement of the $t\bar{t}$ production cross-section using $e\mu$ events with b -tagged jets in pp collisions at $\sqrt{s} = 7$ and 8 TeV with the ATLAS detector. *Eur. Phys. J.*, C74(10):3109, 2014.
- [49] ATLAS Collaboration. Single boson and diboson production cross section in pp collisions at $\sqrt{s} = 7$ tev. ATL-COM-PHYS-2010-695, 2010.
- [50] Nansi Andari, Maarten Boonekamp, Remie Hanna, and Stefano Camarda. Measurement of m_W at 7 TeV: Physics modeling. Technical Report ATL-COM-PHYS-2014-1436, CERN, Geneva, Nov 2014.
- [51] Sidney D. Drell and Tung-Mow Yan. Massive lepton-pair production in hadron-hadron collisions at high energies. *Phys. Rev. Lett.*, 25:316–320, Aug 1970. [Erratum: *Phys. Rev. Lett.*25,902(1970)].
- [52] John C. Collins and Davison E. Soper. Angular distribution of dileptons in high-energy hadron collisions. *Phys. Rev. D*, 16:2219–2225, Oct 1977.
- [53] Jun Gao, Marco Guzzi, Joey Huston, Hung-Liang Lai, Zhao Li, Pavel Nadolsky, Jon Pumplin, Daniel Stump, and C.-P. Yuan. Ct10 next-to-next-to-leading order global analysis of qcd. *Phys. Rev. D*, 89:033009, Feb 2014.
- [54] E. Mirkes. Angular decay distribution of leptons from w-bosons at nlo in hadronic collisions. *Nuclear Physics B*, 387(1):3 – 85, 1992.
- [55] Transverse momentum distribution in drell-yan pair and w and z boson production. *Nuclear Physics B*, 250(1):199 – 224, 1985.
- [56] G. A. Ladinsky and C.-P. Yuan. Nonperturbative regime in qcd resummation for gauge boson production at hadron colliders. *Phys. Rev. D*, 50:R4239–R4243, Oct 1994.
- [57] C. Balázs and C.-P. Yuan. Soft gluon effects on lepton pairs at hadron colliders. *Phys. Rev. D*, 56:5558–5583, Nov 1997.
- [58] Stefano Catani, Daniel de Florian, Giancarlo Ferrera, and Massimiliano Grazzini. Vector boson production at hadron colliders: transverse-momentum resummation and leptonic decay. *Journal of High Energy Physics*, 2015(12):1–47, Dec 2015.
- [59] Thomas Becher, Matthias Neubert, and Daniel Wilhelm. Electroweak gauge-boson production at small qt: Infrared safety from the collinear anomaly. *Journal of High Energy Physics*, 2012(2):124, Feb 2012.

- [60] Gabriela Miu and Torbjörn Sjöstrand. W production in an improved parton-shower approach. *Physics Letters B*, 449(3):313 – 320, 1999.
- [61] The ATLAS collaboration. Measurement of the z/γ^* boson transverse momentum distribution in pp collisions at $\sqrt{s} = 7$ tev with the atlas detector. *Journal of High Energy Physics*, 2014(9):145, Sep 2014.
- [62] Stefano Catani, Leandro Cieri, Giancarlo Ferrera, Daniel de Florian, and Massimiliano Grazzini. Vector boson production at hadron colliders: A fully exclusive qcd calculation at next-to-next-to-leading order. *Phys. Rev. Lett.*, 103:082001, Aug 2009.
- [63] J. Pumplin, D. Stump, R. Brock, D. Casey, J. Huston, J. Kalk, H. L. Lai, and W. K. Tung. Uncertainties of predictions from parton distribution functions. ii. the hessian method. *Phys. Rev. D*, 65:014013, Dec 2001.
- [64] Aleksandra Dimitrievska, Nenad Vranjes, Matthias Schott, and Maarten Boonekamp. Measurement of m_W at 7 TeV: Hadronic recoil corrections. Technical Report ATL-COM-PHYS-2015-344, CERN, Geneva, Apr 2015.
- [65] L. Devroye. "*Non-Uniform Random Variate Generation*". Springer-Verlag, 1986. Available at <http://www.eirene.de/Devroye.pdf>.
- [66] Christoph Zimmermann. *Towards a first precision measurement of the mass of the W-boson with the ATLAS detector at root out s = 7 TeV*. Univ., Mainz, 2016.
- [67] Christoph Zimmermann, Matthias Schott, and Mikhail Karnevskiy. Measurement of m_W at 7 TeV : Muon efficiency corrections and uncertainties. Technical Report ATL-COM-PHYS-2015-073, CERN, Geneva, Feb 2015.
- [68] Nenad Vranjes, Troels Petersen, and Mikhail Karnevskiy. Measurement of m_W at 7 TeV: Muon momentum corrections and uncertainties. Technical Report ATL-COM-PHYS-2014-1433, CERN, Geneva, Nov 2014.
- [69] The ATLAS Collaboration. Electron reconstruction and identification efficiency measurements with the ATLAS detector using the 2011 LHC proton-proton collision data. *The European Physical Journal C*, 74(7):2941, Jul 2014.
- [70] Kyle Cranmer, George Lewis, Lorenzo Moneta, Akira Shibata, and Wouter Verkerke. HistFactory: A tool for creating statistical models for use with RooFit and RooStats. Technical Report CERN-OPEN-2012-016, New York U., New York, Jan 2012.
- [71] Rene Brun and Fons Rademakers. Root — an object oriented data analysis framework. *Nuclear Instruments and Methods in Physics Research Section A: Accelerators, Spectrometers, Detectors and Associated Equipment*, 389(1):81 – 86, 1997. *New Computing Techniques in Physics Research V*.

- [72] H. A. Bethe. Molière's theory of multiple scattering. *Phys. Rev.*, 89:1256–1266, Mar 1953.
- [73] Gerald R. Lynch and Orin I. Dahl. Approximations to multiple Coulomb scattering. *Nucl. Instrum. Meth.*, B58:6–10, 1991.
- [74] Konrad Kleinknecht. *Detectors for Particle Radiation*. Cambridge University Press, 2. a. edition, 1998.
- [75] MAGBOLZ - transport of electrons in gas mixtures. <http://magboltz.web.cern.ch/magboltz/>. Accessed: 2018-11-29.
- [76] Heinz Raether. Electron avalanches and breakdown in gases, 1964.
- [77] K Nikolopoulos, P Bhattacharya, V Chernyatin, and R Veenhof. Electron transparency of a micromegas mesh. *Journal of Instrumentation*, 6(06):P06011, 2011.
- [78] T Zerguerras, B Genolini, F Kuger, M Josselin, A Maroni, T Nguyen-Trung, J Pouthas, P Rosier, Ö Şahin, D Suzuki, and R Veenhof. Understanding avalanches in a Micromegas from single-electron response measurement. *Nucl. Instrum. Methods Phys. Res., A*, 772:76–82. 7 p, 2015.
- [79] Jonathan Bortfeldt. *Development of floating strip micromegas detectors*. PhD thesis, München, 2014. München, Ludwig-Maximilians-Universität, Diss., 2014.
- [80] Michele Bianco, Hans Danielsson, Jordan Degrange, Andreas Döder, Rui De Oliveira, Edoardo Farina, Fabian Kuger, Paolo Iengo, Francisco Perez Gomez, Tai-Hua Lin, Matthias Schott, Givi Sekhniaidze, Federico Sforza, Ourania Sidiropoulou, Chrysostomos Valderanis, Maurice Vergain, and Jörg Wotschack. Construction of two large-size four-plane micromegas detectors. *Nuclear Instruments and Methods in Physics Research Section A: Accelerators, Spectrometers, Detectors and Associated Equipment*, 814:117 – 130, 2016.
- [81] A. Jankowiak. The Mainz Microtron MAMI: Past and future. *Eur. Phys. J.*, A28S1:149–160, 2006.
- [82] M J French, L L Jones, Q R Morrissey, A Neviani, R Turchetta, J R Fulcher, G Hall, E Noah, M Raymond, G Cervelli, P Moreira, and G Marseguerra. Design and results from the APV25, a deep sub-micron CMOS front-end chip for the CMS tracker. *Nucl. Instrum. Methods Phys. Res., A*, 466(2):359–65, 2001.
- [83] J Toledo, H Muller, R Esteve, J M Monzó, A Tarazona, and S Martoiu. The front-end concentrator card for the rd51 scalable readout system. *Journal of Instrumentation*, 6(11):C11028, 2011.

- [84] mmdaq. <http://indico.cern.ch/event/218341/session/1/contribution/22/material/slides0.pdf>, 27.03.2015.
- [85] Tai-Hua Lin, Andreas Dudder, Matthias Schott, Chrysostomos Valderanis, Laura Wehner, et al. Signal Characteristics of a Resistive-Strip Micromegas Detector with an Integrated Two-Dimensional Readout. *Nucl.Instrum.Meth.*, A767:281–288, 2014.
- [86] CERN. cds.cern.ch. Accessed: 2018-12-04.
- [87] T Kawamoto, S Vlachos, L Pontecorvo, J Dubbert, G Mikenberg, P Iengo, C Dallapiccola, C Amelung, L Levinson, R Richter, and D Lellouch. New Small Wheel Technical Design Report. Technical Report CERN-LHCC-2013-006. ATLAS-TDR-020, Jun 2013. ATLAS New Small Wheel Technical Design Report.
- [88] Institute of Nuclear Chemistry, Johannes Gutenberg-University Mainz. <https://www.nuclear-chemistry.uni-mainz.de/reactor/>.
- [89] David Gerick. *Studies of the non-ionizing radiation hardness and temperature dependence of Silicon Photomultipliers for the LHCb Tracker Upgrade*. PhD thesis, Ruprecht-Karls-Universitat Heidelberg, 2014.
- [90] Detector Laboratory, PRISMA Cluster of Excellence, Johannes Gutenberg University Mainz. http://www.prisma.uni-mainz.de/detector_lab.php.
- [91] P. Bernhard, A. S. Brogna, S. S. Caiazza, A. Dudder, P. Gulker, C. Kahra, T. H. Lin, M. Schott, Q. Weitzel, and E. Yildirim. Construction of large-area micro-pattern gaseous detectors. In *2016 IEEE Nuclear Science Symposium*, pages 1–4, Oct 2016.
- [92] Kivy - Open source Python library for rapid development of applications that make use of innovative user interfaces, such as multi-touch apps. <https://kivy.org>.
- [93] Andreas Dudder, Matthias Schott, Gunther Quast, and Lars Vielsack. Self-Made Particle Detectors for High Schools and Universities. *The African Review on Physics*, 13, 2018.
- [94] Bernard Brickwedde, Andreas Dudder, Matthias Schott, and Eda Yildirim. Design, Construction and Performance Tests of a Prototype MicroMegas Chamber with Two Readout Planes in a Common Gas Volume. *Nucl. Instrum. Meth.*, A864:1–6, 2017.
- [95] A. Dudder, T.-H. Lin, F. Neuhaus, M. Schott, and C. Valderanis. Performance studies of a micromegas detector with a pad readout geometry. *Nuclear Instruments and Methods in Physics Research Section A: Accelerators, Spectrometers, Detectors and Associated Equipment*, 824:526 – 527, 2016. Proceedings of the 13th Pisa Meeting on Advanced Detectors.

- [96] Andreas Dudder, Tai-Hua Lin, Matthias Schott, and Chrysostomos Valderanis. Development and Study of a Micromegas Pad-Detector for High Rate Applications. *Nucl. Instrum. Meth.*, A803:29–35, 2015.

Acknowledgements

B

Thank you to my supervisor [REDACTED] for wonderful five years in his group during my Master and PhD thesis. I really enjoyed the free work environment and highly appreciate the trust in my work. It was a pleasure to have the possibility to lead the NSW project as a PhD student.

Thank you to the Graduate School "Symmetry Breaking" for the financial support.

Thank you to my colleagues: [REDACTED] [REDACTED] [REDACTED] [REDACTED] [REDACTED] [REDACTED] [REDACTED] for their support during my work and the enjoyable time in the group.

Thank you to [REDACTED]. [REDACTED] [REDACTED] [REDACTED] [REDACTED] [REDACTED] [REDACTED] [REDACTED] for the cooperation on the branching ratio fraction measurement. [REDACTED], good luck with the continuation of the measurement: To four percent and beyond!

Thank you to the colleagues from LMU Munich, especially [REDACTED] for the cooperation and manifold support in the detector construction setup.

Thank you to the ATLAS NSW collaboration for the cooperation and recognition in the community.

Thank you to [REDACTED] [REDACTED] [REDACTED] [REDACTED] and especially [REDACTED] for the support of the work in the PRISMA DetLab.

Thank you to everybody who joined the ATLAS New Small Wheel Construction. Ein besonderer Dank an [REDACTED] für die zuverlässige und flexible Hilfe.

Vielen Dank an [REDACTED] für allzeit guten Rat und die großartige Unterstützung bei allen mechanischen Projekten und sonstigen Ideen.

Vielen Dank an alle Freunde für viele entspannende und lustige Abende, zahlreiche kulinarische Höhepunkte und schöne gemeinsame Unternehmungen.

Die Wichtigsten zum Schluss: Vielen Dank meiner Familie. Ihr wisst wofür. Auf Euch kann ich mich immer verlassen!

